Space active mirrors - Active optics developments for future large observatories

Marie Laslandes

UNIVERSITE AIX MARSEILLE
ECOLE DOCTORALE PHYSIQUE ET SCIENCES DE LA MATIÈRE

THESE DE DOCTORAT

presentée pour obtenir le grade de
Docteur de l'université d'Aix-Marseille
Spécialité: *Astrophysique et Cosmologie*

par

Marie Laslandes

Miroirs actifs de l'espace

Développement de systèmes d'optique active pour les futurs grands observatoires

---

soutenue publiquement le 6 novembre 2012
devant le jury composé de:

M. Hugues Giovannini _____ Président
M. Sergio Pellegrino _____ Rapporteur
M. Lars Venema _____ Rapporteur
M. Thierry Bret-Dibat _____ Examinateur
M. Vincent Michau _____ Examinateur
M. Christian Singer _____ Examinateur
M. Marc Ferrari _____ Directeur de thèse
M. Emmanuel Hugot _____ Co-Directeur

Laboratoire d'Astrophysique de Marseille
Technopole de Chateau-Gombert
38, rue Frederic Joliot-Curie
13388 Marseille cedex 13

AIX-MARSEILLE UNIVERSITY
DOCTORAL SCHOOL: PHYSIQUE ET SCIENCES DE LA MATIÈRE

PhD THESIS

presented to obtain the title of Doctor
Specialty: *Astrophysics and Cosmology*

by

Marie Laslandes

Space active mirrors

Active optics developments for future large observatories

---

defended the 6th of November 2012
with the following board of examiners:

M. Hugues Giovannini	President
M. Sergio Pellegrino	Reviewer
M. Lars Venema	Reviewer
M. Thierry Bret-Dibat	Examiner
M. Vincent Michau	Examiner
M. Christian Singer	Examiner
M. Marc Ferrari	PhD Supervisor
M. Emmanuel Hugot	Co Supervisor

Laboratoire d'Astrophysique de Marseille
Technopole de Chateau-Gombert
38, rue Frederic Joliot-Curie
13388 Marseille cedex 13

Les miroirs feraient bien de réfléchir un peu plus avant de renvoyer les images.

Mirrors should think longer before they reflect.

Jean Cocteau

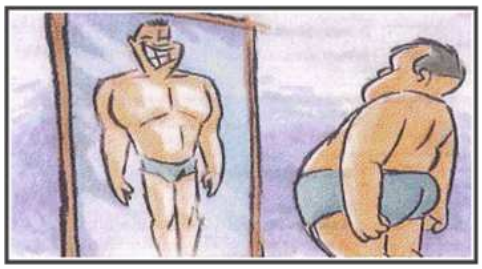

Contents

Notations

General	
Cartesian coordinates	(x, y, z)
Polar coordinates	(r, θ)
Optics	
Wavelength	λ
Diameter	D
Semi diameter	a
Focal length	f
Focal ratio	F
Wave-front	ϕ
Zernike polynomial	Z_i
Zernike coefficient	a_i
Radial and Azimuthal order of a Zernike	n and m
Conic constant	C
Radius of curvature	k
Off-axis distance	R
Mechanic	
Deformation	z
Thickness	t
Young modulus	E
Poisson ratio	ν
Flexural rigidity	D
Intensity of a force	F
Intensity of a uniform load	q
Bending moment	M
Shearing force	V
Stress	σ

Abbreviations table

AO	Adaptive Optics
CM	Command Matrix
COMSA	Correcting Optimized Mirror with a Single Actuator
CTE	Coefficient of Thermal Expansion
DM	Deformable Mirror
E-ELT	European Extremely Large Telescope
ESO	European Southern Observatory
FEA	Finite Element Analysis
FEM	Finite Element Model
FoV	Field of View
GEO	Geostationary Earth Orbit
IF	Influence Function
IM	Interaction Matrix
IR	Infra Red
JWST	James Webb Space Telescope
MADRAS	Miroir Actif Déformable et Régulé pour Applications Spatiales
NTT	New Technology Telescope
OAP	Off-Axis Parabola
OPD	Optical Path Difference
OTF	Optical Transfer Function
PSD	Power Spectral Density
PSF	Point Spread Function
PtV	Peak to Valley
RMS	Root Mean Square
RTC	Real Time Computer
SMP	Stress Mirror Polishing
SNR	Signal to Noise Ratio
SR	Strehl Ratio
SVD	Singular Value Decomposition
TRL	Technology Readiness Level
UV	Ultra Violet
VCM	Variable Curvature Mirrors
VLT	Very Large Telescope
VLTI	Very Large Telescope Interferometer
VOALA	Variable Off-Axis paraboLA
WFE	Wave-Front Error
WFS	Wave-Front Sensor

Introduction

Major astrophysics discoveries have always been driven by advances in instrumentation for astronomy, with telescopes on the front line [Wilson, 1996, 1999]. To see further, it is necessary to increase the collected flux. To see more details, it is necessary to improve the angular resolution. These two characteristics are defined by the primary mirror diameter D: the collecting power evolves with D^2 and the angular resolution with λ/D, λ being the observed wavelength [Hecht, 1987]. Thus, the access to finest observations implies the increase of telescopes' sizes. This evolution, simple to describe, requires many innovations regarding telescopes development.

Firstly, the angular resolution achieved by Earth-based telescopes is limited by the atmospheric turbulence, and by gravity and thermo-elastic deformations. For about 30 years, developments in active and adaptive optics tackle this problem. Both techniques compensate for wave-front errors appearing in the telescope, in order to reach the diffraction limit. On the one hand, adaptive optics systems analyze the turbulence effects and correct them with one or several deformable mirrors [Hardy, 1998]. On the other hand, active optics compensate for large mirrors' deformation: the optimal shape is maintained with push/pull actuators located under the optical surface [Knohl, 1994].
Secondly, there is a technological limit for the manufacturing of large monolithic mirrors. Up to 8 meters diameter, segmented telescopes concepts have to be adopted: the primary mirror will be an assembly of several off-axis segments. Coupling full-sized tool polishing technique with a system warping the substrate, active optics allows the generation of such segments with an excellent optical quality, without high spatial frequency errors [Lemaitre, 1972; Nelson et al., 1980].
Thirdly, the growing complexity of optical instrumentation requires innovative systems. In this context, active optics is useful for variable optical path instruments where an active mirror will allow the correction of aberrations evolving with the instrument configuration [Ferrari, 1998]. Moreover, the generation of exotic optical shapes with active optics can reduce the number of elements in a design, simplifying it [Challita et al., 2011].

As described just above, active optics provides elegant solutions to control the wave-front in telescopes, leading not only to more efficient instruments, but also to simplified optical designs. Dedicated to the correction of optical aberrations, induced by instruments' intrinsic defects, the research in active optics is focused toward the conception of simple and minimalist systems, exactly fulfilling a given need [Lemaître, 2009]. This technique, widely and successfully used on Earth-based instrumentation, could be efficiently used in future spaceborne telescopes.

In space, there is no atmospheric turbulence but drastic constraints on weight and compactness, bringing up the problem of structure stability. Whatever the type of missions, future space obser-

vatories are always designed with a large lightweight primary mirror, monolithic or segmented, deployable or assemblable in flight [Feinberg et al., 2012]. These large mirrors are going to loose their best shapes due to thermal variations seen by the telescope, but also due to the gravity difference between the integration on Earth and the operations in space [McComas, 2002]. As on Earth, it becomes mandatory to compensate for the induced aberrations with active deformable mirrors. The conception of space active systems must take into account specific constraints, notably the weight, the compactness, the mechanical strength, the power consumption, the robustness or the reliability [CNES, 1998]. In this manuscript, we present the definition, the set up and the characterization of smart active systems which will allow a technological breakthrough for future space telescopes.

Outline

In the first chapter, active optics is presented in the context of current astronomy. A quick overview of the image formation and quality in telescopes allows to compare Earth- and Space-based telescopes. The main scientific objectives, for Universe and Earth observations, are then defined, leading to some technical requirements for the telescopes. Active optics is then introduced: the design of active systems is described and its three main application domains are highlighted. A zoom on active optics applications for the large telescopes is finally done, showing the benefits of such a technique.

In the second chapter, the MADRAS (Mirror Actively Deformed and Regulated for Applications in Space) project is described. The aim of this project was the development of a correcting mirror demonstrator, dedicated to the compensation of large primary mirror deformation in space. Starting from the correction requirements in a 3 m class space telescope and from the specific constraints of a space use, a 24-actuators deformable mirror has been designed and fully characterized with Finite Element Analysis. The system has then been manufactured, integrated and its opto-mechanical concept has been validated with interferometric measurements.

In the third chapter, the experimental validation of the MADRAS system in a representative configuration is detailed. The correcting mirror has been tested in closed-loop, on a dedicated test-bed with a telescope simulator representing the large mirror deformation in space. The active system functioning has then been fully demonstrated.

In the fourth chapter, the design of a warping harness for the stress polishing of a segment of the future European-Extremely Large Telescope (E-ELT) is introduced. One of the challenges of the construction of this 39 m segmented telescope is the mass-production of the thousand segments. In this context, a 24-actuators warping system has been conceived, optimized and fully characterized with Finite Element Analysis, demonstrating the possibility and the advantages to manufacture the segments by coupling a simple warping harness with full-sized tool polishing technique.

In the fifth chapter, the extreme simplification of active optics systems is tackled. Starting from specific correction requirements, the design of active systems with one actuator generating one optical mode is possible. Two innovative concepts of deformable mirror with a minimum number of actuators have been developed with the elasticity theory. The optical surface deformation is achieved through the application of bending moments at its edges. The systems' performance are demonstrated with Finite Element Analysis and some examples of application are given.

Bibliography

Z. Challita, E. Hugot, M. Ferrari, D. Le Mignant, S. Vives, and J.-G. Cuby. Extremely aspheric surfaces: toward a manufacturing process based on active optics. volume 8169 of *Society of Photo-Optical Instrumentation Engineers (SPIE) Conference Series*, September 2011.

CNES. *Cours de Technologie Spatiale - Technique et technologies des vehicules spatiaux*. 1998.

L. Feinberg, L. Cohen, B. Dean, W. Hayden, J. Howard, and R. Keski-Kuha. Space telescope design considerations. *Optical Engineering*, 51:011006, January 2012.

M. Ferrari. Development of a variable curvature mirror for the delay lines of the VLT interferometer. *Astronomy and Astrophysics*, 128:221–227, February 1998.

J. W. Hardy. *Adaptive Optics for Astronomical Telescopes*. Oxford University Press, July 1998.

E. Hecht. *Optics 2nd edition*. Addison-Wesley Publishing Company, 1987.

E.-D. Knohl. VLT primary support system. volume 2199 of *Society of Photo-Optical Instrumentation Engineers (SPIE) Conference Series*, pages 271–283, June 1994.

G. Lemaitre. New procedure for making Schmidt corrector plates. *Applied Optics*, 11:1630–1636, 1972.

G. R. Lemaître. *Astronomical Optics and Elasticity Theory - Active Optics Methods*. Astronomy and Astrophysics Library. Springer, 2009.

B. K. McComas. *Configurable adaptive optics for the correction of space-based optical systems*. PhD thesis, University of Colorado at Boulder, 2002.

J. E. Nelson, G. Gabor, L. K. Hunt, J. Lubliner, and T. S. Mast. Stressed mirror polishing. 2: Fabrication of an off-axis section of a paraboloid. *Applied Optics*, 19:2341–2352, July 1980.

R. N. Wilson. *Reflecting Telescope Optics I. Basic Design Theory and its Historical Development.* Astronomy and Astrophysics Library. Springer, 1996.

R. N. Wilson. *Reflecting Telescope Optics II*. Astronomy and Astrophysics Library. Springer, 1999.

Chapter 1

Active optics for large-scale instrumental projects

Thanks to a strong synergy between ground and space telescopes, the most compelling astrophysical questions can be addressed, impacting our knowledge of the Universe, from the Solar system to the cosmological background. The observation of the Earth plays also a dynamic role in the development of space instrumentation.
The purpose of active optics is to control mirrors' shape and deformation, and thereby the wavefront in optical instruments [Murdin, 2000]. This control, at nanometrical precisions, makes possible the realization of high quality astronomical observations and facilitates the data reduction.

Active optics is based on deformable mirrors, dedicated and optimized for specific needs. Allowing the use of very high optical quality components with complex shapes, variable or not, it presents many advantages and has various applications [Freeman and Pearson, 1982]. For about twenty years, active optics has allowed some technological breakthroughs in astronomical instrumentation and is widely present on the large Ground-based telescopes. The development of active optics systems for space is then a logical continuance.

In this chapter, the main science and technology drivers for the design of telescopes are introduced, and active optics is put in this context.
In the first section, the image formation in telescopes is defined and ground- and space-based observatories are compared. In the second section, the instruments requirements for modern astrophysics and Earth-observation are highlighted. In the third section, active optics techniques, from the deformable mirror design to its use, are presented. In the fourth section, the application of active optics to large telescope is described through the Very Large Telescope and the future Ground- and Space-based observatories.

1.1 Image quality in telescopes

The classic metrics for telescopes design are the field of view, the sensitivity and the diffraction limit. Various combinations of these characteristics will define the science done with the observatories. Indeed, the ability to detect and characterize structures at relevant angular scales is directly linked to the telescope definition and it allows conceptual breakthroughs in the understanding of astrophysical and terrestrial phenomena. There is also a strong connection between the science, the performance and the cost.
In this section, the main parameters considered for telescopes designs are reviewed.

1.1.1 Image quality: definition

A telescope is designed for a simple goal: collecting flux in order to provide high quality images of distant objects. The telescope diameter D is one of the most important parameter, it defines the collecting power (proportional to D^2), the angular resolution (proportional to λ/D, λ being the wavelength) and the sensitivity (proportional to D^σ, σ depending on the instrument model). In this section, the main parameters defining the optical quality are explained [Wilson, 1996].

Point Spread Function and Optical Transfer Function

The Point Spread Function (PSF) is the system impulse response, in the telescope focal plane. It gives the image of a distant punctual source and is defined with the Fourier Transform of the complex amplitude of the electric field in the pupil plane E [Mahajan, 1998b]:

$$\mathrm{PSF}(\boldsymbol{\alpha}) = |\mathrm{FT}[E(\boldsymbol{\gamma})]|^2 , \tag{1.1}$$

with $\boldsymbol{\alpha}$ the position vector in the focal plane (α its norm) and $\boldsymbol{\gamma}$ the position vector in the pupil plane (γ its norm) and

$$E(\boldsymbol{\gamma}) = P(\boldsymbol{\gamma}) \exp(i\Phi_{res}(\boldsymbol{\gamma})). \tag{1.2}$$

P is the pupil function (equal to 1 for points inside the pupil and to 0 outside), and Φ_{res} is the residual wave-front, given by the phase of the aberration function $W(\boldsymbol{\gamma})$.

For an ideal telescope with a circular aperture in ideal conditions, $E(\boldsymbol{\gamma}) = P(\boldsymbol{\gamma})$ and the PSF is given by the 2 dimensions Airy function A:

$$A(\boldsymbol{\alpha}) = \frac{\pi D^2}{4\lambda^2} \left[\frac{2J_1\left(\frac{\pi D}{\lambda}\alpha\right)}{\frac{\pi D}{\lambda}\alpha} \right]^2 , \tag{1.3}$$

with J_1 the first order Bessel function, λ the imaging wavelength and D the telescope diameter.

The Full Width at Half Maximum (FWHM) of the Airy disc is equal to λ/D and defines the ultimate resolution of the telescope, it is the diffraction limit.
The comparison between the PSF of an actual telescope and the Airy function allows a first characterization of the optical quality.

Another measurement of the system performance is the Optical Transfer Function (OTF), which corresponds to the frequency response. It allows simplified descriptions of an imaging system's spatial resolution capabilities. The OTF is related to the PSF by the Fourier Transform:

$$\mathrm{OTF}(\boldsymbol{\nu}) = \mathrm{FT}[\mathrm{PSF}(\boldsymbol{\alpha})]. \tag{1.4}$$

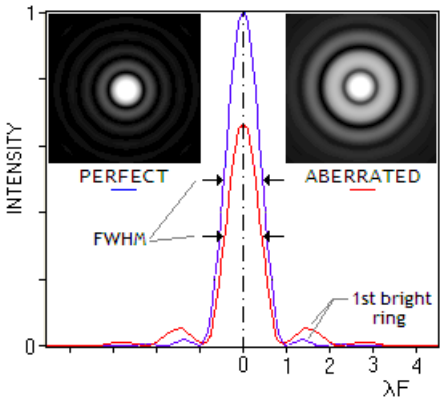

Figure 1.1 : *Intensity distributions of a perfect PSF and an aberrated one.*

Strehl Ratio and residual phase variance

The Strehl ratio SR quantifies the difference between a real PSF and the theoretical one, it describes the ability of the telescope to reach its diffraction limits. It is given by the ratio between the two maximum signal intensity:

$$\mathrm{SR} = \frac{\mathrm{PSF}(\boldsymbol{\alpha} = 0)}{A(\boldsymbol{\alpha} = 0)} = \frac{\int \mathrm{OTF}(\boldsymbol{\nu}) d\boldsymbol{\nu}}{\int \mathrm{OTF}_{Airy}(\boldsymbol{\nu}) d\boldsymbol{\nu}}. \tag{1.5}$$

Blurring the images, a low SR will limit the science. So, the goal is to obtain a SR close to 100%, corresponding to the diffraction limit.

The optical quality of the system is mainly defined by the residual wave-front Φ_{res}, and its variance which characterizes the phase energy:

$$\sigma^2_{\Phi_{res}} = \frac{1}{S} \int (\Phi_{res}(\boldsymbol{\gamma}))^2 \, d\boldsymbol{\gamma} - \left(\frac{1}{S} \int \Phi_{res}(\boldsymbol{\gamma}) d\boldsymbol{\gamma} \right)^2. \tag{1.6}$$

The Maréchal formula allows to link the Strehl ratio to the variance of the residual wave-front:

$$\mathrm{SR} = \exp(-\sigma^2_{\Phi_{res}}). \tag{1.7}$$

So, the Strehl ratio decreases quickly with the residual wave-front, it is then a pertinent criterion to evaluate the impact of optical aberrations on the telescope performance [King, 1968].

Finally, the Power Spectral Density (PSD) gives the spatial frequency distribution of the residual wave-front:

$$\mathrm{PSD}_{\Phi_{res}}(f) = |\mathrm{FT}(\Phi_{res}(\boldsymbol{\gamma}))|^2. \tag{1.8}$$

Signal to Noise Ratio

The Signal to Noise Ratio (SNR) is a crucial data, giving the ratio between a signal and the background noise, it depends of most of the telescope characteristics [Born and Wolf, 1959]. For diffraction limited observations with imaging systems it is defined for a given wavelength as:

$$\mathrm{SNR} \propto D^2 \, \mathrm{SR} \, \sqrt{1/B_\lambda}, \tag{1.9}$$

with D the telescope diameter, SR the Strehl Ratio and B_λ the sky background emission.

1.1.2 Optical aberrations theory

The residual phase in optical instruments can be studied with the optical aberrations theory [Mahajan, 1998a; Born and Wolf, 1959]. The shape of a wave-front in an aberration free system is a perfect sphere. The difference between an actual wave-front and this ideal shape is then a measurement of the aberrations of the system and is given by the optical path length between the two surfaces.

Optical system design is based on Snell-Descartes' law:

$$n_1 sin(\theta_1) = n_2 sin(\theta_2), \tag{1.10}$$

θ_1 and θ_2 being the entrance and exit incident angles and n_1 and n_2 the refractive indexes. It can be developed in the following series:

$$n_1 \left(\theta_1 - \frac{\theta_1^3}{3!} + \frac{\theta_1^5}{5!} + ... \right) = n_2 \left(\theta_2 - \frac{\theta_2^3}{3!} + \frac{\theta_2^5}{5!} + ... \right) \tag{1.11}$$

Gaussian optics only consider the first term of the series, giving a linear approximation. The only describable errors are then the position of the image (tilts) and its size (curvature). But, for any reasonable aperture and field of view, equation 1.11 being not linear, the third order terms must be considered. In this context, the geometrical aberrations theory, formalized by Seidel [1856], introduces five third-order monochromatic aberrations: the distortion (or tilt), the field curvature (or defocus), the astigmatism, the coma and the spherical aberrations.
A tilt aberration is introduced when the spherical wave-front has an angle or is decentered compared to the reference wave-front, it induces a transverse displacement of the image. A defocus aberration is introduced if the image is observed in a plane other than the Gaussian image plane. The three other aberrations are induced by a variation of the focal length with the incident beam. The spherical aberration appears for on-axis object, it is axisymmetric. The astigmatism and coma aberrations impact the image of an off-axis point. These aberrations are due to the optics' shapes in a system and to their relative position. The tilt of a surface will induce tilt, astigmatism and coma aberrations while the translation along the optical axis will induce focus and spherical aberrations [Hecht, 1987].

The third order aberrations are the main errors appearing in optical instruments, but higher terms can also be considered. The wave-front errors are classically decomposed on an orthonormal polynomials base, such as the Zernike polynomials, typically used to described the atmospheric turbulence [Noll, 1976]. It is an orthonormal base of polynomials Z_i, defined on an unitary circular pupil.

$$Z_i(\rho, \theta) = \sqrt{n+1} \begin{cases} R_n^m(\rho)\sqrt{2}cos(m\theta) & \text{if } m \neq 0 \text{ and } i \text{ even} \\ R_n^m(\rho)\sqrt{2}cos(m\theta) & \text{if } m \neq 0 \text{ and } i \text{ odd} \\ R_n^m(\rho) & \text{if } m = 0 \end{cases} \tag{1.12}$$

with

$$R_n^m(\rho) = \begin{cases} \sum_{s=0}^{(n-m)/2} \dfrac{(-1)^s (n-s)!}{s!\left(\frac{n+m}{2} - s\right)!\left(\frac{n-m}{2} - s\right)!} \rho^{n-2s} & \text{if } n-m \text{ even} \\ 0 & \text{if } n-m \text{ odd.} \end{cases} \tag{1.13}$$

This base describes well the optical aberrations: the third order Seidel aberrations correspond to the first Zernike polynomials. It is then used to characterize the wave-front resulting from an optical instrument. In this manuscript, the order defined in Table 1.1 is used.

Table 1.1 : *Zernike polynomials order and corresponding surface representations.*

i	Name	n	m	Phase map
0	Piston	0	0	
1	Tilt y	1	1	
2	Tilt x	1	1	
3	Focus	2	0	
4	Astigmatism3 x	2	2	
5	Astigmatism3 y	2	2	
6	Coma3 x	3	1	
7	Coma3 y	3	1	
8	Trefoil3 x	3	3	
9	Trefoil3 y	3	3	
10	Spherical3	4	0	
11	Astigmatism5 y	4	2	
12	Astigmatism5 x	4	2	
13	Tetrafoil7 y	4	4	
14	Tetrafoil7 x	4	4	
...	...	...	...	

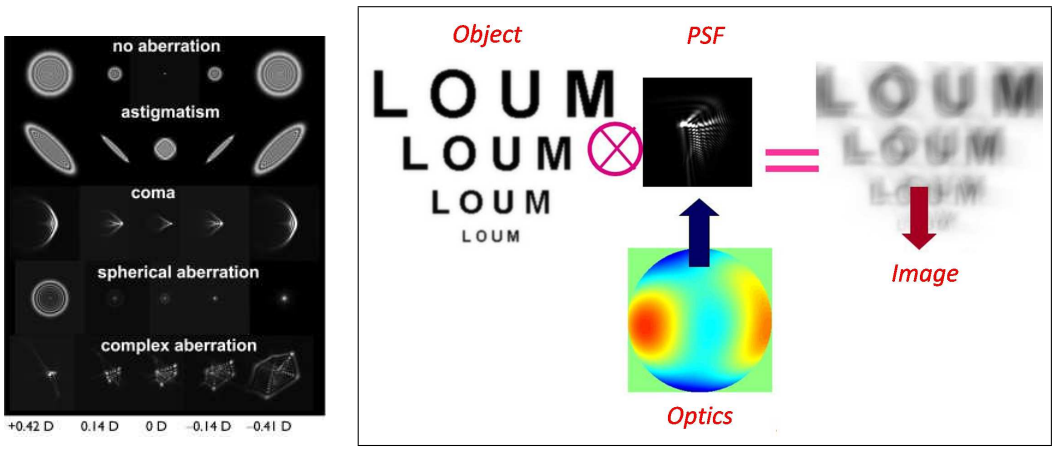

(a) (b)

Figure 1.2 : *Effects of optical aberrations on images: (a) PSF obtained with an optical system containing aberrations (from Wallman and Winawer [2004], D is the focus aberration) - (b) Image of an object through an imaging system containing aberrations (from pabloartal.blogspot.fr, Optics and vision).*

1.1.3 Telescope quality: ground versus space

Driving the collecting power, the diffraction limit and the sensitivity, the main evolution for the future generation of telescope is the diameter increase. The next generation of telescope will be 30-40m class on Earth (E-ELT, GMT) and 8-16m class on Space (JWST, ATLAST). The advantages of Earth telescopes on a practical point of view are obvious: they are easily accessible. In this section, ground and space possibilities are compared.

Environmental constraints

The biggest drawback of ground facilities is the imaging through the Earth atmosphere: its turbulence, absorption and background block some observations and complicate some others [Kuiper, 1952].
Firstly, the turbulence makes difficult the achievement of image quality near the diffraction limit. Nevertheless, the increasing capabilities of Adaptive Optics (AO) provide an efficient correction of this turbulence, allowing to reach space-like performance, especially for the infra-red domain: the Strehl Ratio of a ground-based telescope will then be defined by its adaptive optics performance [Frogel et al., 2009].
Secondly, the absorption does not allow observing the whole electromagnetic spectrum. As shown in Figure 1.3, UV and far Infra-Red observations are not possible from Earth. Some spectroscopic absorption features are even present in the visible domain.
Thirdly, the atmosphere creates a background that needs to be subtracted from observations. This subtraction adds noise and some background variations can lead to systematic errors in the data reduction. In addition to this background, there are some emission lines, limiting the ability to study particular wavelength.
On their side, space instruments are generally designed to reach the diffraction limit at some target wavelength, the available wavelength range available is only limited by the photons collecting system and the background in space is a least one order of magnitude lower than on Earth (see Figure 1.3).

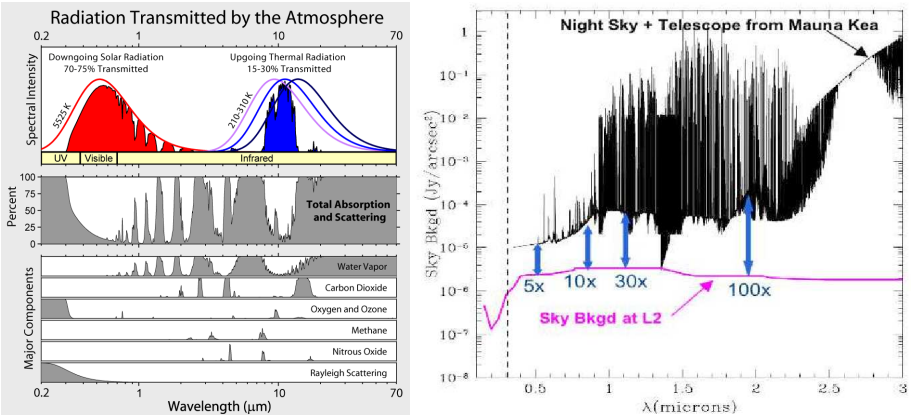

Figure 1.3 : *Left: Atmospheric transmission and absorption bands by molecules in the UV, optical and IR domains (credit www.globalwarmingart.com) - Right: Background flux viewed by a ground telescope, on Mauna Kea, and by a space telescope, at L2 (from Mountain et al. 2009).*

The observations and optical performance on Earth are also limited by the unstable environment, notably the weather, the day-night cycle, the important thermal variations and the gravity effect.
In space, continuous observations can be done, allowing to follow time variable phenomena and to take deep exposures. On Earth, this can only be done by comparing or adding data from different nights, with different observing conditions.
The space environment stability is really convenient for high photometric and geometric precision.

However, in the external space environment, the observations are operated under extreme conditions [Kent, 2010]: the micro-gravity, the cold temperature and the vacuum. The weightless conditions implies that the items on optical benches must be secured, and this without distorting the optical alignment. In addition, the reduced pressure allows the free passage of out-gassed

molecules to the sensitive optical instruments, the reflecting surface material must minimize these effects.
Moreover, a space instrument must have an autonomous power supply, it is generally achieved with solar panels. To finish, micrometeorites and dust environment can damage the instrument, this risk has to be taken into account.

The satellites environment will depend on its orbit, which can be defined by its distance to Earth, the closer being the cheaper. Low Earth Orbit (LEO) represents altitudes up to 2000 km. Medium Earth Orbit (MEO) represents altitudes between 2000 km and 35786 km. High Earth Orbit (HEO) represents altitudes above this distance. Two interesting orbits are the Geostationary orbit (GEO), at 35786 km and the Sun-Earth Lagrangian point L2, at 1500000 km. The GEO orbit is a circular orbit with the same period than Earth, the same area can then be observed continuously. L2 is a location where gravitational forces and orbital motion between Sun and Earth balance each other, so an object around this point will maintain the same relative position.
The main considerations for the orbit choice are the observation time, the target visibility, the ground contact, the solar panel power availability and the cost. For instance, LEO orbit sees large thermal swings, reducing the thermal stability and there are significant stray-light and background, requiring baffles on the instrument. Moreover, the objects of interest can be eclipsed by the Earth, the Sun or the Moon. On the other hand, crossing the Van Allen belts, the MEO and GEO orbits are subject to potentially harmful radiations from solar winds and primary and galactic cosmic rays. The L2 point is ideal on many points but its distance poses an operability problem.

Technological constraints

With acoustic and mechanical vibrations, rapid pressure change and staging shocks, space instruments are subject to traumatizing events during their launch. So, an important consideration for space instruments design is mechanical handling: to survive the launch loads the lowest natural frequency must be above the low frequency limit of the launcher vibrations, avoiding a resonant coupling. In addition, the mechanisms must be kept stationary during launch to avoid the instruments to be misaligned or damaged.
The launcher also brings limitations in terms of mass and size.

The sky coverage is complete in space while it is limited by Adaptive Optics systems on Earth. Indeed, AO requires bright stars as references so it can only cover a part of the sky with such sources. This can limit the ability to do wide field surveys. By using Laser Guide Stars, the sky coverage can be markedly increased but Natural Guide Star are still required for tip/tilt correction. On both Earth and Space, the Field Of View (FOV) is limited by technological and design constraints related to optics and detectors.

Conclusion

There is no perfect environment, the choice of a telescope location is done regarding the instrument performance requirements deriving from the scientific goals but also regarding the mission cost. On the one hand, space provides stability, diffraction limited performance, low background and an access to the entire electromagnetic spectrum. On the other hand, Earth provides access to much more larger optical aperture and the progress in adaptive optics allows the achievement of high quality observations. The cost and the complexity of space missions are considerable compared to the relative easiness to operate Ground-based telescopes.

In many cases, it is possible to couple Earth and Space based capabilities in order to achieve important scientific progress [Kissler-Patig and McCaughrean, 2010]. In the next section, we will see through some examples of science requirements, the excellent complementarity between Earth- and Space-based astronomy.

Table 1.2 : *Ground versus Space: pros and cons.*

	GROUND	SPACE
Diameter	Only limited by technology	Limited by launcher
Wavelength range	Limited by by atmosphere	Only limited by optics and detectors
Telescope availability	Day/Night weather, etc	Depends on orbit
PSF stability	Temperature variation, atmosphere, etc	Microgravity, small thermal variations
Diffraction limit performance	Defined by Adaptive Optics	Reached for target wavelength
Background	High (atmosphere)	Low
Sky coverage	Defined by adaptive optics	Complete
Operability	Easy access	Data transfer Hardly fixable
Technical constraints	Only limited by cost	Launch and space environment

1.2 Instrumental needs for modern astrophysics

1.2.1 Searching for exoplanets and for life

Are we alone in the Universe? Answering this question would be an immense progress in our way to comprehend the Universe. The search for exoplanets has started in the 90's at the Observatoire de Haute Provence, in France where the first exoplanet has been discovered, orbiting around the star 51Pegasus. This Jupiter-mass companion has been indirectly detected thanks to its influence on the host star [Mayor and Queloz, 1995]. Since this day, more than 700 exoplanets have been detected, most of them with indirect methods, such as transit, radial velocity or astrometry and a few with direct imaging (Figure 1.4) [Perryman, 2011].
The search for exoplanets illustrates well the synergy between Earth and Space based observatories. The two main space missions, CoRoT and Kepler, are detecting planet candidates and their follow-up with Earth spectrographs installed on large telescopes, such as HARPS and SOPHIE, allow their validation. Giant planet detection is also possible with high contrast and high angular resolution imaging, and two new generation instruments, GPI [Macintosh et al., 2006] and SPHERE [Beuzit et al., 2010], are currently in development to exploit such techniques for the direct detection of exoplanets.

With an impressive array of tools, the field of exoplanets is in constant evolution, bringing new discoveries almost every day. But the detection of biosignatures in the atmosphere of terrestrial-mass

exoplanets will require a combination of high spatial resolution, high sensitivity and high contrast. The four drivers dictating the need for a space telescope for this application are summarized by Postman et al. [2012]. Firstly, the projected angular radius of an Habitable Zone around a star is typically lower than 100 mas. The adequate sampling of such a zone to isolate an exoplanet requires an angular resolution between 10 and 25 mas. Secondly, the Earth-mass planets are around 25 magnitude fainter than their host stars, it requires then high-contrast imaging to detect them, with a starlight suppression factor of 10^{-9} or 10^{-10}. It can be achieved either with an internal coronograph or an external occulter, but only with high wave-front and pointing stability, impossible to reach with ground-based telescopes [Guyon, 2005]. Thirdly, the detection of a biosignature, such as the presence of oxygen in the atmosphere, requires a direct low resolution spectroscopy of the extremely faint source, with a Signal to Noise Ratio better than 10. Fourthly, the planet harboring life are probably rare, the sample size is then an important issue. A successful search for life will require the observation of hundreds of stars [Kasting et al., 2009]. The number of stars with a possible detection of an exoplanet spectrum is proportional to D^3, D being the telescope optical aperture. The target primary mirror diameter is currently 8m, which will allow the observation of 100 star systems, 3 times each, in 5 years with 20% of the telescope time.

As a conclusion, the detection of signs of life in a star habitable zone requires at least a 8m-class space telescope, providing a SNR around 10, a 10^{-9} starlight suppression, a 0.1 nm wave-front error stability, a 1.5 mas pointing stability and a sensitivity from 0.3 to 2.4 μm with broadband imaging and spectroscopic modes.

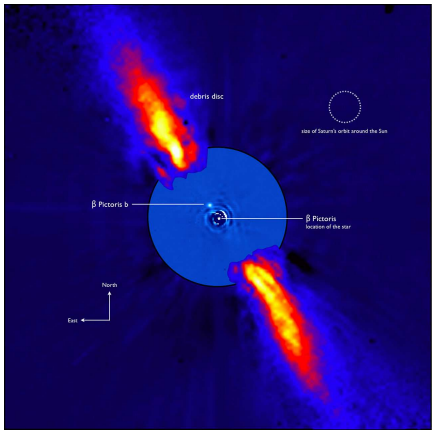

Figure 1.4 : *Direct imaging of β pictoris b (credit ESO).*

1.2.2 Cosmology

During the last century, our understanding of the universe has significantly improved. The observations converge toward a cosmological model, called ΛCDM, and indicate that the universe is in accelerated expansion [Riess et al., 1998]. This expansion is explained by the dark energy, representing 70% of the universe density. This dark energy can be modeled by the cosmological constant of the general relativity theory. Our knowledge of galaxies and Universe formation and evolution stays quite limited, due to the difficulty to observe far back in time. The history of the universe, as understood today, is shown on Figure 1.5. After the emission of the Cosmological Microwave Background (CMB), the Universe went through an epoch called dark ages during which it was neutral. The birth of primordial galaxies has allowed the universe re-ionization, making it observable. For such an observation, we need to go back in time, at 10 billions light years distance,

which corresponds to high redshift observations ($z > 7$).
To explain the galaxies rotation curves, that are flat far from the center instead of decreasing, another component of the Universe needs to be introduced: dark matter, representing 25% of the universe density. The structure and kinematics of these components need to be probed in order to improve their understanding.

The current technological evolutions allow the preparation of large cosmological surveys that will identify billions of galaxies throughout the observable sky. Such missions, as EUCLID in space or BigBOSS on earth, will probe a larger and deeper volume of the universe.
Probing dark matter requires combining proper motions of stars in galaxies with their radial velocities [Strigari et al., 2007]. Once again, this can be achieved by coupling space and earth observations [Postman et al., 2012]. The high number of velocities required to efficiently characterize the dark matter necessitates large primary mirror diameter, only accessible on Earth. The measurement of proper motions with an accuracy better than 10 km/s requires an extremely precise astrometry, at 0.1 mas. This will only be doable in Space, with an excellent thermal stability, coupled with wave-front sensing and controlling, maintaining the focal plane metrology below a 0.01 pixel error. In addition, a wide field of view, containing thousands galaxies, is needed to ensure a sufficient number of background astrometric references.

As a conclusion, a wide field imager, at high angular resolution and high stability, will provide the observation of thousands distant objects, with their internal structures, in a single exposure time. It will increase the data allowing the comprehension of the origin of the Universe.

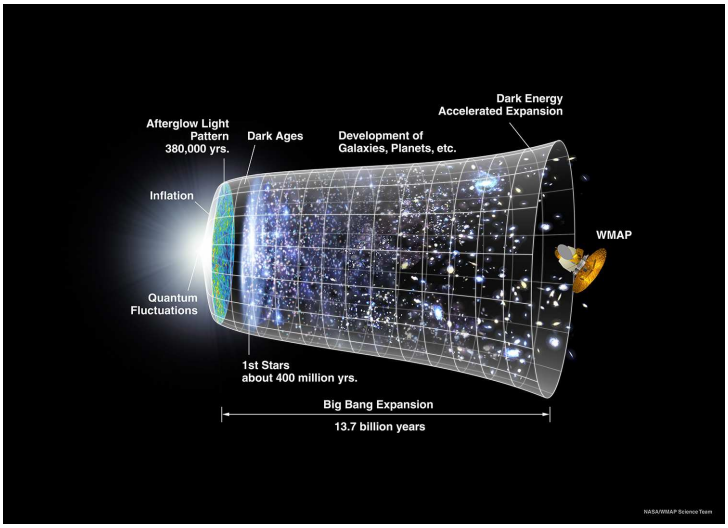

Figure 1.5 : *Timeline of the Universe (credit NASA/WMAP science team).*

1.2.3 Galaxy physics and star formation

Many questions about stars formation and evolution or about the growth of structures in galaxies and in the Universe remain unanswered. The star formation rate density has peaked at a moment observable at redshifts around 2 and 3. At this moment, the galaxies have formed most of their content in stellar mass. These astrophysical processes emit in the entire electromagnetic spectrum, so some observations must be done in space to recover data inaccessible from Earth, in the UV or mid and far Infra-Red for instance [Sembach et al., 2009]. Figure 1.6 presents the results of

the observation of a same galaxy at different wavelengths. Revealing different structures, these observations are complementary and allow to explain the different phases of the galaxies and stars history.

Stellar formation mechanisms are studied through the observation of the Inter Stellar Medium (ISM). The ISM is constituted of gas and dust, mainly composed of hydrogen in different phases. If a molecular cloud is massive enough that the gas pressure is insufficient to support it, it will collapse to form stars. So, the early stages of a star's life are observed through the infrared light from dust and clouds. For instance, observing in the far infrared, the 3.5 m Herschel Space Observatory studies stars and galaxies formation. Moreover, high angular resolution observations of these clouds are required to analyze the assembling processes and the collapse of interstellar clouds.

Galaxies formation studies can be achieved with high spatial resolution and sensitive spectroscopy [Giavalisco et al., 2009]. The absorption and emission lines observed thanks to spectroscopy characterize the galaxies' components. The main diagnostic lines are OVI, SiIII, Lyα, NV and SiIV for the local universe (redshift inferior to 0.3), they are observed in the UV. At higher redshift (that is to say at longer wavelength), the diagnostic lines are Hα, Lyα and OIII. The observational challenge is then to acquire data of sufficient spatial sampling to identify fine structures and with enough spectral resolution and exposure time to detect the diagnostic lines.

As a conclusion, observations from UV to IR, with high angular and spectral resolutions, together with high sensitivity will reveal different features, characterizing the formation and evolution of stars and galaxies.

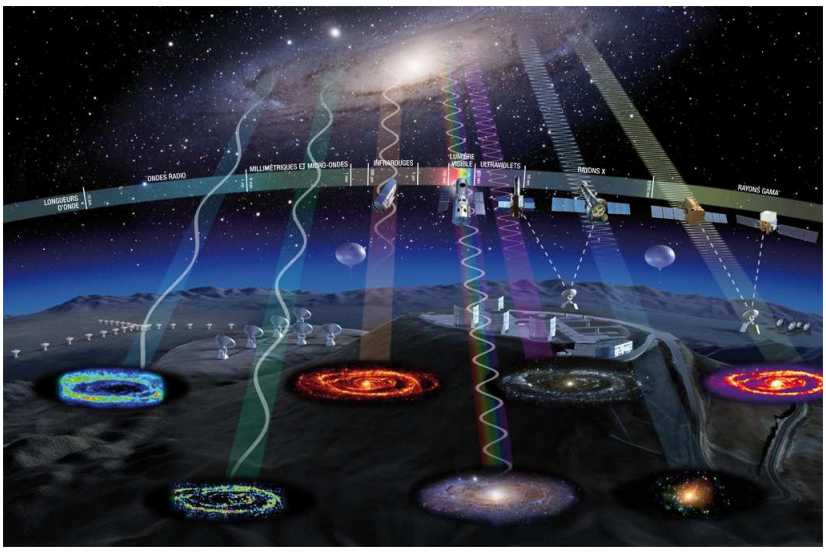

Figure 1.6 : *Andromeda galaxy seen at different wavelengths, with different instruments from Earth or Space (credit CNRS).*

1.2.4 Earth observation

Hundreds of satellites are orbiting around Earth, observing it for many applications such as cartography, defense and security, risk prevention, surveillance, urbanism or Earth sciences (oceanography, hydrology, forestry, atmospheric studies, etc). The biggest need would be a large field of

view and high angular resolution, to see small details in wide areas. There also can be a need for temporal repetitiveness, to observe the same target several times a day, or even continuously [Latry and Delvit, 2009]. We can differentiate missions in low earth orbit (LEO), in geostationnary orbit (GEO) and in intermediate orbit (MEO), the operation altitude depending on the requirement in area covering and revisit. The technologies developed for the Earth observation can also be applied for the exploration of our solar system planets.

For Earth observation, the ultimate achievable resolution is 10 cm, under this value, the observation will be limited by the atmospheric turbulence.
The low orbit satellites are used for imaging. In order to have detailed cartography, the target resolution is 20 cm, which corresponds to a 2 m diameter optical aperture.
The target resolution for geostationnary satellites is around 10 m, also leading to 2 m diameter apertures. The main applications are for security, such as the preventions or follow-up of natural disasters and the ships monitoring.
In any cases, it is also important to have a wide spectral range, in order to image various structure, such as vegetation, seaside or hot points for instance. Furthermore, stereoscopic capabilities, with high resolution in z, will allow the acquisition of 3 dimensional datas, for topography. Large footprint are intended, the swath will be given by the instrument's field of view compared to its orbit. A pointing stability is required to have quality images. The satellites agility is also important, the system must be responsive to specific user requirements. This can be achieved with dynamic image acquisition programming and revisit capacity. Intermediate elliptical orbits bring some instrumental challenges due to the variation of the illumination, the observing altitude and the projection speed.

The Pleiades satellites describe well the current state of the art in the Earth observation domain. It is a 2 satellites constellation (one is currently flying, the other will be launched this year) providing a coverage of Earth's surface with a repeat cycle of 26 days. They are Korsch telescopes, with a 650 mm diameter aperture and a focal ratio of 20. They operate in the visible, on a sun-synchronous, near circular orbit, at a mean altitude of 694 km. The satellites have a swath width of 20 km and can provide an image acquisition anywhere within a 800-km-wide ground strip with a 50 cm resolution [Lamard et al., 2004]. As we can see in Figure 1.8, the images quality achieved with Pleiades is exceptional.

As a conclusion, Earth observation requires agile telescopes with large field of view, high resolution and wide spectral range. The instrumental innovations developed for Earth observation applications could then be adapted for Universe observations.

Figure 1.7 : *Pleiades satellite (credit CNES).*

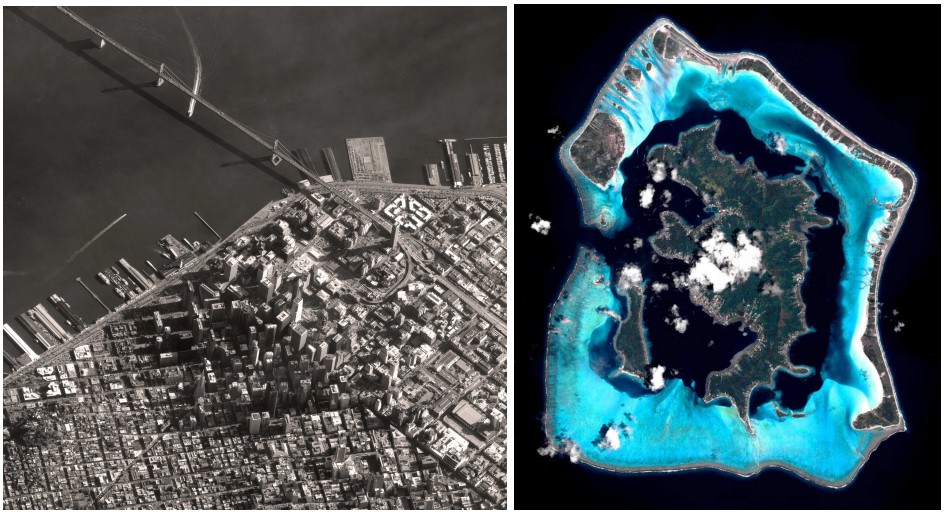

Figure 1.8 : *Images taken with Pleiades: San Francisco and Bora Bora (credit SPOT Image).*

1.2.5 Conclusion: instrumental needs

The main requirement for future telescopes is the access to higher resolution and higher sensitivity with a high wave-front stability. It implies then larger optical aperture. But the scaling of the existing telescope is prohibitive due to mass and bulk. Then, the use of thin or lightweight mirrors, and eventually of deployable structures, becomes mandatory. However, this solution does not facilitate the achievement of stable structures.
In this context, active optics will allow a technological breakthrough by providing a mean to ensure the optical quality in future large telescopes.

1.3 Active optics: an overview

Active optics systems provide excellent optical quality by adjusting the wave-front through the deformation of mirrors. Therefore, the knowledge of mirrors' mechanical behavior has a major role. In this section the elasticity theory, used for the deformable mirror conception, is introduced, and we will see how the optical aberrations theory can be translated in term of mirrors shapes. Then, the Finite Element Analysis method used in this manuscript to optimize active systems is presented. Finally, the three main fields of application of active optics are highlighted.

1.3.1 Active optics: a link between optical aberrations and elasticity theories

Mirrors' shapes described with elasticity theory

Elasticity theory, described in Timoshenko and Woinowsky-Krieger [1959], gives the mechanical behavior of plates under given conditions. The bending properties of a plate depend on:

- its dimensions: thickness, diameter ...
- its mechanical parameters: Young modulus, Poisson ratio, Coefficient of Thermal Expansion ...
- its boundary conditions: supporting parts, clamped parts, free parts ...
- its load case: application of pressure, forces, bending moments, thermal variations ...

For the design of active optics systems, the description of thin circular plate with small deflection is generally applied. This description is valid when the plate fulfills the Love-Kirchoff hypotheses:

- the deflection z is small in comparison to its thickness t,
- the transverse dimensions are bigger than the thickness, of a factor at least 20,
- there is no deformation in the middle plane of the plate, this plane remain neutral during bending,
- the planes normal remain normal to the middle surface after the bending,
- normal stress in the direction transverse to the plate can be disregarded.

Using these assumptions, the deflection of the plate is a function of the two coordinates in the plane of the plate ((x, y) in cartesian coordinates or (r, θ) in polar coordinates). This function satisfies a linear partial equation with given boundary conditions.

The application of elasticity equations allows the determination of plate bending. The equation of the deformation z of a circular plate is:

$$\nabla^2\nabla^2 z = \frac{q}{D}, \tag{1.14}$$

with ∇^2 the Laplacian operator:

$$\nabla^2 = \frac{\partial^2}{\partial x^2} + \frac{\partial^2}{\partial y^2} = \frac{\partial^2}{\partial r^2} + \frac{1}{r}\frac{\partial}{\partial r} + \frac{1}{r^2}\frac{\partial^2}{\partial \theta^2}, \tag{1.15}$$

q a load applied on the plate and D the rigidity, function of the plate thickness t and material properties (its Young modulus E and Poisson ratio ν):

$$D = \frac{Et^3}{12(1-\nu^2)}. \tag{1.16}$$

The resolution of the linear equation 1.14, with given mirror geometry, mechanical properties, boundary conditions and load cases, gives the expected deformation. From the knowledge of the deflection the stress at any points of the plate and the mechanical moments M can be deduced:

$$\begin{cases} M_x = D\left(\dfrac{\partial^2 z}{\partial x^2} + \nu\dfrac{\partial^2 z}{\partial y^2}\right) \\ M_y = D\left(\dfrac{\partial^2 z}{\partial y^2} + \nu\dfrac{\partial^2 z}{\partial x^2}\right) \\ M_{xy} = M_{yx} = D(1-\nu)\dfrac{\partial^2 z}{\partial x \partial y}, \end{cases} \tag{1.17}$$

with M_x and M_y the bending moments; and M_{xy} and M_{yx} the twisting moments. These moments can also be expressed in polar coordinates:

$$\begin{cases} M_r = D\left[\dfrac{\partial^2 z}{\partial r^2} + \nu\left(\dfrac{1}{r}\dfrac{\partial z}{\partial r} + \dfrac{1}{r^2}\dfrac{\partial^2 z}{\partial \theta^2}\right)\right] \\ M_\theta = D\left[\dfrac{1}{r}\dfrac{\partial z}{\partial r} + \dfrac{1}{r^2}\dfrac{\partial^2 z}{\partial \theta^2} + \nu\dfrac{\partial^2 z}{\partial r^2}\right] \\ M_{r\theta} = D(1-\nu)\left[\dfrac{1}{r^2}\dfrac{\partial z}{\partial \theta} - \dfrac{1}{r}\dfrac{\partial^2 z}{\partial r \partial \theta}\right], \end{cases} \tag{1.18}$$

The substrate bending depends on the type of applied loads, but also on their transmission. Concentrated forces induce local deformations, resulting in high spatial frequency errors. In this context, Saint Venant principle tells that the solution given by the deformation equation is valid far from the location of load application [Saint Venant, 1881]. To fulfill this principle, active optics systems are designed with external force configurations, at the boundaries, which minimize the local deformations on the optical surface [Lemaître, 2009].

Mirrors' shapes described as resulting wave-front

The shape of a mirror can be variable or not. Its deformation can either be required (aspherical shape in specific design or movable optical components) or be an inherent defect (deformation under the mirror own weight or shape error due to fixation device).
An optical surface shape can be expressed in terms of Optical Path Difference (OPD) in an instrument, and then in terms of Wave-Front Error (WFE).

The pupil of an optical instrument is generally circular, it is described in polar coordinates. The optical surface shape can be axisymmetric or not.

An axisymmetric surface is a conicoid, represented by the following equation:

$$z_c(r) = \frac{r^2}{k + \sqrt{k^2 - (C+1)r^2}}, \tag{1.19}$$

with k the radius of curvature, giving the focal: $f = 2k$ and C the conic constant, allowing to differentiate several case of conicoids:

- $C < -1$: hyperboloid
- $C = -1$: paraboloid
- $-1 < C < 0$: elongated ellipsoid
- $C = 0$: sphere
- $C > 0$: flattened ellipsoid

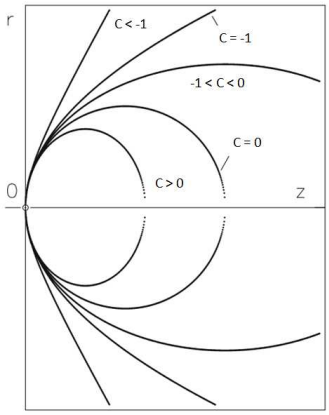

Conicoid sections of same curvature (from Lemaître [2009]):

A non axisymmetric surface can be represented by the following series:

$$z_a(r,\theta) = \sum_{n,m} A_{n,m} r^n cos(m\theta) + B_{n,m} r^n sin(m\theta). \tag{1.20}$$

Aspherical mirror are generally used in off-axis systems, their shapes are described with an axisymmetric component z_c plus the non axisymmetric representation z_a.

Once the mirror shape is known, it can be translated on a wave-front including some optical aberrations. As the turbulent phase is decomposed on the Zernike base [Noll, 1976], the optical surface shape is projected on it, giving the aberrations induced by the mirror.

In conclusion, the knowledge of a mirror deformation allows to determine the wave-front error introduced in the instrument. It is also possible to consider the inverse problem: knowing the WFE, what mirror shape would correct for it? Inverting the elasticity equation allows the determination of a mirror geometry and load case to generate the required deformation.

1.3.2 Active optics design with Finite Element Analysis

Active systems definition is based on the elasticity theory but the design must be refined with Finite Element Analysis (FEA), allowing to confront the analytical results to simulations. The interest of

FEA is that it takes into account details that cannot be described by analytical formulation. With this detailed and quantitative study, the systems mechanical behavior can be realistically characterized.

FEA method performs a numerical computation of a differential equations systems with boundary conditions [Smith and Griffiths, 2004]. The modeling principle consists in subdividing a mechanical structure into elements. The mechanical behavior of these simple sub-domains are well mastered. The elements are connected together with nodes, where the data are collected: displacement, stress, temperature, etc. The computation is performed from nodes to nodes, with continuity conditions and equilibrium between elements. The considered deformable systems are in the domain of linear elasticity. In such a case, a convergence theorem ensures the validity of the solution with a fine meshing, defined by the number of nodes and elements sampling the model.

A method to optimize the deformable mirrors' geometry has been developed for the conception of the systems presented in this manuscript. It considers a linear model and is based on the systems' Influence Function (IF). An Influence Function is defined as the deformation resulting from the unit command on one actuator, the others being at rest.

A system with N actuators has N Influence Functions, constituting a characteristic base B. If M is the number of nodes of the optical surface, B is a NxM matrix: it contains N vectors giving the displacements of the optical surface nodes induced by each actuator. This base is used to decompose the wave-front error to be compensated ϕ_{in}:

$$\phi_{in} = B\alpha, \tag{1.21}$$

with α a set of N coefficients corresponding to the actuators' commands.
These coefficients are determined by inverting B. As B is not a square matrix, the pseudo-inverse B^+ is performed:

$$\alpha = B^+\phi_{in} = (B^tB)^{-1}B^t\phi_{in}. \tag{1.22}$$

Thus, the wave-front actually compensated by the system is:

$$\phi_{cor} = B(B^tB)^{-1}B^t\phi_{in}, \tag{1.23}$$

and the residual wave-front after correction:

$$\phi_{out} = \phi_{in} - \phi_{cor}. \tag{1.24}$$

For a given geometry, a Finite Element model is created and the Influence Functions are recovered by applying a unit command to each actuator, while the others are fixed. The commands can be displacements, forces or pressure, depending on the defined load cases. Then, as described in Figure 1.9, the generation of a given deformation is characterized by determining:
- the actuators' commands α with the projection of the WFE on the IF base (Eq. 1.22),
- the residues of correction ϕ_{out} with the reconstruction of the corrected wave-front (Eq. 1.24),
- the resulting stress σ with the injection of the actuators commands on the finite element model.

The design optimization consists in minimizing these 3 criterions for each required deformation mode.
A classical least square algorithm is used to converge to the optimal geometry [Bonnans et al., 2009]. The optimization output parameters are the system dimensions (thickness, diameter or

length of the different system's parts) but also its material. A coefficient β_i is allocated to each mode according to its maximum amplitude to be corrected. In the same manner, a weight λ can be given to each criterion and upper and lower bounds can be set. At the end, the quantity minimized by the least square algorithm is γ:

$$\gamma(geometry, material) = \sum_i \beta_i [\lambda_{cor} \|\phi_{out}\|^2 + \lambda_\sigma \sigma_{max} + \lambda_\alpha \alpha_{max}], \tag{1.25}$$

with i varying from 1 to N_{mode}, representing the specified correction modes, and $\|\phi_{out}\|^2$ the amplitude (rms) of the residual wave-front, giving the precision of correction.

Once the optimal system geometry is defined, the mechanical and optical behavior is fully characterized with FEA. The precision of correction ($\|\phi_{out}\|^2$) is known for each mode, such as the required actuators' stroke (α) and the level of stress in the mirror (σ).

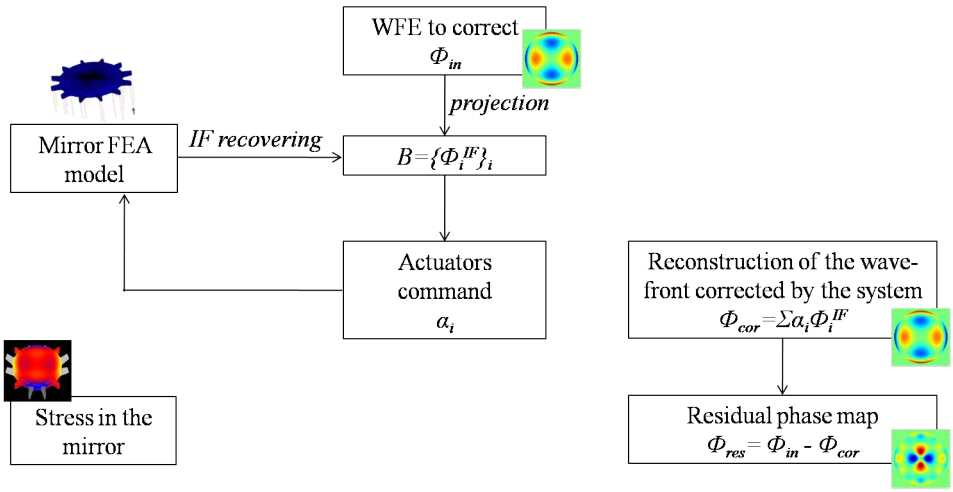

Figure 1.9 : *Method for design optimization, based on the finite element model's influence functions: the three minimized criterions are the stress in the mirror, the actuators commands and the residual wave-front error.*

1.3.3 Access to optimal performance thanks to active optics

These last 20 years, active optics techniques have become essential in large Earth-based telescopes. It is also useful to simplify some optical designs or facilitate the use of multi-configuration instruments. The three main domains of application of active optics are the maintaining of large mirrors optimal shapes, the generation of aspherical mirrors with stress polishing and the in-situ correction of optical aberrations with active deformable mirrors.

Large mirrors deformation compensation

In 1989, ESO New Technology Telescope was the first telescope to benefit from active optics. Its 3.58m diameter primary mirror is in Zerodur and is 24 cm thick. 75 actuators under the optical surface, 3 clamped points and 24 lateral actuators are compensating from the mirror deformation under its own weight. This assembly allows to keep the optimal mirror shape [Wilson et al., 1991]. Since then, most of the 8-10m class Earth-based telescopes have integrated active primary mirrors, like for instance the Gemini North and South, the Keck observatory, the Gran Telescopio Canarias

(GTC) or the Very Large Telescope (VLT).

For the future generation of space observatories, the deformation of large primary mirrors will also become a major issue. As on Earth, space telescopes evolve toward larger diameters but the launch brings strong constraints on weight and compactness. Thus, it becomes mandatory to use lightweight primary mirrors [Dürr et al., 2003; Coulter and Jacobson, 2000] and the structure stability will significantly impact the system performance. Lightweight mirrors are sensitive to the environment variations: thermal variation and absence of gravity will deform the large mirrors, generating optical aberrations in the instrument [McComas, 2002]. An active telescope would then be required in order to keep optimal performance.

In this context, a 24-actuators active mirror has been developed and is presented in Chapters 2 and 3. This correcting device is dedicated to the compensation of large primary mirror deformation in space and its performance has been experimentally characterized, demonstrating the possibility to insert it in future space telescopes.

Segmented and aspherical mirrors generation

With the increase of primary mirror diameters, technical and technological limits have been reached: it is extremely challenging to manufacture monolithic mirrors larger than 8 meters diameter. The size for space telescope is even more limited by the size of the rocket cap, around 3 meters diameter. It is then mandatory to go for segmented telescopes.

Considering a near-parabolic primary mirror, Lubliner and Nelson [1980] describe a mirror segment as an Off-Axis Parabola (OAP) whose shape depends on its position relatively to the global mirror. Its optical surface can be analytically described as a function of the segment semi-diameter a, the off-axis distance R, the parent parabola radius of curvature k and conic constant C. The off-axis segment shape z is described by the general formulation giving the sag of a conic surface ($z_c(r)$ in Equation 1.19), with the radial coordinate r varying from $R-a$ and $R+a$.
The equation is then expressed in local coordinate, described in Figure 1.10, to define the aspheric shape, which can be expanded in power series:

$$z(\rho,\theta) \approx \alpha_{20}\rho^2 + \alpha_{22}\rho^2 cos(2\theta) + \alpha_{31}\rho^3 cos(\theta) + \alpha_{33}\rho^3 cos(3\theta) + \alpha_{40}\rho^4 + \alpha_{42}\rho^4 cos(2\theta), \quad (1.26)$$

with α_{ij} the asphericity coefficients, depending on the OAP characteristics:

$$\begin{cases} \alpha_{20} = \frac{a^2}{k}\left[\frac{2-C\epsilon^2}{4(1-C\epsilon^2)^{3/2}}\right] \\ \alpha_{22} = \frac{a^2}{k}\left[\frac{C\epsilon^2}{4(1-C\epsilon^2)^{3/2}}\right] \\ \alpha_{31} = \frac{a^3}{k^2}\left[\frac{C\epsilon[1-(C+1)\epsilon^2]^{1/2}(4-C\epsilon^2)}{8(1-C\epsilon^2)^3}\right] \\ \alpha_{33} = \frac{a^3}{k^2}\left[\frac{C^2\epsilon^3[1-(C+1)\epsilon^2]^{1/2}}{8(1-C\epsilon^2)^3}\right] \\ \alpha_{40} = \frac{a^4}{k^3}\left[\frac{8(C+1)-24C\epsilon^2+3C^2\epsilon^4(1-3C)-C^3\epsilon^6(2-C)}{64(1-C\epsilon^2)^{9/2}}\right] \\ \alpha_{42} = \frac{a^4}{k^3}\left[-\frac{C^2\epsilon^2[1+5C-C\epsilon^2(6+5C)]}{16(1-C\epsilon^2)^{7/2}}\right]. \end{cases} \quad (1.27)$$

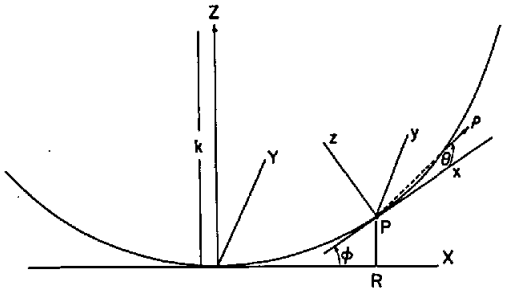

Figure 1.10 : *Definition of the local coordinate of an Off-Axis Parabola, compared to the parent parabola coordinates (from Lubliner and Nelson [1980]).*

Classically, aspherical shapes are manufactured with small robotic polishing tools [Bingham et al., 2000]. This kind of technique is quite long to converge to the required shape and induces high spatial frequency errors on the optical surface, corresponding to the tool size. These errors can be suppressed with a final pass of Ion Beam Figuring (IBF) [Arnold et al., 2010], increasing the manufacturing time.

Active optics offers an interesting alternative for aspherical mirrors generation: the stress polishing. Proposed in the 1930's by Schmidt [1932] for the polishing of the entrance correcting lens of his wide field telescope, this method has been improved by Lemaitre [1972]. It consists in stressing the substrate before spherically polishing it with a full-sized tool. The constraints are relaxed at the end of the process, giving to the mirror the required aspherical shape (Figure 1.11). Not only the use of a large polishing tool avoids the generation of high spatial frequency errors, but it also is a gain of time compared to small tools techniques. Nevertheless, the monitoring of the optical shape with an optical measurement can be necessary during the polishing, in order to readjust the applied constraints.

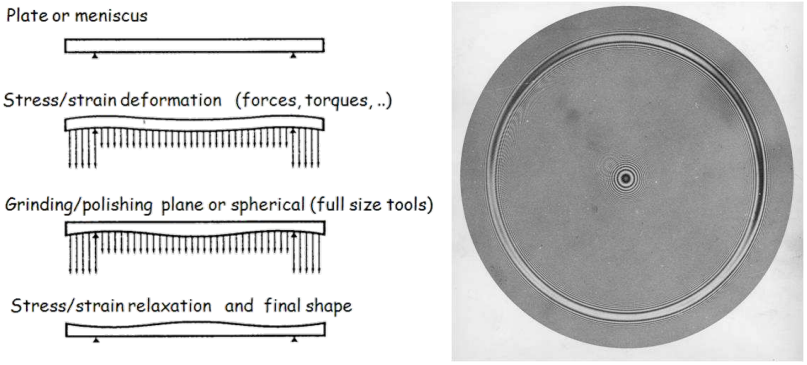

Figure 1.11 : *Stress polishing of a Schmidt plate: principle and interferogramm on a 62 cm Schmidt plate realized for the Observatoire de Haute Provence.*

Stress polishing technique has been adapted by Nelson et al. [1980] to produce the Keck telescopes segments. The Keck observatory is composed of two twin telescopes, located in Hawai. Each 10.95 m diameter primary mirror, is constituted of 36 1.8m hexagonal off-axis segments. The thin circular substrate of each segment has been deformed with 24 arms on its edges, transmitting forces and bending moments during the polishing. The hexagonal cutting is performed at the end of the process. These mirrors being thin, their shape is also maintained in-situ during observations. Since the success of this realization, other projects of segmented telescopes have been initiated,

and stress polishing techniques are under study for the mass production of segments for the future giant telescopes.

As presented in Chapter 4, Stress Mirror Polishing is studied in the framework of the future European Extremely Large Telescope. A dedicated warping harness has been designed and characterized with Finite Element Analysis in order to manufacture a segment prototype for the 39 m primary mirror.

Figure 1.12 : *The Keck twin telescopes and one of their segmented primary mirror (credit Keck Observatory).*

Variable optical aberrations correction

Active mirrors can be included in an instrument optical train to fulfil specific functions. Specifications for such correcting systems directly come from the instrument design and use: environment variations, fixation devices or moving elements can induce aberrations to be corrected in-situ and in real time. Anticipating the correction need, simple and efficient Deformable Mirrors (DM) can be designed regarding the application.

For instance, we have seen that the main wave-front errors appearing in an optical instrument, due to misalignment, are the third order optical aberrations. Deformable mirrors generating astigmatism, coma and/or spherical aberrations are then useful to compensate for these errors. In this context, Freeman and Pearson [1982] present a 3-actuators DM able to compensate for focus and astigmatism, Dainty et al. [1998] have developed a 9 channels bimorph DM generating focus, astigmatism, coma and spherical aberrations, Figueira et al. [2007] show a 4 actuators DM for the correction of focus and astigmatism and Hugot et al. [2008] demonstrate the generation of astigmatism with a single actuator.

The approach developed in Chapter 5 continues this work, by developing simple correcting systems for off-axis optical designs, allowing the correction of several optical modes with a minimum number of actuators.

1.4 Active Optics for large telescopes

1.4.1 The Very Large Telescope: the most advanced Visible/Infra-Red telescope

The ESO/Very Large Telescope is located on Paranal Mount in Chile. It is constituted of 4 identical Unit Telescopes (UT) of 8.2 m diameter. Their combination with interferometry allows to reach

the resolution of a 200 m telescope. This telescope integrates active optics in all of its aspect, illustrating well the benefits of such a technique.

Figure 1.13 : *The VLT on Paranal (credit ESO).*

Active primary mirrors

The VLT primary mirrors are extremely thin: 18 cm for a diameter of 8.2 m. As shown on Figure 1.14, their optical shapes are actively maintained by 150 push/pull actuators, applying one correction per minute [Knohl, 1994]. This active optics has been crucial since the VLT first light, ensuring its good performance and allowing to gain time for the re-calibration and re-focusing steps.
The tip/tilt correction is achieved with the secondary mirror, minimizing the necessary stroke for the primary mirror active system.

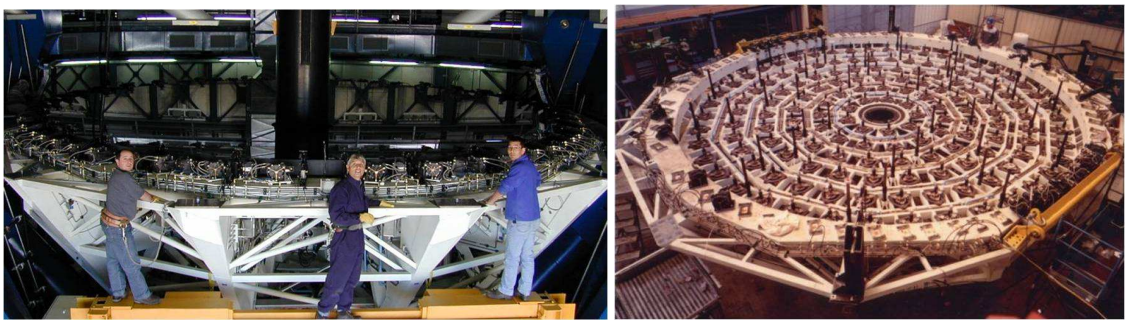

Figure 1.14 : *ESO/VLT active primary mirror (credit ESO)*

Variable Curvature Mirrors

The light beams from the 4 telescopes can be combined in the VLT Interferometric mode. The combination is performed through moving delay lines, which must keep the optical path equal over hundreds meters. The tertiary mirror of each delay line is a Variable Curvature Mirror (VCM), of 16 mm diameter. The application of a pressure on the thin mirrors back face adjusts its radius of curvature from 2800 mm to 84 mm, with an optical surface quality of $\lambda/4$ PtV. This powerful zoom function allows an efficient stabilization of the pupil size and position on the whole delay line range: the pupil is positioned with a precision of 15 cm over 350 m [Ferrari, 1998].

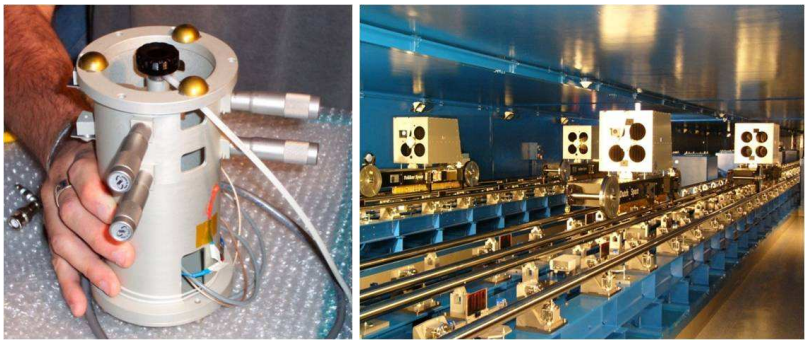

Figure 1.15 : *A Variable Curvature Mirror before its integration on the delay line and the VLTI delay lines (credit ESO).*

Toric Mirrors

The VLT second generation instrument SPHERE, dedicated to exo-planets high contrast imaging. It has been designed considering the main requirements for exo-planets direct detection, which are:

- an off-axis design in order to minimize the diffraction,
- high quality optical surface, without high spatial frequency errors in order to minimize the residual speckles.

For these two reasons, the optical design of SPHERE includes three toric mirrors manufactured with stress polishing.

A toric surface is defined as a sphere plus an astigmatism. This optical shape is obtained by applying two pairs of opposite forces on the mirror periphery, on two orthogonal diameters. With middle and high spatial frequencies errors lower than 2 nm rms, the quality of the three aspherical mirrors will allow high adaptive optics and coronographic performance [Hugot et al., 2012].

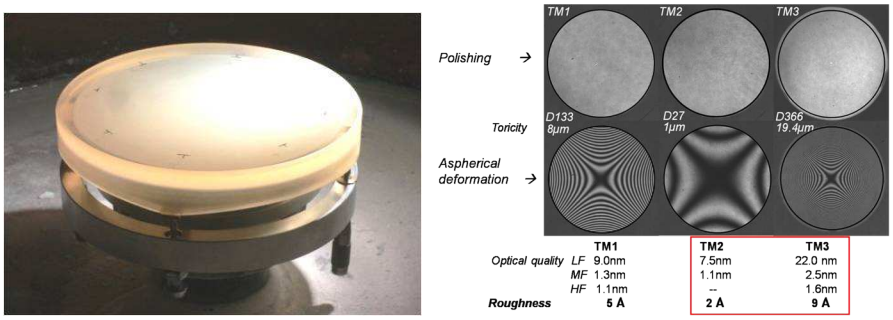

Figure 1.16 : *Toric mirror on its warping harness and interferogramms of the 3 finished mirrors (from Hugot et al. [2009]).*

Conclusion

Since its first light, in 1998, the VLT and VLTI have allowed major astrophysical discoveries. A part of this high efficiency is due to the use of various active optics systems, on many levels. Having demonstrated the possibilities of such techniques, the VLT has paved the way for future telescopes.

1.4.2 Toward large segmented active telescopes: ELT and JWST

The Extremely Large Telescopes: an opto-mechanic challenge

Future Earth based observatories will belong to the 30 meters class telescope. Such a large optical aperture requires the use of segmented primary mirror. There are 3 main projects of giant telescopes (Figure 1.18), all of them planning a first light by 2020-2030: the 24.5 m Giant Magellan Telescope (GMT), which will be located in the Atacama desert in Chile, the Thirty Meter Telescope (TMT), which will be located on Mauna Kea in Hawai, and the 39 m European Extremely Large Telescope (E-ELT), which also will be located on the Atacama desert.
The realization of these giant telescopes presents numerous challenges and requires some technological breakthroughs, for both structures and optical conceptions [Spanò et al., 2006] As for the VLT, active optics will be exploited to its maximum capability.

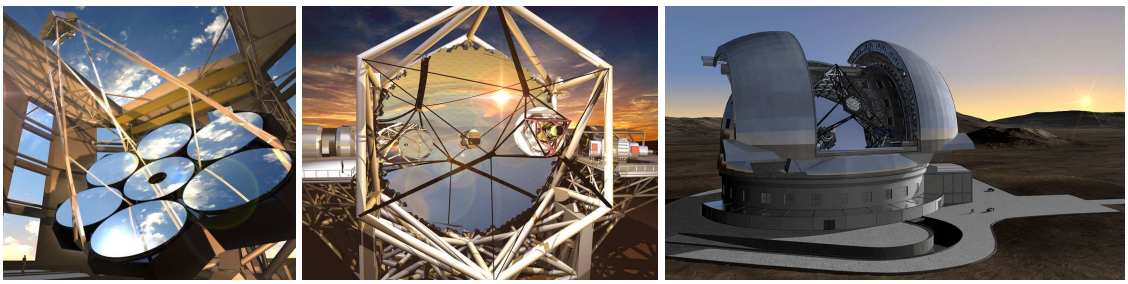

Figure 1.17 : *Future giant telescopes: 24.5 m GMT (credit GMTO), 30 m TMT (credit TMT) and 39 m E-ELT (credit ESO).*

The E-ELT is an active and adaptive five mirrors telescope, this original design will feed the instrument with an optical quality almost diffraction limited over the entire 10 arcmin field of view and on a wavelength range from the visible to the mid infra-red [Delabre, 2008].
The main science goals of this extremely large aperture optical/infrared telescope are the search for exo-planets in the stars habitable zones, the study of the first objects in the Universe and the probing of dark matter and dark energy.

The telescope is a Three Mirror Anastigmat with two additional folding adaptive mirrors. All the mirrors will present many innovations [ESO, 2011].

- *Primary mirror*

Composed of 798 hexagonal segments of 1.45 m, the primary mirror is an ellipsoid of 39.3 m diameter, it has a focal ratio of 0.93 and a central obstruction of 9.4 m diameter. The manufacturing of the 1.45 m segments within the next 6 years is one of the main challenge of the E-ELT project. In this context, stress polishing techniques are envisaged. As for the 8-10 m class, its optical shape will be actively maintained: each segment is supported by a 27 points whiffletree and the segment and supporting structure can be moved in piston and tip/tilt with three position actuators. This active system will not only compensate for the mirror cell deflections due to temperature and gravity effects, but also be used for the global reconstruction of the mirror shape, that is to say the segments co-phasing.

- *Secondary mirror*

The secondary mirror is convex and 4.1 m diameter, it is also an active mirror. The challenge for

this mirror is its fixation: it is mounted on an hexapod and this 12 tons system will be hanging above the primary mirror.

- Tertiary mirror
The tertiary mirror is concave, mildly aspheric, with a diameter of 3.7 m. Once again, it is a thin active meniscus, with a supporting system based on the one developed for the NTT. The fixation device of the tertiary mirror allows its alignment with the secondary and quaternary mirrors.

- Quaternary mirror
The quaternary mirror, inclined at 7.7°, is a thin meniscus (2.4 m diameter and 2 mm thick), segmented in six parts. This flat mirror is adaptive with 6000 actuators. The optical surface will be readjusted at very high time frequencies and is specified to be able to deliver very high Strehl ratios. It will correct in real time for high order wavefront errors (atmosphere and wind shake), and for small amplitude residual tip-tilt and low spatial frequency errors.

- Fifth mirror
The fifth mirror is ultra-lightweight and flat, with an elliptic contour of 2.6 x 2.1 m, it feeds the Nasmyth focus with a beam at F/17.5. It is a fast steering mirror, compensating for image motion at frequencies up to a few Hz. It will allow a tip/tilt field stabilization.

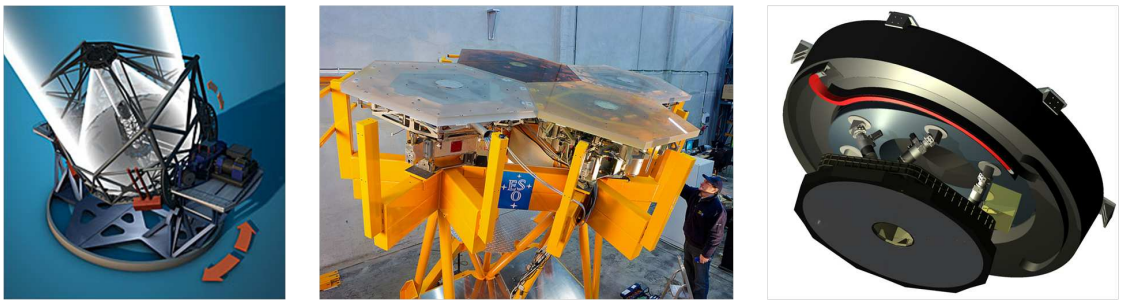

Figure 1.18 : *Opto-mechanical design of the E-ELT - Assembly of 4 segments of its primary mirror - Concept of its quaternary adaptive mirror (credit ESO).*

In conclusion, thanks to an innovative design, including efficient active and adaptive mirrors, the E-ELT will provide a high quality optical beam to its instruments. The construction of this telescope still requires opto-mechanical developments but it will constitute a great milestone in astronomy, regarding both instrumentation and science.

The James Webb Space Telescope: the first active space observatory

The James Webb Space Telescope (JWST) is a 6.5 m space-based Infra-Red (IR) telescope, it will orbit at the Earth-Sun L2 and its launch is foreseen in 2018. Covering a spectral range from 0.6 to 2.7 μm, with imaging and spectroscopic configurations, it will study the epoch when the first stars and galaxies formed and reionized the universe [Gardner et al., 2006].

The optical design of the JWST consists in a Three Mirrors Anastigmat, with a large and well corrected field of view. A fourth actively controlled Fine Steering Mirror folds the optical path and stabilizes the image. These 4 mirrors are in Beryllium, with a reflecting gold coating.

It has a large sun-shield, of the size of a tennis court, protecting the telescope and instruments from a direct sunlight exposition, and in this way providing a passive cooling of the observatory down to 40 K.
The large size of the primary mirror and of the sun-shield, plus the distance between primary and secondary, require the observatory to be folded up into the launch fairing and deployed during its journey to L2 (Figure 1.19).
JWST will then incorporate many innovative technologies, including ultralightweight beryllium optics, a deployable structure, microshutters for objects selection in the spectrograph, a mechanical cryocooler, high quality IR detectors to record extremely weak signals, and, last but not least, a folded segmented primary mirror which will be adjusted with cryogenic actuators.

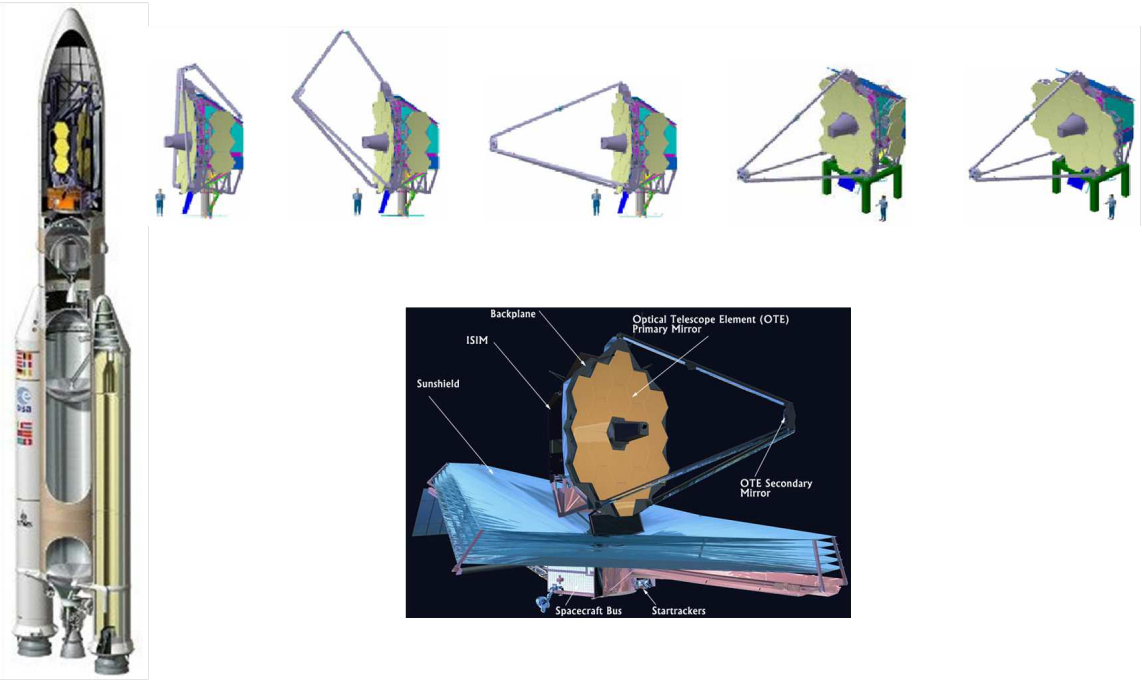

Figure 1.19 : *The James Webb Space Telescope: JWST stowed into its Ariane V rocket cap - deployment steps - Overview of the telescope (credit NASA).*

The primary mirror is 6.5 m diameter, it is concave with a radius of curvature of 16 m. It consists of 18 lightweight hexagonal segments. The low areal density technology for primary mirror is based on a semi-rigid architecture [Kendrick et al., 2001]. The curvature and astigmatism surface errors are difficult to control during the segments manufacturing. Therefore, this type of errors must be compensated in flight. The astigmatism will be corrected with a rigid body decentering, achieved with an hexapod providing 6 degrees of freedom. The adjustment of the surface curvature will be achieved with a flexure system, composed of 6 rods attached at the vertices of the segment at one end and to an actuator below the center. This actuator, pushing or pulling under the mirror center will adjust its curvature. These Primary Mirror Segment Assemblies (PMSA), shown on Figure 1.20, are mounted on a back-plane assembly having deployable wings.
Driving the entire telescope performance, the robustness of such a system is extremely important. For this reason, 3 of the 6 degrees of freedom have only a weak influence on the wave-front, ensuring to keep an efficient system up to 3 dead actuators. In addition, a degradation of the Wave-Front Error (WFE) on one segment is diluted with the WFE from the other segments. The actuators driving the radius of curvature being set in an optimal position before launch, the loss of control of one of them will not impact the overall WFE in a significant way. The most serious risk is the

failure of an actuator to deploy the segment. This effect can be mitigated by use of the 5 remaining actuators to adjust the segment.

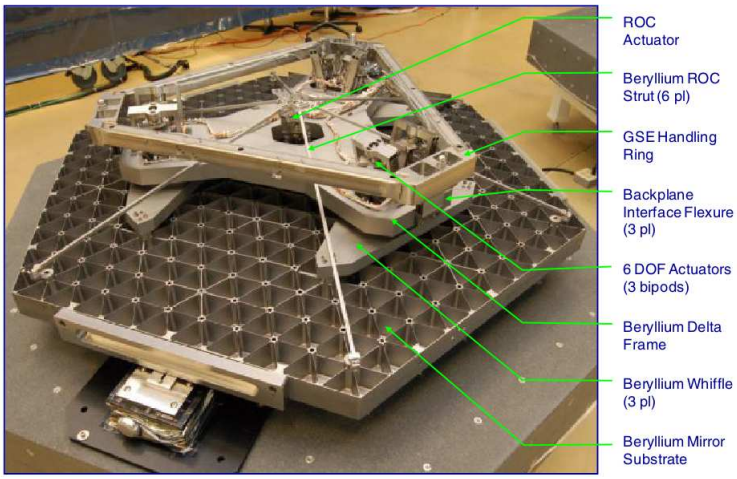

Figure 1.20 : *Backface of a Primary Mirror Segment Assembly (from Lightsey et al. [2012]).*

After the telescope deployment and cooling down, the 18 segments must be co-phased and the overall telescope aligned (see Figure 1.21). The state of the telescope performance is deduced from imagery from the science instrument, which will drive the Wave-Front Sensing and Control (WFSC) process [Contos et al., 2008].
The WFSC will adjust the pose of the individual PMSA to form a phased primary mirror and it will align the primary and secondary mirrors to the fixed tertiary.
The first step of the alignment process is the focusing of the secondary mirror. Then, each segment is individually align to the rest of the telescope, producing 18 images. An average focus is set from there. By sequentially tilting each segment, each image is associated to its segment and the images location is used to correct the tilts. At this point, focus phase retrieval is used for the global alignment and a dispersed Hartmann sensor is used to determine the piston mismatch between segments. The final step is to perform a multi-instrument, multi-field wave-front sensing to align the primary and secondary on the tertiary, reducing field-dependent astigmatism and focus errors.
In order to maintain the telescope performance, the fine phasing process is planned to be done every 14 days.

In conclusion, the JWST will fly with a 6.5 m primary mirror, which is lightweight, segmented, deployable and active. This telescope presents an impressive array of innovative technologies and demonstrates the importance of active optics and wave-front control techniques for the emergence of large space telescopes.

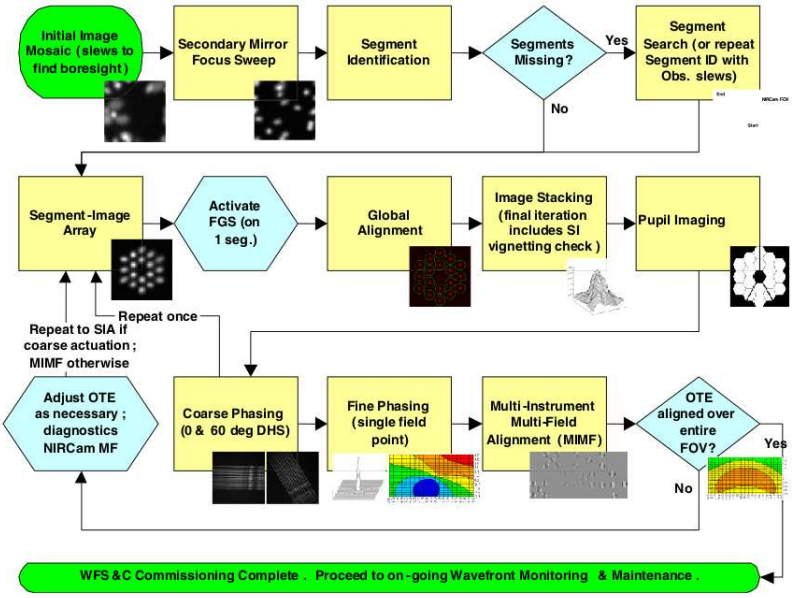

Figure 1.21 : *Wavefront sensing and control method to align and phase the JWST (from Lightsey et al. [2012]).*

1.5 Conclusion

Advances in the domain of Earth observation and in the main fields of astrophysics and astronomy, such as the search for exoplanets, the cosmology or the study of stars and galaxies, will be possible thanks to the development of innovative instrumental solutions, which will allow a major step towards larger observatories. In this context, active optics appears as a key element for the next generation of telescopes, especially in space. In this manuscript, three axis of development are studied:

- the compensation of large primary mirror deformation in space with a small active system, placed in the telescope exit pupil plane,

- the manufacturing of large primary mirror segments using stress polishing technique, with a dedicated warping harness,

- the conceptual development of optimized systems, with a minimum number of actuators, dedicated to a given application.

Bibliography

T. Arnold, G. Böhm, R. Fechner, J. Meister, and A. Nickel et al. Ultra-precision surface finishing by ion beam and plasma jet techniques - status and outlook. *Nuclear Instruments and Methods in Physics Research A*, 616:147–156, May 2010.

J.-L. Beuzit, A. Boccaletti, M. Feldt, K. Dohlen, D. Mouillet, and P. Puget et al. Direct Detection of Giant Extrasolar Planets with SPHERE on the VLT. In *Pathways Towards Habitable Planets*, volume 430 of *Astronomical Society of the Pacific Conference Series*, page 231, October 2010.

R. Bingham, D. Walker, D. Kim, D. Brooks, R. Freeman, and D. Riley. Novel automated process for aspheric surfaces. volume 4093 of *Society of Photo-Optical Instrumentation Engineers (SPIE) Conference Series*, pages 445–450, October 2000.

J.F. Bonnans, J.C. Gilbert, C. Lemarechal, and C.A. Sagastizabal. *Numerical optimization: theoretical and practical aspects*. Springer, 2009.

M. Born and E. Wolf. *Principles of Optics*. Pergamon Press Ltd, London, 1959.

A. Contos, D. Acton, A. Barto, L. Burns, and J. Contreras et al. Verification of the James Webb Space Telescope (JWST) wavefront sensing and control system. volume 7010 of *Society of Photo-Optical Instrumentation Engineers (SPIE) Conference Series*, August 2008.

D. R. Coulter and D. N. Jacobson. Technology for the Next Generation Space Telescope. volume 4013 of *Society of Photo-Optical Instrumentation Engineers (SPIE) Conference Series*, pages 784–794, July 2000.

J. C. Dainty, A. V. Koryabin, and A. V. Kudryashov. Low-Order Adaptive Deformable Mirror. *Applied Optics*, 37:4663–4668, July 1998.

B. Delabre. Optical design for an adaptive anastigmatic five-mirror extremely large telescope. *Astronomy and Astrophysics*, 487:389–397, August 2008.

J. K. Dürr, R. Honke, M. von Alberti, and R. Sippel. Development and manufacture of an adaptive lightweight mirror for space application. *Smart Material Structures*, 12:1005–1016, December 2003.

ESO. E-ELT Construction Proposal. Technical report, ESO, 2011.

M. Ferrari. Development of a variable curvature mirror for the delay lines of the VLT interferometer. *Astronomy and Astrophysics*, 128:221–227, February 1998.

G. Figueira, J. Wemans, H. Pires, N. Lopes, and L. Cardoso. Single adjuster deformable mirror with four contact points for simultaneous correction of astigmatism and defocus. *Optics Express*, 15:5664–5673, April 2007.

R. H. Freeman and J. E. Pearson. Deformable mirrors for all seasons and reasons. *Applied Optics*, 21:580–588, February 1982.

J. Frogel, C. Alcock, M. Bolte, W. Freedman, and R. Kudritzki et al. Frontier Science and Adaptive Optics On Existing and Next Generation Telescopes. volume 2010 of *astro2010: The Astronomy and Astrophysics Decadal Survey*, page 16P, 2009.

J. Gardner, J. Mather, M. Clampin, R. Doyon, and M. Greenhouse et al. The James Webb Space Telescope. *Space Science Review*, 123:485–606, April 2006.

M. Giavalisco, D. Calzetti, M. Dickinson, H. Ferguson, and H. Mo et al. The Quest For a Physical Understanding of Galaxies Across the Cosmic Time. volume 2010 of *astro2010: The Astronomy and Astrophysics Decadal Survey*, page 93, 2009.

O. Guyon. Limits of Adaptive Optics for High-Contrast Imaging. *Astrophysical Journal*, 629: 592–614, August 2005.

E. Hecht. *Optics 2nd edition*. Addison-Wesley Publishing Company, 1987.

E. Hugot, G. R. Lemaître, and M. Ferrari. Active optics: single actuator principle and angular thickness distribution for astigmatism compensation by elasticity. *Applied Optics*, 47:1401–1409, April 2008.

E. Hugot, M. Ferrari, K. E. Hadi, P. Vola, and J. L. Gimenez et al. Active Optics: stress polishing of toric mirrors for the VLT SPHERE adaptive optics system. *Applied Optics*, 48:2932–+, May 2009.

E. Hugot, M. Ferrari, K. El Hadi, A. Costille, K. Dohlen, P. Rabou, P. Puget, and J. L. Beuzit. Active optics methods for exoplanet direct imaging. Stress polishing of supersmooth aspherics for VLT-SPHERE planet finder. *Astronomy and Astrophysics*, 538:A139, February 2012.

J. Kasting, W. Traub, A. Roberge, A. Leger, and A. Schwartz et al. Exoplanet Characterization and the Search for Life. *Astronomy*, 2010:151, 2009.

S. E. Kendrick, T. Reed, and S. Streetman. In-process status of the 1.4-m beryllium semi-rigid Advanced Mirror System Demonstrator (AMSD). volume 4451 of *Society of Photo-Optical Instrumentation Engineers (SPIE) Conference Series*, pages 58–66, December 2001.

B. J. Kent. Implications of the space environment. *ISSI Scientific Reports Series*, 9:625–643, 2010.

W. B. King. Dependence of the Strehl Ratio on the Magnitude of the Variance of the Wave Aberration. *Journal of the Optical Society of America*, 58:655, May 1968.

M. Kissler-Patig and M. McCaughrean. Report on the ESO/ESA Workshop JWST and the ELTs: An Ideal Combination. *The Messenger*, 140:57, June 2010.

E.-D. Knohl. VLT primary support system. volume 2199 of *Society of Photo-Optical Instrumentation Engineers (SPIE) Conference Series*, pages 271–283, June 1994.

G. P. Kuiper. *The atmospheres of the earth and planets.* University of Chicago Press, 1952.

J.-L. Lamard, C. Gaudin-Delrieu, D. Valentini, C. Renard, T. Tournier, and J.-M. Laherrere. Design of the high resolution optical instrument for the PLEIADES HR Earth observation satellites. volume 554 of *5th International Conference on Space Optics*, pages 149–156, June 2004.

C. Latry and J.-M. Delvit. Staggered arrays for high resolution earth observing systems. volume 7452 of *Society of Photo-Optical Instrumentation Engineers (SPIE) Conference Series*, August 2009.

G. Lemaitre. New procedure for making Schmidt corrector plates. *Applied Optics*, 11:1630–1636, 1972.

G. R. Lemaître. *Astronomical Optics and Elasticity Theory - Active Optics Methods*. Astronomy and Astrophysics Library. Springer, 2009.

P. A. Lightsey, C. Atkinson, M. Clampin, and L. D. Feinberg. James Webb Space Telescope: large deployable cryogenic telescope in space. *Optical Engineering*, 51:011003, January 2012.

J. Lubliner and J. E. Nelson. Stressed mirror polishing. 1: A technique for producing nonaxisymmetric mirrors. *Applied Optics*, 19:2332–+, July 1980.

B. Macintosh, J. Graham, D. Palmer, R. Doyon, D. Gavel, and J. Larkin et al. The Gemini Planet Imager. volume 6272 of *Society of Photo-Optical Instrumentation Engineers (SPIE) Conference Series*, 2006.

V. Mahajan. *Optical Imaging and Aberrations I: Ray Geometrical Optics*. SPIE Press, 1998a.

V. Mahajan. *Optical Imaging and Aberrations II: Wave Diffraction Optics*. SPIE Press, 1998b.

M. Mayor and D. Queloz. A Jupiter-mass companion to a solar-type star. *Nature*, 378:355–359, November 1995.

B. K. McComas. *Configurable adaptive optics for the correction of space-based optical systems*. PhD thesis, University of Colorado at Boulder, 2002.

M. Mountain, R. van der Marel, R. Soummer, A. Koekemoer, and H. Ferguson et al. Comparison of optical observational capabilities for the coming decades: ground versus space. astro2010: The Astronomy and Astrophysics Decadal Survey, page 12, 2009.

P. Murdin. *Active Optics*. Encyclopedia of Astronomy and Astrophysics, November 2000.

J. E. Nelson, G. Gabor, L. K. Hunt, J. Lubliner, and T. S. Mast. Stressed mirror polishing. 2: Fabrication of an off-axis section of a paraboloid. *Applied Optics*, 19:2341–2352, July 1980.

R. J. Noll. Zernike polynomials and atmospheric turbulence. *Journal of the Optical Society of America*, 66:207–211, March 1976.

M. Perryman. *The Exoplanet Handbook*. Cambridge University Press, June 2011.

M. Postman, T. Brown, K. Sembach, M. Giavalisco, and W. Traub et al. Advanced Technology Large-Aperture Space Telescope: science drivers and technology developments. *Optical Engineering*, 51:011007, January 2012.

A. G. Riess, A. V. Filippenko, P. Challis, A. Clocchiatti, and A. Diercks et al. Observational Evidence from Supernovae for an Accelerating Universe and a Cosmological Constant. *Astronomical Journal*, 116:1009–1038, September 1998.

A. Saint Venant. *Résumé des leçons de Navier sur l'application de la mécanique*. Dunod, 1881.

B. Schmidt. A coma free telescope. *Mitt.Hamburg Sternv*, pages 7–15, 1932.

L. Seidel. *Astron. Nachr.*, 43:289, 1856.

K. Sembach, M. Beasley, M. Blouke, D. Ebbets, and J. Green et al. Technology Investments to Meet the Needs of Astronomy at Ultraviolet Wavelengths in the 21st Century. volume 2010 of *astro2010: The Astronomy and Astrophysics Decadal Survey*, page 54, 2009.

I.M. Smith and D.V. Griffiths. *Programming the Finite Element Method*. 4th edition. Wiley, 2004.

P. Spanò, F. M. Zerbi, C. J. Norrie, C. R. Cunningham, and K. G. Strassmeier et al. Challenges in optics for Extremely Large Telescope instrumentation. *Astronomische Nachrichten*, 327: 649–673, August 2006.

L. E. Strigari, J. S. Bullock, and M. Kaplinghat. Determining the Nature of Dark Matter with Astrometry. *Astrophysical Journal, Letters*, 657:L1–L4, March 2007.

S. P. Timoshenko and S. Woinowsky-Krieger. *Theory of Plates and Shells*. Engineering Mechanics Series. McGRAW-Hill International Editions, 1959.

J. Wallman and J. Winawer. Homeostasis of Eye Growth and the Question of Myopia. *Neuron*, 43:447–468, 2004.

R. N. Wilson. *Reflecting Telescope Optics I. Basic Design Theory and its Historical Development.* Astronomy and Astrophysics Library. Springer, 1996.

R. N. Wilson, F. Franza, L. Noethe, and G. Andreoni. Active Optics: IV. Set-up and Performance of the Optics of the ESO New Technology Telescope (NTT) in the Observatory. *Journal of Modern Optics*, 38:219–243, February 1991.

Chapter 2

Correcting active mirror for space telescope : MADRAS project

---

Until now, active optics concepts have been developed in the framework of Earth-based observatories. Very soon, the recourse to active systems will become mandatory in space with the telescopes' aperture increase. With its 18 active segments, the James Webb Space Telescope will be a precursor in this domain.

In this chapter, we present the design and opto-mechanical validation of the MADRAS mirror: a correcting mirror dedicated to the in-situ compensation of large, lightweight primary mirrors' deformation in space. The active system is designed to perform the correction in the telescope exit pupil plane, reducing this way the weight, the bulk and the number of actuators.

Firstly, the context of large observatories in space is reviewed and the MADRAS project is introduced. Secondly, the mirror design is detailed, the Multimode Deformable Mirror principle is based on the elasticity theory and it has been optimized with Finite Element Analysis, according to the correction need. Thirdly, the mirror performance is deduced from the FEA: the precision of correction and the mechanical behavior are characterized. Fourthly, the hardware specification, based on the FEA is described and the integrated system presented. Finally, the correcting system is experimentally validated with interferometrical measurements.

The work presented in this chapter has led to the following publication:
- M. Laslandes, M. Ferrari, E. Hugot, G. Lemaitre, In-flight aberrations corrections for large space telescopes using active optics, SPIE 7739, 2010.

2.1 Large space observatories context

2.1.1 Space telescope evolution and needs

Since their beginning, telescopes are evolving towards two main goals: increasing the collecting power and improving the angular resolution. These two characteristics directly depends on the optical aperture: access to finest observations would be possible with larger primary mirrors. However, the launch of space observatories imposes drastic constraints on satellites' weight and compactness. Thus, it becomes mandatory to use lightweight primary mirrors [Feinberg et al., 2012; Postman et al., 2012a]. Up to 3 meters, these mirrors can be contained in a launcher cap in one piece. For larger diameters, it will not be possible to use monolithic mirror with the actual launchers, segmented telescope concepts must be adopted. Such as the James Webb Space Telescope, segmented systems could be launched folded and deployed in flight [Lightsey et al., 2012]. It is also envisaged to launch the instrument in separate pieces which would be assembled in flight [Patterson et al., 2012; Postman et al., 2012b].

Lightweight mirrors are sensitive to the environment variations, so the structure stability will become a major issue in telescopes' design. Thermal variation and absence of gravity will induce large mirrors' deformations, generating optical aberrations in the instrument [McComas, 2002; Kendrew, 2006]. An active telescope would be then required in order to keep optimal performance. It will achieve a two levels correction. Firstly, it will correct a constant bias linked to the difference of gravity between integration on Earth at 1g and operation in space at 0g but also to the average thermal environment and the integration and alignment errors. Secondly, it will compensate for thermo-elastic deformation of the telescope structure and primary mirror, due to thermal fluctuations linked to the satellite orbit. These fluctuations will be of low temporal frequency.
Until now, the space telescopes' image quality was not sensitive to these kinds of deformation, thanks to their dimensions, to their material and to an adapted thermal control. But, for the future important pupil dimensions and the lightweight structures, the gravity and thermo-elastic deformation cannot be modeled with enough precision. The instrument will thus be sensitive to these errors which must be corrected in flight. Moreover, the possibility to compensate for the thermo-elastic errors allows to relax the constraints on the large structures stability.
Two systems will be necessary to compensate for the Wave-Front Errors induced by the expected deformations [Redding et al., 1998]:

- a 5 degrees of freedom mechanism on the secondary mirror to re-align the optics and then compensate for the structure deformation,
- an active system to compensate for the primary mirror deformation.

Active optics systems used in Earth-based telescopes are not directly applicable for space instrumentation. Considerations about weight, size, power consumption, mechanical strength and reliability must be addressed. Two different approaches are under study in order to compensate for these large lightweight mirrors deformations, privileging either the mirror weight or the system simplicity. The first solution consists in maintaining the primary mirror optimal shape with actuators under the optical surface. It requires an important number of actuators [Redding et al., 2012; Cohan and Miller, 2011]. The second solution consists in performing the correction in the exit pupil plane of the telescope, later in the optical train. It requires then a small active mirror with a limited number of actuators [Laslandes et al., 2012]. While the first method is interesting for highly lightweight and flexible mirrors, the second one, simpler to carry out, is ideal for mirrors staying relatively rigid. A correcting mirror, designed for this second approach is presented in this chapter.

2.1.2 MADRAS project

MADRAS (Mirror Actively Deformed and Regulated for Applications in Space) is a collaborative project between Thales Alenia Space, the Laboratoire d'Astrophysique de Marseille, Thales SESO and Shaktiware. It aims at developing a technological demonstrator of a correcting mirror for space telescopes, in order to bring this concept to a Technology Readiness Level (TRL) of 4.

As a study case, 3 meters class space telescopes are considered. Thanks to telescopes' modeling and deformation data from flying telescopes, the active optics requirements can be preliminarily quantified. The requirements are defined according to the application (Earth observation in low or geostationary orbit or astronomical observation at high angular resolution) and according to the telescope type (monolithic or deployable). A synthesis of these different needs has allowed the definition of a common specification for the MADRAS mirror, in terms of correction requirements and frequency, dimensions, mass, electrical consumption and thermal and mechanical environments [Thomas and Liotard, 2010].

In order to have a light and compact system, the correction is done in a plane conjugated to the primary mirror, thus the aberrations generated by the large mirror deformation are compensated in the telescope exit pupil plane, of much more smaller dimensions. In the considered designs, which are Korsch telescopes, the correcting mirror is 100 mm diameter, and its weight is limited to 5 kg.

The expected deformation are decomposed on the Zernike polynomials base, giving the number of Zernike modes to be corrected, with their amplitudes and required precisions. The correction frequency will depend on the orbit and on the structure and mirror materials.
For deployable telescope, the optical configuration consists in a Korsch telescope and the considered materials for the primary mirror segments are Zerodur or CeSic. In such a telescope, the thermo elastic deformations are linked to the baffle system, they mainly induce tip/tilt, defocus, astigmatism and trefoil errors. The Trefoil is due to the mirrors' clamping system which generally consists in a three points fixation.
For a monolithic telescope, the primary mirror will be in ceramic, to limit the weight. The budget error gives four main items limiting the image quality: the mirror manufacturing, the Assembling, Integration and Testing phases, the gravity effects and the on-orbit thermo-elastic deformation. The mirror manufacturing will induce high spatial frequency errors which are not addressed by the active correcting system. The integration and alignment errors will mainly induce coma, astigmatism and spherical aberrations. The gravity and thermo-elastic effects will deform the mirror in the first Zernike modes, up to the fifth order, with amplitudes around 30 nm rms.

The specifications for the MADRAS system are defined by coupling these datas (see Table 2.1): the gravity and thermo-elastic effects must be compensated with the generation of coma3, astigmatism3&5, spherical3, trefoil5&7, tetrafoil7&9 and pentafoil9, at a maximum amplitude of 30 nm rms for each mode. In addition, the generation of coma3, astigmatism3 and spherical3 modes must also correct for integration errors, so their specified amplitude is higher: 200 nm rms for the coma3, 150 nm rms for the astigmatism3 and 50 nm rms for the spherical3. Tip, tilt and focus are not addressed here, they will be corrected by a 5 degrees of freedom mechanism on the secondary mirror, adjusting the alignment. In order to achieve the required optical quality, the residual wave-front error after correction must be less than 5 nm rms for each individual mode and less than 10 nm rms for a global wave-front error, composed of a combination of these modes. As the correcting system addresses the effects of zero gravity and thermal dilatation, the required actuation

frequency is low, the demonstrator operates at 1 Hz.

The project aims at demonstrating the opto-mechanical performance of the mirror, designed for a space use. The correcting system is then designed taking into account space constraints. The system reliability and robustness are studied and the overall system is designed to survive space and launch environments.
In order to improve its Technology Readiness Level to a TRL4, the system performance is characterized in laboratory environment [ESA, 2008].
The validation of the actuators, the electronic and the command consists in a full-fledged study which is currently conducted. The MADRAS project does not focus on this technology and these components are not chosen considering the possibility to use them in space.

This project will be one of the first concrete demonstrations of the ability of active optics to compensate for in-flight deformation in a space telescope. Not only we have seen that active optics will be soon mandatory in large space observatories, but such a system could also be used on smaller telescopes in order to relax the tolerances on the optics dimensions and on the alignment. This would consist in a major innovation and will have a strong impact on the ratio performance over cost reduction, regarding development and assembling, integration and test.

Table 2.1 : *Modes to correct with MADRAS and their maximum amplitudes (target precision of correction < 5 nm rms).*

Mode	Maximum amplitude (nm rms)
Coma3	200
Astigmatism3	150
Spherical3	50
Trefoil5	30
Astigmatism5	30
Tetrafoil7	30
Trefoil7	30
Pentafoil9	30
Tetrafoil9	30

2.2 MADRAS mirror design

The concept of active mirror used for the MADRAS project has been developed by Lemaître [2005]. We present here its deformation principle and the design adaptation for our application.

2.2.1 Multimode Deformable Mirror: principle

The mirror design is based on the similarity between the Zernike polynomials used in the optical aberrations theory [Noll, 1976] and the Clebsch polynomials used in the elasticity theory [Timoshenko and Woinowsky-Krieger, 1959]. The basic geometry is presented in Figure 2.1. It is composed of:

- a meniscus corresponding to a thin circular plate of radius a and thickness t_1,

- an outer ring at the edge of the meniscus, of internal radius a, external radius b and thickness $t_2 > t_1$,

- k_m clamped arms, regularly distributed along the outer ring, going from radius b to radius c, and of thickness t_3.

The mirror deformation is achieved by applying a set of $2k_m$ discrete forces $F_{a,k}$ and $F_{c,k}$, located on both extremity of each arm, that is to say at the two radii a and c, at the angles θ_k defined by:

$$\theta_k = \frac{2\pi(k-1)}{k_m}, \tag{2.1}$$

with k the arm number, varying from 1 to k_m. In addition to these $2k_m$ concentrated forces, a uniform load q can be applied on the mirror back face, by mean of air pressure or depressure.

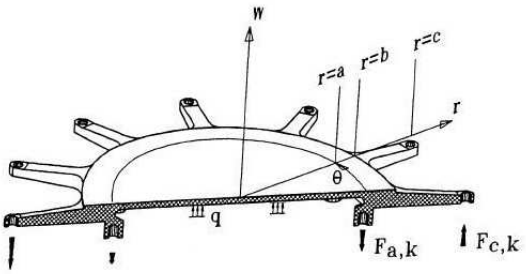

Figure 2.1 : *Vase form Multimode Deformable Mirror design (from Lemaître [2005])*

Such a design provides a convenient distribution of axial forces and bending moments acting along the mirror perimeter. Indeed, the two axial discrete force sets, equally distributed in azimuth angles, allow an angular flexure distribution. And, respecting the Saint Venant principle [Saint Venant, 1881], the point forces are applied sufficiently far from the optical aperture to generate a smooth and continuous surface. The design with two concentric zones of constant rigidity D_1 and D_2 not only allows the minimization of the shear flexure effect but also provides a smooth deformation of the perimeter. The number of radial arms is strongly dependent on the highest order of the angular modulation to be generated and must be optimized for all the required modes.

The elasticity equation can be applied to the two parts of the system (inner meniscus and outer ring) to describe the system deformation and the required forces:

$$\nabla^2\nabla^2 z = \frac{q}{D}, \tag{2.2}$$

with $D = \frac{Et^3}{12(1-\nu^2)}$ the rigidity depending on the thickness t and the material characteristics: Young modulus E and Poisson ratio ν.

Inner meniscus

In this zone, the generated mode has an axial symmetry. So, it can be described as a combination of optical aberrations z_{nm}:

$$z_{in}(r,\theta) = \sum z_{nm}(r,\theta) = \sum A_{nm} r^n cos(m\theta). \tag{2.3}$$

The coefficients A_{nm} are determined by substituting the modes z_{nm} in Equation 2.2:

$$A_{nm}(n^2-m^2)\left[(n-2)^2-m^2\right] r^{n-4} cos(m\theta) = \frac{q}{D}. \tag{2.4}$$

So, if there is no uniform load ($q = 0$), Equation 2.4 has a solution only for $n = m$ and $n = m + 2$, In the same manner, with a uniform load q, the only solution is defined by $n = 4$ and $m = 0$. Moreover, the maximum azimuthal order m is given by the number of applied forces on a diameter: $m_{max} = k_m/2$.
These conditions gives the optical aberrations achievable with the system: they correspond to the first Zernike polynomials.

Outer ring

In this zone, there is no uniform load ($q = 0$), the deformation is defined by:

$$z_{out}(r,\theta) = \sum R_{nm}(r)cos(m\theta), \tag{2.5}$$

where R_{nm} are the Clebsch polynomials, determined by solving Equation 2.4:

$$\left(\frac{\partial^2}{\partial r^2} + \frac{1}{r}\frac{\partial}{\partial r} - \frac{m^2}{r^2}\right)\left(\frac{\partial^2 R_{nm}}{\partial r^2} + \frac{1}{r}\frac{\partial R_{nm}}{\partial r} - \frac{m^2}{r^2}R_{nm}\right) = 0 \tag{2.6}$$

$$=> \begin{cases} R_{n0} = B_{n0} + C_{n0}ln(r) + D_{n0}r^2 + E_{n0}r^2ln(r) \\ R_{n1} = B_{n1}r + C_{n1}r^{-1} + D_{n1}r^3 + E_{n1}rln(r) \\ R_{nm} = B_{nm}r^m + C_{nm}r^{-m} + D_{nm}r^{m+2} + E_{nm}r^{-m+2} \end{cases} \tag{2.7}$$

The coefficients B_{nm}, C_{nm}, D_{nm} and E_{nm} are determined in function of A_{nm} by using the continuity between the two systems zones:
- deformation: $z_{in}(r = a, \theta) = z_{out}(r = a, \theta)$,
- slope: $\partial z_{in}(r = a, \theta)/\partial r = \partial z_{out}(r = a, \theta)/\partial r$,
- bending moments: $M_{r,in}(r = a, \theta) = M_{r,out}(r = a, \theta)$,
- shearing force: $V_{r,in}(r = a, \theta) = V_{r,out}(r = a, \theta)$,

with

$$M_r(r,\theta) = D\left[\frac{\partial^2 z}{\partial r^2} + \nu\left(\frac{1}{r}\frac{\partial z}{\partial r} + \frac{1}{r^2}\frac{\partial^2 z}{\partial \theta^2}\right)\right], \tag{2.8}$$

and

$$V_r(r,\theta) = -D\left[\frac{\partial \nabla^2 z}{\partial r} - (1-\nu)\frac{1}{r}\frac{\partial}{\partial r}\left(\frac{1}{r}\frac{\partial^2 z}{\partial \theta^2}\right)\right]. \tag{2.9}$$

Forces

The forces required to generate a shape z_{in} are determined from the static equilibrium equations, considered on the angular sector around each arm. Force equilibrium gives:

$$F_{a,k} + F_{c,k} = b\int_{\pi(2k-3)/k_m}^{\pi(2k-1)/k_m} V_r(r = b, \theta)d\theta, \tag{2.10}$$

and moment equilibrium:

$$(a-b)F_{a,k} + (c-b)F_{c,k} = b\int_{\pi(2k-3)/k_m}^{\pi(2k-1)/k_m} M_r(r = b, \theta)d\theta. \tag{2.11}$$

The thicknesses of the meniscus t_1 and of the ring t_2 are generally chosen in order to have reasonable values of forces while sufficiently absorbing the local shape errors due to the discrete application of forces. Classically, the ratio t_2/t_1 is around 3.
The forces' values also depend on the arms' length and on the ring radial dimension. Once the basic system design is defined with the elasticity theory, it is refined with Finite Element Analysis.

Conclusion on the MDM design

We have described the concept of deformable mirror adopted for the MADRAS project. It allows the generation of Zernike polynomials defined by $n = m$, $n = m + 2$ and $(n, m) = (4, 0)$ with n and m the radial and azimuthal orders, which correspond well to the specified modes. The number of arms is chosen according to the required angular modulation. In our case, $m_{max} = 5$ so we need at least 10 arms. Due to the symmetry of the other modes, we choose a 12 arms design.
As we have seen, the forces that deform the mirror are applied far from the optical surface, in order to avoid the actuator print-through. Moreover, it decouples the number of actuators from the mirror diameter: the number of required actuators is only driven by the maximum spatial frequency to be corrected. Finally, this design is not associated to one actuator technology: any actuator applying discrete forces can be used with this kind of mirror. The initial geometry of a MDM is now optimized with Finite Element Analysis for the generation of the specified modes.

2.2.2 Final design

The active mirror is a monolithic piece of Zerodur, made up of a circular pupil with an external thicker ring and 12 arms. The optical surface is deformed through 24 actuators applying discrete forces on both sides of each arm. In the design presented in the previous section, the spherical aberration is generated thanks to the application of an uniform load under the optical surface. A pressure system is hardly usable in space, so a central clamping is added to the system. Not only this clamping will allow the spherical correction, but it will also hold the system, notably during launch.
The final design is presented in Figure 2.2, its dimensions have been optimized with Finite Element Analysis. As explained in Chapter 1, Section 1.3.2, we minimize the residual WFE and the level of stress in the mirror for each mode. The only fixed dimension was the pupil diameter of 90 mm. The weight and compactness are also major parameters to be optimized.

The final optimized design has a 3.5 mm thick mirror, an outer ring 11 mm thick and 5 mm long, and arms 15 mm long and 8 mm thick. The central clamping is done through a 12 mm diameter and 8 mm thick cylinder. In order to minimize the level of stress, the transition zones (between arms and ring and between central clamping and mirror back face) are smoothed with a transition of radius 4 mm.
The following Zerodur characteristics are used [Döhring et al., 2008]:

- Young modulus: E=90.6 GPa,
- Poisson ratio: ν=0.243,
- Mass density: d=2.53 g/cm^2.

The actuators are modeled by springs with a given stiffness and length. These values are characteristics for piezoelectric actuators, we use the data of the Cedrat PPA40M, which are the actuators envisaged for our system [Cedrat Technologies]. They are 48 mm long, have a stiffness of 20000 N/mm and provide a maximum stroke of 40 μm, and a maximum applied force of 800 N. The top extremity of the actuator is a node of the model, representing the force location (either under an arm or under the ring), and the bottom extremity is represented by a node clamped in the (x, y) plane. A displacement along the z axis is applied on the bottom spring node to simulate the actuation.
The other boundary condition on the model is the central clamping: the bottom nodes of this part are fixed in the 3 directions.

The Finite Element Model has 63708 hexaedrical elements and 77979 nodes. The optical surface contains 100 nodes on a diameter and 120 angular sectors, providing a sufficient sampling to characterize its deformation: up to 50 cycles per pupil.

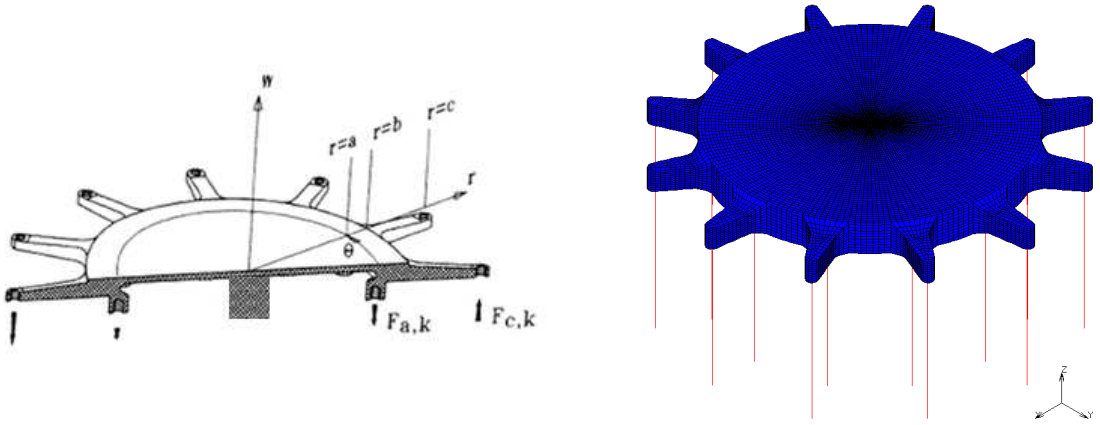

Figure 2.2 : *Left: Functioning principle of the MADRAS mirror - Right: Finite Element Model of the MADRAS mirror, with actuators represented by springs in red (63708 hexaedral elements, 77979 nodes (5881 nodes on the surface)).*

2.3 FEA performance

2.3.1 Influence Functions and Eigen Modes

The system Influence Functions are directly recovered on the FEA model by applying a displacement of 1 μm on one actuator while the others are fixed at their bottom extremity, the springs' stiffness allowing their elongation. This boundary condition simulates then well the reaction of the neighbor actuators. The 24 IF are shown in Figure 2.3.

From the IF base, the system eigen modes can be deduced, by performing a Singular Value Decomposition (SVD) [Golub and van Loan, 1996]. Let B be the base containing the 24 IF, it is a matrix containing 24 vectors giving the displacement of each nodes of the optical surface. This non square matrix can be decomposed in three matrices:

$$B = u\lambda v^t, \tag{2.12}$$

with u and v unitary matrices (defined by $u^{-1} = u^t$), corresponding to the system eigen vectors in the mirror and command domains and λ a diagonal matrix containing the system eigen values.
The eigen modes base M is then defined by:

$$M = Bv. \tag{2.13}$$

The eigen modes are shown on Figure 2.4, they constitute an orthogonal base, representing all the deformations that the system can achieve. As expected, the modes are similar to the Zernike polynomials.
The eigen value of each mode gives an energy information: the smaller is an eigen value, the harder it is to generate the corresponding eigen mode. On Figure 2.4, the eigen modes are sorted from the less to the more energetic: the modes with a small angular modulation are easier to

generate, they will require less force. The eigen values dispersion can be characterized with the conditioning factor χ:

$$\chi = \frac{\lambda_{max}}{\lambda_{min}}. \tag{2.14}$$

In our case, this factor is equal to 99.
As an eigen mode with a low value will require more energy and propagate the noise in an experimental system, the conditioning factor is an indicator of the system stability. To improve this factor, some eigen values can be filtered.

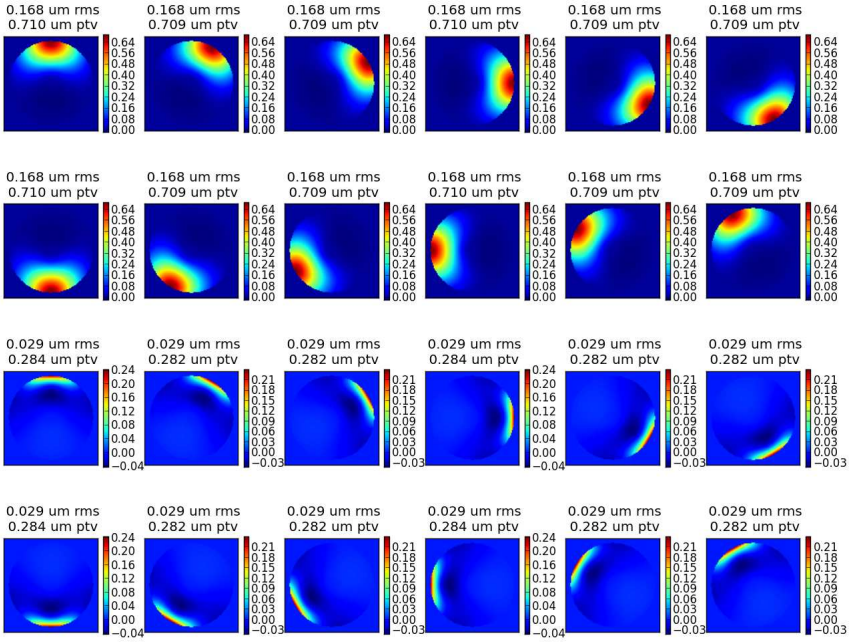

Figure 2.3 : *System Influence Functions (for a command of 1 µm) - FEA results (unit=[µm]).*

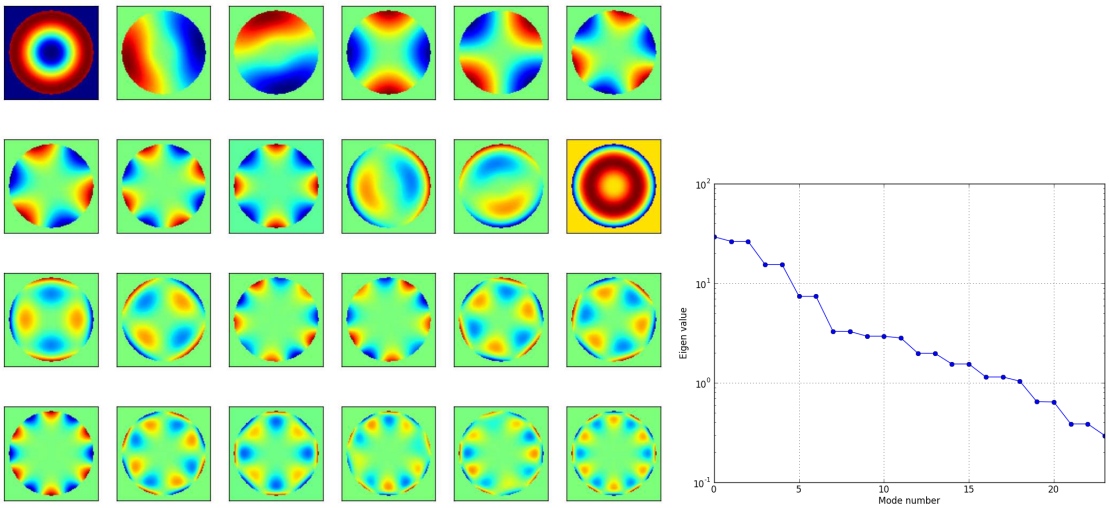

Figure 2.4 : *System eigen modes (from the less to the most energetic) and associated eigen values (from the simulated IF).*

2.3.2 Mode correction

As explained in Chapter 1, Section 1.3.2, the precision of correction of a given WFE is deduced from its projection on the influence functions. So, each specified Zernike, deduced from the deformation maps of primary mirrors in space, is decomposed on the IF base. We have seen in Section 2.1 that the correction of tip, tilt and focus will be addressed by a 5 degrees of freedom mechanism on the secondary mirror, it is simulated here by adding four virtual influence functions corresponding to these modes.
This addition allows to limit the impact of the central clamping. Indeed, the influence of the central clamping can be seen on the eigen modes (Figure 2.4): the modes looking like tilts and comas have a circular central footprint. In order to minimize the effect of this clamping, the slope at the center of the optical surface must be equal to 0, that is to say the generation of $\rho cos(\theta)$ or a $\rho sin(\theta)$ components must be avoided. The influence functions of tip and tilt ensure the non generation of these deformations.

Each specified mode is projected on the 27 Influence Functions base (24 “real“ IFs and 3 “virtual“ ones) in order to determine the residuals WFE expected after the correction and the required actuators' strokes. The computed commands are then injected into the finite element model to characterize the mechanical behavior: the resulting forces and stress are recovered.

Coma3 correction

Figure 2.5 presents the performance for the correction of 200 nm rms of coma3, deduced from the simulated IF. On this figure we can see:
- the specified mode, projected on the IF,
- the coefficients resulting from this projection, corresponding to the actuators commands,
- the reconstructed mode, corresponding to the WFE actually corrected by the system,
- the residual WFE, after the correction.

All the phase maps are shown without their components of piston, tip, tilt and focus.
The correction of this mode is highly efficient: the expected residual WFE is 0.7 nm rms and its shape correspond to harmonics of coma. The required commands are well modulated in $cos(\theta)$ and the maximum displacement is 0.6 μm for the internal actuator and 2.5 μm for the external ones.
Injecting these commands on the FEA model, we verify that the deformation is as expected (Figure 2.6). As explained before, the shape generated on the mirror for this mode correction only corresponds to the terms in $\rho^3 cos(\theta)$ of the Zernike polynomials describing the coma3 (the term in $\rho cos(\theta)$ is handled by the tilt virtual IF). The resulting stress and forces are recovered on the FEA model. The maximum stress is located at the junction between arm and ring and is equal to 1.01 MPa. The resulting forces appear on the mirror, at the actuator location. They follow the displacement modulation and have a maximum value of 5.8 N for the internal actuators and 4.3 N for the external ones.

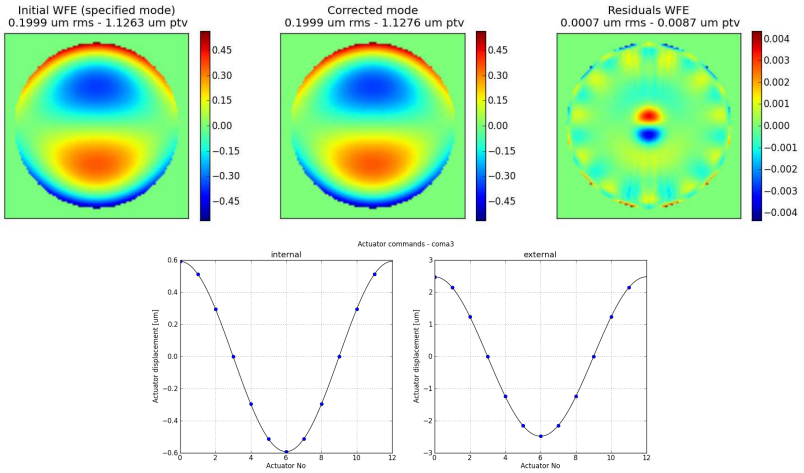

Figure 2.5 : *Performance for the correction of Coma3 computed with the simulated IF: Top: required mode - generated mode - residues (piston, tip, tilt and focus substracted - Unit:[μm]) - Bottom: Required actuators' displacement.*

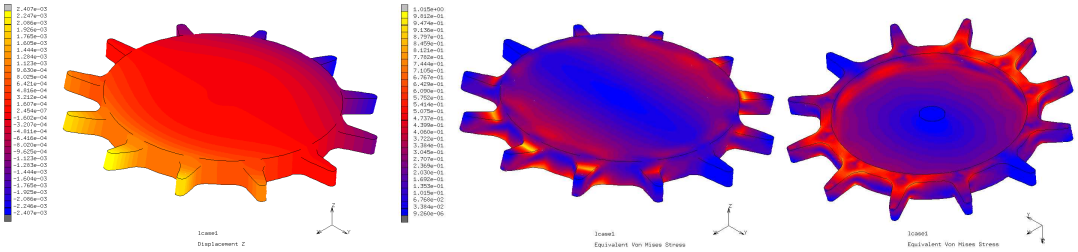

Figure 2.6 : *Mechanical behavior of the mirror for the generation of the $\rho^3 cos(\theta)$ component of the coma3, from FEA: resulting deformation [mm] and stress [MPa].*

Astigmatism3&5 correction

The astigmatism3&5 are also efficiently corrected. The residual after the correction of 150 nm rms of astigmatism3 is 2.5 nm rms. And the residual for 30 nm rms of astigmatism5 is 1.8 nm rms. Both residual phase maps are composed of harmonics of astigmatism. We recover the $cos(2\theta)$ modulation in the commands. The maximum displacements required for the astigmatism3 correction are 0.27 μm for the internal actuators and 0.29 μm for the external ones. The maximum resulting forces are respectively 1 N and 0.3 N. The maximum displacements required for the astigmatism5 correction are 0.09 μm for the internal actuators and 0.48 μm for the external ones. The maximum resulting forces are respectively 2.6 N and 1.5 N. The commands for both astigmatisms generation being low, they do not induce a lot of stress: the maximum level of constraint is 0.14 MPa for the astigmatism3, located at the internal actuator location, and 0.36 MPa for the astigmatism5, located at the junction between arm and ring.

Spherical3 correction

The spherical3 can be corrected thanks to the central clamping but the correction is not as efficient as with a uniform load, because the load configuration and induced force are not exactly the same. The residual WFE after the correction of 50 nm rms of spherical3 is expected to be 5.8 nm rms, which is slightly above the 5 nm rms specification. Nevertheless, this clamping constitutes a good trade-off: it allows the correction of the spherical aberration with a relative efficiency while

providing a system compatible with a space use in term of simplicity and mechanical strength: the central clamping holds the system for the launch, avoiding the recourse to an external system which could be a single point failure. The residuals are composed of higher order spherical aberrations. The required commands are constant for both rings of actuators: -0.5 μm for the internal ones and -0.74 μm for the external ones. The resulting forces are low: 0.15 N for the internal actuators and 0.42 for the external ones. The maximum stress occurs on the back face of the mirror, at the junction with the central clamping, it is 0.25 MPa.

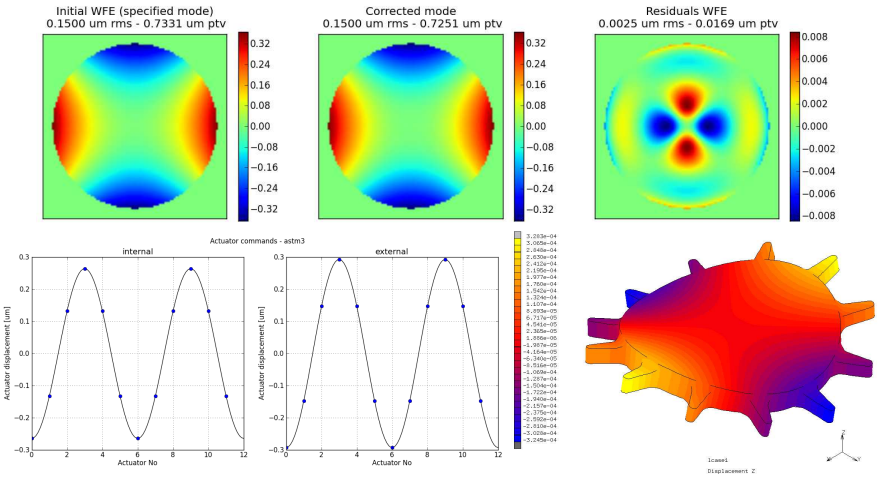

Figure 2.7 : *Performance for the correction of Astigmatism3, from FEA: Top: required mode - generated mode - residues (piston, tip, tilt and focus substracted - Unit:[μm]) - Bottom: Required actuators' displacement and resulting mirror deformation [mm].*

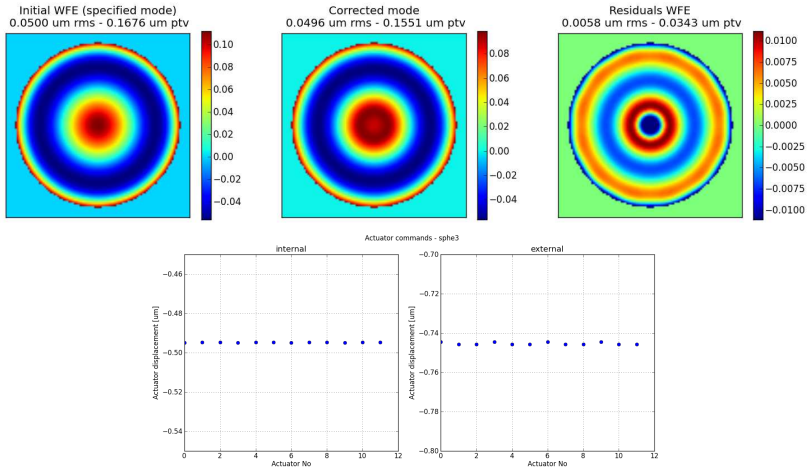

Figure 2.8 : *Performance for the correction of Spherical3 computed with the simulated IF: Top: required mode - generated mode - residues (piston, tip, tilt and focus substracted - Unit:[μm]) - Bottom: Required actuators' displacement.*

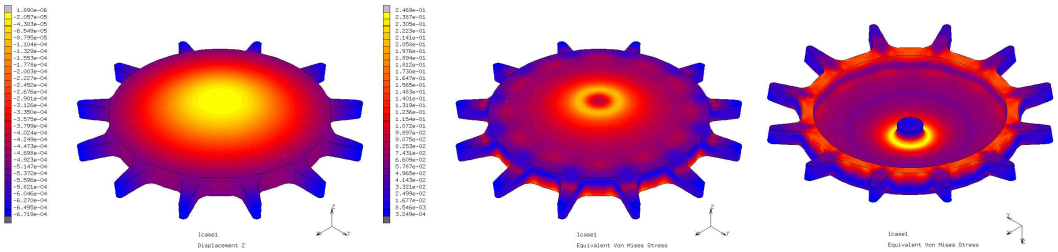

Figure 2.9 : *Mechanical behavior of the mirror for the generation of spherical3, from FEA: resulting deformation [mm] and stress [MPa].*

Trefoil5&7 correction

The residual after the correction of 30 nm rms of trefoil5 is 0.2 nm rms. And the residual for 30 nm rms of trefoil7 is 1.6 nm rms. Both residual phase maps are composed of modes modulated in $cos(9\theta)$. The required commands are well modulated in $cos(3\theta)$. The maximum commands required for the trefoil5 correction are 0.11 μm (and 0.88 N) for the internal actuators and 0.1 μm (and 0.01 N) for the external ones. The maximum commands required for the trefoil7 correction are 0.24 μm (and 5.13 N) for the internal actuators and 0.8 μm (and 3.2 N) for the external ones. The maximum level of constraint is here 0.1 MPa for the trefoil5, located at the internal actuator location, and 0.77 MPa for the trefoil7, located at the junction between arm and ring.

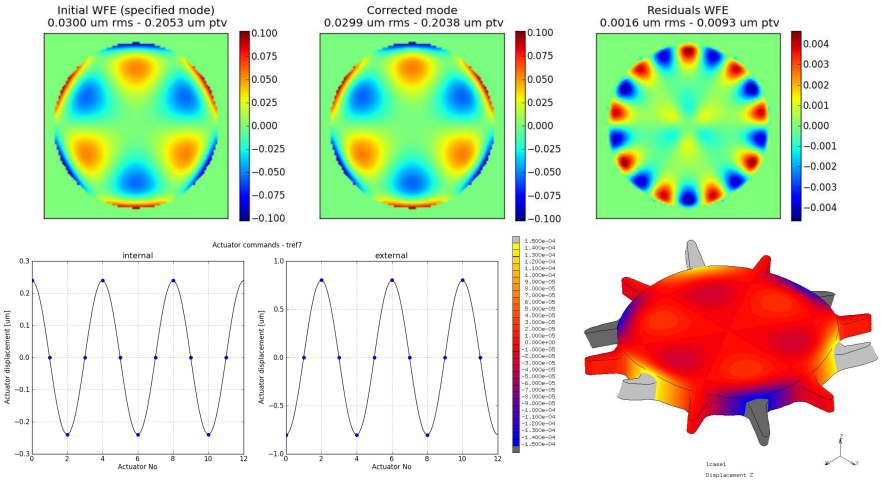

Figure 2.10 : *Performance for the correction of Trefoil7, from FEA: Top: required mode - generated mode - residues (piston, tip, tilt and focus substracted - Unit:[μm]) - Bottom: Required actuators' displacement and resulting mirror deformation [mm].*

Tetrafoil7&9 correction

The residual after the correction of 30 nm rms of tetrafoil7 is 1.4 nm rms. The residual phase map is composed of modes modulated in $cos(8\theta)$. The required commands are well modulated in $cos(4\theta)$. The maximum displacements required for this mode correction are 0.25 μm for the internal actuators and 0.19 μm for the external ones. The maximum resulting forces are respectively 2.9 N and 0.26 N. The maximum level of constraint is here 0.27 MPa, located at the internal actuator location.

The spatial frequency of the tetrafoil9 is high (both radially and angularly), it corresponds to an energetic eigen modes. This mode is then less efficiently corrected, it requires more displacement and induces more stress. The residual after the correction of 30 nm rms of tetrafoil9 is 4.5 nm rms. The maximum displacements are 0.45 μm for the internal actuators and 1.4 μm for the external ones. The maximum resulting forces are respectively 8.75 N and 6.54 N. The maximum level of stress is here 1.58 MPa, located at the junction between arm and ring.

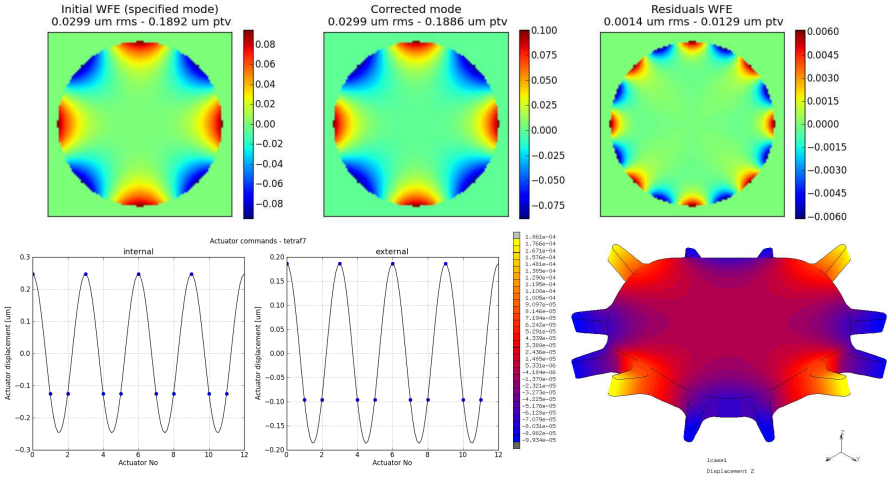

Figure 2.11 : *Performance for the correction of Tetrafoil7, from FEA: Top: required mode - generated mode - residues (piston, tip, tilt and focus substracted - Unit:[μm]) - Bottom: Required actuators' displacement and resulting mirror deformation [mm].*

Pentafoil9 correction

The pentafoil has 5-fold rotational symmetry, while the system presents symmetries 2, 3, 4 and 6. It is one of the more energetic eigen mode, so, the correction of this mode is the most problematic. The residual after the correction of 30 nm rms of pentafoil9 is 6.8 nm rms. The residual phase map is composed of modes modulated in $cos(7\theta)$. The required commands are well modulated in $cos(5\theta)$. The maximum displacements required for this mode correction are 0.52 μm for the internal actuators and 0.42 μm for the external ones. The maximum resulting forces are respectively 6.73 N and 1.3 N. The maximum level of stress is here 0.61 MPa, located at the internal actuator location.

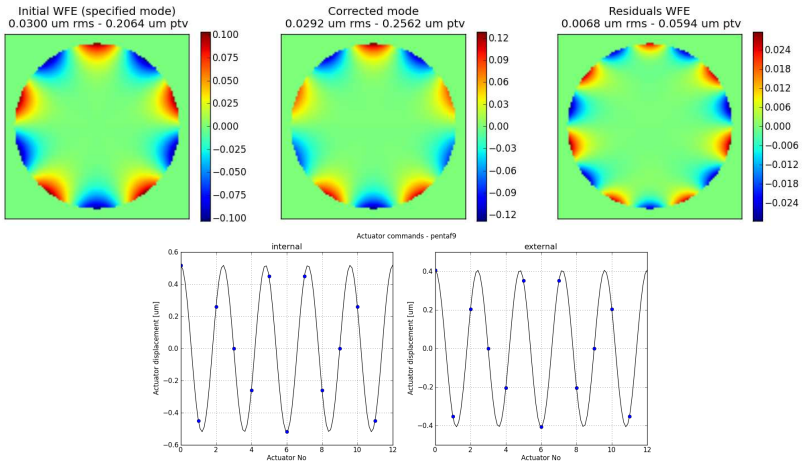

Figure 2.12 : *Performance for the correction of Pentafoil9 computed with the simulated IF: Top: required mode - generated mode - residues (piston, tip, tilt and focus substracted - Unit:[µm]) - Bottom: Required actuators' displacement.*

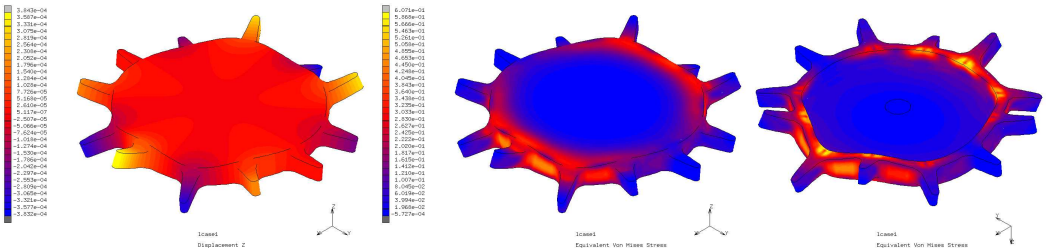

Figure 2.13 : *Mechanical behavior of the mirror for the generation of pentafoil9, from FEA: resulting deformation [mm] and stress [MPa].*

2.3.3 Global WFE correction

With the performance of correction of each mode, the overall system performance can be deduced. A Wave-Front Error ϕ_{in} will be composed of a random combination of the 9 specified modes $\phi_{mode,i}$.

$$\phi_{in} = \sum_{i=1}^{9} \lambda_i \phi_{mode,i}, \tag{2.15}$$

with λ a random coefficient between -1 and 1 (the amplitude of ϕ_{mode} is the specified mode maximum amplitude).
As the study comes within the context of linear mechanics, the performance of correction of each separate mode are simply added to determine the performance of a mode combination.

Worst case

In the worst case, the system will have to correct the 9 modes at their maximum specified amplitude, in the same orientation and at the same time. The study of this case gives the limit performance of the system.
The computed commands of each mode are added: the worst case correction requires a maximum displacement of 3 μm for the internal actuators and of 6.9 μm for the external ones. And it induces

maximum resulting forces of 34 N for the internal actuators and 18 N for the external actuators. The residues computed for each mode are also added and the residual amplitude is the quadratic sum of each residual amplitude: the residual wave-front after the correction of the worst case will be 10.7 nm rms. This value gives the worst precision of correction that we expect with the system, it is slightly above the 10 nm rms specified for the correction of a global wave-front but as this case has a small probability to appear, it is acceptable. We have seen that the maximum level of stress is not located in the same place for each mode (on the arm, the actuator location or the center). So, in the worst case the maximum constraints will be lower than the sum of the values given for each mode, which is 5.10 MPa. The knowledge of the level of stress is important to ensure the mechanical strength of the system. The elasticity limit of Zerodur is considered to be around 12 MPa, according to the statistical studies of breakage performed by SCHOTT [Hartmann et al., 2009], so we have a safety factor higher than two. There is no risk to pass over this limit for the system functioning in the specified range of correction.

Representative WFE

With the worst case study we have seen that the system mechanical behavior is not critical. The global precision of correction is now determined by performing a statistical study on the correction of 1000 random WFE, as defined in Equation 2.15. The coefficient λ_i gives the modes' amplitude, they are drawn using a uniform law. If ϕ_{res_mode} is the residual WFE obtained after the correction of the mode ϕ_{mode} and σ_{res_mode} its RMS value, the global residues will be:

$$\phi_{res} = \sum_{i=1}^{9} \lambda_i \phi_{res\_mode,i}, \tag{2.16}$$

and its amplitude:

$$\sigma_{res} = \sqrt{\sum_{i=1}^{9} \lambda_i^2 \sigma_{res\_mode,i}^2} \tag{2.17}$$

The results of 1000 random corrections are presented in Figure 2.14, the expected mean precision is then 5.9 nm rms, with a standard deviation of 1.5 nm rms.

2.3.4 Conclusion on the Finite Element Analysis

The performed FEA has allowed a complete conception, optimization and characterization of the MADRAS mirror. The mirror mechanical behavior has been validated: the achievable deformations allow to correct the specified WFEs and the level of stress is well below the material breakage. The precision of correction is promising: 7 modes are corrected within the 5 nm rms specification. The spherical3 and pentafoil9 aberrations are slightly less well corrected due to the central clamping and a symmetry mismatch. Nevertheless, this correction is sufficient: for a representative WFE, the expected mean correction is 6 nm rms, which is well underneath the 10 nm rms specified. The FEA also gives the needs in term of actuator stroke and we will see in the next section that the finite element model can be used to define the geometrical tolerances and the integration procedure.

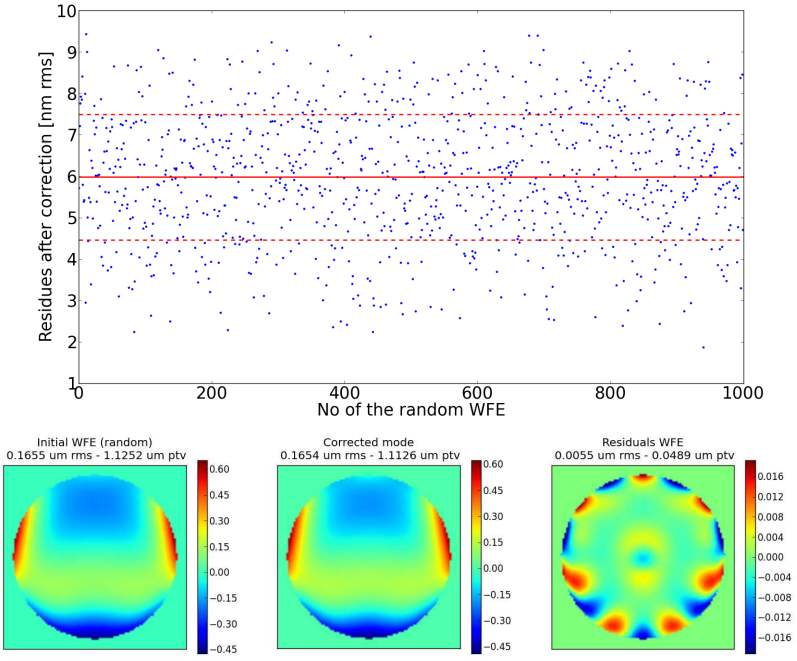

Figure 2.14 : *Performance of correction for random WFEs: amplitudes of residues computed for 1000 random phase maps and example of correction.*

Table 2.2 : *Correcting mirror performance (from FEA).*

MODE	WFE amplitudes [nm rms]		Actuator strokes [μm]		Forces [N]		Stress [MPa]
	Injected	Residues	d_a	d_c	F_a	F_c	Max
Coma3	200	0.7	0.59	2.48	5.84	4.31	1.02
Astigmatism3	150	2.5	0.27	0.29	1.02	0.30	0.14
Spherical3	50	5.8	0.50	0.74	0.15	0.42	0.25
Trefoil5	30	0.2	0.11	0.10	0.88	0.01	0.10
Astigmatism5	30	1.8	0.09	0.48	2.57	1.53	0.36
Tetrafoil7	30	1.4	0.25	0.19	2.90	0.26	0.27
Trefoil7	30	1.6	0.24	0.80	5.13	3.20	0.77
Pentafoil9	30	6.8	0.52	0.42	6.73	1.30	0.61
Tetrafoil9	30	4.5	0.45	1.40	8.75	6.54	1.58
Worst case	265.3	10.7	3.02	6.90	33.97	17.87	<5.10

2.4 Hardware specification and integration

2.4.1 Actuators

In this section, we will see how to integrate the actuators PPA40M in our system in order to fulfill the stroke requirements. Then, based on the system influence functions, we will characterize the actuators regarding the system performance: the impact of their precision of displacement and of a dead actuator is studied.

Required displacement

Table 2.2 summarizes the performance and the actuators' requirement for each mode and for the worst case. It gives the required actuator stroke: the internal actuators must be able to apply a ±3 μm displacement, and the external actuators must be able to apply a ±7 μm displacement. The chosen actuators provide a 40 μm stroke but it is not symmetric: the achievable range of displacement is -5 μm/+35 μm. This range is sufficient for the internal actuator but more negative stroke is required for the external actuators. This can be achieved by adding an offset to the reference position of the external actuators of 5 μm in comparison to the internal ones. The stroke requirement for the external actuator is then -2 μm/+12 μm, which is in the available range.
So, when the actuators are at rest, the system is under stress: the mirror is convex, with a maximum level of stress in the Zerodur of 3.4 MPa.

Precision of displacement

The actuators' stroke is 40 μm. If it is coded on 12 bits (1 bit for the sign and 11 bits for the value), the precision on the displacement is $\pm 20/2^{11} = \pm 10$ nm. The impact of a displacement error in this range is studied in order to determine whether or not this precision is acceptable for the system performance.

A displacement error on one actuator will induce a residual WFE given by the influence function amplitude: an internal actuator applying a 10 nm displacement induces a WFE of 1.7 nm rms, and of 0.3 nm rms for the external actuators. So, in the worst case, if all the actuators apply a 10 nm error displacement, it will add a WFE of $\sqrt{12 \times 1.7^2 + 12 \times 0.3^2} = 5.98$ nm rms.
More probably, the error on the displacement will be a random value between ±10 nm, different for each actuator. The additional WFE will then be:

$$\sigma_{act} = \sqrt{\sum_{i=1}^{12} \frac{1.7 {p_i}^2}{10} + \sum_{j=1}^{12} \frac{0.3 {p_j}^2}{10}}, \tag{2.18}$$

with p_i and p_j the random errors on the displacement for the internal and external actuators. We study the mean impact by performing a statistical analysis on 1000 random sets of displacement errors. Thus, a precision of ± 10 nm on the actuator command will induce a mean error of 3.3 nm rms, with a standard deviation of 0.4 nm rms. This error will be added to the residual WFE of correction computed in the previous section. So, taking into account the actuator precision of ±10 nm, the expected mean precision of correction will be slightly damaged: it goes from 5.9 nm rms (perfect commands) to 6.8 nm rms. This value remains nevertheless acceptable and in the 10 nm rms specification.

The impact of the actuators' precision can also be directly studied on a mode correction. Let ϕ_{in} be the initial WFE and α_0 the command deduced from the WFE projection on the influence functions base B (with $B^+ = (B^t B)^{-1} B^t$ the pseudo-inverse):

$$\alpha_0 = B^+ \phi_{in}. \tag{2.19}$$

The residual wave-front after correction ϕ_{res} is calculated by comparing the initial WFE and the reconstructed phase ϕ_{cor}. The actuator precision is taken into account in the reconstruction by adding a random set of 24 coefficients p (in the ±10 nm range) to the optimal commands α_0:

$$\phi_{cor} = B(\alpha_0 + p) \Rightarrow \phi_{res} = \phi_{in} - \phi_{cor} \tag{2.20}$$

As before, a statistical study is performed to have a representative idea of the impact. The study of the modes correction with this method allows to recover the additional 3.3 nm rms of additional error implied by the actuator misplacement. Thus, the bigger impact appears on the modes which were highly well corrected (see Figure 2.15), but they stay in the 5 nm rms specification. So, a 10 nm precision on the actuator displacement is acceptable for the required performance.

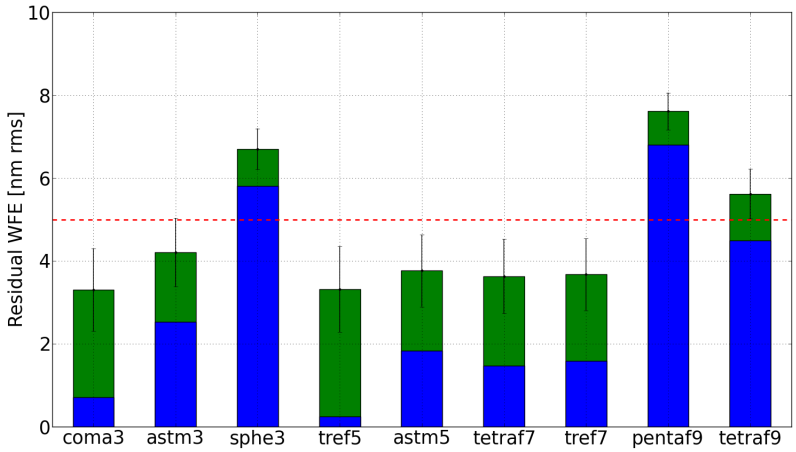

Figure 2.15 : *Impact of a 10 nm precision of the actuator displacement on the specified mode correction: blue: ideal performance - green: mean performance with a 10 nm actuator precision (FEA results).*

Dead actuator

The impact of a dead actuator can also be characterized. When an actuator is dead, the piezoelectric actuation is no longer provided. It is modeled by a clamped point at the spring bottom extremity. Thanks to the actuator stiffness, the actuation point, on the spring top extremity will follow the deformation.
The occurrence of dead actuator can be modeled in two different ways, depending if there is a system recalibration or not. Without recalibration, the mode to be corrected is still projected on the 24 IF but the command of the dead actuator is forced to 0 for the wave-front reconstruction. With a recalibration, the mode projection is done on the 23 remaining IF so the dead actuator will be compensated by its neighbors. Not only this case is advantageous, but, as we will see in Figure 2.17, it is also essential to keep a reasonable performance.

The impact of a dead actuator depends on the actuator location and on the mode to be corrected. The performance of correction is calculated for each mode and for each actuator. Figure 2.16 presents the residuals after each specified mode correction as a function of the dead actuator, computed taking into account a recalibration. As we can see, the performance degradation follows the modulation of the considered mode: some actuators are not solicited for some mode so their failure will not be seen.
On the top of Figure 2.17 the mean resulting residuals and the worst and best cases for a system with a dead actuator are presented. The obtained performance (with and without a recalibration) are compared to the performance of a fully functional system. It is clear that a recalibration is mandatory: the impact of a dead actuator without a recalibration is dramatic, all the modes are corrected above the 5 nm rms specification. It is then not conceivable to keep using the 24 influ-

ence functions base if one actuator is missing.

Considering a recalibration, the corrections of Coma3 and Trefoil5&7 are the most impacted by the occurrence of a dead actuator but these modes are initially the best corrected, so it is not too critical in term of amplitude of residual WFE. For a chosen azimuthal order m, modes with the greatest radial order n, are less influenced by the loss of one actuator. We also can note that the correction of Pentafoil9 is not much damaged by the loss of one actuator, this is due to the fact that the symmetry of the mode does not correspond to the symmetry of the system, so this symmetry is not broken with the loss of an actuator. To finish it is interesting to note that the corrections of the modes defined with $n = m$ are more damaged by the loss of an internal actuator, while the modes defined by $n = m + 2$ are more dependent on external actuators. This fact will allow balancing the impact of a dead actuator with respect to a global WFE correction.
In conclusion, the loss of one actuator degrades the performance in a reasonable way: the correction stays within the specifications.

Then the evolution of the mean correction performance with the number of dead actuators is studied: for a given number of dead actuators, 50 random sets of dead actuators are drawn and the correction of 100 random WFEs is performed for each set of deteriorated IF bases (Figure 2.17, bottom). Logically, the residues increase with the number of dead actuators, but we can see that with 2 dead actuators the system is still well functioning: the mean precision is 10.7 nm rms, with a standard deviation of 2.1 nm rms. Such a result comes from the intrinsic redundancy of the system: 24 actuators are used for the generation of only 17 modes (the spherical aberration and the 8 other specified Zernike oriented in both x and y directions). This performance is a major advantage for space use, ensuring the robustness and reliability of the MADRAS concept.

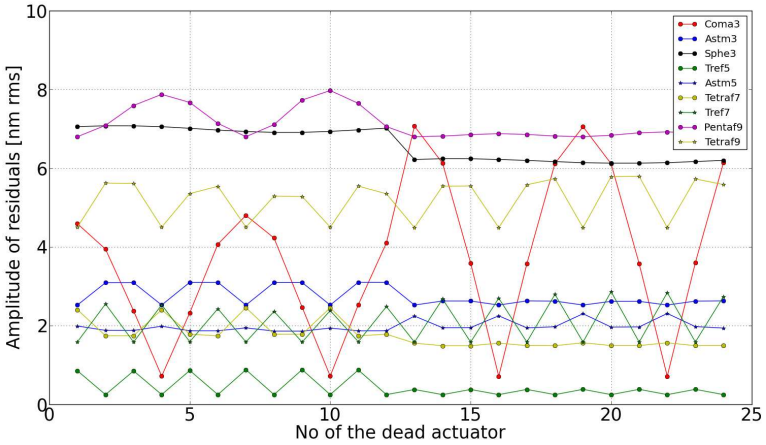

	Max	Mean
Coma3	9.8	5.3
Astm3	1.2	1.1
Sphe3	1.2	1.1
Tref5	3.5	1.7
Astm5	1.2	1.1
Tetraf7	1.7	1.2
Tref7	1.8	1.3
Pentaf9	1.2	1.1
Tetraf9	1.3	1.2

Figure 2.16 : *System performance with one dead actuator (FEA results, considering a recalibration): Left: residual amplitude for the correction of each specified mode depending on the dead actuator (No 1 to 12: internal actuators - No 13 to 24: external actuators) - Right: maximum and mean factors by which the residues are increased.*

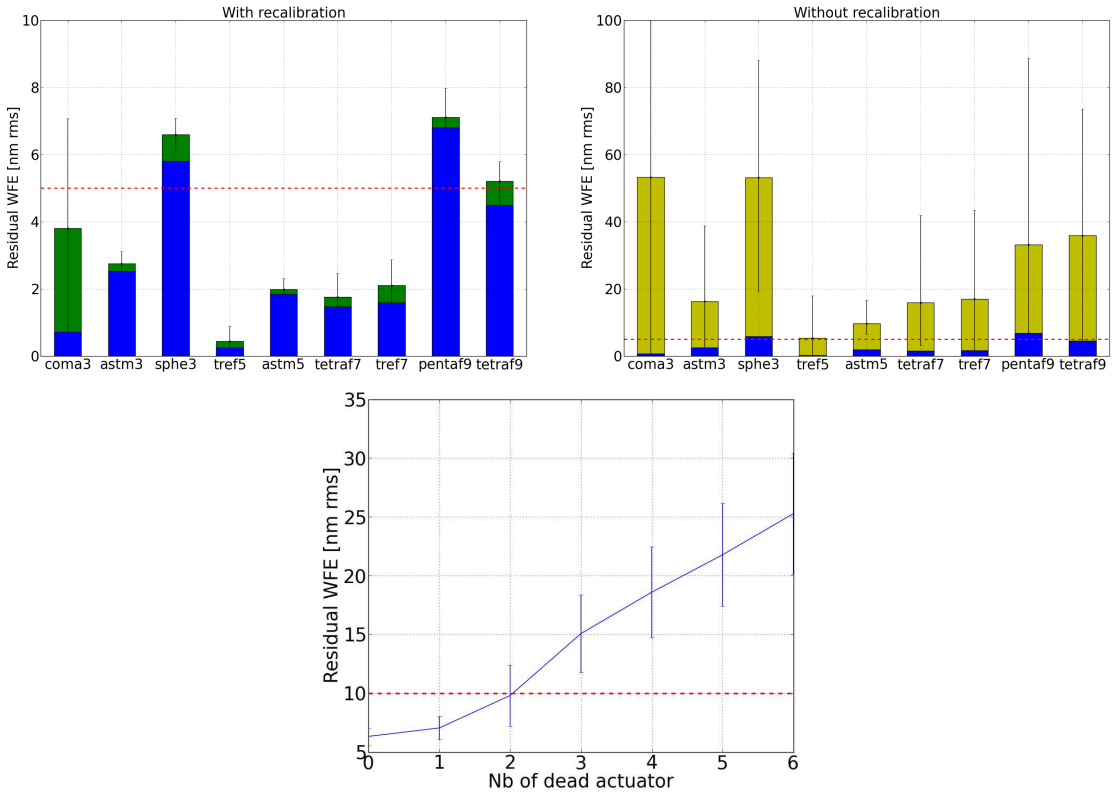

Figure 2.17 : *Top: Comparison of the mean precision of correction of a system fully functional and a system with one dead actuator (with or without recalibration) - Bottom: Evolution of the mean residual wave-front with the number of dead actuators, with a recalibration (statistics on 5000 random WFEs and sets of dead actuators).*

2.4.2 Estimating geometric sensitivities with FEA

Mirror thickness uniformity

The thickness variation is modeled with a wedge between the back face and the optical surface (see Figure 2.18). The altitude difference between the lower and the upper points of the optical surface is denoted by h, and is linked to the wedge angle θ.

Finite element models are computed for different values of θ and, as explained before, the residual error of each specified mode is deduced from the recovered IF. The wedge influence is different for each mode. Generations of Coma3 and Spherical3 are the most affected by a parallelism defect between the two mirror's faces, but the impact stays negligible: a 0.5° wedge angle, corresponding to a thickness uniformity of 0.9 mm, will induce an additional WFE of less than 0.3 nm rms.
Thanks to the approach based on the decomposition on the IF base, the system is not very sensitive to a lack of parallelism between the faces of the mirror: the commands are automatically adapted to compensate for small deviations due to manufacturing errors.
So, the tolerance on the mirror thickness distribution is chosen in order to limit the required actuators' displacement and the stress in the material, while ensuring a feasible machining of the blank. For that we study the worst case scenario, that is to say the correction of the 9 specified modes at the same time. A wedge angle of 0.1°, corresponding to an out of parallelism of the two mirror's faces of ± 0.1 mm, will increase the required actuator stroke and the stress in the material by 3%,

which is acceptable.
This specified value of thickness uniformity, easily achievable during the mirror polishing will not damage the computed ideal performance.

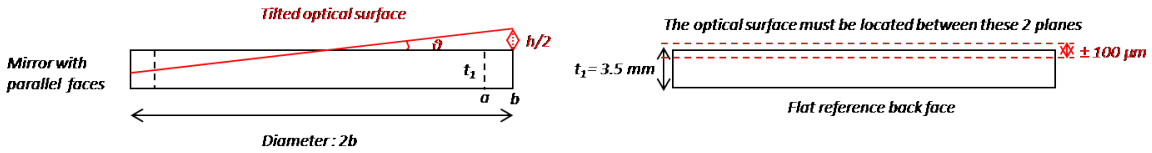

Figure 2.18 : *Principle of modeling of a thickness uniformity with a prism of angle θ and final thickness uniformity specification.*

Actuator orientation

In the same manner, the impact of actuator tilt, with respect to the z axis, can be studied. On the finite element model, the tilt θ is simulated by translating the inferior actuator extremity of a distance d. The resulting force will have a component along the optical axis and a transverse component. Once again, it will not impact the performance of correction but it will increase the necessary stroke by a factor $\sqrt{tan^2(\theta) + 1}$ (see Figure 2.19).
The tolerance on actuator orientation is then computed by considering the margin of the actuator stroke: the orientation must be precise at $\pm 0.1°$.

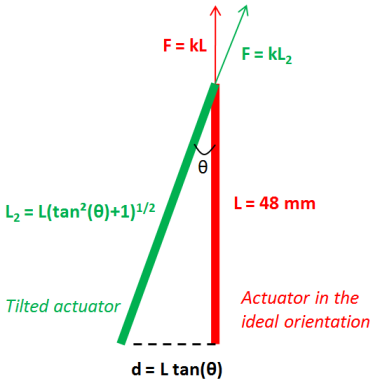

Figure 2.19 : *Tilted actuator configuration showing the consequence on the force value.*

2.4.3 Complete mirror system

The mirror geometry has been defined and validated with Finite Element Analysis. The mirror is integrated on a dedicated structure, designed for a space use (except for the electronics). The overall system is numerically studied and validated before its manufacturing and integration.

Main components

The correcting system is composed of three main parts: the mirror, the supporting structure and the actuators.

As seen before, the mirror is a piece of Zerodur, with a central meniscus, an outer ring, 12 arms and a central cylinder which will be fixed. The mirror is polished on the 100 mm diameter aperture and presents a good optical quality: the shape error is 3 nm rms.

The supporting structure is composed of a cone and a reference plate, both in Invar. The reference plate is rigidified with thin ribs so that the deformation of the plate will be negligible. The cone is fixed on the reference plate with 12 screws and the mirror will be glued in the superior part of the cone, on the bottom perimeter of the central clamping. The reference plate has 24 holes for the actuators integration.

The 24 piezoelectric actuators are tied to the mirror and to the reference plate via elastic universal joints (U joint). The joints are screwed on both extremities of the actuator, absorbing the flexion and twisting movements. On the mirror side, the joints are glued into holes located on the inferior face, under the arms and the ring. On the reference plate side, the joints are glued inside intermediate pieces, screwed on the plate.

Finally, the system will be clamped with three bipods. This fixation device, screwed on 3 points at 120° of the reference plate, has been designed in order to provide an isostatic condition.
The overall system can be seen in Figure 2.21, it weighs 4 kg and is 80 mm height, for a diameter of 150 mm.

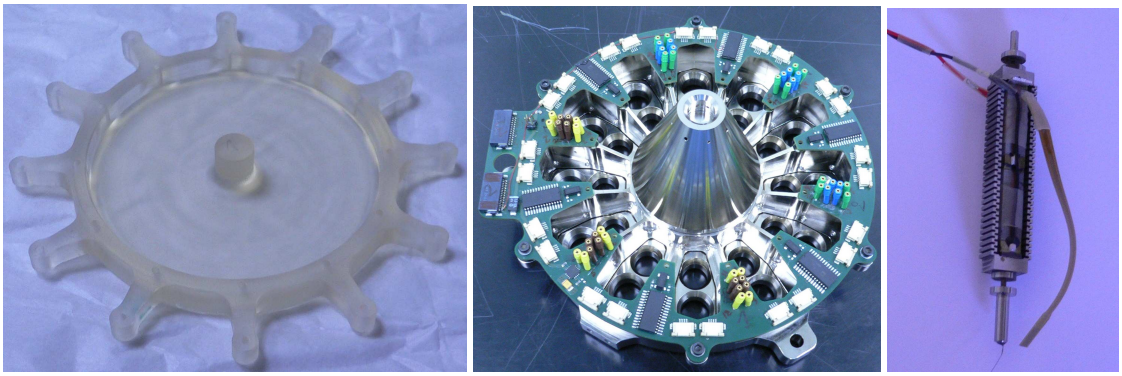

Figure 2.20 : *Left: MADRAS mirror - Center: MADRAS reference plate and cone (electronic card integrated on the reference plate) - Right: one of the 24 MADRAS actuators, with its 2 U joints.*

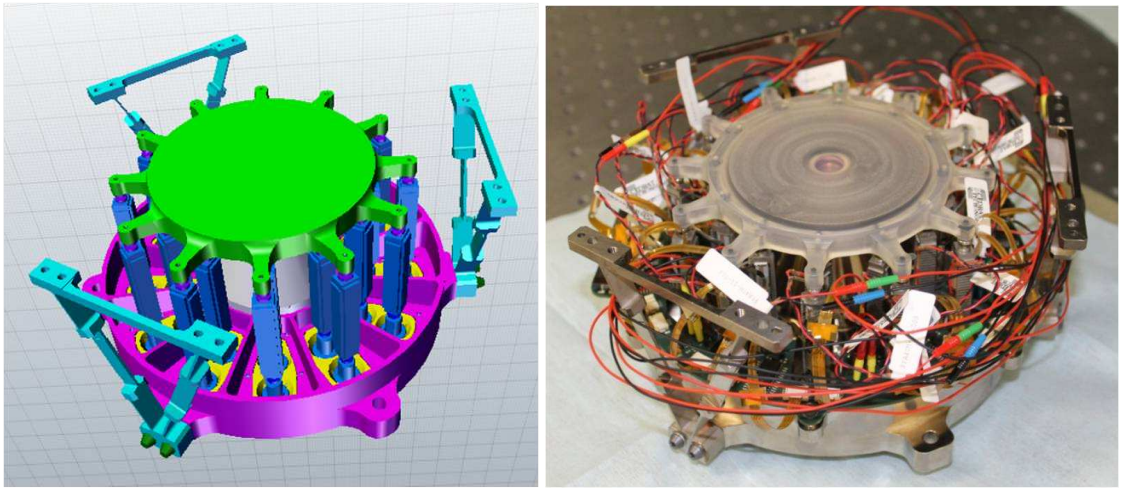

Figure 2.21 : *Left: Model of complete mirror system (credit TAS) - Right: Integrated system.*

Numerical validation

The entire system is modeled with FEA, in order to verify that the structure does not change the correcting performance or the mirror mechanical behavior. A dynamic analysis is also performed to simulate the launch vibration.

The main differences between the model of the complete mirror system and the model of the mirror alone come from the boundary conditions:

- the reference plate, on which the actuators are clamped, is not infinitely rigid but rigidified with ribs and fixed on 3 points;
- the central pad is not completely clamped but glued on its periphery.

The Influence Functions are recovered from the complete system model and the study of each specified mode is performed, as in Section 2.3.2. Figure 2.22 presents the precision of correction and the required stroke for the 9 Zernike polynomials. In the worst case, the residual WFE after correction is 11.2 nm rms (to be compared to the 10.7 nm rms computed for the mirror alone). And the maximum required strokes are 4 μm for the internal actuators, and 8.5 μm for the external actuators. These values are within the available actuators' stroke. In conclusion, the performance of the complete system differs in a negligible way from the performance of the mirror alone. The characterization performed previously is still accurate and the complete mirror system design is validated.

Quasi-static and dynamic analyses are performed in order to simulate the system mechanical behavior during the launch.
The mechanical strength of the system is estimated under quasi-static loads of 30g, applied along the three axis. The main stressed part is located around the mirror central clamping (see Figure 2.23). The maximum stress is equal to 0.9 MPa for the load case in the x and y directions and to 1.1 MPa for the load case in the z direction. During launch, this kind of load is applied to the system in the 3 directions, at the same time, so the stress induced by the 3 studied load cases will be added. In addition, we have seen in Section 2.4.1 that the mirror is constrained at rest: the offset of the external actuators induces a stress of 3.4 MPa, also located around the central clamping. So, in total, the maximum stress in the mirror during the launch will be 6.3 MPa, giving a security

factor of 2 regarding the elastic limit of Zerodur.
A modal analysis has also been performed, giving the first mode at 233 Hz, which is a classical value for the design of space structure, considering the resonance frequency of the launchers [CNES, 1998]. This validates the rigidity of the structure and the flexibility of the 3 fixation devices.
So, the the quasi-static and dynamic analysis have confirmed the system design, according to the launch environment.

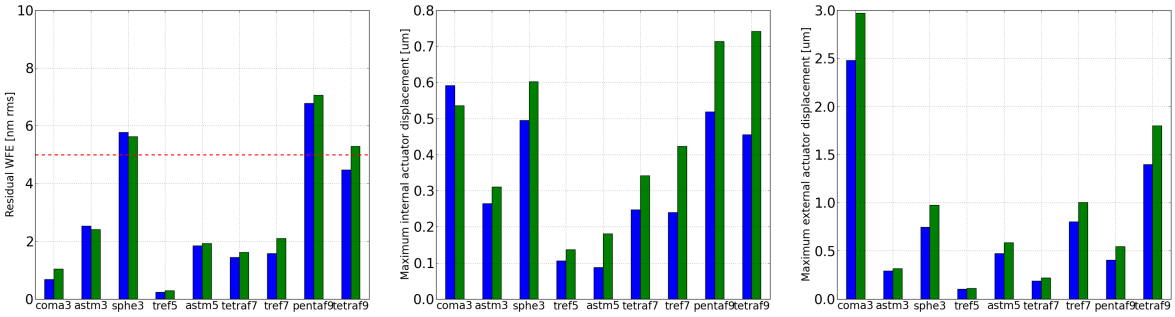

Figure 2.22 : *Verification of the complete mirror system performance.*

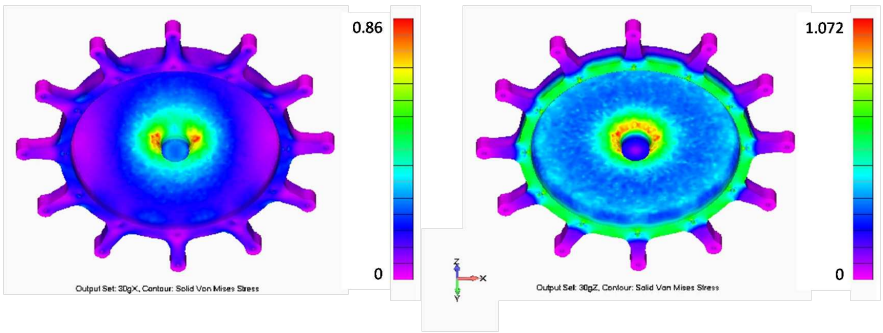

Figure 2.23 : *Stress in the mirror due to a load of 30g in the x (or y) direction (left) and in the z direction (right) (Unit = [MPa]) (Credit SESO).*

2.4.4 System integration

The integration is performed with the mirror facing down and supported by a prismatic transparent plate. The optical surface is monitored with a Fizeau interferometer, in order to verify that the process does not stress the mirror.
The main steps of the integration are:

- gluing of the mirror to the cone of the supporting structure,
- gluing of the actuators,
- integration of the 3 bipods,
- electronic connection.

For the gluing of the central clamping, the cone is brought on the mirror and the parallelism between reference plate and mirror back face is ensured by three calibrated cylinders located on three internal actuators positions at 120° (see Figure 2.24, left).

The actuators are firstly glued to the mirror and then to the reference plate. During this step, the actuators must not weigh on the mirror, so a system of counter-weight has been conceived. An intermediate piece on the reference plate allows a fine guiding of the actuators, ensuring their orientation. The glue shrinkage has induced an important deformation of the optical surface: 258 nm rms mainly composed of focus, spherical and astigmatism (see Figure 2.24, right).
With the FEA model, we can deduce the corresponding actuator displacement: roughly 2 μm. In operation, it will be possible to go back to a flat mirror by compensating for this effect, pushing on the actuators.

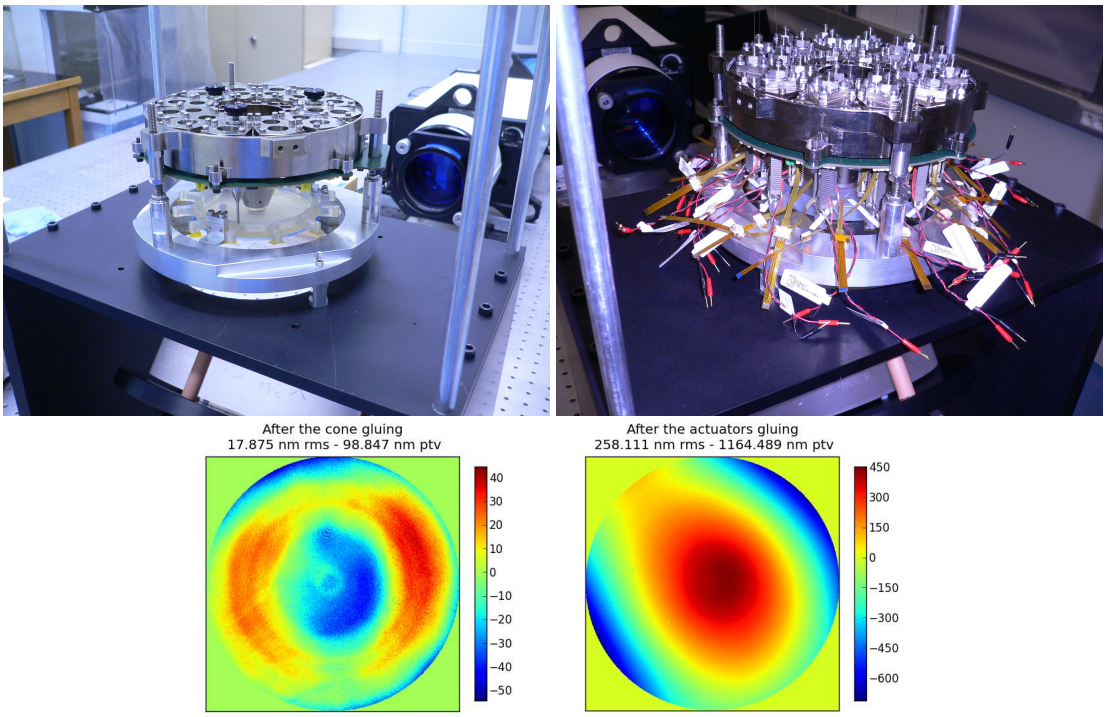

Figure 2.24 : *Pictures of 2 integration steps and corresponding interferograms of the optical surface, measured with the Fizeau interferometer. Left: reference plate and cone integration on the mirror - Right: System with the actuators integrated.*

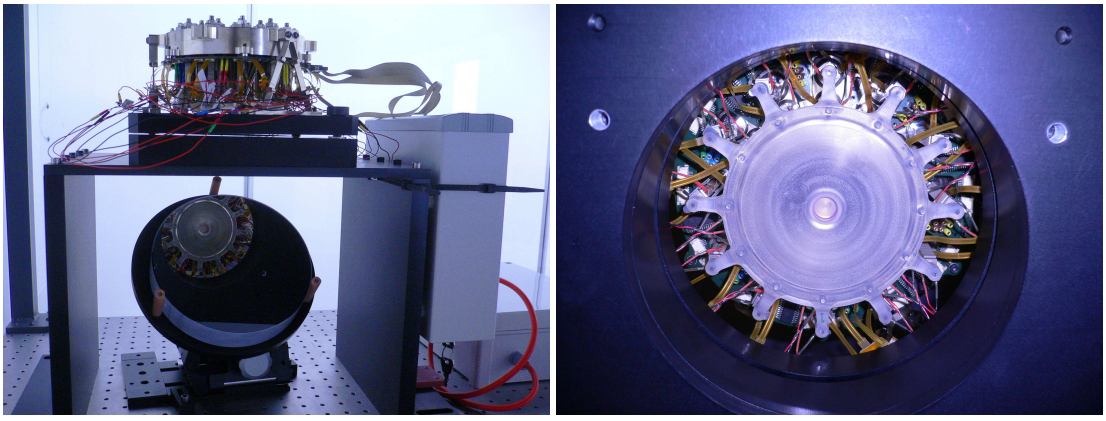

Figure 2.25 : *Integrated system on its test platform and optical surface viewed from below.*

2.5 Complete mirror system validation with interferometry

2.5.1 Test set-up

Once the system is integrated, a first round of tests is conducted with a Fizeau interferometer, directly measuring the optical surface deformation. The mirror is still facing down and mounted on a tip/tilt plate. The goal of the measurement is to validate the mechanical design and the integration by correlating simulations and measurements. The interferometer has an optical aperture of 100 mm diameter and a flat reference is used. In order to minimize the measurement noise, an averaging of 9 measurements is systematically performed. The deformation maps are given on a grid of 550x550 pixels and the measurement precision is 1 nm.

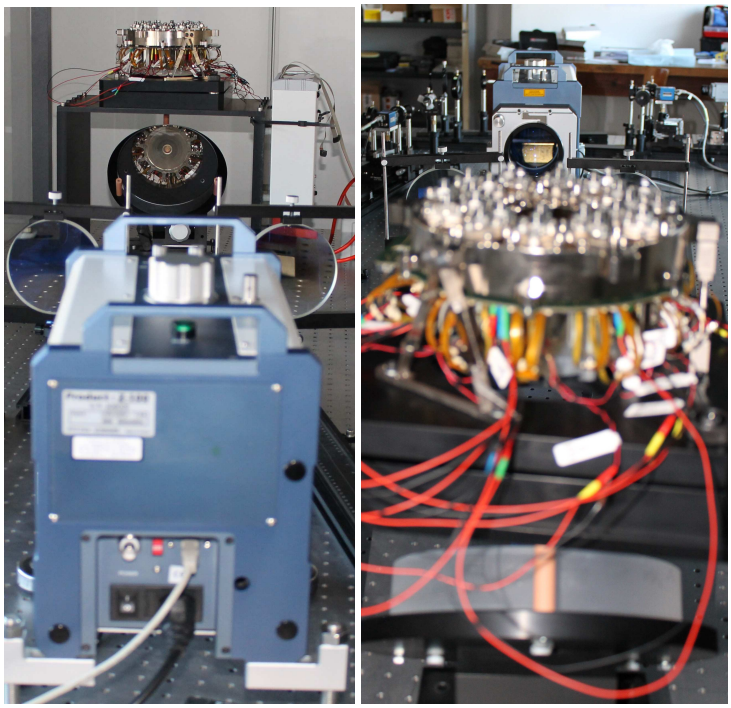

Figure 2.26 : *MADRAS interferometrical testing.*

2.5.2 Influence Function

The 24 system's Influence Functions are measured by applying a push/pull command to each actuator while the others are at rest. The Influence Function is the half difference of the deformation maps resulting from the push and the pull commands.
The measured IF are presented on Figure 2.27. Their shape can be compared to the ones expected from FEA by normalizing the deformation maps (to a unitary rms amplitude). As we can see on Figure 2.28, measured and simulated IFs are really similar, the main difference is located near the actuation point.

The system eigen modes are determined by performing a Singular Value Decomposition of the IF base. As the measured IFs are similar to the simulated ones, the expected shapes are well recovered (Figure 2.29). Nevertheless, the conditioning factor (ratio between the extreme eigen

values) is 1.3 times bigger than in the simulation. This is due to the fact that the last eigen modes contain some noise, due to their low amplitudes.

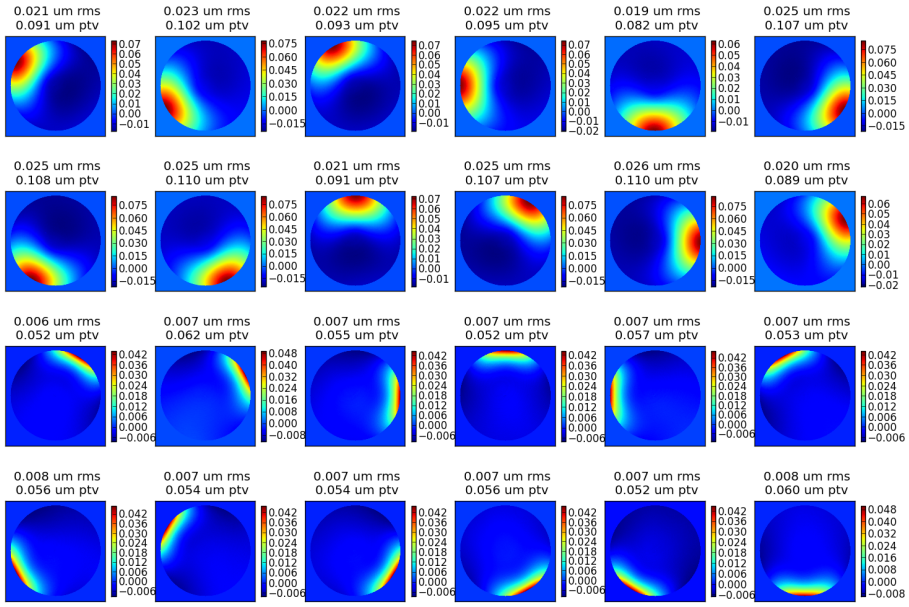

Figure 2.27 : *Mirror Influence Functions, measured with a Fizeau interferometer, for a command of 1V (Unit:µm).*

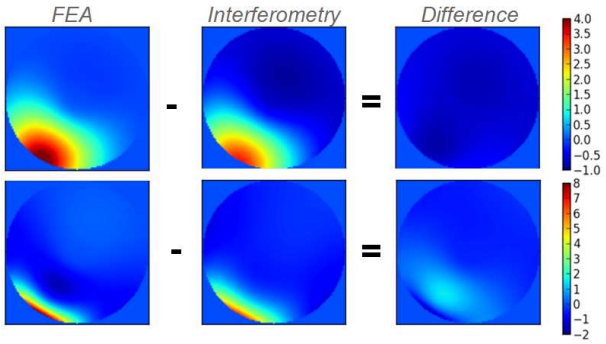

Figure 2.28 : *Comparison of the normalized simulated and measured influence functions (Top: internal actuator - Bottom: external actuator).*

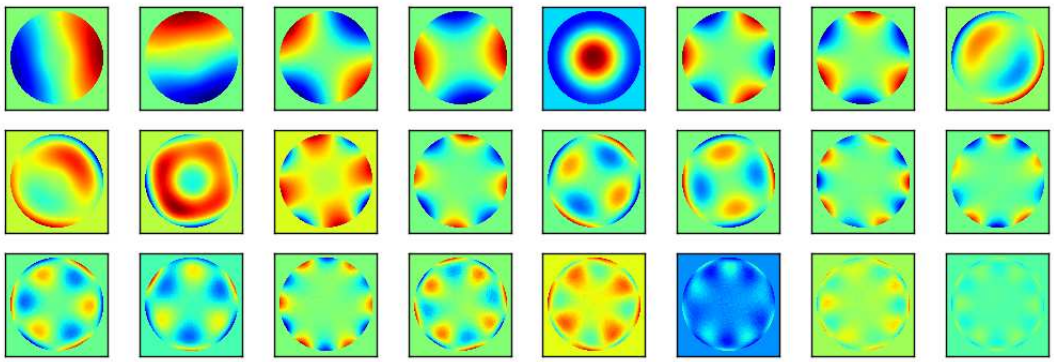

Figure 2.29 : *System eigen modes, from the less to the more energetic, from the measured IF.*

2.5.3 Performance of the complete mirror system

From the Influence Functions, the opto-mechanical performance of the mirror can be deduced. Each specified mode, at its maximum amplitude, is projected on the measured IF base to determine the mirror correction capacity.
As the IF are similar to the FEA results, the expected precision of correction are well recovered (Figure 2.30). In the worst case, the total residual error is 11.1 nm rms, and the mean precision computed on 2000 random WFE is 6.3 nm rms, with a standard deviation of 1.5 nm rms.

The last thing to verify is that all the expected wave-front errors can be corrected with the available commands (-20V/+20V for the internal actuators and -20V/+60V for the external ones). The necessary commands computed for each mode are then added, giving the required commands for the worst case: -5/+20 V for the internal actuators and -20/+25 V for the external ones. So, the worst case can be corrected by the system.

In conclusion, the results expected from the Finite Element Analysis are confirmed. The interferometric measurements of the equipped mirror Influence Functions have allowed the complete validation of the opto-mechanical performance of our system.

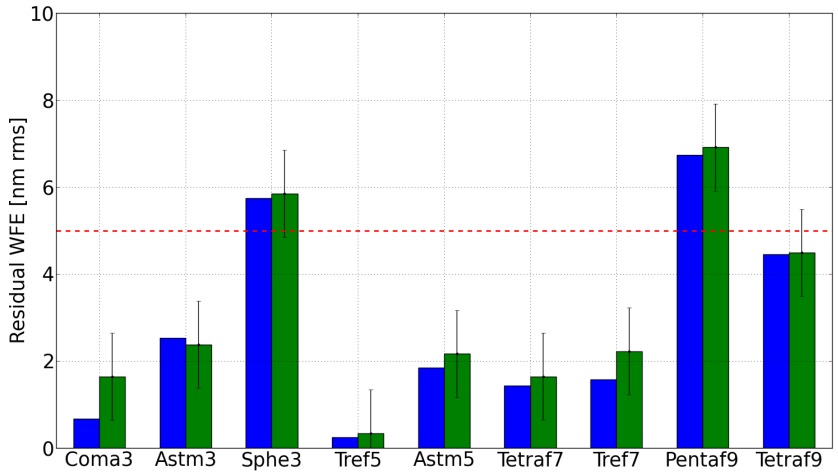

Figure 2.30 : *Residual WFE computed for each specified modes, with simulated and measured IF (errorbars correspond to the interferometer precision: ± 1 nm).*

2.6 Conclusion

The MADRAS mirror has been conceived in order to demonstrate the possibility to compensate the deformations expected in a large space telescope, with large lightweight primary mirror sensitive to the environment variations. Such a system would be inserted in the telescope exit pupil plane, to feed the instrument with a corrected wave-front.

The correcting mirror has 24 actuators, it is 130 mm diameter, 80 mm height and weights 4 kg. During the design phase, the specific space constraints have been considered, notably with the material choice and the mechanical strength during launch.

Extensive Finite Element Analysis have allowed a complete opto-mechanical system characterization: the correction ability of the system, deduced from simulation is really high. The 9 main Zernike modes expected to appear in a space telescope are corrected with a precision better than 5 nm rms and a global WFE is corrected with a 6 nm rms precision.
From the FEA results, the specifications on the system hardware have been defined and the equipped system designed and integrated.

The functioning of the complete mirror system has been validated with interferometric tests. The measured influence functions are similar to the simulated one, so the performance are well recovered. The opto-mechanical concept of the MADRAS system is validated.

We will see in the next chapter the demonstration of its performance in closed loop, in a representative configuration.

Bibliography

Cedrat Technologies. Technical data sheet PPA40M. Technical report, Cedrat Technologies.

CNES. *Cours de Technologie Spatiale - Technique et technologies des vehicules spatiaux*. 1998.

L. E. Cohan and D. W. Miller. Integrated modeling for design of lightweight, active mirrors. *Optical Engineering*, 50(6):063003–+, June 2011.

T. Döhring, R. Jedamzik, A. Thomas, and P. Hartmann. Forty years of ZERODUR mirror substrates for astronomy: review and outlook. volume 7018 of *Society of Photo-Optical Instrumentation Engineers (SPIE) Conference Series*, July 2008.

ESA. Technology Readiness Levels Handbook for Space Applications. Technical report, European Space Agency, 2008.

L. Feinberg, L. Cohen, B. Dean, W. Hayden, J. Howard, and R. Keski-Kuha. Space telescope design considerations. *Optical Engineering*, 51:011006, January 2012.

G. H. Golub and C. F. van Loan. *Matrix computations*. Johns Hopkins University Press, 1996.

P. Hartmann, K. Nattermann, T. Döhring, R. Jedamzik, and M. Kuhr et al. ZERODUR glass ceramics for high stress applications. volume 7425 of *Society of Photo-Optical Instrumentation Engineers (SPIE) Conference Series*, August 2009.

S. Kendrew. *Lightweight Deformable Mirrors for Ground- and Space-Based Imaging Systems*. PhD thesis, University College London, 2006.

M. Laslandes, C. Hourtoule, E. Hugot, M. Ferrari, and C. Lopez et al. Space active optics: performance of a deformable mirror for in-situ wave-front correction in space telescopes. volume 8442 of *Society of Photo-Optical Instrumentation Engineers (SPIE) Conference Series*, September 2012.

G. R. Lemaître. Active Optics: Vase or Meniscus Multimode Mirrors and Degenerated Monomode Configurations. *Meccanica*, 40:233–249, 2005.

P. A. Lightsey, C. Atkinson, M. Clampin, and L. D. Feinberg. James Webb Space Telescope: large deployable cryogenic telescope in space. *Optical Engineering*, 51:011003, January 2012.

B. K. McComas. *Configurable adaptive optics for the correction of space-based optical systems*. PhD thesis, University of Colorado at Boulder, 2002.

R. J. Noll. Zernike polynomials and atmospheric turbulence. *Journal of the Optical Society of America*, 66:207–211, March 1976.

K. Patterson, N. Yamamoto, and S. Pellegrino. Thin deformable mirrors for a reconfigurable space telescope. 53rd AIAA Structures, Structural Dynamics, and Materials Conference, 2012.

M. Postman, T. Brown, K. Sembach, M. Giavalisco, and W. Traub et al. Advanced Technology Large-Aperture Space Telescope: science drivers and technology developments. *Optical Engineering*, 51:011007, January 2012a.

M. Postman, B. Sparks, L. Fengchuan, K. Ess, and J. Green et al. Using the ISS as a testbed to prepare for the next generation of space-based telescopes. volume 8442 of *Society of Photo-Optical Instrumentation Engineers (SPIE) Conference Series*, July 2012b.

D. Redding, S. Basinger, A. Lowman, A. Kissil, and P. Bely et al. Wavefront sensing and control for a Next-Generation Space Telescope. volume 3356 of *Society of Photo-Optical Instrumentation Engineers (SPIE) Conference Series*, pages 758–772, August 1998.

D. Redding, D. Coulter, and J. Wellman. Active Optics for Low-Cost Astronomical Space Telescopes. volume 219 of *American Astronomical Society Meeting Abstracts*, page 136.05, January 2012.

A. Saint Venant. *Résumé des leçons de Navier sur l'application de la mécanique*. Dunod, 1881.

E. Thomas and A. Liotard. MADRAS - Spécifications de besoin de l'Optique Active. Technical report, Thales Alenia Space, 2010.

S. P. Timoshenko and S. Woinowsky-Krieger. *Theory of Plates and Shells*. Engineering Mechanics Series. McGRAW-Hill International Editions, 1959.

Chapter 3

MADRAS mirror performance in closed loop

In the previous chapter, the validation of the concept and opto-mechanical performance of the MADRAS mirror has been presented. The second objective of the project is the demonstration of the mirror functioning in a representative configuration, in closed loop.
This chapter describes this characterization on a dedicated test-bed, including a telescope simulator, representing the deformation of a 3 m primary mirror. The conducted tests allow a complete demonstration of the correcting system performance.

Different steps of tests have been performed and are described in this chapter.
In a first part, the test-bed is presented. In the second and third parts, the calibration of both the optical set-up and the active correcting loop is detailed. The fourth part highlights the results obtained for the specified Zernike modes correction. In the fifth part, the correction of a representative wave-front error is analyzed.

The work presented in this chapter has led to the following publication (see Appendix D):
- M. Laslandes, C. Hourtoule, E. Hugot, M. Ferrari, C. Lopez, C. Devilliers, A. Liotard, F. Chazallet, Space active optics: performance of a deformable mirror for in-situ wave-front correction in space telescope, SPIE 8442, 2012.

3.1 Test bed overview

3.1.1 Objectives

We have seen in the previous chapter the ability of the MADRAS mirror to generate the shapes allowing the compensation of the expected deformation of a large lightweight primary mirror in a 3m-class telescope. The next step is the demonstration of its functioning in a representative configuration, within an active correction loop. The MADRAS mirror is then coupled to a Wave-Front Sensor (WFS) and a Real Time Computer (RTC) and the correction performance of this system is characterized.

A telescope simulator will inject a Wave-Front Error on the correcting mirror and the efficiency of the active loop is studied by comparing the measurements before and after correction.
The goal is to fully characterize the mirror behavior so several types of measurements are performed: wave-front sensing, imaging and interferometry.

3.1.2 Design

The test bed is composed of a telescope simulator and the active correction loop. Shack-Hartmann wave-front sensing and imaging Point Spread Function (PSF) will allow a complete validation of the mirror in term of optical quality. While functioning, the mirror deformation is monitored with the Fizeau interferometer directly looking at the mirror. In addition, force sensors are placed on the actuators, in order to verify the system mechanical behavior.

The test bench, shown in Figure 3.1 is composed of the following elements:

- A source point and a collimating lens, simulating the observation of a distant object.

- A telescope simulator generating the WFE expected in a 3m-class telescope. It is an adaptive optics loop, composed of a 20 mm diameter and 88-actuators magnetic Deformable Mirror (DM88, [Rooms and Charton, 2007]), a 3 mm diameter 28x28 sub-apertures Shack-Hartmann Wave-Front Sensor (WFS1) and a Real Time Computer (RTC1). The actuators are positioned on a 10×10 grid, allowing to generate all the required spatial frequencies and the oversampling of the WFS1 allows to accurately measure the residual wave-front, up to 14 cycles per pupil.

- An active correction loop, composed of the MADRAS mirror, a second 3 mm diameter 28x28 sub-apertures Shack-Hartmann Wave-Front Sensor (WFS2) and a second Real Time Computer (RTC2).

- Four beam expanders, relaying the pupil between the DM88 which is the entrance pupil, the WFS1, the MADRAS mirror and the WFS2.

- Two imaging cameras located in focal planes before and after the correction.

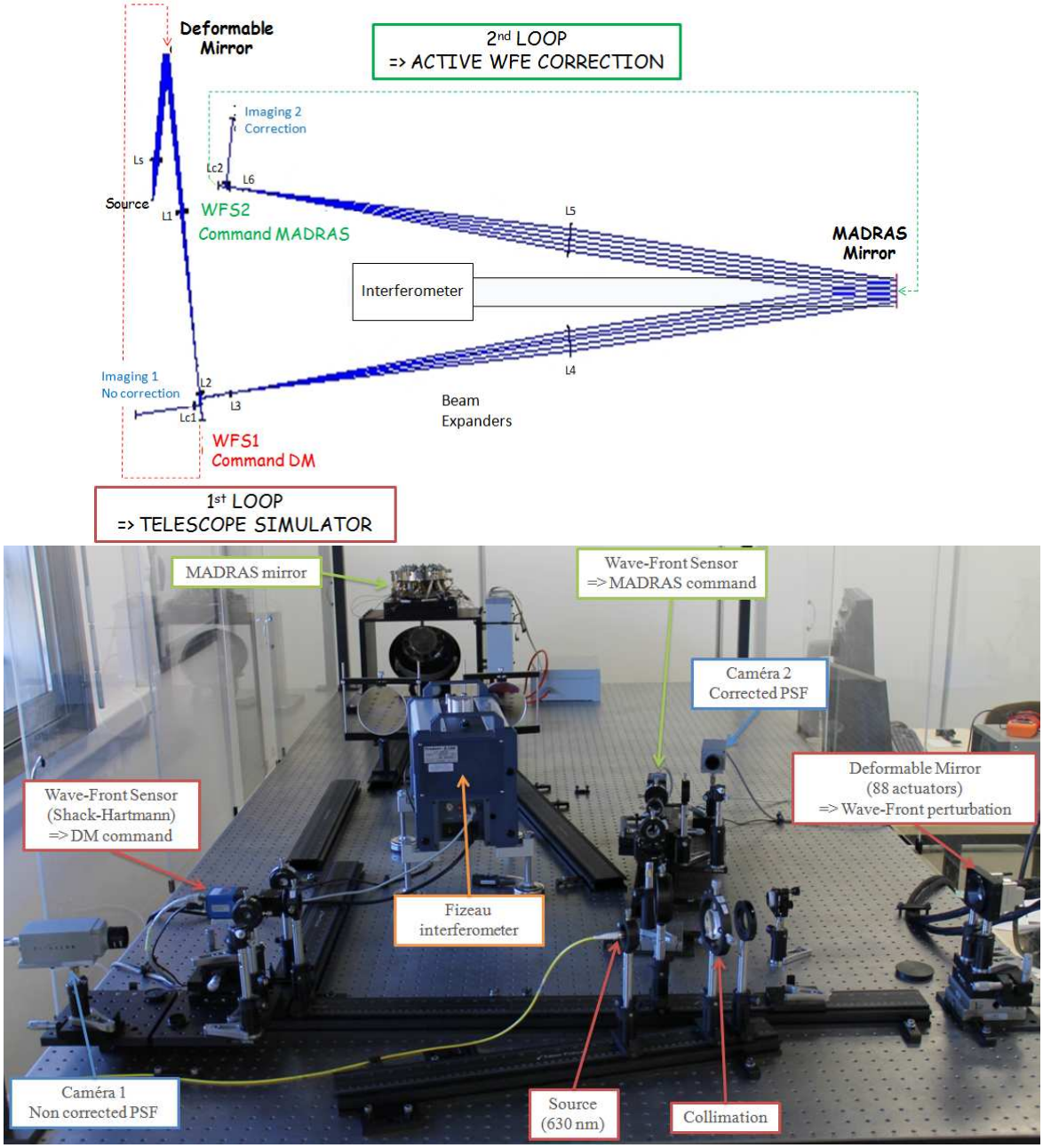

Figure 3.1 : *MADRAS test-bed: optical design and picture.*

3.1.3 Data analysis

The wave-front is measured by Shack-Hartmann wave-front sensors. It is a pupil plane measurement of the local wave-front slopes within sub-apertures defined by a micro-lenses array. Each part of the wave-front is focused by one lens on a camera and the position of the spot in each sub-aperture is proportional to the wave-front slope [Tyson and Frazier, 2004].
This sensor gives the difference between the measured wave-front and a reference. The slope θ is given by the lens focal length f and the spot displacement δ, in comparison to the reference:

$$\theta = \frac{\delta}{f}. \tag{3.1}$$

The spot displacement is measured for each sub-aperture, in the two axis of the detector x and y, giving two sets of slopes. The spot position is determined by searching the center of gravity considering the intensity.

From the local slopes S_{xy}, the wave-front can be reconstructed with the Zernike polynomials [Lane and Tallon, 1992; Lukin et al., 2010].
The Wave-Front Sensor model is defined by the lenses focal length and diameter, the number of sub-apertures and the camera dimension and number of pixel. From this model, a Zernike base in phase Z_{phase} can be described in slope Z_{slope}. Then the measured slopes S_{xy} can be projected on the Zernike base (with Z^{+}_{slope} the pseudo-inverse), giving the different components c_Z of the studied wave-front ϕ:

$$c_Z = Z^{+}_{slope} S_{xy} \Rightarrow \phi = Z_{phase} c_Z. \tag{3.2}$$

So, starting with a given base, the wave-front can be reconstructed. In our study, low and high spatial frequencies are distinguished. The low frequencies are defined by the 42 first Zernike polynomials (with the order defined in Chapter 1, Section 1.1.2). It includes all the modes achievable by the MADRAS mirror.
The high frequencies are defined by the higher order Zernike modes. The high frequencies components of the wave-front error will neither be corrigible by the MADRAS mirror or come from its deformation. So, the correction performance are computed without considering these modes. Moreover, as the mirror is not supposed to correct for tip, tilt and focus, these aberrations are also removed from the measured wave-front.

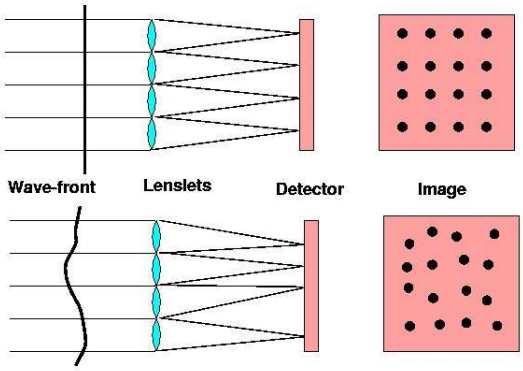

Figure 3.2 : *Principle of a Shack-Hartmann Wave-Front Sensor: Top: reference wave-front - Bottom: the wave-front error induces a displacement of the spot regarding the reference wave-front (from www.ctio.noao.edu).*

3.2 Test bed characterization

The optical bench is first aligned with flat mirrors instead of the 2 deformable mirrors. The DM88 is then installed in order to characterize its precision for the WFE generation but also to calibrate the optical set-up errors. The MADRAS mirror is finally installed to perform the active correction.

3.2.1 WFE generation

The wave-front injected on the test-bed with the first loop simulating the telescope needs to be precisely calibrated. The parameters of this loop (exposure time, camera dynamic and loop gain) are chosen in order to optimize the WFE generation precision and to minimize the turbulent wave-front.
The loop calibration consists in recording the 88 influence functions of the DM88 and then in defining the number of eigen modes to be used when computing the commands. 70 modes are kept, allowing a good convergence of the loop [ALPAO, 2011].

Firstly, the target of the loop is a flat wave-front. The residual WFE is directly given by the WFS1 measurement (difference between the measured wave-front and the reference one). 1000 phase maps ϕ_k are recorded in order to determine both static aberrations and turbulence.

The static error ϕ_{stat} is given by the average of the $N = 1000$ phase maps:

$$\phi_{stat} = \frac{1}{N} \sum_{k}^{N} \phi_k. \tag{3.3}$$

It has an amplitude of 16 nm rms, mainly composed of high spatial frequency errors, corresponding to the DM88 actuators print-through. Considering only the low frequency Zernike polynomials (up to the sixth order), the residual error is 8 nm rms (see Figure 3.3).
The turbulent phase maps $\phi_{turb,k}$ are deduced by subtracting the static error to each measured phase maps:

$$\phi_{turb,k} = \phi_k - \phi_{stat}. \tag{3.4}$$

By definition, the turbulence has a null average, the data of interest is given by the amplitude of the turbulent phase [Lesieur, 1994; Andrew, 2004]. Figure 3.3 presents the evolution of this amplitude with time, allowing the deduction of the average turbulence: 6 nm rms (Figure 3.3).

The precision of generation of the 9 specified modes is also studied. The reference is defined by the required mode and the difference between the wave-front measured by the WFS1 and this target gives the precision of generation. As for the flat wave-front, a precision of 8 nm rms (for the low frequencies) is recovered for each specified mode.

3.2.2 Aberrations of the bench

The bench calibration is done with a flat mirror, precise at $\lambda/20$ PtV, instead of the MADRAS mirror.
The parameters of the WFS2 are defined in order to have the same value of turbulence than for the WFS1. As the optical path seen by the WFS2 is 3 times longer, the turbulence is more important and needs to be better averaged: the exposure time is then bigger, in order to integrate more photons.

The bench static aberrations are deduced from the WFS2 measurement when a flat wave-front is injected by the DM88: the difference between the measured wave-front and a collimated wave-front is 19 nm rms, considering low spatial frequencies (Figure 3.4). It includes alignment errors and the error of the flat wave-front generation.

For the WFE correction, there will be two possibilities: either these static aberrations will be corrected by the MADRAS mirror or not. The choice will depend on the goal of the experiment:

- In order to have the best optical quality at the exit focal plane, the reference wave-front must be the collimated one, so the bench errors will be corrected by MADRAS.

- In order to determine the precision of correction of a calibrated wave-front error, the reference wave-front must include these bench errors, so MADRAS will only correct the injected WFE.

In conclusion, the measurement of this phase map is important, it will constitute a reference for the next tests.

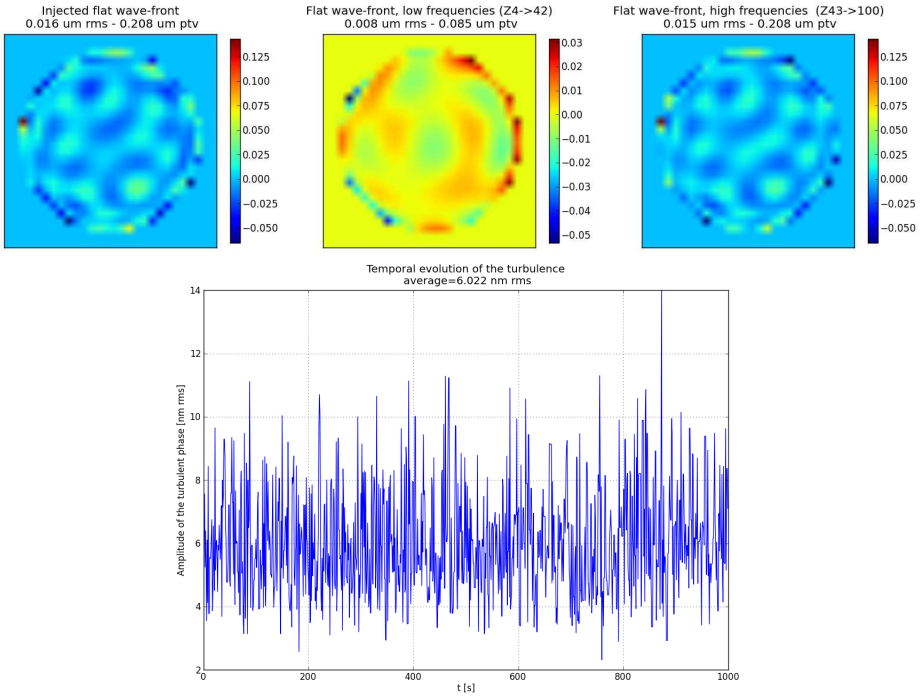

Figure 3.3 : *Characteristics of the loop generating the WFE: precision of the generated flat wave-front and turbulence.*

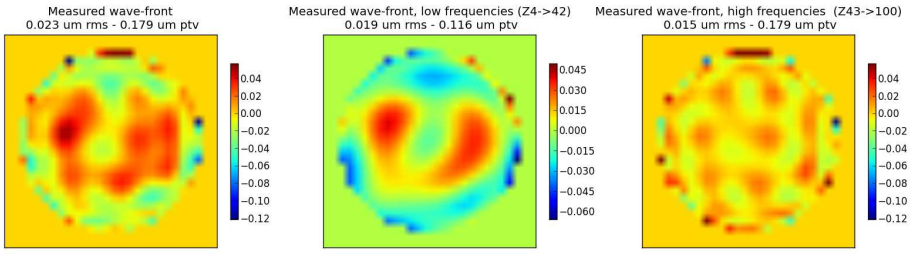

Figure 3.4 : *Aberrations of the bench, including misalignement and the wave-front generation errors (average of 100 measurements).*

3.3 Active correcting loop calibration

Once the test bench has been calibrated and the reference recorded, the MADRAS mirror is installed and the active correction loop is set in place.

3.3.1 Interaction Matrix and Control Matrix

The active system calibration consists in determining the Interaction Matrix (IM): the influence functions are measured with the WFS2 by applying a push/pull on each actuator while the others are at rest. The Control Matrix (CM) is then computed using the Singular Value Decomposition of IM:

$$\text{IM} = u\lambda v^t \Rightarrow \text{CM} = u^t \lambda_f^{-1} v. \tag{3.5}$$

λ_f is a diagonal matrix containing the system eigen values. As the low eigen values will propagate the noise, the last eigen modes can be filtered by forcing their eigen values to zero.
This filtering allows decreasing the conditioning factor, it will stabilize the command law. Figure 3.5 presents the decrease of the conditioning factor with the number of removed modes. To ensure a system functioning with reasonable commands, the last three modes are filtered.
This calibration must be performed regularly, in order to keep an optimal control law.

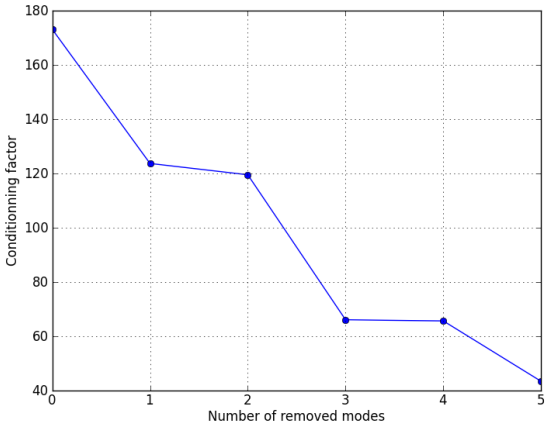

Figure 3.5 : *Evolution of the system conditioning with the number of considered modes.*

To simulate the external handling of tip, tilt and focus, three virtual influence functions, corresponding to these three modes are added to the interaction matrix, thus the command law will compute 27 commands: 24 for the actuators and 3 virtual commands. These last three values will simply not be sent to the system. This method allows to address any components of tip, tilt or focus on the 3 dedicated influence functions: thus, the system will not generate these modes.

3.3.2 Loop Noise

The loop noise gives the precision of the measurements. It is characterized by correcting the turbulent phase: a reference is defined at an instant t and the active loop target is defined as this wave-front. The resulting wave-front error corresponds to the loop noise. From its amplitude variation (Figure 3.6), we deduce that a wave-front is measured at ± 4.8 nm rms.
The noise level is decreased of a factor $1/\sqrt{N}$ by averaging N measurements, so the precision is reduced to ± 0.5 nm rms by averaging 100 measurements.

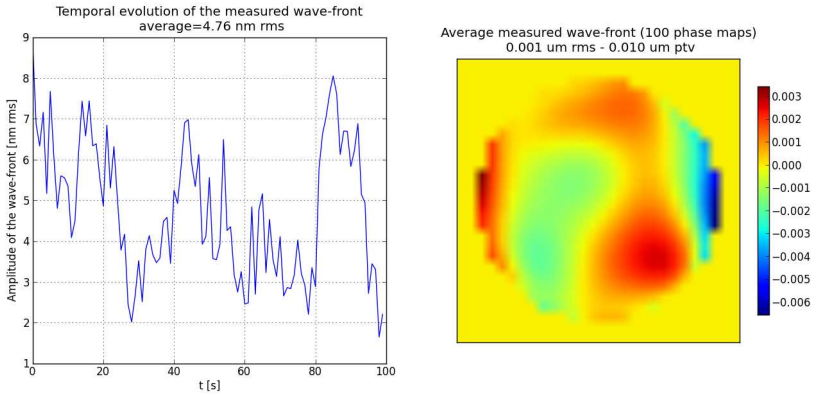

Figure 3.6 : *Results of the correction of the turbulent phase to determine the measurement precision: evolution of the amplitude of 100 measured WFE and averaged WFE.*

3.3.3 Flattening

We have seen in Section 3.2.2 that there are some aberrations in the optical path, due to misalignment and wave-front generation error, inducing a WFE of 19 nm rms.
Moreover, MADRAS optical surface contains some integration bias, mainly due to the actuators integration (see Section 2.4.4). At rest the mirror shape is deformed of 258 nm rms, mainly composed of focus and astigmatism.

For an efficient PSF measurement, the first step is to correct these WFEs seen by the Wave-Front Sensor. As we have seen in Section 3.2.2, the target for the flattening can be defined in different manners:

- the reference wave-front is a flat one, this reference will lead to the best achievable optical quality, MADRAS mirror will compensate for both the integration bias and the external aberrations, due to misalignment.

- the reference wave-front is the measured wave-front with a flat mirror instead of MADRAS, thus MADRAS mirror will only compensate for its shape error, converging to a flat optical surface. As the optical aberrations coming from the test bench are low, their correction will not impact the performance of the mirror neither in terms of actuators' stroke or precision of correction, so we choose to correct them. This allows to have the best PSF imaging at the test-bed output.

The flattening is performed by injecting a flat wave-front with the DM88 and closing the active correction loop on the defined reference wave-front (see the method on top of Figure 3.8). The residual wave-front error after flattening is 12.2 nm rms (see Figure 3.7).
We will see in the next Section that this residual wave-front will be the target for the next corrections.

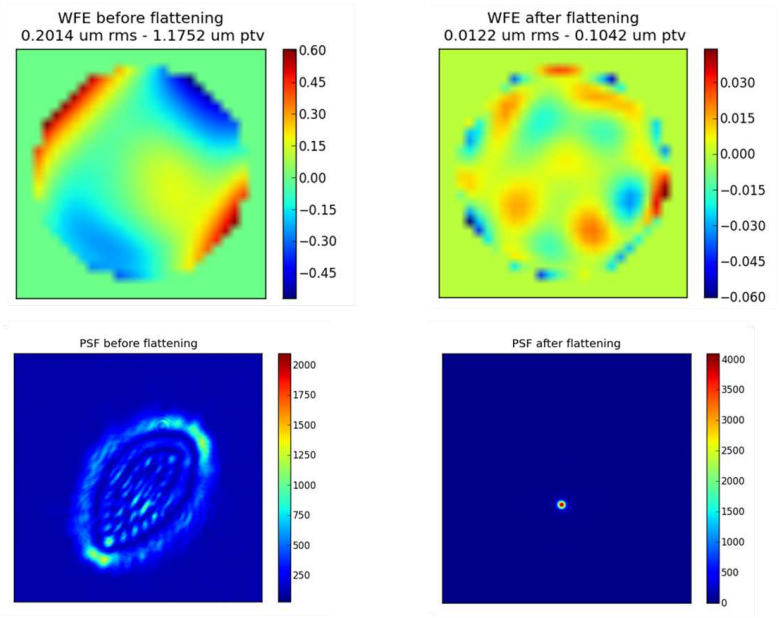

Figure 3.7 : *WFE and PSF before and after flattening considering a flat wave-front as the reference (piston, tip, tilt, focus and high spatial frequencies subtracted).*

3.4 Mode correction

Once the bench and the active loop are calibrated, the correction of each specified Zernike mode is studied by generating them with the DM88.

3.4.1 Operation

The goal is here to demonstrate the ability of the active correction loop to correct for calibrated incoming WFE. Thus, the performance of the integration bias compensation is not considered. The correction characterization is performed in two steps, summarized in the diagrams of Figures 3.8 and 3.9:

1. Flattening with MADRAS (with the DM88 injecting a flat wave-front), as explained in Section 3.3.3. This step provides a good optical quality and defines the offset commands V_{offset}, allowing to keep a large dynamic for the WFS. Moreover, it defines the reference slopes: the target wave-front is the one measured after this flattening.
2. Mode correction (with the DM88 injecting the specified mode).

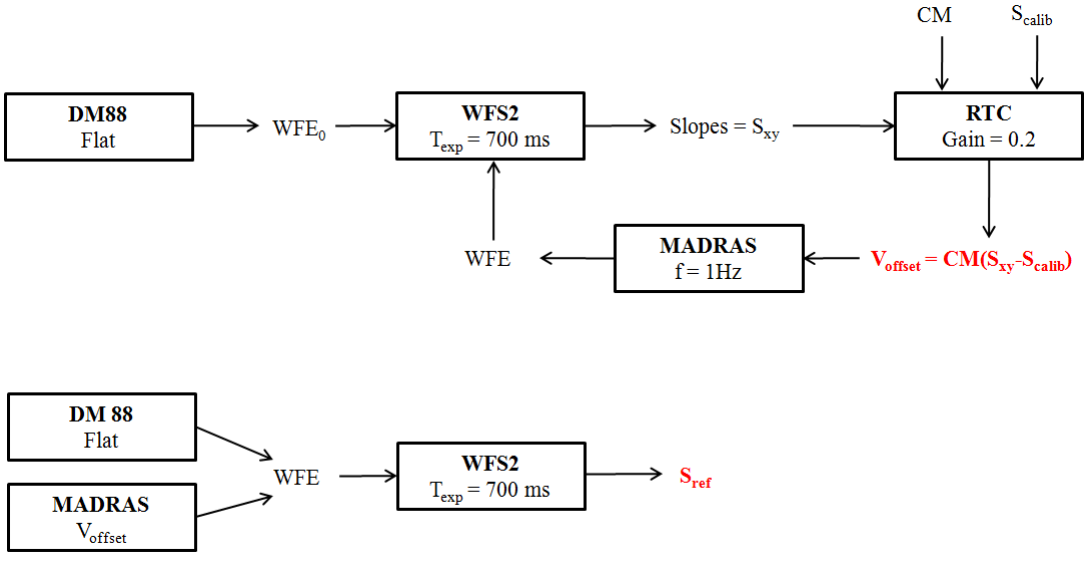

Figure 3.8 : *Method of definition of the inputs for the correction loop with the flattening.*

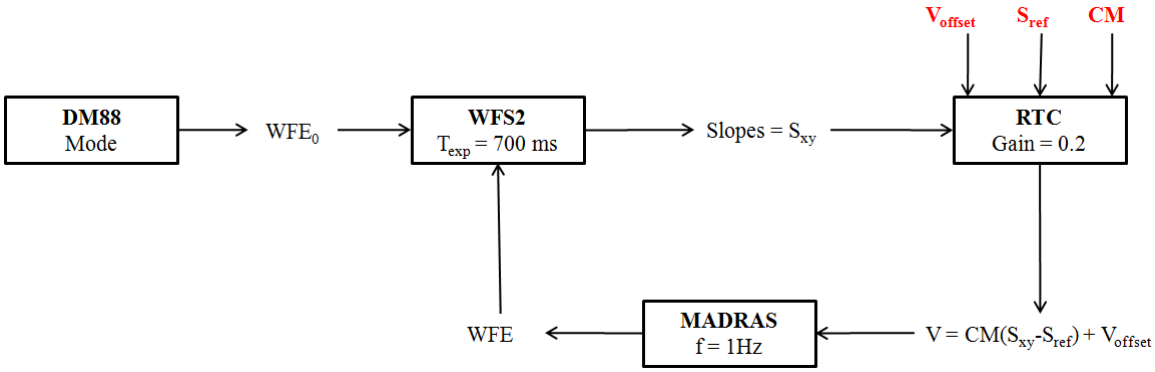

Figure 3.9 : *Functional diagram explaining the correction of a WFE injected by the first loop. The three inputs are the Command Matrix CM (deduced from the Interaction Matrix), the offset commands V_{offset} and the reference slopes S_{ref} (both deduced from the flattening, as explained in Figure 3.8).*

3.4.2 Specified modes

The performance measured for each mode are presented in Figure 3.10. The expected precision of correction, deduced from the Influence Functions measurement with the Fizeau interferometer (Chapter 2, Section 2.5), is recovered for most of the modes.

All of the specified Zernike modes are corrected with a precision better than 8 nm rms. As expected from simulations, the correction of Astigmatism3&5, Trefoil5&7 and Tetrafoil7&9 is highly efficient, the residual wave-front error is below 5 nm rms, and Pentafoil9 correction precision is around 7 nm rms.
The amplitude of the residuals measured for all these modes (except for the tetrafoil7) is slightly superior to the expected one. This difference has several contributors:

- The sampling of the WFS (28x28 points) is less important than the sampling of the interferometer (550x550 points), it can reduce the measurement precision.

- The interferometric measurement is direct while for the WFS the reconstruction from the slopes to the phase is done on a given Zernike polynomials base. Moreover the optical path is longer and contains many optics that can slightly move. These two factors introduce some errors.

- Due to the virtual handling of tip, tilt and focus, the control matrix is not optimal, it can impact the correction of some components.

Coma and Spherical are currently corrected with a precision of 6 and 8 nm rms, but this result could be improved up to the values expected from the interferometric measurement by working on the command matrix or by inserting on the test bench real systems to adress the tip, tilt and focus modes. Indeed, the correction of Coma and Spherical modes is less efficient due to the method used for the tip, tilt and focus filtering in the control matrix. Both coma and tilt modes have a component in $cos(\theta)$ in there mathematical expressions, and both focus and spherical aberrations have a component in ρ^2. Thus, the generations of these modes are linked. Adding virtual influence functions probably impacts the correction. Other methods have been investigated to define the control matrix, in order to improve the performance but for now none have given better results. We have tried the following methods [Roddier, 1999]:

- Adding pseudo-measurements in the interaction matrix, that is to say for each influence function we add three points to the WFE map, corresponding to their components in tip, tilt and focus. Thus, the three first eigen modes will correspond to these modes and they can be filtered before computing the command matrix.

- Filtering the tip, tilt and focus components directly in the measured influence functions so that the three modes are absent from the eigen modes and the resulting matrix command would not allow the system to generate these modes.

- Adding components of tip, tilt and focus in each influence function in order to have three eigen modes corresponding to these modes, they are then filtered before computing the command matrix.

In Section 2.1.1, we have seen that in a representative configuration, a 5 degrees of freedom mechanism will address the 3 modes. Tip, Tilt and Focus influence functions will then be real, automatically solving the raised problem. A simple evolution of the test bed will be soon integrated to solve the tip, tilt handling: MADRAS mirror is going to be installed on a motorized tip/tilt plat-form, driven by two actuators.

In Figures 3.11 to 3.13 we present the wave-front shapes before and after correction for the specified Coma3, Astigmatism3 and Astigmatism5. The residual shapes and amplitude are closed to the ones expected from simulation (see Section 2.3.2). For each specified mode, the PSF before and after correction have been recorded, illustrating well the benefits of the correction. The optical shape of the mirror has been measured with the Fizeau interferometer, constituting another validation of the correction: the measured deformation correspond well to the injected WFE.

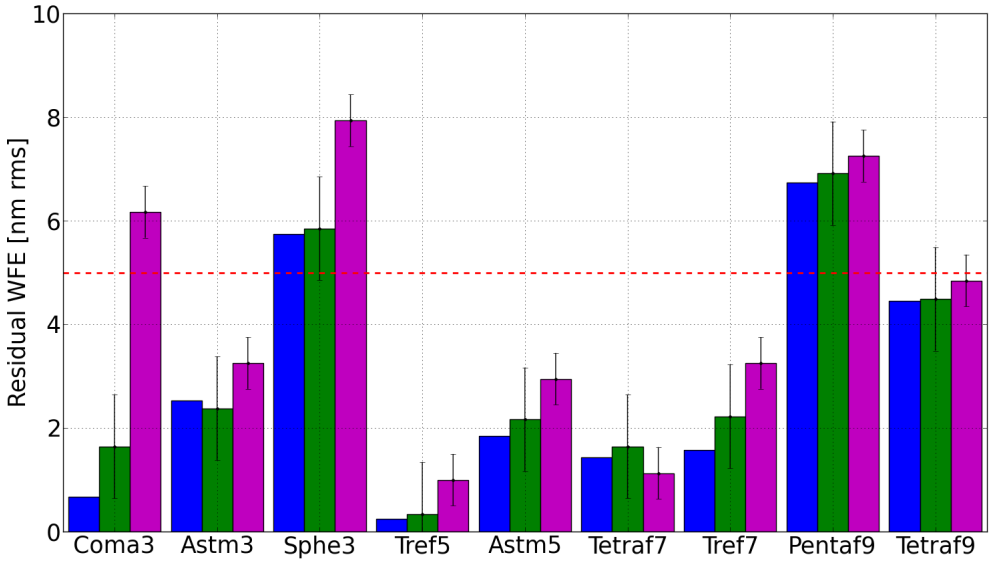

Figure 3.10 : *Closed loop MADRAS performance: residual WFE measured by the WFS2 after the correction of each specified mode (in violet), compared to the expected performance, from interferometric measurements (in green) and from FEA (in blue) (errorbars correspond to the interferometer and WFS precisions).*

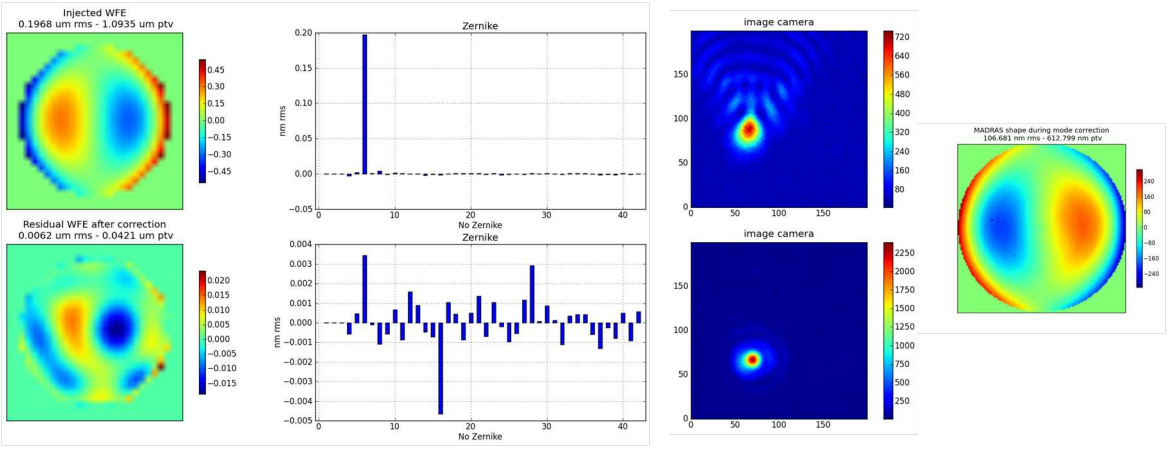

Figure 3.11 : *Coma3 correction: WFE before (196.8 nm rms) and after (6.2 nm rms) correction - Zernike decomposition of the WFEs - PSF before and after correction - Optical shape of the mirror (106.7 nm rms).*

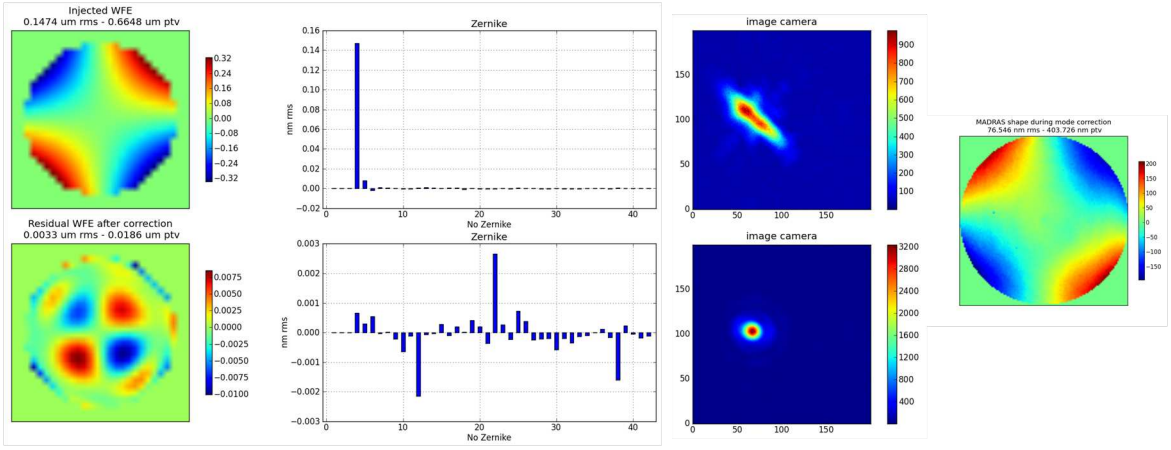

Figure 3.12 : *Astigmatism3 correction: WFE before (147.4 nm rms) and after (3.3 nm rms) correction - Zernike decomposition of the WFEs - PSF before and after correction - Optical shape of the mirror (76.5 nm rms).*

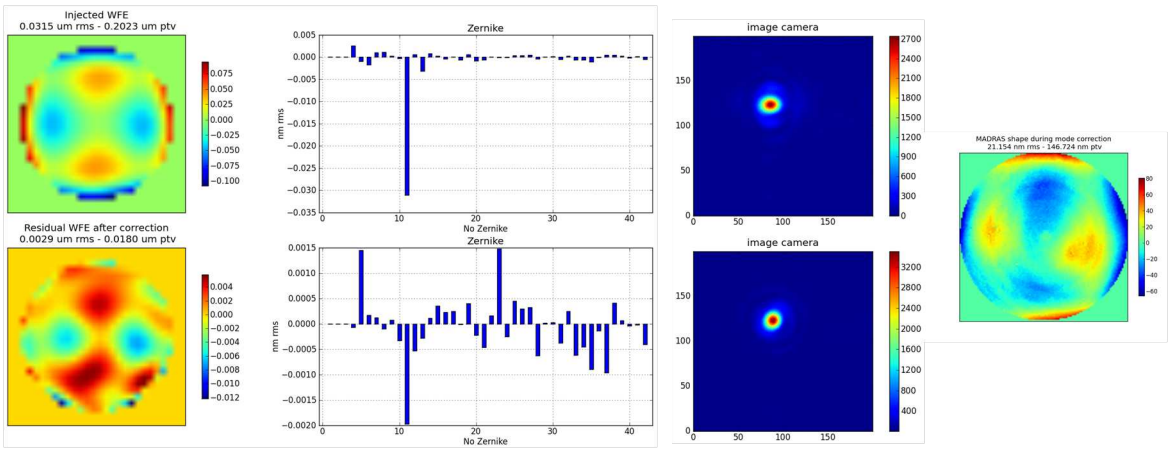

Figure 3.13 : *Astigmatism5 correction: WFE before (31.5 nm rms) and after (2.9 nm rms) correction - Zernike decomposition of the WFEs - PSF before and after correction - Optical shape of the mirror (21.4 nm rms).*

3.4.3 Stability in open loop

The previous tests have been done in closed loop. For a space application, the ideal operation will be the WFE correction in open loop, in order to save power and increase the lifetime of the system. For this reason, a stable system is mandatory, at least over a timescale corresponding to the required correction frequency. Piezo-electric actuators are not known for their stability, they are generally used with a closed loop on a strain gauge. In this section, the system behavior is then characterized in open loop, regarding the precision of correction.

A stability study is performed over two consecutive cycles of 30 minutes each, with a correction of the WFE at the start of each cycle.
The results of this test for the 4 first specified modes are presented on Figure 3.14. We can see that the residual amplitude dramatically increases with time, none of the mode stays within the specification of correction. The precision is less damaged after the second actuation than after the

first one This is due to the fact that the applied displacements are smaller so there is less relaxation.

This test clearly demonstrates that the actuators currently used would hardly be suitable for a space use. They have allowed to validate the opto-mechanical concept of the mirror but some extensive studies need to be done on actuators technologies. For instance, mechanical actuators, such as micro-motors, seem more adapted. They are more stable and can remain blocked in a position after turning off the electric supply. This kind of actuators is notably used in the James Webb Space Telescope [Mulvihill et al., 2003].

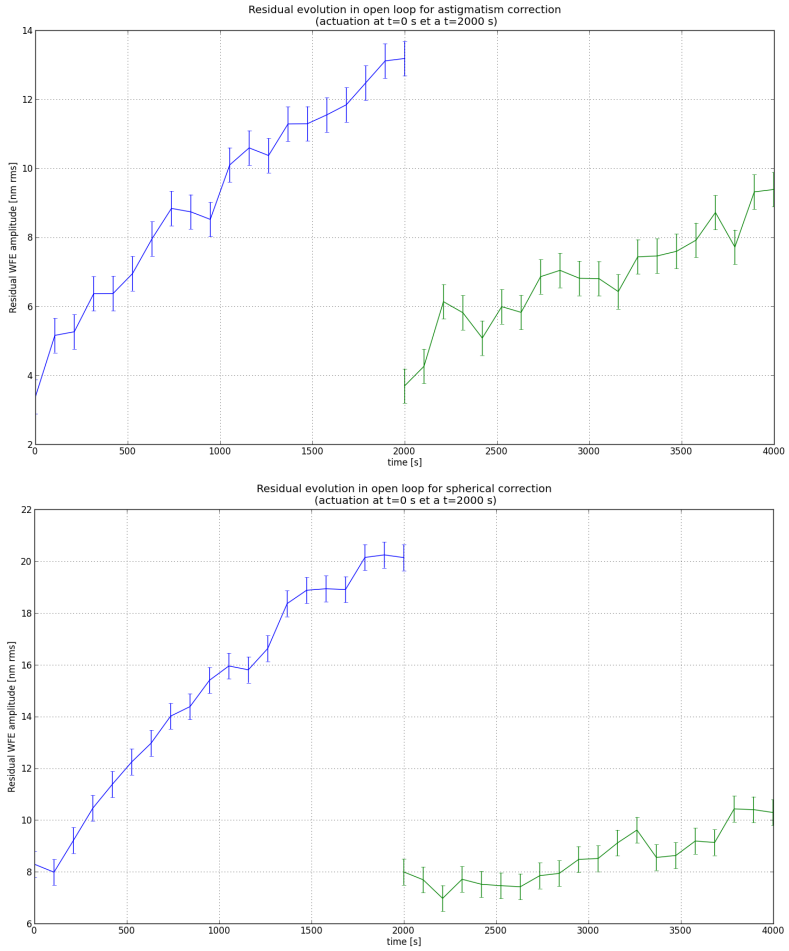

Figure 3.14 : *Stability of the correction in open loop: evolution of the residual wave-front after the correction of 150 nm rms of Astigmatism3 and 50 nm rms of Spherical3. Two cycles are performed for each mode with an actuation of the correction at the start of each cycle (at t=0s and t=2000s).*

3.5 Representative WFE correction

After having demonstrated the system capacity to correct each specified mode separately, the correction performance is studied regarding the deformation expected in space telescopes.
In order to perform a statistical study as in Section 2.3.3, the linearity of the system must be verified.

3.5.1 Linearity

Firstly, we want to validate the fact that if $\phi_{res,mode}$ is the residual WFE after the correction of ϕ_{mode}, the residual after the correction of $\alpha\phi_{mode}$ will be $\alpha\phi_{res,mode}$.

The linearity of the actuator response is analyzed by recovering the Influence Functions for different commands: a voltage range from the minimum to the maximum command is applied to each actuator, the command being increased every two minutes. As we can see on the top of Figure 3.15, each IF amplitude evolves linearly with the applied voltage. This behavior will then allow the linearity for a mode correction. For instance, if a ramp of astigmatism is injected on the active correction loop, the residual WFE amplitude evolves linearly with the injected amplitude (Figure 3.15, bottom). This test is performed for all the specified modes, confirming the system linear behavior.

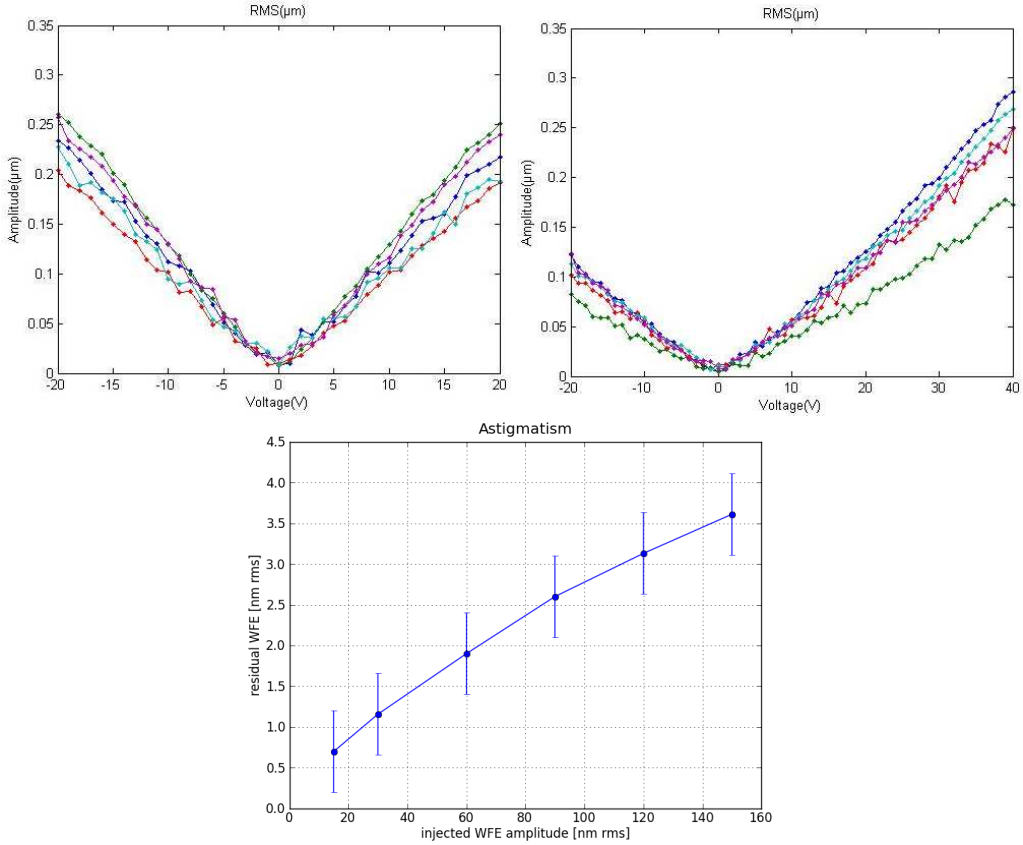

Figure 3.15 : *System linearity: Top: linearity of the Influence Functions amplitude with the applied voltage (left: 5 internal actuators, right: 5 external actuators) - Bottom: Evolution of the residual of an astigmatism correction with the injected amplitude of astigmatism.*

3.5.2 Mode combination

Secondly, we want to validate the fact that if $\phi_{res\_mode,i}$ is the residual WFE after the correction of $\phi_{mode,i}$, the residuals after the correction of $\sum_i \phi_{mode,i}$ will be $\sum_i \phi_{res\_mode,i}$.

This validation is performed by injecting combinations of the specified mode studied before. For each combination, the resulting residual wave front RMS amplitude must be the quadratic sum of the individual residuals.
Numerous combinations have been analyzed and this behavior is verified for all the cases. This also allows to study the worst case, if all the specified modes are injected at the same time, the residual WFE after correction is 14.6 nm rms.

Table 3.1 : *Examples of mode combination correction.*

WFE (specified mode)	Expected [nm rms]	Measured [nm rms]
Astigmatism3 + Spherical3	$\sqrt{3.3^2 + 7.9^2} = 8.6$	8.3
Astigmatism3 + Trefoil5	$\sqrt{3.3^2 + 1^2} = 3.4$	3.5
Coma3 + Spherical3	$\sqrt{6.2^2 + 7.9^2} = 10.0$	9.3
Astigmatism5 + Tetrafoil7	$\sqrt{2.9^2 + 1.1^2} = 3.1$	3.3
Coma3 + Astigmatism3 + Spherical3	$\sqrt{6.2^2 + 3.3^2 + 7.9^2} = 10.6$	9.7

3.5.3 Global performance

The mirror behavior being linear, a statistical study on 2000 random WFEs is performed, giving the expected mean residual wave-front after correction. MADRAS system is then able to compensate for the deformations expected in space telescopes with a mean precision of 8.2 nm rms, with a standard deviation of 1.8 nm rms. The mean precision of the MADRAS correcting system is then within the 10 nm rms specification.

An example of representative WFE is presented in Figure 3.16: the injected wave-front error is 129 nm rms and the corrected wave-front is 8.7 ± 0.5 nm rms. Once again, the gain for the PSF measurement is obvious.

With a better correction of coma3 and spherical3, the mean performance and the precision of correction for the worst case could be improved up to the values deduced from the interferometrical measurements (Section 2.5.3): 6.2 nm rms for the mean precision and 11.1 nm rms for the worst case. In the short term, a real tip, tilt and focus correction will be implemented on the test bench, with a motorized plateform.

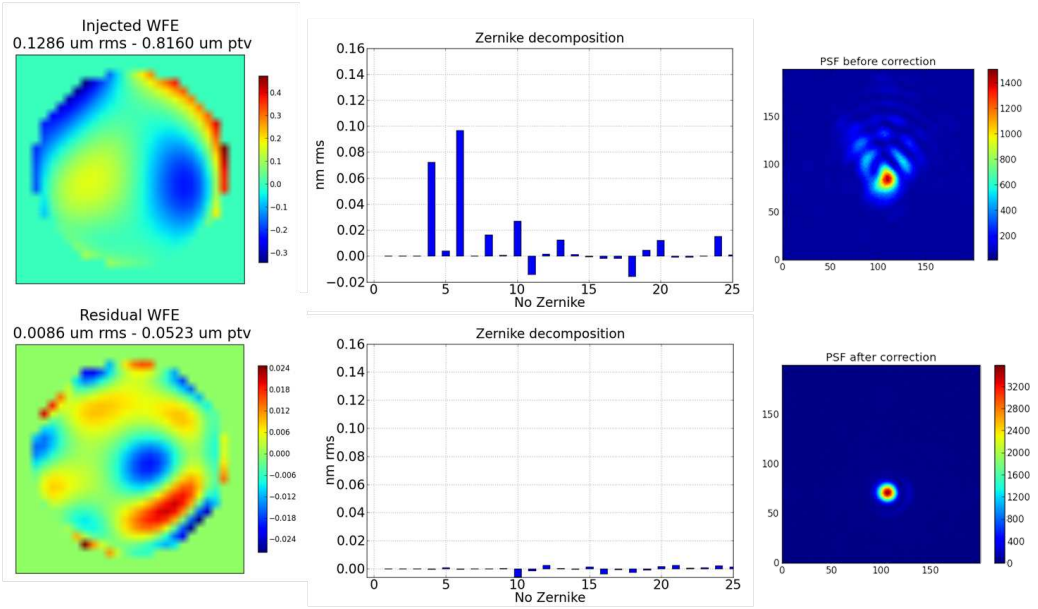

Figure 3.16 : *Correction of a random WFE (the given wave-front is an average of 100 measurements, tip, tilt and focus substracted).*

3.6 Conclusion

The ability of the MADRAS system to compensate for the expected deformations in future space telescopes has been demonstrated. In the previous chapter the opto-mechanical design has been validated. In this chapter, the correction system was integrated in a representative flight configuration, demonstrating the correction of the expected primary mirror deformation in closed loop. The mean precision of correction of the MADRAS mirror is 8.2 nm rms. The conducted tests has brought the system to a TRL4, the next step will logically be to reach the TRL5, that is to say to space qualify the system. As the system has been designed considering space constraints, this TRL should be easily reached.

Three limitations have been identified.
Firstly, the tip, tilt and focus handling in the command matrix which, at the moment, disturbs the coma and spherical correction. However, it will not be a problem in a telescope, where these 3 modes will be corrected by a 5 degrees of freedom mechanism on the secondary mirror.
Secondly, the integration bias on the optical surface shape which defines the system performance: the actuators integration has deformed the optical surface and the flattening is achieved with a residual error of 12 nm rms. The error budget for the integration must be decreased to reach a better performance.
Finally, an effort must be done on the actuator technology. Piezoelectrics have been chosen because their use is well known and the project was not focused on actuators, but they are not necessarily the optimal solution for space use. The determining parameters will be their stability and the possibility to maintain their positions without continuous supplying power.

The MADRAS test bed has been conceived for the characterization of space active systems. It will now be used to test wave-front sensors for moving and extended sources, which can be coupled to the MADRAS mirror. Moreover, other types of active mirrors could be tested on the same test bench.

Bibliography

ALPAO. Low-Speed DM88-25 - User's manual. Technical report, ALPAO, 2011.

L. Andrew. *Field Guide to Atmospheric Optics*. SPIE Field Guides. 2004.

R. G. Lane and M. Tallon. Wave-front reconstruction using a Shack-Hartmann sensor. *Applied Optics*, 31:6902–6908, November 1992.

M. Lesieur. *La Turbulence*. Collection Grenoble Sciences. 1994.

V. P. Lukin, N. N. Botygina, O. N. Emaleev, and P. A. Konyaev. Wavefront sensors and algorithms for adaptive optical systems. volume 7736 of *Society of Photo-Optical Instrumentation Engineers (SPIE) Conference Series*, July 2010.

M. L. Mulvihill, M. E. Roche, J. L. Cavaco, R. J. Shawgo, Z. A. Chaudhry, and M. A. Ealey. Cryogenic deformable mirror technology development. volume 5172 of *Society of Photo-Optical Instrumentation Engineers (SPIE) Conference Series*, pages 60–67, October 2003.

F. Roddier. *Adaptive optics in astronomy*. Cambridge University Press, 1999.

F. Rooms and J. Charton. Deformable magnetic mirrors for adaptive optics. *Photoniques*, 27: 38–40, 2007.

R. Tyson and B. Frazier. *Field Guide to Adaptive Optics*. SPIE Field Guides. 2004.

Chapter 4

Giant telescopes: segments manufacturing with stress polishing

---

Future generations of Earth-based observatories will require 30-40 m class telescopes. The realization of these giant telescopes will be challenging on many levels and will lead to many innovations. As we have seen in Chapter 1 (Section 1.4.2), there are currently 3 main projects that are developing giant telescopes: the 24.5 m Giant Magellan Telescope, the Thirty Meter Telescope and the 39 m European Extremely Large Telescope.

Due to manufacturing constraints, these telescopes will be segmented: the GMT will be composed of seven 8.4 m circular segments and the TMT and E-ELT of respectively 492 and 798 hexagonal 1.45 m segments. The segment size comes from the current manufacturing capabilities: 8.4 m is the largest achievable diameter for monolithic mirrors and 1.45 m is the maximum diameter of the polishing machine of the main industries. In this chapter, we focus on the active optics contribution for the E-ELT segments manufacturing.

In the first section we present the E-ELT design and the problematic of segments manufacturing, which has led to the realization of a segment prototype with Stress Mirror Polishing (SMP). In the second section, the warping harness design and optimization is detailed, such as the performance computed with Finite Element Analysis. In the third section we present the system realization and testing.

The work presented in this chapter has led to the following publication:
- M. Laslandes, N. Rousselet, M. Ferrari, E. Hugot, J. Floriot, S. Vives, G. Lemaitre, J.F. Carré, M. Cayrel, Stress polishing of E-ELT segment at LAM - Full scale demonstrator status, SPIE 8169, 2011.

4.1 The E-ELT and its large segmented primary mirror

4.1.1 A 5 mirror telescope

As described in Section 1.4.2, the E-ELT optical design has the particularity of including adaptive optics mirrors directly in the telescope. Its design, presented on Figure 4.1, consists in a Three Mirror Anastigmat with two additional folding adaptive mirrors, and provides an optical quality almost diffraction limited over the entire 10 arcmin field of view and on a wavelength range from the visible to the mid infra-red [Delabre, 2008; ESO, 2011].
Two Nasmyth platforms at either sides of the telescope will contain several instruments in the same time. The beam can also be redirected through relay optics to a Coudé focus.

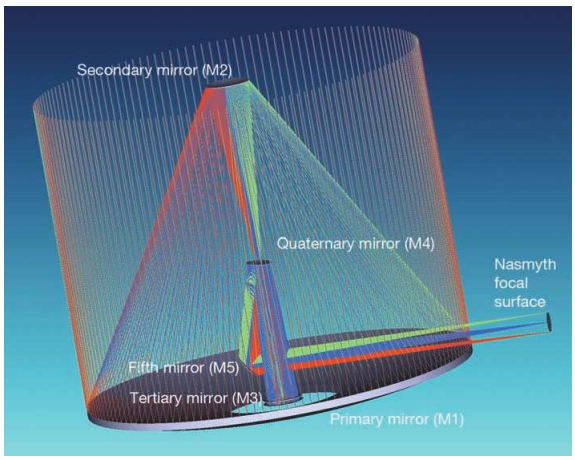

Figure 4.1 : *Optical design of the E-ELT telescope (credit ESO).*

4.1.2 A 39 m diameter primary mirror

The segmented primary mirror provides a near annular optical aperture, its outer diameter is 39.3 m and its inner diameter is 9.4 m. The mirror is elliptic concave with a 69 m radius of curvature and a conic constant of -0.996. It is made of 798 quasi-hexagonal segments, measuring 1.45 m corner to corner and 50 mm thick at the center. There are 10 rings of segments and the hexagonal shape allows having a six-fold symmetry segmentation pattern. The mirror is then constituted of 133 different Off-Axis Parabola families [Cayrel, 2011].
In addition to the 798 segments, a spare for each family is required to be able to immediately replace a segment needing recoating. So, a total of 931 segments, grouped in 133 families of 7, is needed for the telescope operation. To achieve first light around 2020, the current planning assures 6 years for the manufacturing of about one thousands segments. After a definition and preparation phase, there will be approximately 3 years for mirror production, that is to say a segment must be manufactured every day.

The main steps for the segments manufacturing are the following:
- grinding and polishing of a circular substrate to obtain the required aspherical shape with a precision of 1λ rms,
- hexagonal cutting,
- installation of the segment on its whiffletree providing its active support,
- Ion Beam Finishing to remove the shape errors due to the cutting, the integration on the

whiffletree and the polishing process.
At the end of this process, the segment shape must be obtained with a maximum residual error of 10 nm rms.

The cost and time constraints being extremely strong, ESO has launched some studies of the different possibilities for the polishing and the generation of the aspherical shapes [Dierickx and Cayrel, 2011]. Two main competitive studies for the manufacturing of 7 segments prototypes have been launched in 2009 (SAGEM/REOSC and Optic Glyndwr) and the first segments were finished recently. Both polishing methods are based on computer controlled grinding and polishing with sub-aperture tools [Zheng et al., 2010; Burge et al., 2001]. These small tool techniques need to be compared to the Stress Mirror Polishing technique, using a large tool. SMP could have a strong impact regarding the manufacturing time. By avoiding the use of sub-aperture tools, the polishing time can be strongly reduced and the method will converge to a smooth optical quality with less than 1 μm rms of wave-front error. By avoiding the generation of high spatial frequency errors, due to the small tool marks, the time spent on the final IBF pass will also be reduced [Arnold et al., 2010].

The 36 hexagonal segments of each Keck telescope have been successfully manufactured with stress polishing [Pepi, 1990], and the TMT consortium has chosen this technology for the mass production of their segments. SMP should then be considered for the E-ELT segments fabrication. In such a case, the impressive number of segments requires a validated, reliable and repeatable method.

4.1.3 Segment prototype with stress mirror polishing

The study pursued at LAM, under ESO contract, is the only academic study performed for the manufacturing of E-ELT segments [Laslandes et al., 2011]. The aim of the project is to demonstrate the manufacturing of the outermost E-ELT segment by stress polishing in order to propose a technical solution to be used by industrial partners for the segments mass production. The process is based on a LAM/Thales SESO patent.

The key points to be demonstrated are the following:
- Warp a circular blank into the required asphericity with a wave-front error lower than 1 μm rms. As the segment hexagonal cutting and installation on its whiffletree induces some residual deformations, the final IBF step cannot be avoided. There is then a margin on the generated segment shape during the polishing process, but the smaller the error, the bigger the gain of time.
- Measure the asphericity generated via mechanical gauges and compare this to interferometrical tests. This will allow the determination of the best metrology tool to control the deformation for an eventual industrialization.
- Ensure repeatability of the warping within tight tolerances.
- Ensure stability in time and under polishing conditions.

A segment optical surface shape is calculated by applying the OAP equations presented in Section 1.3.1 (Eq 1.27) with the characteristics of the E-ELT primary mirror, summarized in Table 4.1. This allows determining the different Zernike modes composing the shape of the optical surface (Figure 4.2).

Table 4.1 : *E-ELT M1 characteristics for the definition of each segment optical shape*

Radius of curvature	k = 69m
Conic constant	C = -0.996
Minimum off-axis distance	R_{min} = 6.3 m
Maximum off-axis distance	R_{max} = 18.9 m
Segment semi-diameter	a = 0.7125 m

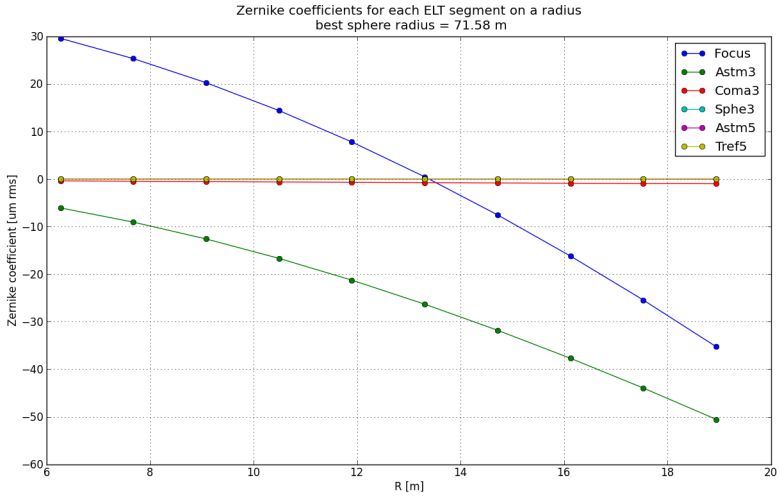

Figure 4.2 : *Evolution of the Zernike composing a segment optical shape as a function of the off-axis distance on a radius of the E-ELT M1.*

These coefficient are calculated for an initial blank with a given radius of curvature which is the same for all the segments. This dimension L corresponds to the radius of the best fit sphere for all the segments, it depends on the three parameters k, R and C:

$$L = \frac{2k(1 - C\epsilon_{max}^2/2)^{3/2}}{2 - C\epsilon_{max}^2/2}, \tag{4.1}$$

with $\epsilon_{max} = R_{max}/k$.
In the E-ELT M1 case, this radius is 71.6 m, it also gives the radius of curvature for the polishing tool. The advantage of using this best sphere radius is that it provides a unique polishing configuration for all the segments. It also better guarantees the continuity of curvature between segments. However, the amplitude of the required deformation could be reduced by using a different optimal radius for each segment, it would decrease the focus mode amplitude. For mass production, it could be envisaged to define several families of segments with a polishing tool radius optimized and different for each family.
In the outermost segment case, the optical surface deformation to generate has an amplitude of 61.6 μm rms, with mainly 35.3 μm rms of focus, 50.3 μm rms of astigmatism3 and 1.0 μm rms of coma3.

In conclusion, the main interest in the Stress Mirror Polishing method is because of the versatility of the warping harness, a single harness design can be used to generate all the segments. This fact, coupled to the possibility of using the same polishing tool from one segment to the next, will facilitate mass production. The study conducted at LAM not only aims at demonstrating the performance of the stress polishing method with the dedicated warping harness, but also at proving the process repeatability, reliability and industrialization possibility.

4.2 Warping harness design

One of the goals of this project is to realize Stress Mirror Polishing without using exotic mirror geometry, such as thickness distribution. This can be performed by using a warping harness able to warp the segments into their OAP shape, independently of the blank. The blank will then be glued on the harness. The concept of Deformable Mirror used in the MADRAS project (see Chapter 2) is efficient to generate the required shapes. Moreover the 24 actuators will allow a relaxation of the error budget allocated to the polishing and the integration: the several degrees of freedom will compensate for the eventual deformations due to the system interfaces.

4.2.1 System description and modeling

Substrate warping principle

The steps of the stress mirror polishing process are adapted from the method to manufacture Schmidt plates [Lemaitre, 1972], and can be summarized as follow:

- Gluing of the circular blank on the warping harness,
- Warping the blank to the inverse of the required shape,
- Spherical polishing of the stressed blank with a full-sized tool,
- Stress relaxation,
- Ungluing the mirror.

The warping harness principle is the one of Multimode Deformable Mirror, developed by Lemaître [2005]. Contrary to the MADRAS system, the system is composed of 3 distinct parts: the circular blank, the warping harness and a layer of glue bonding the two parts together (Figure 4.3). The mirror is warped with 24 actuators applying forces and by a uniform pressure applied on the substrate back face (Figure 4.4).
In order to minimize the residual deformation, the required forces and the level of stress in the mirror, the method presented in the Chapter 1, Section 1.3.2 is applied. The final optimized system is detailed hereafter.

Geometry

- *Blank*

The initial blank will be the same for all the segments and its radius of curvature is given by the best fitting sphere radius (see Section 4.1.3, Equation 4.1). The substrate is in Zerodur and has been provided by ESO, its geometry cannot be optimized for our study. At the beginning of the project, the primary mirror diameter was 42 m, corresponding to an additional ring of segments, and its radius of curvature was 84 m. In this case, the best sphere radius is 86.5 m. The radius of curvature of our blank is then slightly different from the 71.6 m computed in Section 4.1.3. Therefore, the Zernike modes to generate the outermost segment are modified, the required amplitudes are presented in Table 4.2.
The blank is plano-concave, 1.52 m diameter and 50.7 mm thick at its center, it weighs 235 kg.

Table 4.2 : *Amplitudes RMS of the Zernike required to generate the outermost off-axis segment with the initial blank.*

Zernike	Amplitude [μm rms]
Focus	22.4
Astigmatism3	31.1
Coma3	0.6

- Warping harness

The harness is in stainless steel, it is a 80 mm thick ring with an external diameter equal to the blank diameter: 1.52 m. Starting from a classical Multimode Deformable Mirror (presented in Section 2.2.1), the geometry has been optimized to minimize the level of stress at the interface between the ring and the mirror and the residual deformation on the optical surface.
Instead of 12 arms, the systems has 12 "forks" regularly clamped on the external part of the ring. This innovation improves the deformation continuity at the mirror edges, increasing the shape generation precision. The distance between internal and external actuators of a same fork is 300 mm. The entire harness weighs 110 kg.

- Glue

A layer of glue is deposited on the ring. The chosen glue is DP460 [3M Schotch-Weld, 1997] whose behavior is well known and has already been used for stress polishing. The optimal glue thickness is provided by the manufacturer: 150 μm. Initially, the glue is modeled as a uniform band, we will see further the optimization of the gluing geometry.

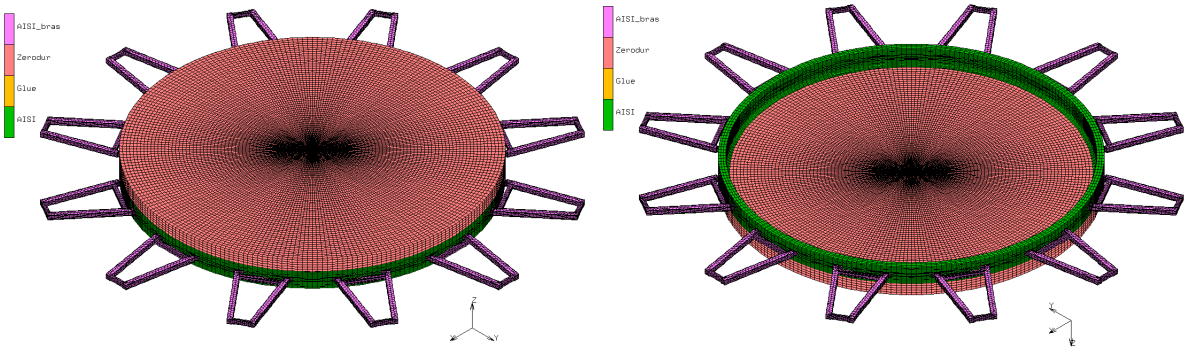

Figure 4.3 : *Finite Element Model of the substrate and the warping system with its different parts (98976 elements - 127398 nodes).*

Boundary conditions

The system has 25 degrees of freedom: 24 mechanical actuators applying displacements on the forks tangential beams and a uniform pressure applied under the optical surface.
An actuator is simply modeled by the application of a nodal displacement, inducing reaction forces. An isostatic support condition is defined on the model, ensuring its stability.

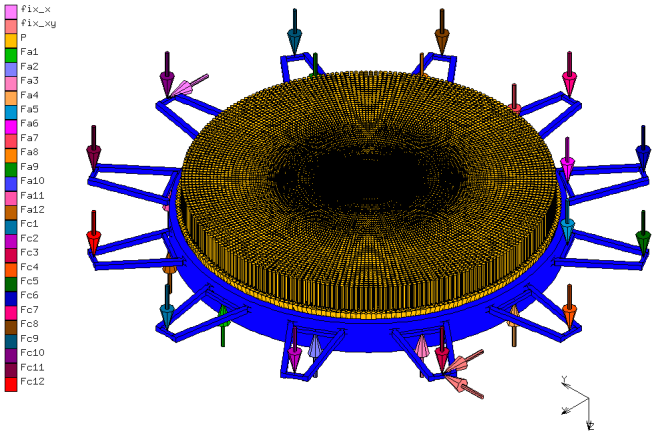

Figure 4.4 : *Boundary conditions applied to the Finite Element Model: 25 actuators (24 displacement and a pressure) and isostatic supporting conditions.*

4.2.2 Design optimization and FEA performance

Influence Functions (IF)

The model is symmetrical, as the required deformation, it is then possible to simplify the approach of decomposition on the Influence Functions. Rather than recovering the 25 IF on the FEA model, we define some "modal IF" corresponding to the required modes. A Multimode Deformable Mirror design allows the generation of the Zernike polynomials defined by $n = m$ and $n = m + 2$ with n and m the polynomials' radial and azimuthal orders. The modes to generate are here focus ($m = 0$), coma ($m = 1$) and astigmatism ($m = 2$).
The focus is an axisymmetrical mode, coma is modulated in $cos(\theta)$ and astigmatism in $cos(2\theta)$, the applied displacements must follow these different modulations, with the angle θ given by the fork position. The modal IF are defined by working on the two rings of actuators (internal and external).

The actuators are either applying a displacement or are clamped, and an actuation induces reaction forces: for a fork, the application of a positive displacement on one actuator generates a positive reaction force on this actuator and an opposite force on the second actuator of the fork. Thus, the application of the same displacement on all the actuators of a ring will produce the same effect for both rings, the focus generation can then be achieved with a single ring of actuators. It is also possible to use a unique ring for the coma generation. Indeed, a MDM can generate two modes modulated in $cos(\theta)$: tilt and coma. By clamping the internal actuators and applying the modulated displacement on the external ones, the tilt generation is locked and the coma generated. For its part, the astigmatism generation requires the use of the two rings of actuators. The 25th actuator is the pressure applied on the mirror back face to compensate for the gravity effect and improve the focus generation precision.

Five modal Influence Functions are then defined in order to generate the required shape (Figure 4.5):

- Focus mode: application of a unitary displacement on the 12 external actuators (internal actuators fixed).

- Coma mode: application of a displacement modulated in $cos(\theta)$ on the 12 external actuators (internal actuators fixed).

- Astigmatism1 mode: application of a displacement modulated in $cos(2\theta)$ on the 12 internal

actuators (external actuators fixed).

- Astigmatism2 mode: application of a displacement modulated in $cos(2\theta)$ on the 12 external actuators (internal actuators fixed).

- Pressure mode: application of a uniform pressure on the substrate back face (internal and external actuators fixed).

The projection of the required deformation on these 5 modal IF instead of the 25 individual ones is equivalent to a mode filtering. This way, the generated spatial frequencies are only the required ones. The final segment will be hexagonal, but the warped substrate is circular and the Zernike polynomials are defined on a circular pupil. As only the deflection on the hexagonal zone must be optimized, an hexagonal mask is simply applied on the deformation maps: the projection is then done only on the region of interest.

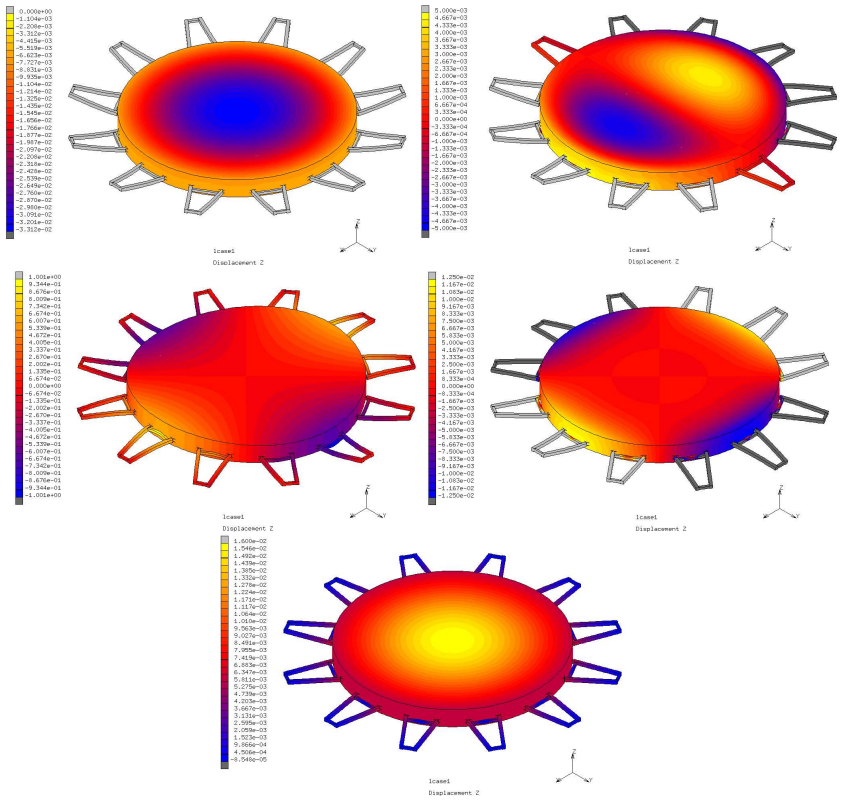

Figure 4.5 : *The 5 modal Influence Functions, recovered on the Finite Element Model (Unit:[mm]).*

Performance

- Warping precision

The projection of the required deformation on the base composed of the 5 modal Influence Functions allows the numerical reconstruction of the optical surface shape which will actually be generated by the system (Figure 4.6). The residual deformation is deduced by comparing reconstructed and required shapes. Thus, the FEA predicts that the optical surface shape will be generated with a precision of 20.2 nm rms on the hexagonal pupil (Figure 4.7).

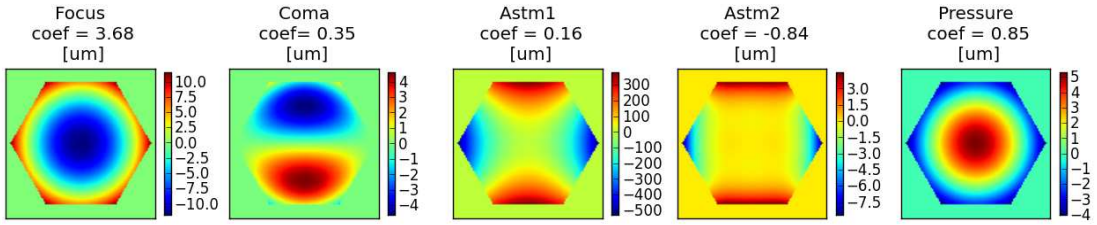

Figure 4.6 : *Influence Functions on the hexagonal pupil and coefficients from the projection of the required deformation on the IF base. The mirror finale shape is reconstructed by adding these IF, weighted by their projection coefficients.*

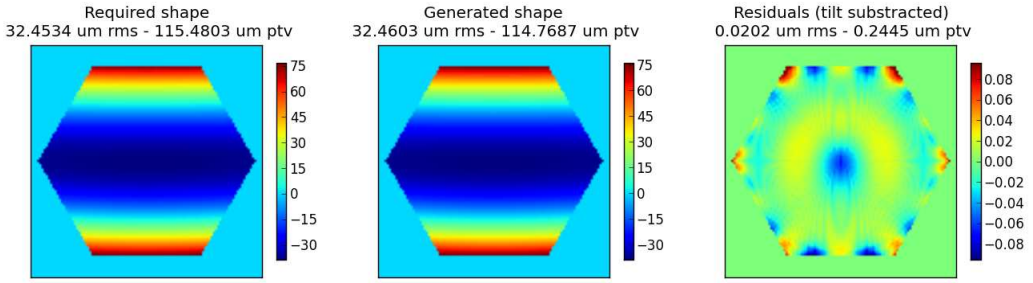

Figure 4.7 : *Warping precision: Required shape - Shape generated by the system - Residual deformation (FEA results - Unit:[µm])*

- Necessary displacements and pressure

The command for each actuator is deduced from the projection coefficients c_i, presented in Figure 4.6. Each fork is defined by its angular position θ, varying from 0° to 360° by steps of 30°.
As seen in the previous section, the internal actuators only drive the astigmatism mode, their displacements are then:

$$d_{int}(\theta) = c_{astigmatism1} cos(2\theta). \tag{4.2}$$

The external actuators displacements are defined as a combination of the different modes:

$$d_{ext}(\theta) = c_{focus} + c_{coma} cos(\theta) + c_{astigmatism2} cos(2\theta). \tag{4.3}$$

And the pressure is directly known:

$$P = c_{pressure}. \tag{4.4}$$

The required commands for the 24 displacement actuators and the pressure actuator are shown on Figure 4.9. The internal actuators displacement varies from -0.158 mm to +0.158 mm. The external actuators displacement is much higher, between +2.497 mm and +4.516 mm. In order to limit this stroke, notably due to the focus, the system could be integrated with an offset between internal and external actuators positions. With an offset of 3.506 mm, the necessary stroke would be reduced to ± 1.010 mm. The required pressure is 0.85 mN/mm^2, corresponding to 8.55 g/cm^2. This pressure is opposite to the gravity load.

- Forces and level of stress

The commands calculated above are injected in the FEA model in order to characterize the overall system mechanical behavior.
Firstly, the resulting deformation is as expected. (Figure 4.8).
Secondly, the reaction forces can be recovered on the model. The forces on the actuators depend

on the applied displacements. They range between -4790 N and 202 N for the internal actuators, and between 1424 N and 3052 N for the external actuators (Figure 4.9).
Thirdly, the level of stress in the different parts of the system is studied. The stress in the mirror must be lower than the Zerodur elasticity limit (≈ 10 MPa [Hartmann et al., 2009]). This condition is well verified on the FEA model: the maximum stress in the mirror is equal to 4.3 MPa and is localized on the mirror bottom edge (Figure 4.8).
The warping harness being in stainless steel, the level of stress in this part is not critical. Around 200 MPa, the maximum stress is localized in the forks, at the link between radial and tangential beams. At the junction between forks and ring, the stress is around 50 MPa.
The glue absorbs the constraints between the ring and the mirror: the maximum stress in the glue is 5.5 MPa, at the interface with the ring, and it decreases on the glue thickness to reach a stress of 4.3 MPa at the interface with the mirror.

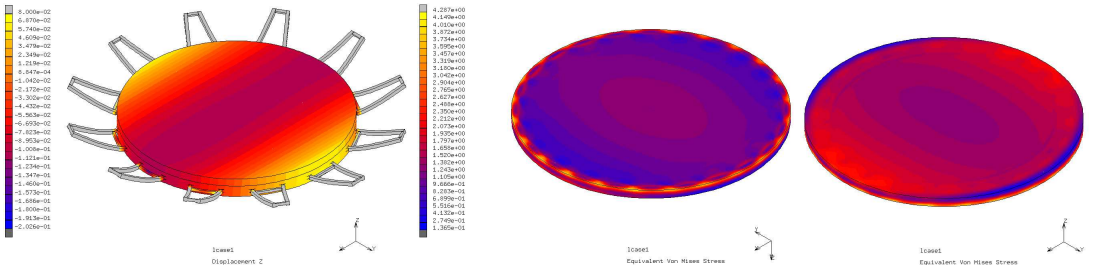

Figure 4.8 : *System deformation [mm] and stress appearing in the mirror during the deformation [MPa] - FEA results.*

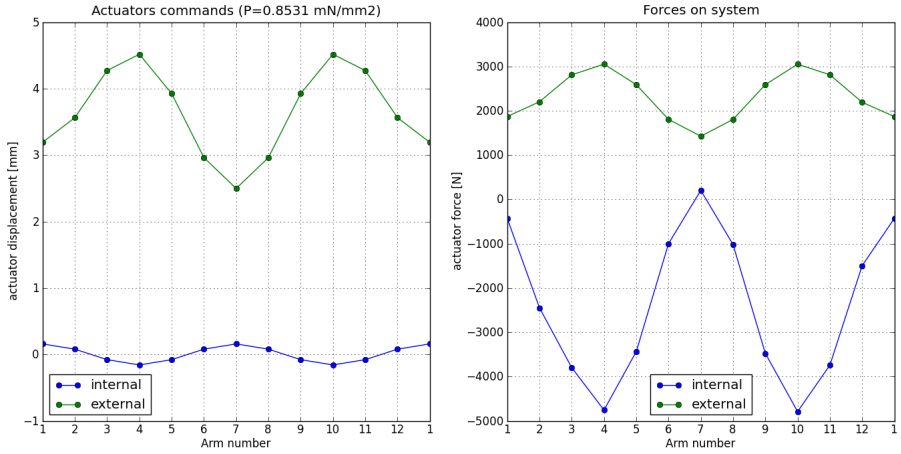

Figure 4.9 : *Commands injected to the actuators and resulting forces recovered on the FEA model.*

4.2.3 Error sources characterization

With Finite Element Analysis, we have characterized the system mechanical behavior in terms of nodes displacement, forces and stress for the generation of the nominal required shape. The model is also used to characterize the expected sources of error. The first studied contribution is the gravity effects, which must be considered throughout the manufacturing process. The deformation induced by the polishing itself is also studied. To finish, the gluing geometry is optimized considering both feasibility and residual deformation.

Gravity effects

The substrate is deformed by its own weight during the different manufacturing steps, the resulting deformation depends on its support conditions and on the segment shape (circular or hexagonal). It is essential to know the gravity contribution to the overall segment shape, notably for the radius of curvature measurement.
The gravity is modeled by the application of a uniform pressure on the entire system. The Zerodur mass density ρ is 2.53 g/cm^3. Considering the mirror as a cylinder of diameter D=1520 mm and thickness h=50 m, the pressure applied on the substrate is $P = mg = \rho(h\pi\frac{D^2}{4})g = 12.5\ g/cm^2$.

At the beginning of the process, the mirror is measured while being simply supported by a foam. It is then integrated on its warping harness for stress polishing. It is finally installed on a whiffle-tree, conceived to minimize the gravity effects on the hexagonal segment. The goal is here to compensate for the gravity effects during the stress polishing process.

- Substrate on the foam
The reference measurement of the substrate is carried out when it is simply supported by a polyethylene foam. We will see in Section 4.3.1 that this foam would also be used during polishing. Circular with the same diameter than the mirror, the foam is modeled as a deformable body with a low Young modulus. Its characteristics (Young modulus, mass density and thickness) are chosen in order to sufficiently filter the external environment effects while providing a sufficiently stable support for the measurements. From the Stress Mirror Polishing experience acquired throughout the ages at LAM, the requirements are a compression of 50 % under the blank own weight (12.5 g/cm^2) and the pressure polishing (20 g/cm^2), with a thickness around two third of the tested mirror. The foam characteristics are summarized in the Table 4.3.

Table 4.3 : *Characteristics of the cylindrical foam used for the mirror testing.*

Mass density	45 kg/m^3
Diameter	1520 mm
Thickness	30 mm
Young modulus	5 kPa
Poisson ratio	0.3

The optical surface deformation in this configuration is predicted with Finite Element Analysis. One of the foam faces is clamped and the mirror is placed on the other. The gravity load is applied on all the model elements and the displacements of the optical surface nodes are recovered. The substrate is deformed of 114 nm rms on the circular pupil, mainly in a focus mode (Figure 4.10). This deformation induces a 10 mm radius of curvature variation. For a nominal value of 86.5 m, this variation can be neglected.

- Substrate glued on the warping harness
Once the mirror tested on the foam, it is integrated on the warping harness and the gravity will act on the integrated system. For this modeling, the 24 nodes corresponding to the actuators are clamped and the gravity load is applied to the overall model. The induced deformation, shown in Figure 4.10, is axisymmetric, with an amplitude of 3.6 μm rms on the circular pupil (3.2 μm rms on the hexagonal pupil).
Combining the pressure and focus modes presented in Section 4.2.2, this deformation can be compensated. By applying a -24.6 μm to the external actuators and a 12.7 g/cm^2 pressure on the mirror

back face, the deformation due to gravity is limited to 0.4 nm rms on the hexagonal pupil (Figure 4.11). Moreover, this compensation allows the system to return to a non stress state.

- *Substrate on its whiffletree*

An active supporting system has been developed by Castro and Hernandez [2008] to minimize the final hexagonal segment deformation under gravity. As it provides an efficient support, it is envisaged to test the circular mirror shape on this whiffletree. The mirror deformation under its own weight must then be characterized on this system.
The whiffletree is modeled with a spring assembly: 3 groups of 12 springs having a fixed point (Figure 4.12), and, as before, a pressure representing the gravity load is applied on the FEA model. In the hexagonal mirror case, we verify that the gravity induces a minimal deformation, 48 nm rms amplitude. The deformation is more significant for the circular mirror: 208 nm rms amplitude, mainly composed of focus, spherical and hexafoil (Figure 4.10). This differential shape, coming from the supporting conditions, will need to be taken into account while testing the circular mirror on the whiffle-tree.

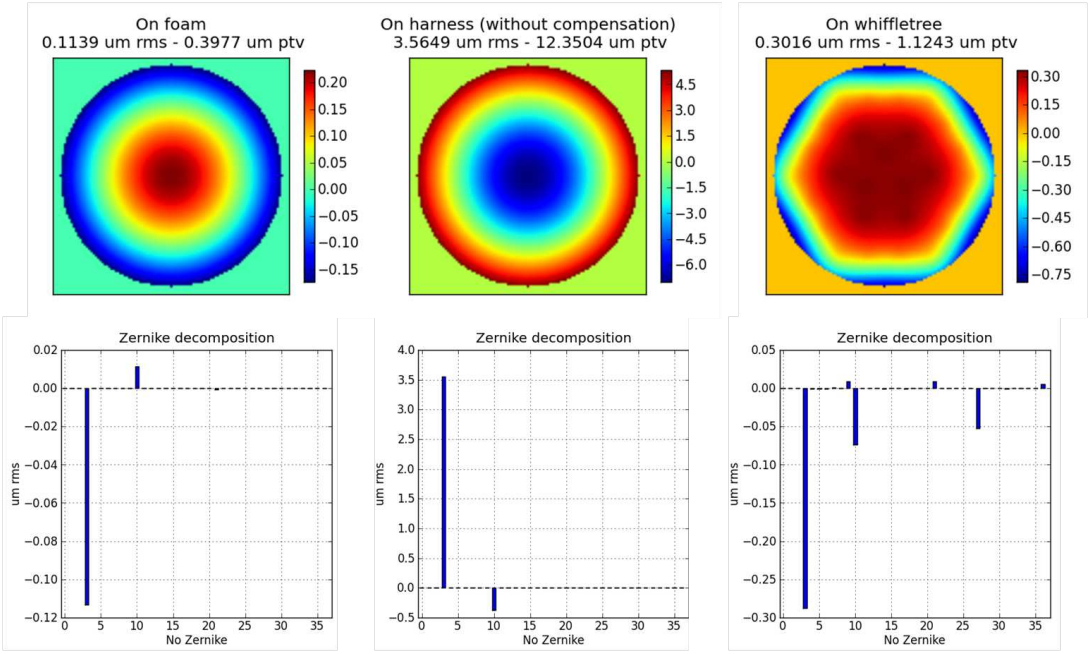

Figure 4.10 : *Optical surface deformation induced by the gravity load for the different steps of the segment manufacturing: deformation maps and Zernike decomposition (FEA results - Unit:[µm]).*

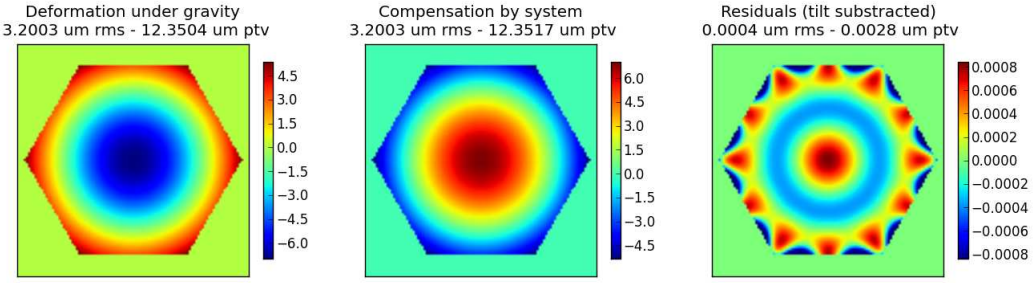

Figure 4.11 : *Gravity effects compensation with the warping harness: performance (FEA results - Unit:[µm]).*

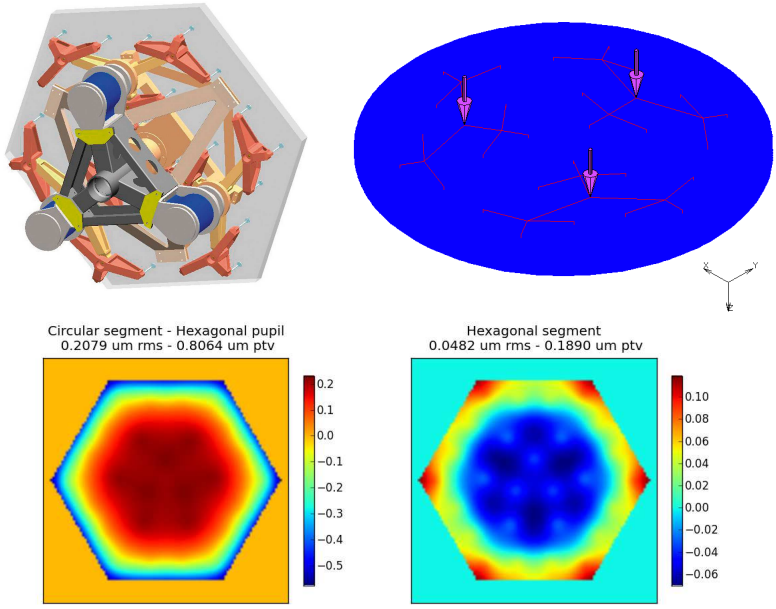

Figure 4.12 : *Mechanical design of the whiffle-tree supporting the segments (credit ESO) - Finite Element Model of the circular blank supported by the whiffle-tree - Comparison of the circular and hexagonal segments deformations on this system (Unit:[µm]).*

Polishing effects

The mirror will be polished with a large tool having the same radius of curvature than the mirror and a diameter 10 % smaller. During the polishing, the mirror rotates and the polishing tool has a translation motion, with a maximum decentering of 1/7th of the substrate diameter. The resulting motion of the polishing tool regarding the mirror is then sinusoidal. The polishing tool applies a pressure of 20 g/cm^2 on the mirror. For FEA, the polishing is modeled with a pressure field, moving on the mirror surface.
The deformation induced by the polishing pressure varies with the tool position. The systematic resulting deformation is deduced by integrating the different deformations in time. 25 tool positions are studied with FEA: a 20 g/cm^2, 1368 mm diameter pressure field is applied on the model, with the 24 actuation points fixed (Figure 4.13). The resulting deformation is recovered for each position (Figure 4.13) and the average of the 25 deformation maps gives the shape error induced by the polishing. It is an axisymmetric deformation, composed of focus and spherical aberrations, with an amplitude of 6 μm rms on the circular pupil (Figure 4.14).

As the warping harness is conceived to generate focus, it is possible to correct this shape error. To achieve this compensation, the back face pressure is used. The pressure value minimizing the polishing effect evolves with the position of the tool, it varies between 18.24 and 30.58 g/cm^2. It does not seem feasible to make the pressure vary during the polishing, an optimal constant pressure, minimizing the systematic deformation, must be applied. The average of the pressure values computed for each position is 22.60 g/cm^2, also corresponding to the value deduced from the deformation map projection on the pressure mode. This load case application gives a systematic deformation of 18 nm rms, mainly composed of spherical harmonics (Figure 4.14).

In conclusion, the back-face pressure can be efficiently used to compensate for both gravity and polishing effects.

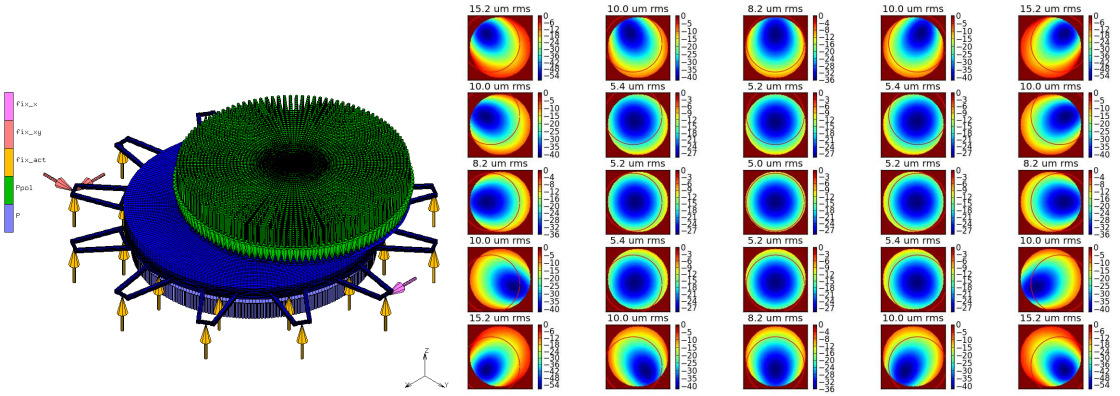

Figure 4.13 : *Left: Boundary Conditions on the Finite Element Model for the polishing simulation: the polishing tool applies a 20 g/cm^2 pressure on 90% of the optical surface - Right: Optical surface deformation for 25 polishing tool positions (Unit:[µm]).*

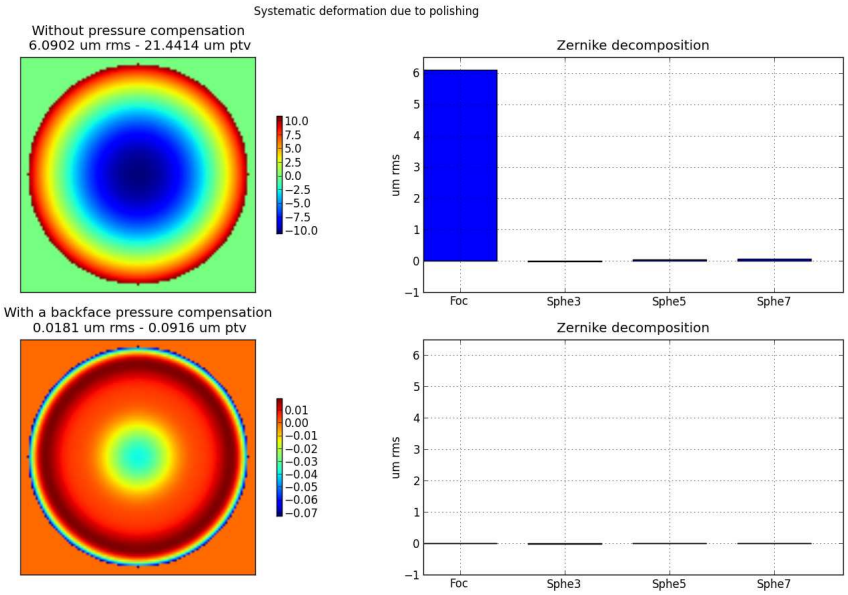

Figure 4.14 : *Systematic deformation due to polishing without back face pressure (top) and with a compensation of 22.6 g/cm^2 on the mirror back face (bottom): deformation maps and Zernike decomposition (FEA results - Unit:[µm]).*

Gluing effects

There are several complex issues related to gluing: the glue must ensure the continuity between mirror and harness in order to avoid the generation of residual deformation but the system must also be unglued easily. The goal here is to define an optimized glue geometry which does not modify the system performance regarding both shape generation precision and actuators commands. Thus the system characterization, performed in the previous section, will not be changed.
The required deformation decomposition on the influence functions allows certain tolerances for the system set up. As the system is able to compensate for its own weight, it can also compensate for other defaults, such as gluing inhomogeneity, in the limit of the actuators stroke and system symmetry.

- Thickness and parallelism

The optimal glue thickness is 150 μm. An inhomogeneity in the thickness is equivalent to a parallelism error between the ring and the mirror back face. To simulate this effect, a prismatic layer of glue is modeled. The glue thickness can reasonably be monitored at ± 30 μm, corresponding to an angle of 0.003° for the mirror diameter. This 20% thickness error tolerancing induces a shape error of 0.1 nm rms, which is negligible.

- Geometry

The ungluing is performed with a formic acid chemical attack. In order to maximize the accessible surface of glue, a geometry with discrete pads is adopted. It will also facilitate the control of the thickness, improving the parallelism between mirror and ring.
The Finite Element Model allows the characterization of the glue geometry contribution on the deformation. The ideal case is a uniform band, used in the previous models, the objective is to define a geometry getting close to this case. In order to keep a good homogeneity, two rings of 25 mm diameter pads are applied in staggered rows: one on the internal edge of the harness and the other on the external edge (see Figure 4.15). The optimal number of pads is determined by searching the configuration giving the same performance than with the uniform band. With 2 rings of 48 pads, the residual deformation has an amplitude of 21.1 nm rms, to be compared with the previous 20.2 nm rms. This difference being negligible, this gluing strategy is adopted.

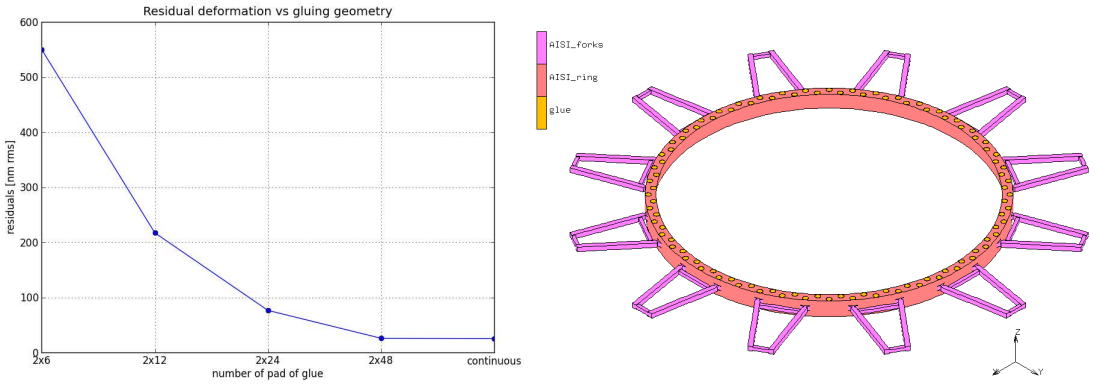

Figure 4.15 : *Residual deformation evolution in function of the gluing geometry and chosen gluing model.*

4.2.4 Overall system performance and specifications

Residual deformation

The different contributions to the system final performance have been evaluated in the previous paragraphs. The final commands correspond then to the sum of the commands computed to generate the required shape and to compensate for gravity and polishing loads. In the same manner, the residual deformation is the sum of the residual deformation obtained in the three cases, it will then be 23.4 nm rms on the hexagonal pupil. The total residual deformation shown in the top of Figure 4.16 corresponds to the residuals just after polishing, before the stress relaxation.

Ion Beam Figuring simulation

At the very end of the SMP process, the stress is relaxed and the residual map is the opposite.
The final pass of Ion Beam Figuring can be simulated by applying a Gaussian filtering on the residual deformation map [Shanbhag et al., 2000]. The canal width used to send the ions on the optical surface gives the Full Width at Half Maximum of the Gaussian, a FWHM of 50 mm is used here. The stress polishing does not induce high spatial frequency errors, so almost all the residuals can be removed with this last step: after the IBF simulation, the final error shape if 3 nm rms (Figure 4.16).

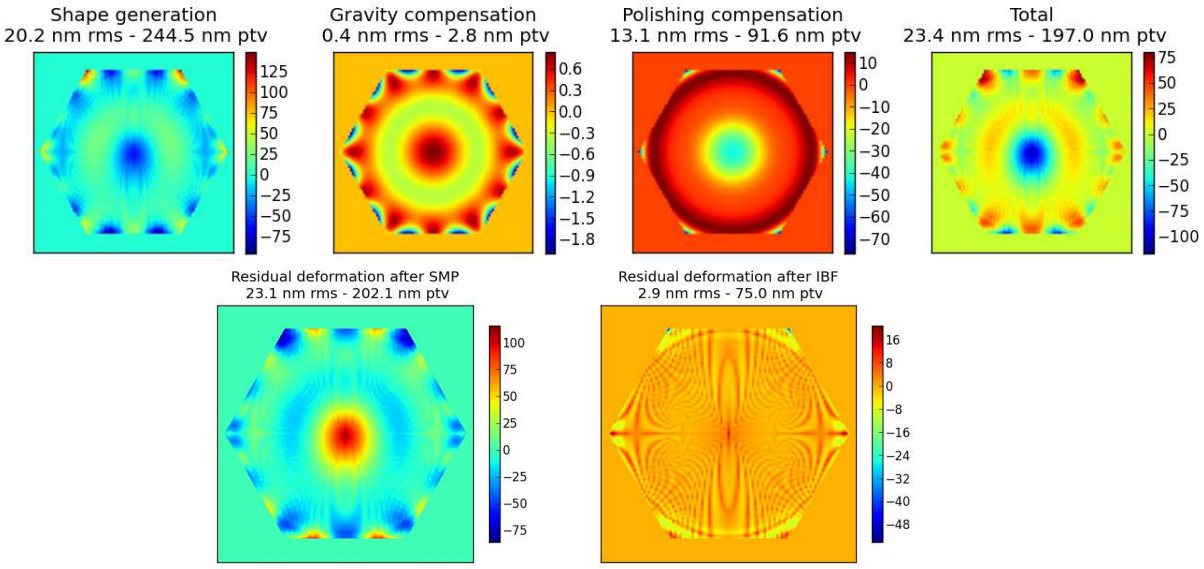

Figure 4.16 : *Final residual deformation obtained just after polishing (top), after stress relaxation and IBF (bottom) (Unit:[nm]).*

Actuators specifications

The performed Finite Element Analysis not only allow the prediction of the system performance but also the definition of the specifications definition for the prototype hardware. The required actuator stroke is directly deduced from the actuator commands (Table 4.4) and the actuator precision must also be studied in order to evaluate its impact on the system performance.

-Actuators displacement

The maximum stroke for the 24 actuators is around 5 mm. As for the MADRAS system (Chapter 2, Section 2.4.1), a statistical study is performed to determine the required displacement precision. For this study we need to recover the 25 system influence functions. A random displacement value, between $-p$ and $+p$ (p being the considered precision), is added to the nominal actuator command. The resulting deformation is then reconstructed with the deteriorated coefficients, and the impact on the shape generation precision can be deduced. To have a representative idea of this impact, a statistical analysis is performed on 1000 random draws. This study is done for several precision values, giving the evolution of the expected performance with the actuators' precision (Figure 4.17).

A precision of 0.5 μm for the displacement actuators is a good trade-off between feasibility and shape generation precision. With this condition, the mean residual deformation has an amplitude of 20.6 nm rms, with a standard deviation of 0.3 nm rms. This amplitude is compared to the 20.2 nm rms obtained with the "perfect" model: an actuator precision of 0.5 μm induces a shape error of $\sqrt{20.6^2 - 20.2^2} = 4$ nm rms.

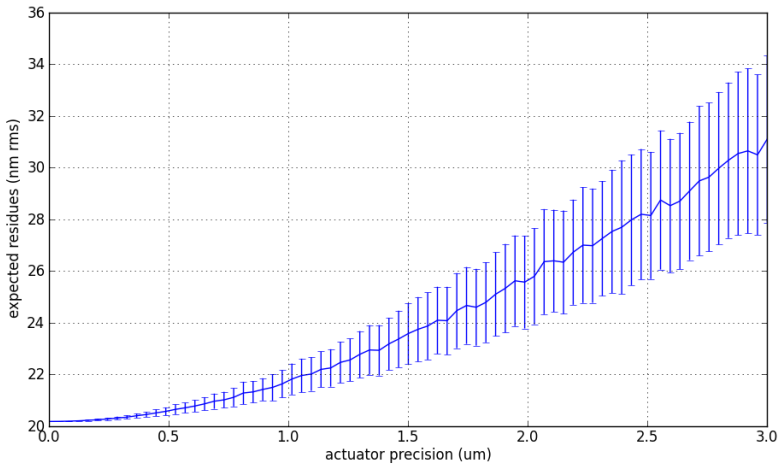

Figure 4.17 : *Shape generation precision as a function of actuators' displacement precision.*

-Pressure actuator

The required pressure on the substrate back face is 43.8 g/cm^2. The required precision on this value is determined in order to have a total residual deformation lower than 25 nm rms. With the nominal commands, the residual deformation is 23.4 nm rms. Adding the error due to the displacement actuators precision of 0.5 μm, this residual error is $\sqrt{23.4^2 + 4^2} = 23.7$ nm rms. The precision on the pressure must then induce an error inferior to $\sqrt{25^2 - 23.7^2} = 7.9$ nm rms.

As a pressure of $1 mN/mm^2$ induces a deformation of 2.4 μm rms, the precision is directly deduced: the pressure must be applied at $\pm 0.0033\ mN/mm^2$, corresponding to $\pm 33\ mg/cm^2$.

On the prototype, the pressure is applied by pushing up a 1420 m diameter plate under the blank. The required pressure is then applied with a force on the plate, equal to $F = PS = 6936.5$ N, with a precision of 7.4 N. The plate is moved by three actuators, each of them applying a force of $F/3 = 2312.2$ N with a precision of 1.7 N.

Table 4.4 : *Overall system performance - The target precision on the final optical shape is 1 µm.*

	Shape generation	Gravity compensation	Polishing compensation	Total
Residual deformation (nm rms)	20.2	0.4	13.1	23.4
Internal actuators displacement (mm)	-0.158 +0.158	-	-	-0.158 +0.158
External actuators displacement (mm)	2.497 4.516	-0.025	-	2.472 4.491
Back face pressure (mN/mm^2)	0.85	1.27	2.26	4.38
Internal actuators force (N)	-4790 202	137	-	-4653 339
External actuators force (N)	1424 3052	-	-	1424 3052
Maximum stress in the mirror (MPa)	4.3	-	-	4.3

4.3 Experimental testing

Once the system defined and characterized with Finite Element Analysis, the hardware definition and detailed conception phase has been initiated. The system has finally been manufactured and integrated, it is currently under testing.

4.3.1 Prototype

The integrated system is composed of several parts that are described below.

- Polishing machine

LAM is equipped with a 2.5 m polishing machine, able to use either computer control polishing techniques or classical polishing with full sized tool. It has been adapted for Stress Mirror Polishing. This facility, named POLARIS (POLishing Active and Robotic Integrated System) is dedicated to Research & Development programs. It is installed under a testing tower in order to directly control the optical quality of manufactured pieces during polishing, allowing a gain in terms operation-count.

- Substrate

For our study, the substrate has been spherically polished beforehand. This way, it is possible to measure the optical surface deformation with an interferometer at different moments of the process.

- Warping harness and displacement actuators

As defined in Section 4.2.1, the warping harness is composed of a ring and 12 forks.
The actuators are mechanical screws with a thread of 0.5 μm, corresponding to the precision defined in the previous section. The graduations allow the application of a displacement while a force sensor, integrated on each screw gives the system response.

- Foam and pressure actuator

The mirror is glued on the ring and its back face is also supported by a polyethylene foam, placed on a plate.

The pressure is applied by pushing up the 1420 mm diameter plate supporting the foam. with 3 micrometric differential screws, also equipped with force sensors. These screws are positioned at 120° on a diameter of 990 mm. Due to this actuation, the plate is slightly deformed in three points but this deformation is absorbed by the foam, it is then negligible.

- Position sensors

In order to have a direct mechanical measurement of the substrate deformation, Linear Variable Differential Transformer (LVDT) are used: these position sensors are directly in contact with the blank back face. The system having 25 degrees of freedom, it has 25 eigen modes (Figure 4.19), 25 sensors are then required to determine the induced deformation. The sensors are uniformly distributed under the surface in order to have an optimal sampling: a sensor at center, a ring of 12 sensors on the diameter defining the optical pupil and another ring of 12 sensors on the semi diameter.

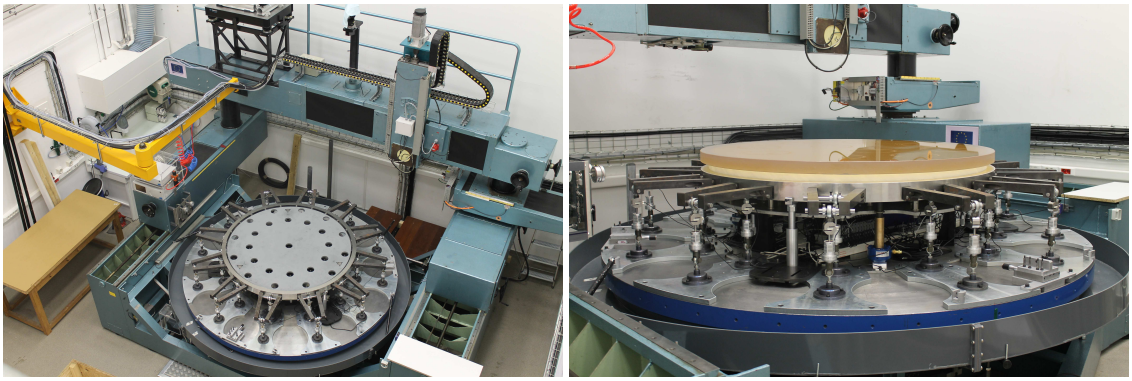

Figure 4.18 : *Left: Warping harness installed on the polishing machine - Right: Side view of the integrated system.*

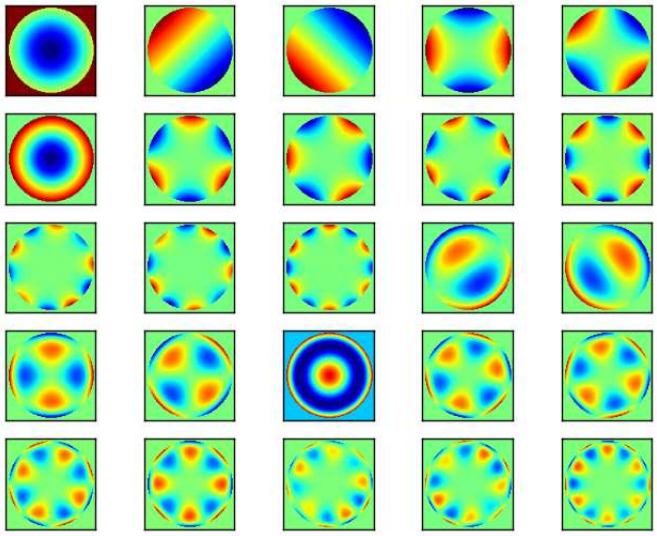

Figure 4.19 : *System Eigen Modes*

4.3.2 Testing means

An optical set up has been mounted to measure the mirror optical surface with interferometry. Moreover, a whole set of mechanical sensors and gauges allows a complete system characterization, in both optical and mechanical aspects. The different tests will validate the performance measurement and will spot out the best control mean for an eventual industrialization.

A specific design, with a compact optical train, has been developed using a large folding sphere, of 1.5 m diameter, placed at 9 m above the segment. This configuration allows reducing the length of the test setup from 84 m (mirror radius of curvature) down to 19 m. As the main objective of the study is to demonstrate the optical quality of the warping, working in a differential configuration is sufficient: a calibration of the test setup is necessary to fix the reference. Even if theoretically the aberrations of the optical path will not limit the system performance, the aberration of the setup are compensated with optical correctors placed close to the focus, in order to work close to a zero aberration mode. The illuminating mirror has a focal plane at 6 m, where a flat folding mirror send the beam to a Fizeau interferometer. Three testing configurations are defined, with three different correcting optics, creating flat reference surfaces:

- Testing of the spherical mirror with a correcting group compensating for the spherical aberration introduced by the illuminating mirror.
- Testing of the warped mirror with a correcting group mainly compensating for the generated astigmatism and focus.
- Testing of the polished mirror which corresponds to the inverse of the previous configuration.

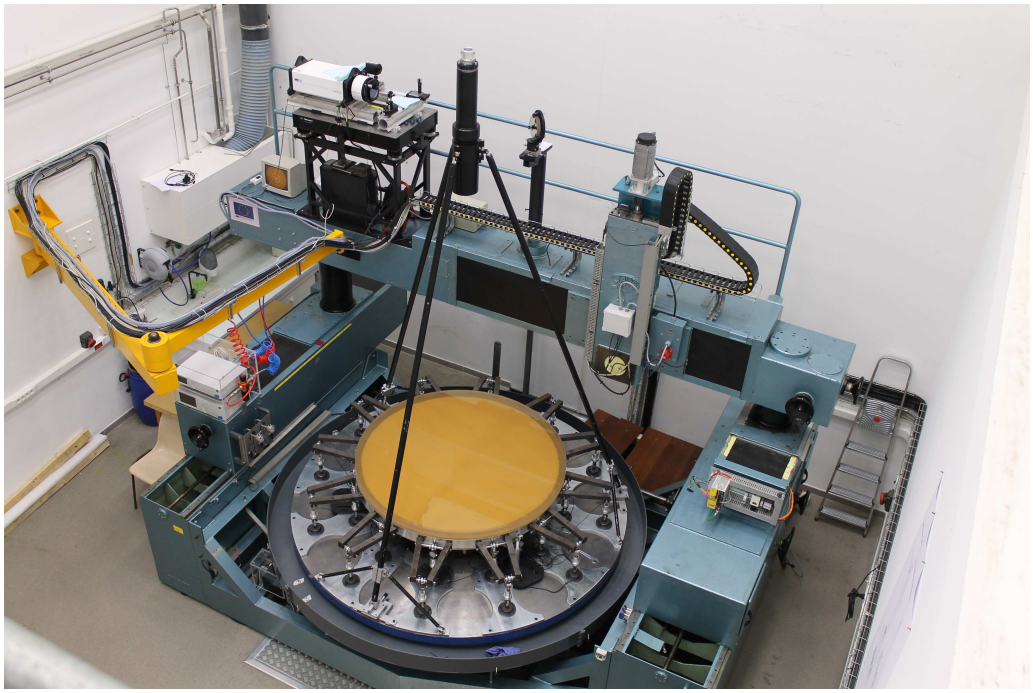

Figure 4.20 : *Mirror on its warping harness and optical test set-up*

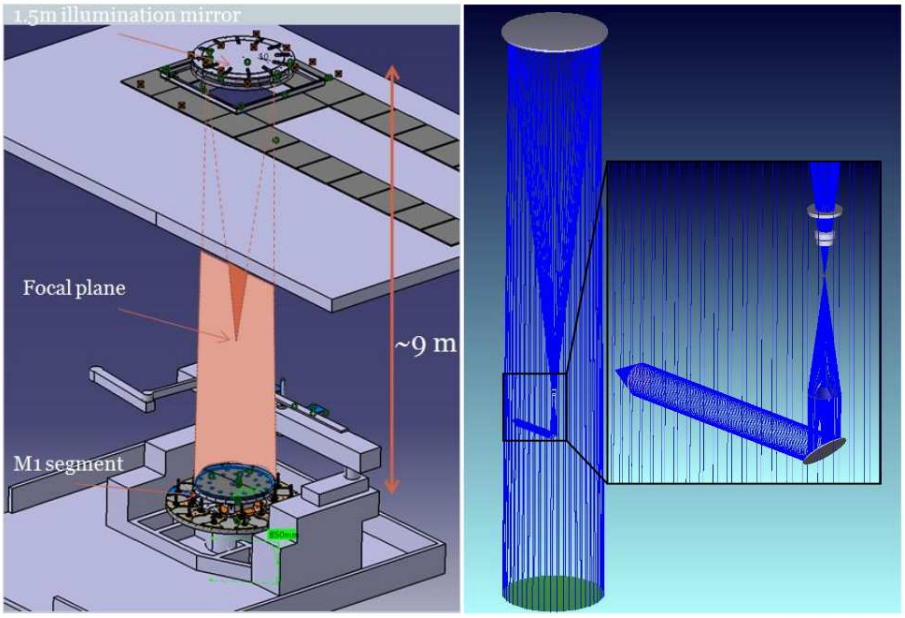

Figure 4.21 : *Implementation and optical design of the segment test bed.*

4.4 Conclusion

The possibility to manufacture the segments of the E-ELT with stress polishing is currently being demonstrated. The conceived warping harness would allow the manufacturing of all segments types with the same equipment. The gain of time compared to small tool polishing techniques will not only be achieved thanks to the unique polishing configuration, but also to the definition of an efficient method to converge quickly to the final shape. Furthermore, the absence of high spatial frequency errors will decrease the necessary IBF time.

24 mechanical actuators around the mirror plus the application of a uniform pressure on the back face are necessary to achieve the deformation. Finite Element Analysis have shown the possibility to generate the outermost off-axis segment with a residual deformation of 25 nm rms, for a goal at 1 μm rms. This value includes the errors due to the warping, but also to the gravity compensation, the polishing and the actuators precision. The hardware has been conceived to recover for the best the FEA results. A dedicated test set-up is now ready, it will characterize the system both optically and mechanically, in order to demonstrate the stress polishing technique but also to determine the best metrology for an industrial use.

Once the process has been fully demonstrated and characterized, the mass production of the E-ELT segments could be envisaged. Thanks to strong collaborations with industrial partners, the technological knowledge could be easily transferred. The TMT consortium has already selected this technology as the baseline for the mass production of the telescope segments, proving the strong gain offered by the stress mirror polishing process.

Bibliography

3M Schotch-Weld. DP460 Technical Data. Technical report, 3M Schotch-Weld, 1997.

T. Arnold, G. Böhm, R. Fechner, J. Meister, and A. Nickel et al. Ultra-precision surface finishing by ion beam and plasma jet techniques - status and outlook. *Nuclear Instruments and Methods in Physics Research A*, 616:147–156, May 2010.

J. H. Burge, B. Anderson, S. Benjamin, M. K. Cho, K. Z. Smith, and M. J. Valente. Development of optimal grinding and polishing tools for aspheric surfaces. volume 4451 of *Society of Photo-Optical Instrumentation Engineers (SPIE) Conference Series*, pages 153–164, December 2001.

J. Castro and E. Hernandez. Analysis of the surface error requirement for the primary mirror segments of the E-ELT. Technical report, Compania Espanola de Sistemas Aeronauticos, 2008.

M. Cayrel. M1 geometrical properties and construction parameters for the 39-M EELT. Technical report, ESO, 2011.

B. Delabre. Optical design for an adaptive anastigmatic five-mirror extremely large telescope. *Astronomy and Astrophysics*, 487:389–397, August 2008.

P. Dierickx and M. Cayrel. Statement of Work for the Polishing, Integration and Final Figuring of the Segment Assemblies of the Primary Mirror of the 39-m EELT. Technical report, ESO, 2011.

ESO. E-ELT Construction Proposal. Technical report, ESO, 2011.

P. Hartmann, K. Nattermann, T. Döhring, R. Jedamzik, and M. Kuhr et al. ZERODUR glass ceramics for high stress applications. volume 7425 of *Society of Photo-Optical Instrumentation Engineers (SPIE) Conference Series*, August 2009.

M. Laslandes, N. Rousselet, M. Ferrari, E. Hugot, and J. Floriot et al. Stress polishing of E-ELT segment at LAM: full-scale demonstrator status. volume 8169 of *Society of Photo-Optical Instrumentation Engineers (SPIE) Conference Series*, September 2011.

G. Lemaitre. New procedure for making Schmidt corrector plates. *Applied Optics*, 11:1630–1636, 1972.

G. R. Lemaître. Active Optics: Vase or Meniscus Multimode Mirrors and Degenerated Monomode Configurations. *Meccanica*, 40:233–249, 2005.

J. W. Pepi. Test and theoretical comparisons for bending and springing of the Keck segmented 10 M telescope. *Optical Engineering*, 29:1366–1372, November 1990.

P. M. Shanbhag, M. R. Feinberg, G. Sandri, M. N. Horenstein, and T. G. Bifano. Ion-Beam Machining of Millimeter Scale Optics. *Applied Optics*, 39:599–611, February 2000.

Y. Zheng, X.-N. Li, W.-Y. Guo, Z.-C. Dong, B. Liang, and Z.-B. Jiang. Investigation of sub-aperture polish techniques for manufacturing astronomical mirror. volume 7739 of *Society of Photo-Optical Instrumentation Engineers (SPIE) Conference Series*, July 2010.

Chapter 5

Optimized active systems: 1 actuator - 1 mode

The systems developed in the previous chapters, for the MADRAS and E-ELT M1 projects have 24 actuators. For MADRAS, this number is necessary to generate the specified modes while ensuring a certain redundancy. For the E-ELT M1 segments, there are only three modes to generate, a 24 actuators design is used in order to optimize the deformation on the mirror periphery.

The correction need is generally limited to a few modes. An active system having as many eigen modes as actuators, it is possible to conceive deformable mirrors simplified to the extreme, with one actuator driving one optical mode. Starting with a correction need specific to an instrument (compensation of aberrations due to a variable optical path, compensation of thermo-elastic deformation, etc.), correction modes can be defined and an optimal system can be designed. The interest in minimizing the number of degrees of freedom is obvious: a system with few actuators is easy to set up and monitor, the required power supply is low and the few components limit the weight.

In this chapter we present two innovative deformable systems with an optimized number of actuators: one actuator per optical mode. In the first section, the warping principle is detailed. In the second section, the Variable Off-Axis paraboLA (VOALA) system is introduced: it is a 3-actuators deformable mirror generating the three main modes forming an off-axis parabola. In the third section, the Correcting Optimized Mirror with a Single Actuator (COMSA) system is introduced: it is a system allowing the correction of a given combination of optical aberrations with a single actuator. In the fourth section, some examples of applications for Infra-Red or visible instrumentation are presented.

The work presented in this chapter has led to the deposit of two patents and to the following publication (see Appendix C):
- M. Laslandes, E. Hugot, M. Ferrari, Active optics: deformable mirrors with a minimum number of actuators, Journal of the European Optical Society, 2012.

5.1 Adapting the influence functions to the correction requirements

As in the previous chapters, the active systems are conceived with the elasticity theory. The warping harness design is here defined in order to minimize the number of actuators, it is based on the deformation of a thin shell through the application of bending moments at its edges.
The inputs for the optimization are the correction requirements. The goal is then to match the system's influence functions with the optical modes to be corrected. In this framework, two concepts of deformable mirror have been developed and patented [Laslandes et al., 2011a,b].

5.1.1 System simplification: context

Ray tracing and Finite Element Analysis software are used to anticipate the correction needs in an instrument [Fischer et al., 2008]. The optical design gives the evolution of the aberrations according to the instrument configuration. The structure boundary conditions and environment variations give the thermo-mechanical deformation. The WFE appearing in an instrument can then be predicted in the early design phases, and a simple, dedicated correcting system can be developed. The use of such systems can be essential for some applications. As we have seen in the previous chapters, simplicity, weight, size and power consumption considerations take an important place in space systems designs. Moreover, an optimized and simple warping system for the mass production of large primary mirror segments could improve the process efficiency. To finish, the use of a simple deformable optical component in a multi-configuration instrument, with variable optical path would allow the apparition of innovative optical architecture using specific correcting functions.
For instance, we have seen in Chapter 1, Section 1.3.3 that the ESO/Very Large Telescope Interferometric mode is equipped with Variable Curvature Mirrors, allowing an efficient refocusing and pupil stabilization. This instrument is on-axis, the focus error to be compensated is due to the variable delay line position. In an off-axis interferometer, the same type of compensation will be required, but with additional aberrations: astigmatism and coma will also appear, making the correction modes more complex.

A Wave-Front Error can be defined as:

$$WFE(\rho, \theta, t) = \sum_k A_k(t)\phi_k(\rho, \theta). \tag{5.1}$$

with ϕ_k the optical modes and A_k their amplitudes, evolving over time. An optical mode is then defined as a linear combination of Zernike, c_{ij_0} being their initial amplitudes:

$$\phi_k(\rho, \theta) = \sum_{i,j} c_{ij_0} Z_{ij}(\rho, \theta). \tag{5.2}$$

Some works already present deformable mirrors with a limited number of actuators. For instance, Dainty et al. [1998] have developed a 9 channels bimorph deformable mirror, to generate focus, astigmatism, coma and spherical, and Freeman and Pearson [1982] present a 3-actuators deformable mirror able to generate focus and astigmatism. In these systems, the forces are directly applied on the optical surface, inducing an important print-through effect. The resulting high spatial frequency errors deteriorate the correction performance.

In the work presented here, the number of actuators is minimized by applying the forces far from the optical surface. In this manner, the number of actuators is uncoupled from the mirror diameter

and the generation of high spatial frequency errors is avoided. Moreover, it dissociates the actuator precision from the shape generation precision and it makes the deformable mirror independent of the actuator technology.
By coupling the elasticity equations and Finite Element Analysis, we detail hereafter an innovative and simple concept to warp mirrors [Laslandes et al., 2012].

5.1.2 System simplification: design

Both developed deformable systems are based on the modification of an optical surface curvature through the application of uniform bending moments at its edges, as described by Timoshenko and Woinowsky-Krieger [1959]. The warping principle is shown in Figure 5.1: the moments are generated on an intermediate plate with a central force and transmitted to the mirror edges via a flexible outer ring. The system is constituted of five main parts: three plates (mirror, intermediate plate and rigid reference plate) and two rings linking the plates together. The central actuator, applying a force or a displacement on the system, is located between the intermediate and reference plates.

The behavior of the intermediate plate is deduced from the equations describing a circular plate of semi-diameter a with clamped edges and a force F applied on its center. The deflection is then composed of a curvature term plus a logarithmic term, illustrating the direct action of the force on the plate:

$$z(r) = \frac{Fr^2}{8\pi D} log\frac{r}{a} + \frac{F}{16\pi D}(a^2 - r^2). \tag{5.3}$$

The moments induced at the edges of the plate are constant:

$$M_g = -\frac{F}{4\pi}. \tag{5.4}$$

These moments are transmitted at the edges of the mirror through the flexible ring. The induced mirror deformation z_{mirror} is deduced from the elasticity equation describing this load case (application of bending moments M_g at the edges of an axisymetric clamped plate):

$$D\frac{\partial^2 z_{mirror}}{\partial r^2} = -M_g, \tag{5.5}$$

with D the plate rigidity and the following boundary conditions:

$$z_{mirror}(r = a) = 0 \quad and \quad \frac{\partial z_{mirror}}{\partial r}(r = 0) = 0. \tag{5.6}$$

The resolution of this differential equation conducts to a focus mode:

$$z_{mirror}(r) = -\frac{M_g}{2D}(r^2 - a^2) = \frac{Fa^2}{8\pi D}(\rho^2 - 1). \tag{5.7}$$

So, the mirror curvature is achieved through the application of bending moments all around the plate. These moments are generated by a central force on an intermediate plate, allowing the respect of the Saint Venant principle: the action is applied far from the optical surface in order to generate a smooth deformation. We will see in the following sections how to adapt this principle to generate other aberrations.

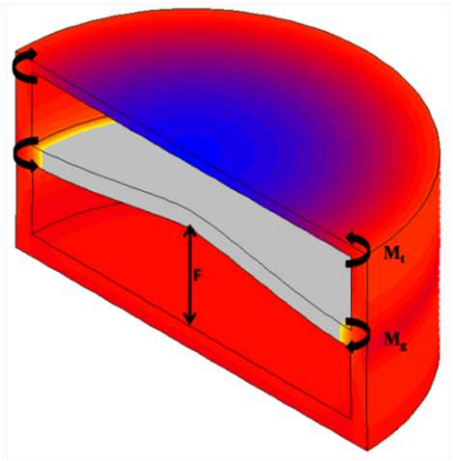

Figure 5.1 : *Section of the finite element model of a circular system generating Focus. The application of a force F on the intermediate plate induces bending moments M_g at the plate edges, which are transmitted to the mirror edges ($M_t = M_g$).*

5.1.3 System simplification: optimization method

Minimizing the number of actuators is only possible with a strong preliminary work to specify the correction requirements. Starting with an instrument design and operating environment, the WFE can be predicted and decomposed on optical modes, as described in Section 5.1.1. The problematic is then to adapt the warping method presented in Figure 5.1 in order to compensate for the expected WFE with a single actuator for each required optical mode.

The elasticity equations give the bending moments to be applied at the edges of the mirror to generate the required optical surface deformation $z(r, \theta)$:

$$M_t(r,\theta) = -\frac{Et^3}{12(1-\nu^2)}\left[\frac{\partial^2 z(r,\theta)}{\partial r^2} + \nu\left(\frac{1}{r}\frac{\partial z(r,\theta)}{\partial r} + \frac{1}{r^2}\frac{\partial^2 z(r,\theta)}{\partial \theta^2}\right)\right], \tag{5.8}$$

where t is the plate thickness, E its Young modulus and ν its Poisson ratio.

This defines the main system characteristics: the geometry is adapted in order to generate these required bending moments by actuating the intermediate plate. Then, this basic system geometry can be optimized with Finite Element Analysis. In a first time, the system is modeled as a monolithic piece. The back face of the reference plate is fixed and forces are applied on the intermediate plate to simulate the actuators. For prototyping it is planned to assemble 3 parts together: the central part will consist in the intermediate plate with the 2 rings, the mirror will be glued on the top ring and the reference plate will be glued or screwed on the bottom ring. As explained in Chapter 1, Section 1.3.2, the FEA optimization is performed considering both optical quality and the mechanical behavior of the system:

- the optimization output parameters are the system dimensions and the actuators characteristics,

- the optimization criteria are the shape generation precision, defined as the rms error of the deformation, but also the maximum level of stress in the material σ_{max}, and the required force F.

In order to use the deformable mirrors in optical systems for visible or infra-red observations, their optical precision is specified around $\lambda/20$. Thus, our goal is to design deformation systems

accurate to a few tens of nanometers.

5.2 "Variable Off-Axis paraboLA" system (VOALA)

5.2.1 Application domain

We have seen in Section 1.3.3 that an Off-Axis Parabola is characterized by its pupil semi-diameter a, radius of curvature k, conic constant C and off-axis distance R. The optical surface shape z_{mirror}, can then be deduced from these parameters. It is composed of a sphere plus terms corresponding to the first optical aberrations:

$$z_{mirror}(\rho, \theta, a, k, R, C) = \sum c_{ij}(a, k, R, C) Z_{ij}(\rho, \theta) \tag{5.9}$$

where c_{ij} are the optical modes amplitudes and Z_{ij} the Zernike polynomials, described in Table 5.1.

Table 5.1 : *Equations of Zernike coefficients and polynomials as a function of OAP characteristics (with the reduced parameter $\epsilon = R/k$).*

	c_{ij} (RMS) - first order approximation	Z_{ij}
Focus	$c_{20} = \frac{a^2}{2\sqrt{3}k} \frac{2-C\epsilon^2}{4(1-C\epsilon^2)^{3/2}}$	$Z_{20} = \sqrt{3}(2\rho^2 - 1)$
Astm3	$c_{22} = \frac{a^2}{\sqrt{6}k} \frac{C\epsilon^2}{4(1-C\epsilon^2)^{3/2}}$	$Z_{22} = \sqrt{6}\rho^2 cos(2\theta)$
Coma3	$c_{31} = \frac{a^3}{3\sqrt{8}k^2} \frac{C\epsilon[1-(C+1)\epsilon^2]^{1/2}(4-C\epsilon^2)}{8(1-C\epsilon^2)^3}$	$Z_{31} = \sqrt{8}(3\rho^2 - 2)\rho cos(\theta)$
Tref5	$c_{33} = \frac{a^3}{\sqrt{8}k^2} \frac{C^2\epsilon^3[1-(C+1)\epsilon^2]^{1/2}}{8(1-C\epsilon^2)^3}$	$Z_{33} = \sqrt{8}\rho^3 cos(3\theta)$
Sphe3	$c_{40} = \frac{a^4}{6\sqrt{5}k^3} \frac{8(C+1)-24K\epsilon^2+3C^2\epsilon^4(1-3C)-C^3\epsilon^6(2-C)}{64(1-C\epsilon^2)^{9/2}}$	$Z_{40} = \sqrt{5}(6\rho^4 - 6\rho^2 + 1)$
Astm5	$c_{42} = \frac{a^4}{4\sqrt{10}k^3} \frac{-C\epsilon^2(1+5C-C\epsilon^2(6+5C)}{16(1-C\epsilon^2)^{7/2}}$	$Z_{42} = \sqrt{10}(4\rho^2 - 3)\rho^2 cos(2\theta)$

Starting with the equations giving the amplitudes of each Zernike polynomials as a function of the OAP characteristics, a domain where the first three aberrations are predominant compare to the others can be defined: Trefoil5, Spherical3 and Astigmatism5 are negligible when their amplitude is lower than a given threshold a_{th} which depends on the considered application. It gives conditions on quadruplets (a,k,C,R):

$$\begin{cases} c_{33} < a_{th} \Rightarrow a < \left[a_{th}\sqrt{8}k^2 \frac{8(1-C\epsilon^2)^3}{C^2\epsilon^3[1-(C+1)\epsilon^2]^{1/2}}\right]^{1/3} \\ c_{40} < a_{th} \Rightarrow a < \left[a_{th}6\sqrt{5}k^3 \frac{64(1-C\epsilon^2)^{9/2}}{8(C+1)-24C\epsilon^2+3C^2\epsilon^4(1-3C)-C^3\epsilon^6(2-C)}\right]^{1/4} \\ c_{42} < a_{th} \Rightarrow a < \left[a_{th}4\sqrt{10}k^3 \frac{16(1-C\epsilon^2)^{7/2}}{-C\epsilon^2(1+5C-C\epsilon^2(6+5C)}\right]^{1/4}. \end{cases} \tag{5.10}$$

The Variable Off-Axis paraboLA concept is a 3-actuators deformation device designed to generate any combinations of Focus, Astigmatism3 and Coma3, in the limit of actuators stroke and system's mechanical strength. Thus, for a given maximum amplitude of residual aberrations, the set of OAPs achievable with the VOALA system can be defined.

5.2.2 Focus and Coma generation

As explained in Section 5.1.2, a circular plate can be deformed in a focus mode by applying constant uniform bending moment at its edges. These moments are generated on the intermediate

plate with a central force (see Figure 5.1).

On the same principle, the moment distribution to apply at the mirror edges to generate a coma mode can be calculated. The required coma deformation is described by the following formula:

$$z_{mirror}(r,\theta) = \left[\left(\frac{r}{a}\right)^2 - 1\right]\frac{r}{a}cos(\theta). \tag{5.11}$$

Injecting it in Equation 5.8, we obtained the expression of bending moments at the mirror edges:

$$M(r=a,\theta) = \frac{-2D}{a^2}(3+\nu)cos(\theta). \tag{5.12}$$

Thus, the application of an azimuthal moment distribution at the mirror edges induces a coma mode on the optical surface.
Timoshenko and Woinowsky-Krieger [1959] described the deformation z of a circular plate clamped at its edge under the application of a central mechanical moment:

$$z(\rho,\theta) = \left(A\rho + B\rho^3 + D\rho log\rho\right)cos(\theta), \tag{5.13}$$

with A, B and D three constants depending on the amplitude of the applied moment and on the plate material and dimensions.
Injecting this deformation in Equation 5.8, we deduced that this load case generate the required moment distribution at the plate edges. So a coma mode can be obtained on the mirror by applying a central moment on the intermediate plate. To generate this central moment, a central pad is added on the intermediate plate and a transverse force is applied on this pad (see Figure 5.2).

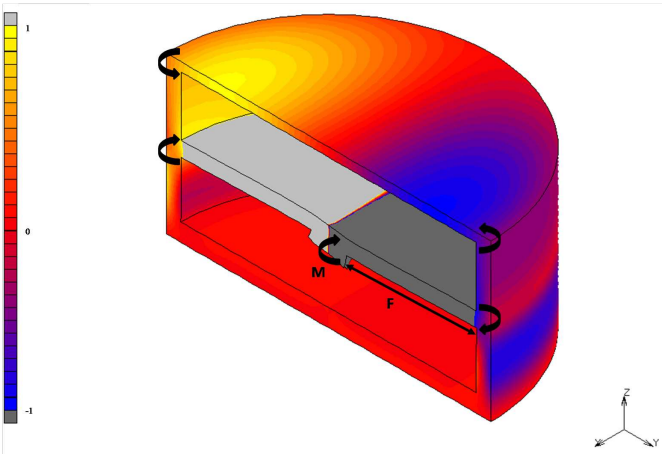

Figure 5.2 : *Section of the finite element model of a circular system generating Coma. A transverse force F is applied on the central pad, inducing a central moment M on the intermediate plate.*

Combining the actions of 2 actuators located on a diameter of the central pad, both focus and coma modes can be generated (see Figure 5.3):

- the application of two equal forces corresponds to a central force application and induces a focus mode,
- the application of two opposite forces corresponds to a central moment application and induces a coma mode,
- other forces configurations induce a combination of focus and coma.

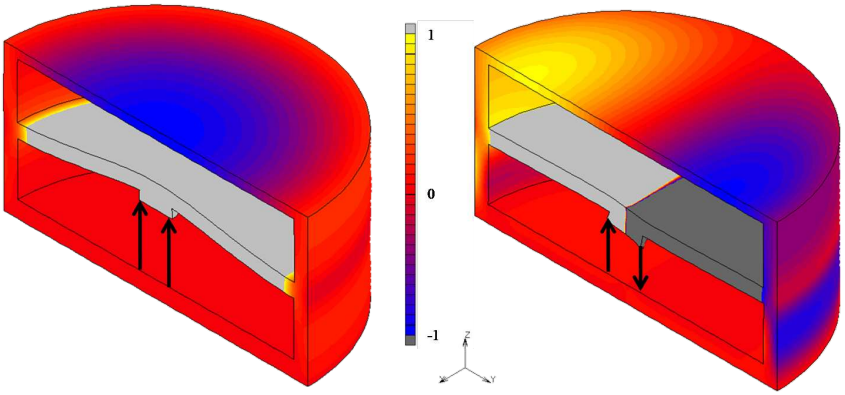

Figure 5.3 : *Finite element model of the 2-actuators system presenting the deformations obtained with the load cases corresponding to Focus and Coma generations.*

5.2.3 Astigmatism generation

The required astigmatism deformation is:

$$z_{mirror}(r,\theta) = \left(\frac{r}{a}\right)^2 cos^2(\theta). \tag{5.14}$$

By injecting it in Equation 5.8, the required bending moment modulation is deduced:

$$M(r=a,\theta) = \frac{-2D}{a^2}(1+3\nu)cos(2\theta). \tag{5.15}$$

Thus, the application of a $cos(2\theta)$ modulation at the edges of the system induces an astigmatism mode on the optical surface.
The principle of astigmatism generation with one actuator, developed by Hugot et al. [2008], can be added to the previous system. The required modulation can be generated by applying two pairs of opposite forces on two orthogonal diameters of the intermediate plate. On the finite element model, we study the evolution of the deformation versus this diameter. The optimum diameter will then be the one minimizing the residual deformation. The four forces can be generated from a single point, located between two rigid orthogonal beams. Each beam is linked to two points of the diameter. Applying a central force pushing away the two beams, the required forces are transmitted to the four points.
Figure 5.4 presents the FEA model for this astigmatism generation. We can note that the two-beams system can conveniently be installed on either side of the intermediate plate, depending on the available space.

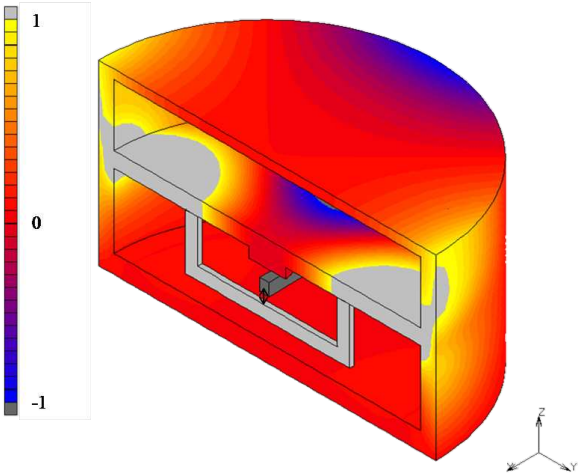

Figure 5.4 : *Section of a finite element model presenting the principle of Astigmatism generation with VOALA.*

5.2.4 Modes combination and alternative design

The 3-actuators system described above is able to compensate for combinations of focus, astigmatism and coma. One actuator directly drives the astigmatism generation while focus and coma are generated with a combination of the two other actuators. With this system, coma and astigmatism are oriented.
Astigmatisms in both x and y directions could be generated with an additional beams system, turned of $\pi/4$ in comparison to the first one. It is also possible to integrate the deformable mirror on a rotating platform, driven by one actuator, the system rotation will then allow the generation of an astigmatism with any orientation.
An interesting alternative appears with the generation of the two coma modes: with 4 actuators, located on two orthogonal diameters of the pad, focus, coma x, coma y and astigmatism x can be created. Figure 5.5 presents the different load cases for the generation of each mode. As explained just above, a fifth actuator rotating the system would provide the last astigmatism. This improvement leads to a 5 actuators/5 modes deformable mirror.

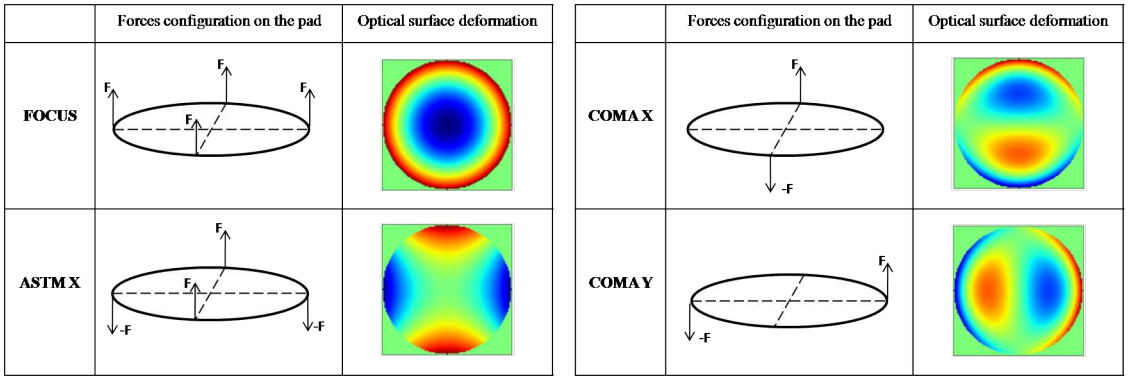

Figure 5.5 : *Alternative VOALA design: generation of 4 Zernike polynomials with 4 actuators on the pad. A fifth actuator allowing a system rotation can be added in order to generate the second astigmatism mode.*

5.3 "Correcting Optimized Mirror with a Single Actuator" system (COMSA)

5.3.1 Application domain

In some instruments, the wave-front error is a combination of optical aberrations, evolving linearly over time. There is then a single optical mode to correct:

$$WFE(t) = A(t) \sum \alpha_{ij} Z_{ij}. \tag{5.16}$$

It is possible to adapt the single actuator concept presented in Figure 5.1 to generate a combination of focus plus other optical aberrations. As before, the design method consists in modifying the system geometry to match the actuator influence function with correction requirements. The three parameters to be optimized are the system contour, the intermediate plate thickness distribution and the actuator location.

5.3.2 Contour adaptation

To add other modes to the focus generation, the axisymmetry of the system must be broken. The bending moments at the mirror edges can be modulated by modifying the system contour: the radius of curvature will then vary both angularly and radially.

The contour ρ_c, is defined as a function of the required deformation on the circular pupil z_{mirror}. It is also defined by the system boundary conditions: the mirror has clamped edges. So, the required deformation is extended until it crosses the $z = 0$ plane and the system contour is defined as the intersection between this plane and the deformation surface. This contour is expressed as a function of the angular coordinate θ, and the modes amplitudes α_{ij}, as described in Equation 5.17:

$$z_{mirror}(\rho_c, \theta) = \sum \alpha_{ij} Z_{ij}(\rho_c, \theta) = 0 \qquad => \qquad \rho_c = f(\theta, \alpha_{ij}). \tag{5.17}$$

Example: Focus and Astigmatism

If the WFE to be corrected is a combination of focus and astigmatism, the required mirror shape is:

$$z_{mirror}(\rho, \theta) = \alpha_{20}(2\rho^2 - 1) + \alpha_{22}\rho^2 cos(2\theta), \tag{5.18}$$

with α_{20} and α_{22} the modes' amplitudes.
The contour ρ_c is then an ellipse whose axes ratio is linked to the amplitudes ratio $\gamma = \alpha_{22}/\alpha_{20}$:

$$z_{mirror}(\rho_c, \theta) = 0 \qquad => \qquad \rho_c(\theta) = \sqrt{\frac{1}{2 + \gamma cos(2\theta)}}. \tag{5.19}$$

Due to the square root, the equation has no solution for some amplitude ratio. The contour is then defined for a given domain of focus and astigmatism combination. The condition on the amplitudes is:

$$2 + \gamma cos(2\theta) > 0 \quad \forall\theta \qquad => \qquad |\frac{\alpha_{22}}{\alpha_{20}}| < 2. \tag{5.20}$$

Figure 5.6 shows the contour evolution with the amplitudes ratio γ. The extreme case $\gamma = 2$ corresponds to a cylindrical mode, and the moments are transmitted only through two plates (see Figure 5.6).

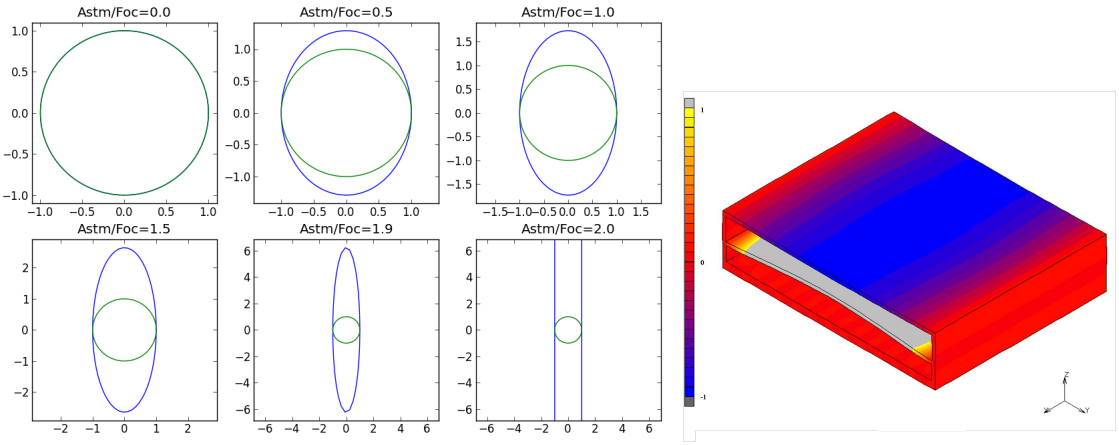

Figure 5.6 : *Left: Contours for different combinations of focus and astigmatism (circular pupil in blue) - Right: Finite element model of the rectangular system for* $\gamma = 2$.

Example: other modes combinations

The calculation achieved just above can be done for any combinations of focus and other modes. The conditions on the different amplitudes ratios will give the domain where the COMSA system can be used. Figure 5.7 presents examples of contour computed to generate some combination of aberrations.
We can note that, even if the contour is complex, the optical pupil is always circular.

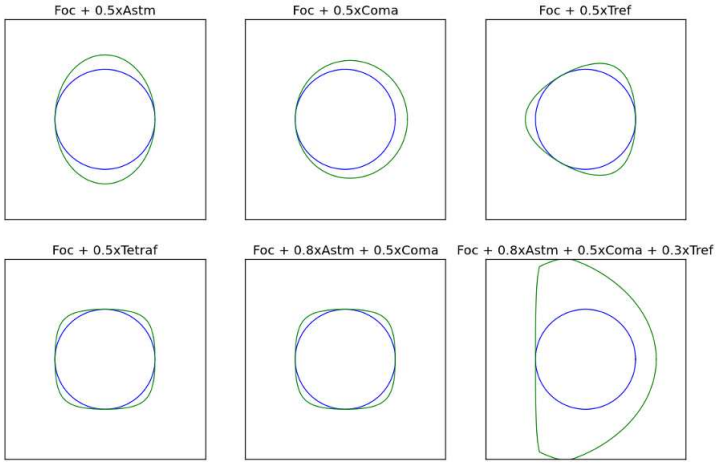

Figure 5.7 : *Contours for different optical modes combinations, deduced from the resolution of Equation 5.17 (circular pupil in blue).*

5.3.3 Thickness distribution

Once the contour is defined, it gives the moment distribution at the intermediate plate edges M_g, generated with a central force on this plate:

$$M_g(\theta) = \frac{F}{4\pi}\rho_c(\theta) = \frac{F}{4\pi}\frac{r_c(\theta)}{a}, \tag{5.21}$$

where F is the applied force, $r_c(\theta)$ is the distance from the center to the edge for a given orientation and a is the optical pupil radius.

On the other hand, Equation 5.8 gives the exact bending moment M_t inducing the required deformation. The required moment modulation on the mirror edges is then determined by applying this equation on the mirror coordinates system (r_c, θ), defined by its contour:

$$M_t(\theta) = -\frac{Et^3}{12(1-\nu^2)}\left[\frac{\partial^2 z(r_c,\theta)}{\partial r_c(\theta)^2} + \nu\left(\frac{1}{r_c(\theta)}\frac{\partial z(r_c,\theta)}{\partial r_c(\theta)} + \frac{1}{r_c(\theta)^2}\frac{\partial^2 z(r_c,\theta)}{\partial \theta^2}\right)\right], \tag{5.22}$$

with

$$\frac{\partial^2 z(r_c,\theta)}{\partial \theta^2} = \frac{\partial^2 z(r_c,\theta)}{\partial r_c^2}\left(\frac{\partial r_c(\theta)}{\partial \theta}\right)^2 + \frac{\partial z(r_c,\theta)}{\partial r_c}\frac{\partial^2 r_c(\theta)}{\partial \theta^2}. \tag{5.23}$$

The generated moments M_g are transmitted to the mirror edges (M_t) and induce the optical surface deformation. Then the generated moments (Eq 5.21) must be equal to the required ones on the mirror edges (Eq 5.22). As it can be seen in Equation 5.22, the thickness of the plate has an influence on the produced moments. We adapt this thickness on the intermediate plate in order to generate the required moments: solving $M_g(\theta) = M_t(\theta)$ gives the angular thickness distribution of the intermediate plate edges, $t_c(\theta)$, generating the required bending moments with the system contour:

$$t_c(\theta) = \left[\frac{12(1-\nu^2)F}{4\pi E}\frac{r_c(\theta)}{a}\left[\frac{\partial^2 z(r_c,\theta)}{\partial r_c(\theta)^2} + \nu\left(\frac{1}{r_c(\theta)}\frac{\partial z(r_c,\theta)}{\partial r_c(\theta)} + \frac{1}{r_c(\theta)^2}\frac{\partial^2 z(r_c,\theta)}{\partial \theta^2}\right)\right]^{-1}\right]^{1/3}. \tag{5.24}$$

This thickness distribution is achieved by creating angular sectors, whose thickness vary linearly from the center to the edges. The thickness at the edge is given by the above formula and the thickness at the center of the plate is an average of the computed values (see Figure 5.8).

Example: focus and astigmatism

If we take back the example of generation of focus and astigmatism, the generated moments are determined by combining Equations 5.19 and 5.21:

$$M_g(\theta) = \frac{F}{4\pi}\sqrt{\frac{1}{2+\gamma cos(2\theta)}}. \tag{5.25}$$

And the required moments are determined by injecting Equations 5.18 and 5.19 in Equation 5.22:

$$M_t(r_c,\theta) = \frac{-Et_c(\theta)^3\alpha_{20}}{6(1-\nu^2)a^2}(2+\gamma cos(2\theta))\left[1+\nu\left(1+\gamma\frac{(\gamma sin^2(2\theta)+2cos(2\theta))(2+\gamma cos(2\theta))+3sin^2(2\theta)}{(2+\gamma cos(2\theta))^2}\right)\right] \tag{5.26}$$

The intermediate plate angular thickness distribution is then deduced by equalizing Equations 5.25 and 5.26:

$$t_c(\theta) = \left[\frac{-6F(1-\nu^2)a^2}{4\pi E\alpha_{20}(2+\gamma cos(2\theta))}\left[1+\nu\left(1+\gamma\frac{(\gamma sin^2(2\theta)+2cos(2\theta))(2+\gamma cos(2\theta))+3sin^2(2\theta)}{(2+\gamma cos(2\theta))^2}\right)\right]^{-1}\right]^{1/3} \tag{5.27}$$

An example of thickness variation at the edges of the intermediate plate for a ratio astigmatism/focus of 0.2 is presented further, in Figure 5.12, and the detail of the intermediate plate is shown in Figure 5.8, with amplified thickness variations.

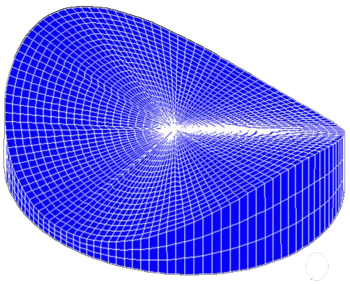

Figure 5.8 : *Example of an elliptical intermediate plate with an angular thickness distribution, defined for a generation of focus and astigmatism (scaled 30 times along the z axis).*

5.3.4 Actuation point location

The last system parameter is the force location. We have seen in Equation 5.21 that transmitted bending moments depend on the distance between force location and edges. Considering a decentering of (x_d, y_d), the new distance $r'_c(\theta)$, induces a new bending moment generation and Eq. 5.21 becomes:

$$M_{r_c}(\theta) = \frac{F}{4\pi}\frac{r'_c(\theta)}{a} = \frac{F}{4\pi a}\sqrt{r_c(\theta)^2 + x_d^2 + y_d^2 - 2r_c(\theta)(x_d cos(\theta) + y_d sin(\theta))}. \tag{5.28}$$

The induced modulation in $cos(\theta)$ and $sin(\theta)$ correspond to a generation of tilt and coma, their amplitudes depending on the shifting distance. So, these two modes can be generated either by defining a specific contour or by decentering the actuator. In order not to degrade other modes quality, the thickness distribution can eventually be recalculated equalizing Eq. 5.22 and 5.28.

5.4 Examples of application

5.4.1 Field compensation in an interferometer

Correction specifications for the IASI-NG interferometer

IASI-New Generation is a future satellite for meteorology and atmospheric study. It has a direct heritage from the flying satellites IASI (Infrared Atmospheric Sounding Interferometer) [Phulpin et al., 2007]. It will observe in the thermal infrared with unprecedented spatial sampling and coverage. The design of the instrument is presented in Figure 5.9, consisting in a modified Genzel interferometer [Griffiths and Homes, 2006]. A convergent light passes in a beam-splitter and the reflected and transmitted beams are focused onto flat folding mirrors, the resulting divergent beams are sent to two off-axis parabola and then to a double sided moving cube corner, applying the Optical Path Difference (OPD). The beams go back into the same optics and are combined into the beam splitter.

The cube corner displacement induces differential aberrations between the two interferometer arms: the OPD induces a focus error and the incident angle on the OAP induces astigmatism, coma and tilt, also evolving with the OPD. These errors are predictable with ray tracing software and they are shown in Figure 5.9. As we can see, the amplitudes of focus and astigmatism are two order of magnitude higher than the amplitudes of coma and tilt. Moreover, the amplitude of each mode evolves linearly and the amplitudes ratio between two modes is constant. So, the correction requirement can be defined as a single optical mode, combining the 4 aberrations.

The required compensation can be achieved with one of the two folding flat mirror, which will be active [IASI-NG team, 2010]. The mirror is 80 mm diameter and the maximum amplitude to be corrected is 26 μm rms. The WFE only need to be minimized on nine sounding points of 15 mm diameter, spread in the mirror plan (see Figure 5.13). The residual WFE on each sounding point must be less than 50 nm rms. Given the predominance of focus and astigmatism modes, if they are corrected with a high accuracy, the compensation of tilt and coma could not be necessary.

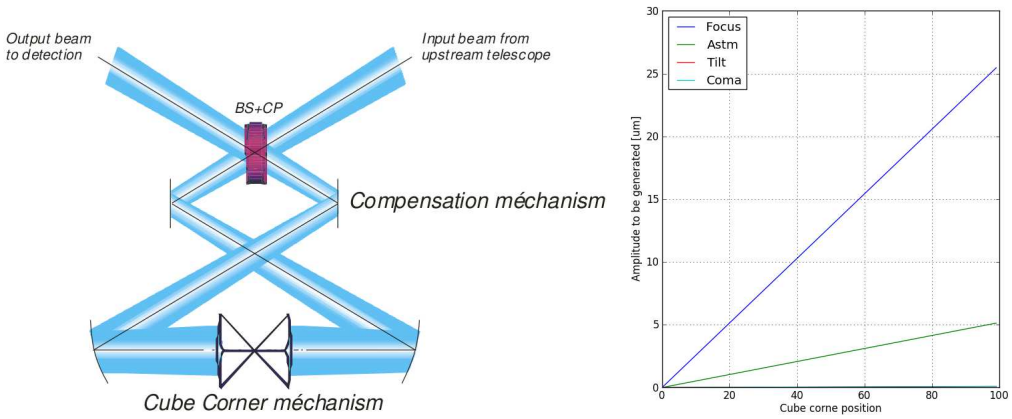

Figure 5.9 : *Design of the compensated Genzel instrument and differential aberrations appearing in the interferometer (credit TAS).*

Possible correcting systems

Several concepts of deformable mirror have been envisaged for this application.

- A Multimode Deformable Mirror (MDM), similar to the correcting mirror developed for the MADRAS project, is able to compensate for the 4 required aberrations with a high precision. But the number of actuators (24) seems disproportionate compared to the need.

- A Variable Curvature Mirror (VCM) can compensate for focus with a pressure application [Hugot et al., 2009]. A combination of focus and astigmatism could be generated by this system if it is elliptic. Even if the optical quality of such a system is excellent, the use of a pressure system in space seems to be too complex.

- A Beam Steering Mirror (BSM) can compensate for focus and astigmatism with a fixed central point and four external actuator [Madec et al., 2006]. While the generation of astigmatism is highly precise, the generation of focus is limited by the central clamping: from 5 μm rms of amplitude, the optical quality is not sufficient due to the local effects of the clamping and of the actuation points.

So, none of these existing techniques are satisfactory for this application. As there is only one global optical mode to correct, the COMSA concept can be applied. It will offer an elegant and efficient solution with a single mechanical actuator.

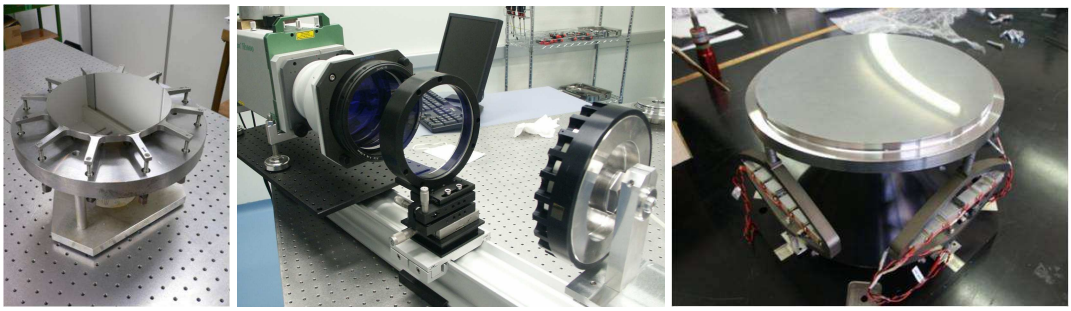

Figure 5.10 : *Prototypes of correcting mirrors developed at LAM: 12 arms MDM - VCM on its test set-up - 4 actuators BSM.*

Performance of the dedicated COMSA system

In a first time, the system is designed to compensate only for focus and astigmatism and the performance is optimized for the maximum deformation.

The model of the system, with its characteristics is presented in Figure 5.12.
The ratio between the astigmatism and focus is $\gamma = 5.128/25.466 = 0.201$. As described in Section 5.3.2, the corresponding contour is an ellipse with an axis ratio of $\sqrt{\frac{2+\gamma}{2-\gamma}} = 1.106$. As the pupil diameter is $2a = 80$ mm, the ellipse minor axis has this dimension and the major axis is 88.48 mm.

The required deformation being relatively important, the system needs to be flexible. The material chosen is then aluminium (Young Modulus E=75 GPa and Poisson ratio ν=0.33). The mirror thickness t is chosen considering the focus generation on a circular system. From Equation 5.7, the relation between the required amplitude of focus, the system dimension and the force is deduced:

$$a_{20} = \frac{Fa^2}{16\sqrt{3}\pi D} \quad => \quad F = \frac{4\pi E}{\sqrt{3}(1-\nu^2)}\frac{a_{20}}{a^2}t^3. \tag{5.29}$$

Figure 5.11 shows the evolution of the force with the mirror thickness to generate the required focus amplitude. The aspect ratio (diameter/thickness) is generally chosen around 10, but in this case the required force is 2500 N, which is too high. Indeed, the final required force will be higher than this theoretical value for two reasons: firstly, the astigmatism generation on the elliptical system will require an additional force; secondly, a part of the generated moments will be absorbed by the system. A good trade-off between force value and aspect ratio is a thickness of 3 mm, requiring a force of 1000 N for the focus generation. Moreover a plate with this thickness is easily manufacturable and will allow the mechanical strength required for space use.

The thickness of the intermediate plate is computed as detailed in Section 5.3.3 with a mean thickness of 2 mm. The mirror being thicker than the intermediate plate, it allows to have a high ratio between deformation amplitude of the plate and the mirror. Thanks to that, the mirror's deformation precision is improved compared to the plate deformation precision.

The other dimensions are optimized with Finite Element Analysis in order to minimize the residual deformation on the optical surface and the force and stress values. The overall system is 35 mm high for a diameter of 90 mm. The height can be adapted according to the actuator size.

The precision of correction obtained on the FEA model is high for the focus and astigmatism combination: the residual after the correction of the maximum WFE is lower than 30 nm rms on each sounding point. (Figure 5.13 and Table 5.2).

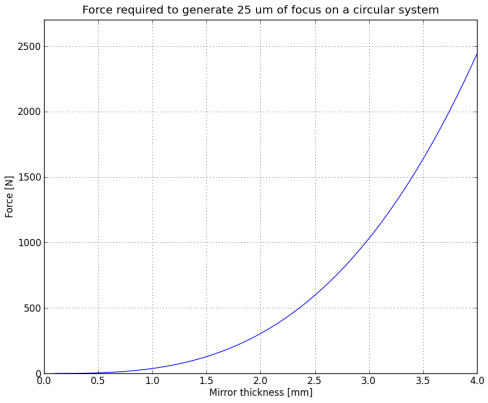

Figure 5.11 : *Evolution of the required force to generate 25 µm of focus on a circular system with the thickness of the mirror.*

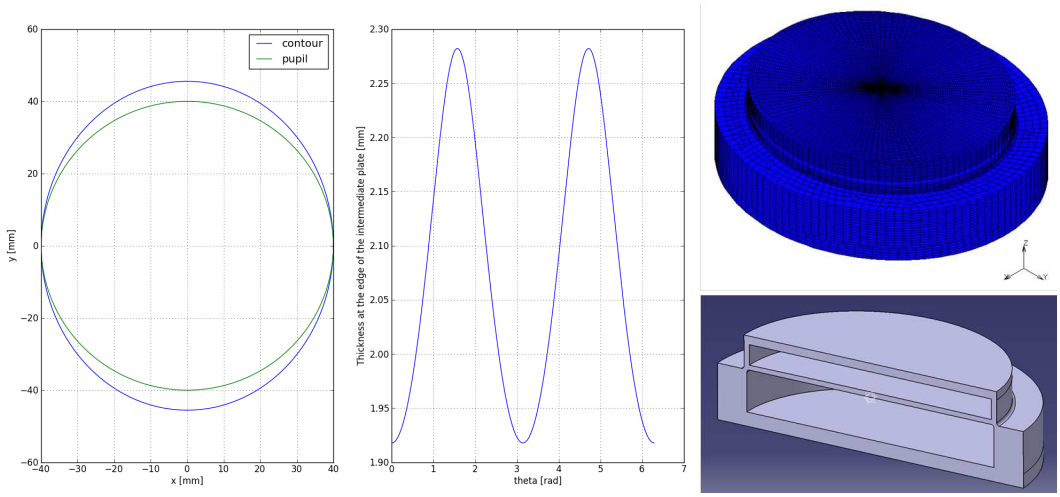

Figure 5.12 : *Definition of the system compensating for the focus and astigmatism of the IASI interferometer (115230 hexaedral elements - 139350 nodes, 1000 nodes per sounding point).*

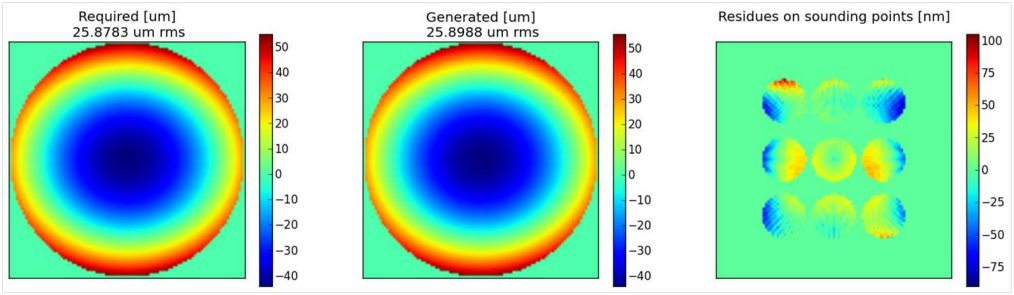

Figure 5.13 : *Performance for the generation of focus and astigmatism with a centered force: Required and generated phase maps on the overall optical pupil and residual phase map on the sounding points (FEA results).*

Once the generation of these 2 aberrations is proven, we study the correction of focus, astigmatism, tilt and coma simultaneously. Firstly, due to the small amplitude of the 2 additional aberrations, the exact same system can be used. The residual WFE will remain in the specifications, below 50 nm rms on each sounding point (Table 5.2).

In order to improve this performance, the force can be decentered. As explained in Section 5.3.3, it will add tilt and coma modes. We study the evolution of the generated deformation with the force translation: the optimum deformation is obtained for a decentering of 0.35 μm toward the y axis. With this configuration, the WFE expected in the instrument will be corrected with a precision better than 30 nm rms on each sounding point (Figure 5.14 and Table 5.2).
Not only this analysis gives the optimal actuator location but it also gives an indication on the tolerance on the actuator positioning: a misplacement of 0.35 μm does not significantly impact the system performance.

The required force is 2500 N and the maximum stress is 150 MPa. Both values are acceptable: the force is feasible for many actuators and the stress is below the elastic limit of aluminium. The maximum constraint is located in the flange linking the bottom ring to the intermediate plate, the design of this zone could eventually be modified to better absorb the constraints.

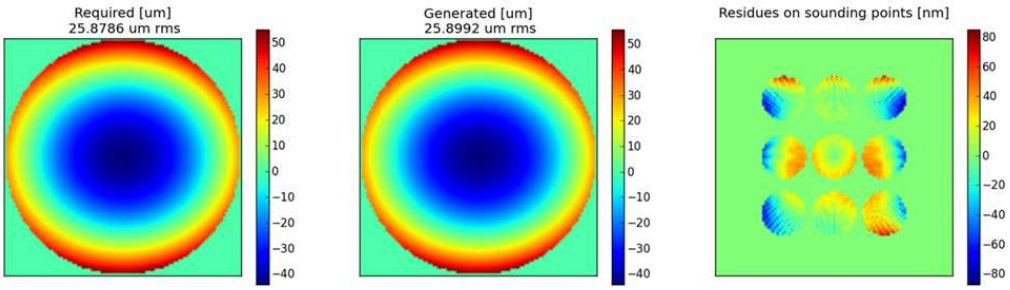

Figure 5.14 : *Performance for the 4 modes generation with a decentered force: Required and generated phase maps on the overall optical pupil and residual phase map on the sounding points (FEA results).*

Table 5.2 : *FEA performance of the system with a centered and a decentered force. The residual deformation is given for each sounding point, considering the generation of focus and astigmatism only and considering the generation of the 4 aberrations*

Sounding point		1	2	3	4	5	6	7	8	9
System with a centered force	Residues for foc + astm (nm rms)	25.1	10.4	32.2	24.7	9.9	27.3	20.8	13.0	22.0
System with a centered force	Residues for total WFE (nm rms)	48.7	12.5	55.4	36.3	28.3	16.0	50.0	18.7	28.1
System with a decentered force	Residues for total WFE (nm rms)	29	10.0	28.9	27.1	9.8	25.7	23.6	13.2	22.8

Conclusion

Through this example, we have detailed the design of a deformable mirror with a single actuator, dedicated to the compensation of an optical mode composed of the four optical aberrations appearing in a Genzel interferometer, due to the cube corner displacement. The required correction is efficiently performed with this simple and compact system, adapted to a space use.

5.4.2 Off-Axis Parabola generation

As a study case, we consider the generation of a 100 mm diameter Off-Axis Parabola with each concept, with a focal ratio of 1, and a 45° off-axis angle. Using the formulas describing an OAP, such an optical shape can be decomposed as a sphere of radius 200 mm plus terms of focus (α_{20} = 1.73 μm rms), astigmatism3 (α_{22} = 2.03 μm rms) and coma3 (α_{31} = 0.35 μm rms).
VOALA and COMSA systems are designed as described in the previous sections and their performance are computed with Finite Element Analysis. The systems are modeled as monolithic pieces, with a clamped reference plate. The material chosen is aluminum, for its flexibility (Young's modulus E = 75 GPa, Poisson ratio ν = 0.33). Both finite element models have 115230 hexaedral elements and 139350 nodes. There are 5900 nodes on the optical surface allowing a good characterization of the optical quality: with a sampling of 100 nodes on a diameter and 120 angular sectors, the deformation is described up to 50 cycles per pupil.

Shape generation precision

From the Finite Element Analysis, the systems' performance is characterized by computing the optical precision, defined as the difference between required and generated shapes.

- *VOALA performance*

The required mirror shape is decomposed on the three system's influence functions, recovered on the Finite Element model: it gives the values of the forces to apply on each actuator (see Figure 5.15). As we can see in Fig. 5.16, the mirror shape is generated with a high precision: the residual deformation is 15.2 nm rms and is mainly composed of astigmatism angular harmonics.

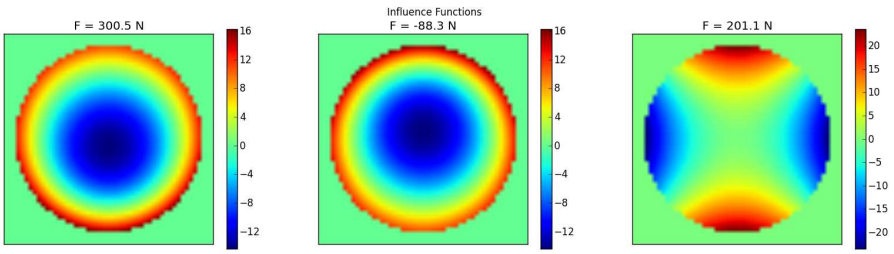

Figure 5.15 : *VOALA system influence functions (1st actuator on the central pad - 2nd actuator on the central pad - 3rd actuator between the two beams) and their projection coefficients to generate the required OAP (FEA results - Unit:[nm]).*

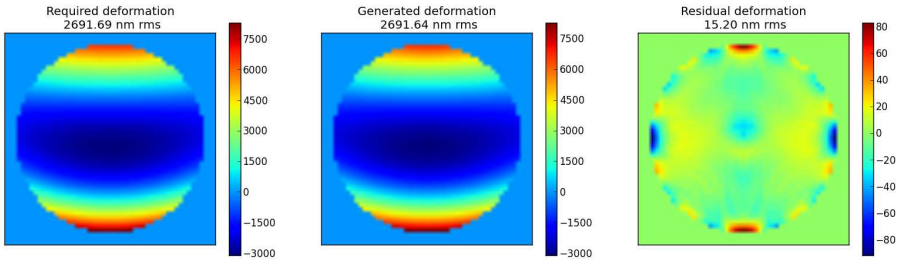

Figure 5.16 : *VOALA system performance for the OAP generation: Required deformation (deduced from the OAP characteristics) - Optical surface deformation (generated by the 3 actuators) - Residual deformation (FEA results - Unit:[nm]).*

- *COMSA performance*

Starting with the given combination of optical aberrations, the methodology explained in Section 5.3 is applied to design the COMSA system. The computed contour and thickness distribution are presented in Figure 5.17. The finite element model performance is promising: with only one actuator, the optical surface shape of 2.7 μm rms is generated with a residual deformation of 14.4 nm rms (see Figure 5.18).

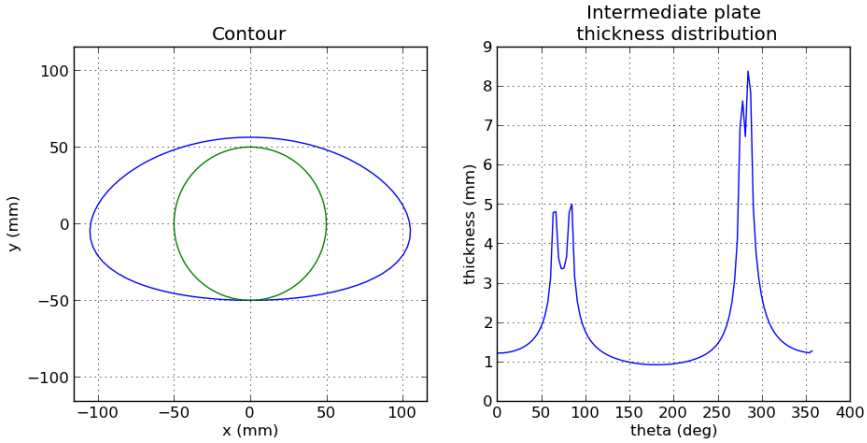

Figure 5.17 : *Analytical solution for OAP generation with COMSA: System contour and thickness distribution defined by the required OAP.*

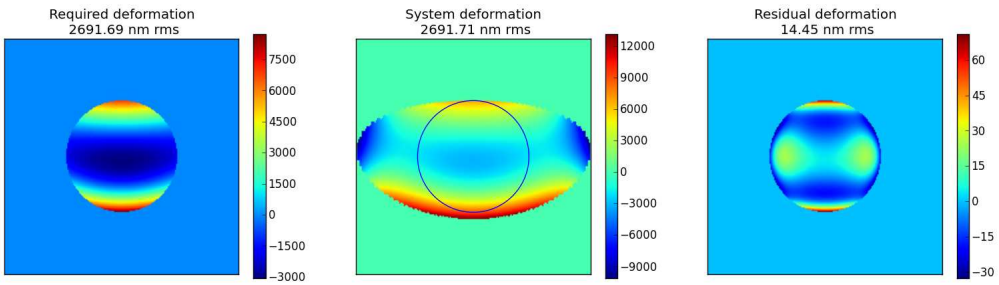

Figure 5.18 : *COMSA system performance: Required deformation (deduced from the OAP characteristics) - Optical surface deformation (generated by the actuator force) - Residual deformation on pupil (FEA results - Unit:[nm]).*

Range of achievable OAP

Both systems are optimized to generate the required OAP but they can achieve a whole range of optical shapes. The generable OAPs are given by the system characteristics, the actuator available stroke and the system mechanical strength.

Able to generate any combination of focus, astigmatism and coma, the VOALA system covers a wide range of OAPs. The precision of generation will depend of the amplitudes required for the three aberrations. To determine an optimal range of use, the generation of each mode is characterized separately (see Table 5.3). With a 0.2 % precision, the focus generation is highly efficient and it does not require a lot of force, so it is not a critical mode. Astigmatism is generated with 0.7 % precision, the required force is almost twice higher than for the focus but is splited among four points on the system so this mode will not induce too much mechanical stress either. As the required amplitude of coma was lower of one order of magnitude compared to the other modes, its weight in the system optimization was less important. It leads to a generation of coma slightly less efficient: 1.1 % of residual deformation with higher force required on actuators.

Table 5.3 : *System performance for the generation of 1 µm rms of each mode with the VOALA system (FEA results).*

	Act1 (pad) (N)	Act2 (pad) (N)	Act3 (beams) (N)	Residues (nm rms)
FOCUS	61.3	61.3	0	1.92
COMA	555.4	-555.4	0	10.94
ASTM	0	0	99.9	7.01

The COMSA system covers a more specific range of OAPs. It can generate the combinations of aberrations defined by its contour and thickness distribution, the optical shape evolves linearly with the value of the force applied:

$$z_{mirror}(\rho, \theta, F) = A(F)(\alpha_{20}Z_{20}(\rho, \theta) + \alpha_{22}Z_{22}(\rho, \theta) + \alpha_{31}Z_{31}(\rho, \theta)), \tag{5.30}$$

with $A(F)$ a coefficient linking the amplitude of the deformation to the force F.
Figure 5.19 shows the aberrations combinations achievable with the studied system and the corresponding OAP. The residual deformation depends on the amplitude of the required deformation, the precision of generation is 0.5% for this entire set of OAP.

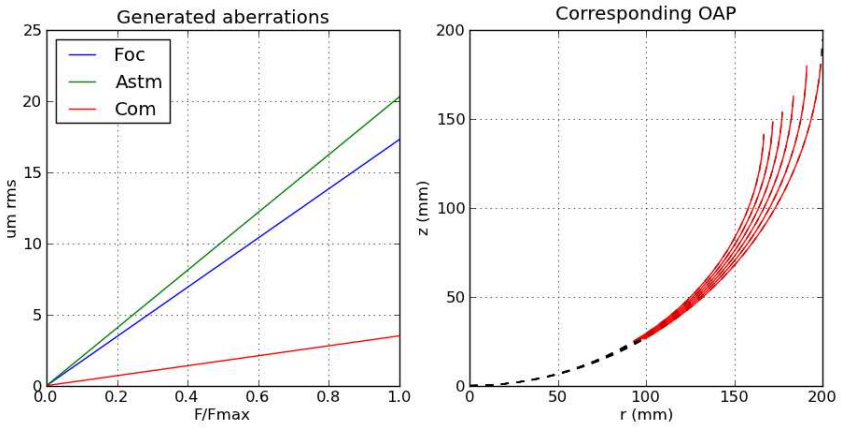

Figure 5.19 : *Aberrations achievable with the COMSA system and corresponding OAP.*

Conclusion on the OAP generation

The VOALA and COMSA concepts are well adapted to the generation of Off-Axis Parabola. Any OAP can be generated with the VOALA system, the necessary stroke and the residual deformation is given by the individual mode performance, which can be optimized according to the need. The range of OAP achievable with the COMSA system is defined by the system contour and available stroke, and the performance of generation is optimized for one optical shape.

5.4.3 Zoom system

Classically, the realization of an off-axis zoom system with a high range of magnification and a wide field of view requires several complex lenses, often with a prohibitive weight and cost for a space use. But the magnification function can be achieved with two active mirrors, without moving parts. Such a system offers an elegant and simple alternative solution with less optical surfaces and degrees of freedom.

Madec et al. [2008] and Wick and Martinez [2004] have presented on-axis zoom systems using active mirrors. The first one uses two Variable Curvature Mirrors, whose actuators are pressure systems allowing a magnification factor up to 3. The second one uses two micromachined deformable membrane mirrors with 59 actuators per mirror allowing a magnification factor up to 4. These approaches can be improved by designing an off-axis zoom system, using a minimum number of mechanical actuators. Indeed, the required optical shapes are relatively simple and can be generated with the VOALA and COMSA concepts.
Firstly, both radii of curvature need to be changed to provide the zoom function. Secondly, one of the two active mirrors must compensate for the astigmatism and coma, which are the main aberrations induced by the off-axis design.

As an example, a 2 mirrors zoom has been conceived with a ray-tracing software. The system has a field of view of ±0.5° and a 50 mm diameter pupil located between the two mirrors. The two mirrors are parabolas of 60 mm diameter and the incidence angle on these mirrors is 6°.
In the initial configuration, both mirrors have a radius of curvature of 400 mm, providing a magnification factor of 1. The off-axis error is compensated by adding an astigmatism mode on the second mirror optical surface, with an amplitude of 5.56 μm rms. So, in the initial configuration,

the first mirror is a parabola and the second mirror is toroidal. The mirrors characteristics have been optimized regarding the optical quality in the exit image plane.

Starting from this configuration, we modify the radius of curvature of the first mirror and optimize the second mirror shape in order to maintain the optical quality at the system output. Thus, the radius of curvature of the second mirror is also modified, providing the magnification function. The focus mode on each mirror is directly linked to the mirror radius of curvature:

$$a_{20} = \frac{a^2}{4k\sqrt{3}}. \tag{5.31}$$

In addition, terms of astigmatism and coma are added to the optical surface of the second mirror. Figure 5.20 shows the two extreme configurations of this system, allowing a magnification factor from 0.75 to 1.5. Beyond these values, the optical quality is deteriorated.

Figure 5.21 presents the evolution of the mirrors' shape with the magnification factor. The first mirror deformation can be achieved with a single actuator, driving focus. And the second mirror can be controlled with no more than three actuators. We can see on Figure 5.21 that the three modes on the second mirror evolve linearly with the magnification factor, but in this case, the ratio between the modes is not constant. The design could be modified in order to have constant ratios, a single optical mode could then be defined as the sum of the three aberrations and a single actuator could be used to generate the required deformation.

This simple study case demonstrates the possibility and the advantages to use the developed concepts in a zoom system. For a prototyping, the initial configuration would need to be optimized regarding the required magnification factor, field of view and the resulting necessary mirrors' deformation.

Such a system could be used in satellites observing Earth on elliptical orbits. The distance to the object varies there with the telescope altitude and with its viewing angle. The adaptation of the magnification factor would allow to maintain the angular resolution and field of view, ensuring optimum image quality in different configurations. In addition, the ability to generate off-axis aberrations would compensate for any misalignment in the optical system, due to thermal expansion or to gravity variations, relaxing the system specifications on stability.

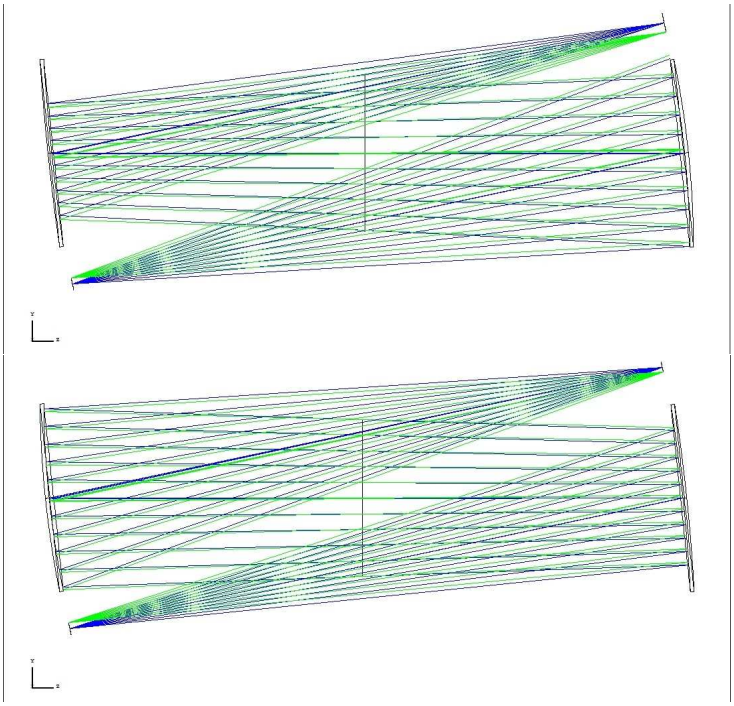

Figure 5.20 : *Extreme configurations of the zoom system (magnification 1.5 and 0.75).*

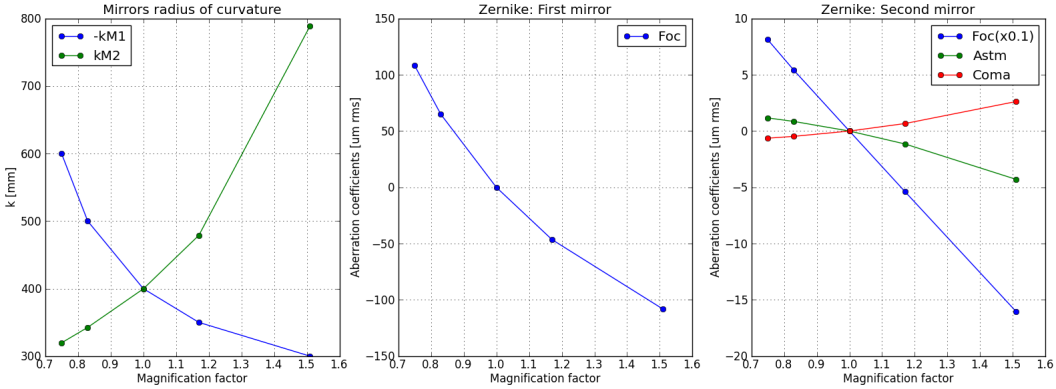

Figure 5.21 : *Evolution of the mirrors' characteristics in function of the zoom magnification factor (from Zemax). The aberration coefficients correspond to the difference with the initial optical shapes.*

5.5 Conclusion

The two concepts presented in this chapter allow the generation of an optical mode with one actuator. Moreover, the number of actuators does not depend on the mirror size and, thanks to the deformation through bending moments transferred at the mirror edges, its action does not induce any print-through effects. The optical surface is deformed through the application of bending moments at the mirror edges. The system geometry is relatively simple: the bending moments are generated by the application of forces on an intermediate plate and they are transmitted to the mirror with a ring linking the plates together. This warping structure is clamped on a reference plate through another ring.

The VOALA system is able to generate independently focus, astigmatism and coma with one actuator per mode. The COMSA system has a single actuator, generating a given combination of optical aberrations. Such optimized systems are designed to fill-in an optical function defined by a specific instrument design and they will allow an efficient Wave Front Error compensation. The expected performance of these active optics systems have been computed with Finite Element Analysis, showing excellent performance for optical/IR applications. The next step is the manufacturing of prototypes to experimentally validate the simulation results.

The inherent simplicity of the systems detailed in this section will allow the development of variable optical designs, leading to innovative optical architectures. The minimum number of degrees of freedom makes this type of system convenient to use in many applications. Smart optical designs will contain few elements with simple active mirrors. These mirrors will provide new functions, increase the instrument performance by in situ correcting the alignment errors and relax the stability and positioning constraints. The compensation of field effects, non common path aberrations or optics deformation are also major applications: a simple correcting deformable mirror in the optical train will allow significant constraints relaxation on systems assembly and integration as well as on operational stability.

The next generation of Earth- and Space-based large lightweight segmented telescopes will benefit from simple active mirrors, allowing an in-situ active compensation with a minimum volume, weight and power consumption.
For instance, Patterson et al. [2010] propose a diluted, reconfigurable pupil telescope with a primary mirror constituted of several movable off-axis parabolas, whose asphericity depends on the required configuration. The variable off-axis parabola will relax the positioning constraints between the sub-pupils, by adjusting the shape depending on the position. The position will not need to be precisely controlled but only precisely known, thus simplifying the control/command systems especially in the case of formation flying observatories.
Moreover, the future giant Earth-based telescopes will have adaptive optics systems assisted by Laser Guide Stars (LGS), requiring a laser beam refocalization. Indeed, the LGS spot is formed on the atmosphere Sodium Layer and the distance between this layer and the telescope pupil can vary from 80 to 200 km, depending on the line of sight [Madec et al., 2010; Challita et al., 2011]. The induced defocusing effect on the LGS wave-front sensor can be compensated with the presented simple systems.
To finish, these simple deformation devices, generating OAP, can be coupled to stress polishing technique for the manufacturing of large primary mirrors' segments.

Bibliography

Z. Challita, E. Hugot, F. Madec, M. Ferrari, and D. Le Mignant et al. Active optics: variable curvature mirrors for ELT laser guide star refocusing systems. volume 8172 of *Society of Photo-Optical Instrumentation Engineers (SPIE) Conference Series*, September 2011.

J. C. Dainty, A. V. Koryabin, and A. V. Kudryashov. Low-Order Adaptive Deformable Mirror. *Applied Optics*, 37:4663–4668, July 1998.

R. Fischer, B. Tadic-Galeb, and P. Yoder. *Optical System Design*. Press Monograph, January 2008.

R. H. Freeman and J. E. Pearson. Deformable mirrors for all seasons and reasons. *Applied Optics*, 21:580–588, February 1982.

P. Griffiths and C. Homes. *Instrumentation for Far-infrared Spectroscopy*. Wiley, 2006.

E. Hugot, G. R. Lemaître, and M. Ferrari. Active optics: single actuator principle and angular thickness distribution for astigmatism compensation by elasticity. *Applied Optics*, 47:1401–1409, April 2008.

E. Hugot, M. Ferrari, G. Lemaitre, F. Madec, and S. Vives et al. Active Optics for High dynamic variable curvature mirrors. *Optics Letters*, 34:3009–3011, 2009.

IASI-NG team. IASI-NG Interferometer - Deformable Mirror for Field Compensation. Technical report, Thales Alenia Space, 2010.

M. Laslandes, E. Hugot, and M. Ferrari. Correcting device with a deformable mirror for the compensation of at least one aberration with a known evolution. *Patent Pending (CNES, TAS, CNRS and Université de Provence), FR1153390*, 2011a.

M. Laslandes, E. Hugot, M. Ferrari, and A. Liotard. Mirror with mechanical device to generate optical aberrations. *Patent Pending (TAS, CNES, CNRS and Université de Provence), FR1102805*, 2011b.

M. Laslandes, E. Hugot, and M. Ferrari. Active Optics: deformable mirrors with a minimum number of actuators. *Journal of the European Optical Society*, 7:12036, 2012.

F. Madec, E. Prieto, P.-E. Blanc, E. Hugot, and S. Vives et al. New beam steering mirror concept and metrology system for multi-IFU. volume 6273 of *Society of Photo-Optical Instrumentation Engineers (SPIE) Conference Series*, July 2006.

F. Madec, E. Hugot, J.-L. Gimenez, F. Tracol, and M. Ferrari et al. An active optics concept for the multi-object spectrograph EAGLE. volume 7018 of *Society of Photo-Optical Instrumentation Engineers (SPIE) Conference Series*, July 2008.

F. Madec, D. Le Mignant, E. Chardin, E. Hugot, and S. Mazzanti et al. Development and performance of the EAGLE active optics LGS WFS refocusing system. volume 7736 of *Society of Photo-Optical Instrumentation Engineers (SPIE) Conference Series*, July 2010.

K. Patterson, S. Pellegrino, and J. Breckinridge. Shape correction of thin mirrors in a recongurable modular space telescope. volume 7731 of *Society of Photo-Optical Instrumentation Engineers (SPIE) Conference Series*, July 2010.

T. Phulpin, D. Blumstein, F. Prel, B. Tournier, P. Prunet, and P. Schlüssel. Applications of IASI on MetOp-A: first results and illustration of potential use for meteorology, climate monitoring, and atmospheric chemistry. volume 6684 of *Society of Photo-Optical Instrumentation Engineers (SPIE) Conference Series*, September 2007.

S. P. Timoshenko and S. Woinowsky-Krieger. *Theory of Plates and Shells*. Engineering Mechanics Series. McGRAW-Hill International Editions, 1959.

D. V. Wick and T. Martinez. Adaptive optical zoom. *Optical Engineering*, 43:8–9, January 2004.

Conclusions and perspectives

The future of telescopes lies in large diameter, to reach high angular resolution and collecting power. With such an evolution, the achievement of high quality images will require an efficient wave-front control, ensuring the system stability.

The next generation of space-based telescopes will be 2-3 m diameter for Earth observation and 8 m diameter for Universe observation. It requires lightweight and eventually segmented mirrors in order to keep a reasonable weight and compactness to fit current or future launchers' cap. The next generation of ground-based telescope will be 30-40 m diameter. It also requires segmented and lightweight mirrors, for feasibility.
Active optics is then mandatory to compensate for the mirrors' deformation. On Earth, all the 8 m class telescopes already integrate active primary mirrors, compensating for gravity and thermo-elastic deformation. In space, the environment variations will also induce significant deformation on lightweight structures. The two main contributors are the difference of gravity between integration at $1g$ and operations at $0g$ and the thermal variations due to the day/night cycles.
Active optics is also used for the development of efficient manufacturing techniques for the telescopes' segments. Combining warping systems and full-sized tool polishing, Stress Mirror Polishing provides high quality optical surface, free from high spatial frequency errors.
Finally, the use of simple dedicated correcting system will simplify some optical designs, by reducing the number of optics, will allow the definition of new instrument architecture, by providing new optical functions and will relax some constraints on the systems stability and integration.

MADRAS project

The MADRAS (Mirror Actively Deformed and Regulated for Applications in Space) project has demonstrated the performance of a correcting mirror dedicated to the compensation of large mirror deformation in space.
Instead of maintaining the large primary mirror optical shape, the correction is performed in a pupil relay, allowing a reduction of the number of actuators and of the active system weight. The developed system has only 24 peripheral actuators, it is 130 mm diameter (for a pupil of 90 mm) and 80 mm high, it weights 4 kg and has been conceived regarding the space constraints (low weight, size, power consumption and CTE, mechanical strength, robustness and reliability).

Firstly, the design has been optimized with Finite Element Analysis, regarding the correction requirements of a 3 m class space telescope. FEA has also allowed to ensure the mechanical strength

of the system and to define the specifications on the hardware and the integration.
Secondly, the system has been manufactured and integrated. The opto-mechanical concept has then been validated with interferometric measurements: the measured influence functions are equivalent to the simulated one and the expected performance are thus recovered.
Finally the mirror functioning in closed loop has been tested on a dedicated test-bed. A telescope simulator generates the wave-front errors expected in a space telescope. The active correction loop is composed of the MADRAS mirror, driven by a Real Time Computer analyzing the data measured by a Shack Hartmann wave-front sensor. The effects of the correction are visualized thanks to imaging cameras and a Fizeau interferometer.
By sending calibrated wave-front error on the correcting mirror, its performance has been experimentally demonstrated. The developed system is able to compensate for the expected deformation in a 3 m class telescope with a precision of 8 nm rms.

This project has brought the developed active mirror technology up to a TRL4/5: the system functioning has been fully validated in a laboratory environment and the mechanical design has considered the space constraints (vacuum and thermal behavior and strength to the launch environment).
In the optical train of future telescopes, such a system will ensure the system stability while relaxing the tolerances on the assembling and integration.

E-ELT M1 project

Taking up the deformation concept of MADRAS and adapting it to stress polishing, a segment prototype for the E-ELT primary mirror is currently under manufacturing. The demonstration of such a process capabilities will encourage the mass production of the E-ELT thousand segments using stress mirror polishing.

Finite Element Analysis have allowed to optimize the warping harness geometry and to fully characterize the opto-mechanical performance. The warping harness is composed of a ring and 12 forks, with 2 actuators per fork. The Zerodur blank is glued on the harness and warped into the shape of the E-ELT outermost segment, which has a 32 μm rms asphericity. Finite Element Analysis has shown that the warping is efficient: the residual deformation is 20 nm rms.
The study has also considered other sources of errors: by anticipating the effects of the gravity and of the polishing pressure, it is possible to compensate for them. A uniform pressure under the optical surface will reduce the resulting shape errors.
At the end, taking into account the errors due to the warping, the gravity, the polishing and the actuators precision, the residual deformation is lower than 25 nm rms.
The simulation of the Ion Beam Figuring step predicts that the residual shape error will be reduced to 3 nm rms.
The system is now under testing: the optical surface will be measured with a Fizeau interferometer and position and force sensors will give direct information about the system mechanical behavior. This complete characterization will allow to demonstrate the warping precision and to determine the best way to monitor the mirror deformation during the polishing process for an eventual industrialization.

Stress polishing efficiency, in terms of obtained optical quality and gain of time compared to classic robotic techniques, places this technique as a serious candidate for the mass production of the E-ELT segments.

VOALA and COMSA concepts

The minimization of the number of actuators will allow the development of simple correcting systems, dedicated to a given application.
Starting from some correction specifications, minimalist active mirrors can be developed with a simple goal: one optical mode must be generated with one actuator. In this context, two systems have been conceived with the elasticity theory and their performance have been validated with Finite Element Analysis.

VOALA (Variable Off-Axis paraboLA) and COMSA (Correcting Optimized Mirror with a Single Actuator) are two concepts of deformable mirror, based on the warping of a thin shell through the application of bending moments at the system edges. The moments are generated on an intermediate plate with an actuator applying a force and they are transmitted to the mirror with a flexible ring. Such a system avoids the generation of actuator print-through on the mirror.
VOALA system has 3 actuators allowing the generation of focus, astigmatism and coma, the three main modes composing an off-axis parabola. COMSA system has a single actuator and an adapted contour, allowing the generation of a given combination of aberrations.

The minimum number of actuators makes this type of system interesting for a space use: it is easy to set up and monitor and it presents a limited weight and power consumption.
By offering new optical functions, these concepts could lead to innovative telescopes and instrument architectures. For instance, zoom system based on two active mirrors are already under study, and it is envisaged to include correcting mirror in off-axis interferometer, to compensate for non common path aberrations.
The developed concepts will also allow a relaxation on the systems integration and stability at a limited cost.

Perspectives

The active mirrors presented in this thesis allow the generation of optical aberrations with a high precision, in terms of both low and high spatial error frequencies. This efficiency, and the limited number of actuators make these systems advantageous to use in the framework of large telescopes, notably in space.

The MADRAS demonstrator has allowed a major step, proving the possibility and the gain to insert such a simple active system in a space telescope. To go further, two main axes need to be studied: the wave-front analysis and the actuator technology.

- *Wave-front analysis*

The best strategy to command an active mirror in space needs to be determined. The aberrations can be measured in the instrument focal plane, with phase diversity, in a pupil plane, with Shack-Hartmann wave-front sensing, or even directly on the mirror, with mechanical sensors or interferometry. The reference also needs to be defined: the correction can be performed on a wave-front coming from a distant star, from an internal source or from the object of interest. In this context, phase diversity and Shack-Hartman wave-front sensing on a moving extended object are currently under study. Both techniques will be tested on the MADRAS test bench.

- *Actuator technology*

A significant study on the actuators must be conducted, notably to ensure the correction stability in open loop. A trade-off must be done in order to determine whether it is better to have an ultra-stable system or a low-level control loop, maintaining the actuators' position (with stress gauges for instance). At the moment, the best solution appears to be mechanical actuators, such as micro-motors, able to maintain their position even without power supply.

The performance of the VOALA and COMSA concepts have been characterized with Finite Element Analysis. As for the MADRAS project, an experimental demonstration need to be performed. For this purpose, an off-axis zoom system with two active mirrors based on these concepts will be developed.
The manufacturing of aspheric surfaces by stress polishing with this type of warping harness could also be demonstrated and used at minimal cost.
Finally, numerous applications can be envisaged for these two systems and the design of innovative instruments, based on these active mirrors, constitutes an interesting work. Among many other possibilities, three developments can be cited:

- the insertion of an elliptical COMSA system in an off-axis interferometer. Such an application has already been studied but still need to be realized.
- the conception of an active system for Laser Guide Star (LGS) refocusing, which will be a major step for adaptive optics assisted by LGS, for the future extremely large telescopes.
- the elaboration of a reconfigurable diluted pupil telescope with variable off-axis parabolas.

For space applications, the robustness and reliability of the systems are major aspects to be considered. Thus, the actuators' redundancy is mandatory. The developed systems having a few actuators, it is easy to integrate several actuators in series, avoiding a single point failure. We have seen that the MADRAS system presents an intrinsic redundancy, due to the fact that there are more actuators than modes to be corrected. Similarly, a thin active primary mirror, with many actuators under its optical surface will also present such a redundancy. Moreover, it will allow the use of more flexible mirrors. Nevertheless, the direct action on the mirror will generate print-through effects and the weight of the many actuators and their electronics must be taken into account, such as the control complexity. Depending on the application, a trade-off must be done between the mirror weight, the number of required actuators, the system reliability and of course the cost.

The interest in active optics has been demonstrated many times over the past decades. It has allowed some technological breakthroughs in the field of Earth-based astronomy, helping to improve our knowledge of the Universe. It is now a logical extension to insert active systems in the next generation of space telescopes. In the short term, active correcting mirrors will be used to compensate for large lightweight primary mirrors' deformation, ensuring the achievement of the best optical quality. In the long term, the development of active systems, providing new optical functions, will encourage the appearance of innovative and simplified optical designs that will improve our observation capabilities.

Appendix A

Miroirs actifs de l'espace: Synthèse

Introduction

Avec le télescope en première ligne, les grandes découvertes astrophysiques ont toujours été permises par d'importants développements dans le domaine de l'instrumentation pour l'astronomie [Wilson, 1996, 1999]. Pour voir plus loin, il faut collecter plus de flux, pour voir plus de détails, il faut augmenter la résolution angulaire. Ces deux caractéristiques dépendent directement du diamètre D du miroir primaire: la puissance collectrice évolue avec D^2 et la résolution angulaire avec λ/D, λ étant la longueur d'onde observée [Hecht, 1987]. Ainsi, l'accès à des observations plus fines implique l'augmentation de la taille des télescopes. Cette évolution, simple à décrire, nécessite de nombreuses innovations quant au développement des télescopes.

Premièrement, la résolution angulaire des télescopes terrestres est limitée par la turbulence atmosphérique ainsi que par les effets de la gravité et les déformations thermo-élastique. Depuis environ 30 ans, les développements en optique active et adaptative adressent ce problème. Ces deux techniques permettent d'atteindre la limite de diffraction du télescope en compensant les erreurs de front d'onde. Les systèmes d'optique adaptative analysent les effets de la turbulence atmosphérique et les corrigent à l'aide d'un ou plusieurs miroirs déformables [Hardy, 1998]. L'optique active compense quant à elle les déformations des grands miroirs: la forme optimale est maintenues grâce à des actionneurs poussant ou tirant sous la surface optique [Knohl, 1994].
Deuxièmement, il existe une limite technologique pour la fabrication de grands miroirs monolithiques. Pour les diamètres supérieurs à 8 mètres, les concepts de télescopes segmentés doivent être adoptés: le miroir primaire sera un assemblage de plusieurs segments hors-axe. En couplant la technique de polissage avec un outil pleine taille à un système déformant le substrat, l'optique active permet la génération de segments avec une excellente qualité optique, sans erreur de haute fréquence spatiale [Lemaitre, 1972; Nelson et al., 1980].
Troisièmement, la complexité croissante des instruments optiques nécessite l'émergence de systèmes innovants. Dans ce cadre, l'optique active est utile pour les instruments à chemin optique variable où un miroir actif permet la correction d'aberrations évoluant avec la configuration de l'instrument [Ferrari, 1998]. De plus, la génération de surfaces optiques exotiques avec l'optique active peut permettre de réduire le nombre d'éléments dans un design optique, le simplifiant ainsi

[Challita et al., 2011].

Comme décrit ci-dessus, l'optique active offre des solutions élégantes pour contrôler le front d'onde dans les télescopes, menant non seulement à des instruments plus efficaces mais également à des designs optiques simplifiés. Dédiée à la correction d'aberrations optiques induites par les défauts intrinsèques aux instruments, la recherche en optique active est focalisée sur la conception de systèmes simples et minimalistes, répondant exactement à un besoin donné [Lemaître, 2009]. Cette technique, utilisée largement et avec succès pour l'instrumentation au sol, pourrait être efficacement utilisée dans les futurs télescopes spatiaux.

Dans l'espace, il n'y a pas de turbulence atmosphérique mais des contraintes drastiques quant au poids et à la compacité des instruments. Ceci pose le problème de la stabilité des structures. Quel que soit le type de missions, les futurs observatoires spatiaux sont toujours conçus avec un grand miroir primaire allégé, monolithique ou segmenté, déployable ou assemblable en vol [Feinberg et al., 2012]. Ces grands miroirs vont perdre leur forme optimale à cause des variations thermiques vues par le télescope, ainsi qu'à cause de la différence de gravité entre l'intégration sur Terre et les opérations dans l'espace [McComas, 2002]. Comme sur Terre, il devient donc essentiel de compenser les aberrations induites par la déformation des grands miroirs à l'aide de miroirs actifs.
La conception de systèmes actifs pour le spatial doit considérer des contraintes spécifiques telles que le poids, la compacité, la résistance mécanique, la consommation énergétique, la robustesse ou la fiabilité [CNES, 1998]. Dans ce manuscrit, nous présentons la définition, la mise en place et la caractérisation de système d'optique active dédiés qui permettront une rupture technologique pour la prochaine génération de télescopes spatiaux.

Dans le premier chapitre, l'optique active est présentée dans le contexte de l'astronomie moderne. Dans les deuxième et troisième chapitres, le projet MADRAS (Miroir Actif Déformable et Régulé pour Applications Spatiales) est décrit. Ce projet a permis le développement d'un démonstrateur de miroir correcteur actif, dédié à la compensation de la déformation des grands miroirs primaires dans l'espace. Dans le quatrième chapitre, le design d'un harnais de déformation pour le polissage sous contraintes d'un segment du futur télescope géant européen (European-Extremely Large Telescope: E-ELT) est introduit. Cette étude a permis de démontrer la possibilité et les avantages de fabriquer les segments en couplant un harnais de déformation simple à la technique de polissage avec un outil pleine taille. Dans le cinquième chapitre, la simplification à l'extrême des systèmes d'optique active est abordée. En partant de besoins de correction spécifiques, il est possible de concevoir des systèmes actifs avec un actionneur générant un mode optique.

L'optique active pour les grands projets instrumentaux

Grâce à une importante synergie entre télescopes spatiaux et télescopes terrestres, les grandes questions de l'astronomie moderne peuvent être adressées, améliorant ainsi notre connaissance de l'Univers, du système solaire à la cosmologie. L'observation de la Terre joue aussi un rôle majeur pour le développement de l'instrumentation spatiale. Le principal besoin pour les futures missions spatiales, défini par les buts scientifiques, est l'accès à une meilleure résolution angulaire avec une meilleure sensibilité et une haute stabilité du front d'onde. Pour cela, de nouveaux concepts de grands télescopes allégés, compacts ou déployables, doivent être développés et l'insertion de systèmes d'optique active sera indispensable pour obtenir la stabilité du front d'onde requise

[Postman et al., 2012].

En effet, le but de l'optique active est de contrôler le front d'onde dans les instruments optiques, via la forme et la déformation des miroirs [Murdin, 2000]. Ce contrôle, à des précisions nanométriques, rend possible la réalisation d'observations astronomiques de très grande qualité et facilite la réduction des données.
L'optique active est basée sur des miroirs déformables, dédiés et optimisés pour des besoins spécifiques. En permettant l'utilisation de composants de très bonnes qualité optique, avec des formes complexes, variables ou pas, cette technique présente de nombreux avantages et possède des applications variées [Freeman and Pearson, 1982]. Les trois domaines d'application de l'optique active sont le maintien de la forme optimale des grands miroirs, la correction in-situ d'aberrations optiques dans les instrument et le polissage sous contraintes d'optiques asphériques.
Le design d'un système actif est défini dans un premier temps grâce à la théorie de l'élasticité, décrivant notamment la déformation des plaques minces [Timoshenko and Woinowsky-Krieger, 1959]. Puis ce design est affiné et optimisé grâce à des analyses éléments finis, permettant une caractérisation complète du système [Smith and Griffiths, 2004].

Depuis une vingtaine d'années, l'optique active a permis des ruptures technologiques dans le domaine de l'instrumentation pour l'astronomie et est largement présente sur les grands télescopes terrestres. Le développement de systèmes d'optique active pour le spatial est donc la suite logique.

Miroir actif correcteur pour les télescopes spatiaux: le projet MADRAS

Jusqu'à maintenant, les différents concepts d'optique active ont été développés dans le cadre des observatoires terrestres. Avec l'augmentation de la taille des télescopes, le recours à des systèmes actifs deviendra bientôt indispensable dans l'espace [Feinberg et al., 2012]. Avec ses 18 segments actifs, le James Webb Space Telescope sera un précurseur dans ce domaine [Gardner et al., 2006].

Dans cette partie, nous présentons le design et la validation opto-mécanique du miroir MADRAS (Miroir Actif Déformable et Régulé pour Applications Spatiales) qui est un système correcteur dédié à la compensation in-situ de la déformation des grands miroirs primaires allégés dans l'espace. En effet, de tels miroirs vont être sensibles aux variations de l'environnement, ils seront notamment déformés par la dilatation thermique, dépendant de l'orbite du télescope et par la différence de gravité entre l'alignement sur Terre à 1g et les opérations dans l'espace à 0g [McComas, 2002; Kendrew, 2006]. Dans l'étude MADRAS, le système actif est conçu pour effectuer la correction du front d'onde dans le plan pupille de sortie du télescope, réduisant ainsi le poids, l'encombrement et le nombre d'actionneurs.

Premièrement, les spécifications de correction ont été définies en étudiant les déformations attendus dans les télescopes spatiaux de classe 3m. La projection des erreurs de front d'onde résultantes sur la base des polynômes de Zernike a permis d'identifier les aberrations optiques à corriger: ce sont les 9 premiers modes à des amplitudes maximales entre 30 et 200 nm rms [Thomas and Liotard, 2010].

Deuxièmement, le design mécanique du système a été optimisé grâce à des analyses par éléments finis, en considérant ces besoins de correction ainsi que sur les contraintes spécifiques du spatial. Le miroir actif est basé sur le principe de Miroir Déformable Multimode [Lemaître, 2005]. En

Zérodur, il est composé d'un ménisque central de 90 mm de diamètre, d'un anneau extérieur plus épais, de 12 bras et d'une attache central. 24 actionneurs piézoélectriques, placés aux 2 extrémités de chacun des bras, permettent de déformer la surface optique. Les analyses par éléments finis ont permis de caractériser complètement les performances du système. La précision de correction de chacun des modes optiques spécifiés a été déduite grâce à la projection de ces modes sur les fonctions d'influence du système. Tous les modes sont efficacement corrigés, avec des résidus de correction autour de 5 nm rms. La tenue mécanique du système a ensuite été vérifiée en étudiant le taux de contraintes dans le Zérodur. Une étude de tolérancement sur le modèle élément finis a permis de spécifier le miroir équipé et son intégration. Pour finir, l'analyse de l'impact d'actionneurs morts sur les performance du système a permis d'assurer sa fiabilité: même avec deux actionneurs morts, le miroir correcteur fonctionne toujours dans les spécifications.

Troisièmement, le système a été fabriqué et intégré. Le concept opto-mécanique a alors été validé par interférométrie: les fonctions d'influence mesurées sont équivalentes à celles simulées et les performances de correction attendues sont donc retrouvées. Cette étude permet de valider la modélisation du systèmes et nous donne les performances ultimes de celui-ci: les résidus après la correction des modes optiques spécifiés seront compris entre 1 et 6 nm rms et une erreur de front d'onde plus représentative (composée d'une combinaison aléatoire des modes spécifiés) sera corrigé avec une précision moyenne de 6 nm rms.

Enfin, le système MADRAS a été expérimentalement validé dans une configuration représentative. Le fonctionnement du miroir en boucle fermée a été démontré sur un banc de test dédié. Un simulateur de télescope génère les erreurs de front d'onde attendues dans les télescopes spatiaux. La boucle de correction active est composée du miroir MADRAS, piloté par un calculateur temps réel analysant les mesures d'un analyseur de surface d'onde Shack-Hartmann. Les effets de la correction sont également visualisés grâce à des caméras d'imagerie et à un interféromètre de Fizeau. En envoyant une erreur de front d'onde calibrée sur le miroir correcteur, ses performances ont été expérimentalement validées. Le système développé est capable de compenser les déformations attendues dans un télescope de 3 m avec une précision entre 6 et 8 nm rms.
Le fonctionnement du système actif développé a ainsi été complètement démontré.

En conclusion, le projet MADRAS a permis de démontrer les performances d'un miroir correcteur dédié à la compensation de la déformation d'un grand miroir dans l'espace.
Au lieu de maintenir la surface optique du miroir primaire, la correction est effectuée dans un relais de pupille, réduisant ainsi le nombre d'actionneurs et le poids du système. Le système développé a 24 actionneurs périphériques, il fait 130 mm de diamètre (pour une pupille de 90 mm) et 80 mm de haut, il pèse 4 kg et a été conçu en considérant les contraintes spécifiques du spatial (faible masse, taille, consommation énergétique, CTE, résistance mécanique, robustesse et fiabilité).
Le projet MADRAS a permis à la technologie de miroir actif d'atteindre un TRL4/5: le fonctionnement du système a été complètement validé en ambiance laboratoire et le design mécanique a été conçu en prenant en compte les contraintes du spatial (comportement en vide et en thermique et tenue mécanique au décollage).
Inséré dans le train optique des futurs télescopes, un tel miroir correcteur assurerait la stabilité du système tout en relâchant les spécifications sur l'assemblage et l'intégration.

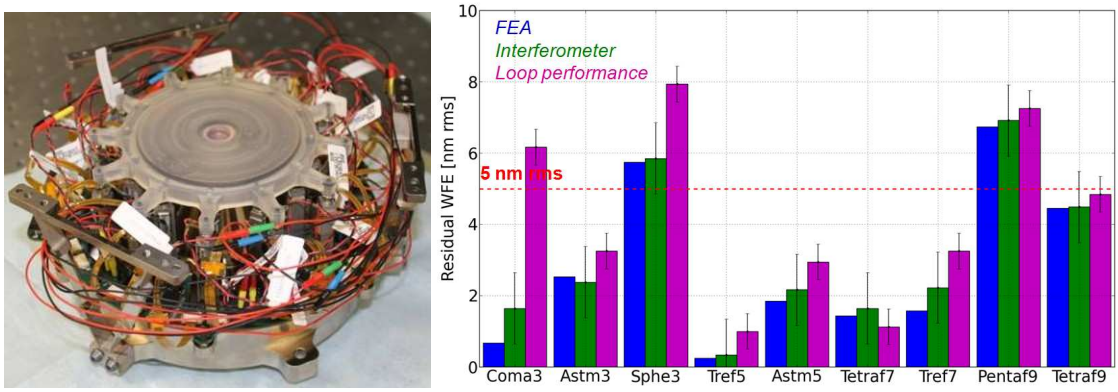

Figure A.1 : *Gauche: Le miroir MADRAS équipé - Droite: Précision de correction des 9 modes spécifiés (Bleu: performances simulées - Vert: performances déduites des mesures interférométriques - Violet: performances mesurées en boucle fermée).*

Télescopes géants: polissage sous contraintes d'un segment

La prochaine génération d'observatoires terrestres requière des télescopes de la classe 30-40 m. La réalisation de ces télescopes géants présentent de nombreux challenges technologiques, notamment en optique et en mécanique, et va mener à de nombreuses innovations [Delabre, 2008].
Les trois grands projets actuels de télescopes géants sont le Giant Magellan Telescope (24.5 m), le Thirty Meter Telescope (30 m) et le European Extremely Large Telescope (39 m). Pour des raisons de faisabilité de fabrication, ces télescopes seront segmentés: le GMT sera composé de sept segments circulaires de 8.4 m de diamètre et le TMT et l'E-ELT de respectivement 492 et 798 segment hexagonaux de 1.45 m [Cayrel, 2011]. La taille des segments vient des capacités de production actuelles: 8.4 m est le plus grand diamètre accessible pour des miroirs monolithiques et 1.45 m est le diamètre maximum des machines de polissage des principales entreprises.

Dans cette partie, nous étudions la possibilité d'utiliser la technique du polissage sous contraintes pour la production en masse du millier de segments de l'E-ELT. La technique du polissage sous contraintes consiste à déformer un blank, à le polir sphérique avec un outil pleine taille puis à relâcher les contraintes. Le miroir poli prendra alors l'inverse de la déformation appliquée initialement, et ce sans les erreurs de hautes fréquences spatiales qui auraient été induites par un polissage classique avec des petits outils [Lemaitre, 1972; Nelson et al., 1980].
Dans ce contexte, le concept de déformation de Miroir Déformable Multimode utilisé pour MADRAS a été adapté pour la conception d'un harnais de déformation pour polir sous contraintes un prototype de segment du miroir primaire de l'E-ELT. Le système a été entièrement fabriqué et intégré, il est actuellement en cours de test.

Les analyses par éléments finis ont permis d'optimiser la géométrie du harnais de déformation et de caractériser complètement les performances opto-mécaniques du système. Le harnais de déformation est composé d'un anneau et de 12 fourches externes, chaque fourche ayant 2 actionneurs. Le substrat de Zérodur est collé sur ce harnais et déformé selon la forme du segment de l'E-ELT le plus hors-axe (32 μm rms d'asphéricité). Les analyses par éléments finis ont montré que la mise sous contraintes est efficace: l'erreur sur la forme obtenue est de 20 nm rms.
Lors de l'étude nous avons également analysé les autres sources d'erreur: en anticipant les effets de la gravité et de la pression de polissage, il est possible de les compenser. L'application d'une pression uniforme sous la surface optique réduira en effet l'erreur de forme.

Finalement, en considérant les erreurs dues à la mise sous contraintes, à la gravité, au polissage et à la précision des actionneurs, la déformation résiduelle est inférieure à 25 nm rms.
La simulation de la dernière étape d'attaque ionique permet de prédire l'erreur de forme résiduelle finale: 3 nm rms.

Le système développé est actuellement testé: la surface optique sera mesurée avec un interféromètre de Fizeau et des capteurs de position et de force donneront une information directe sur le comportement mécanique du système. Cette caractérisation complète permettra de démontrer la précision de la déformation et de déterminer le meilleur moyen pour contrôler la déformation du miroir pendant le polissage pour une éventuelle industrialisation.

L'efficacité du polissage sous contraintes, quant à la qualité de surface obtenue et au gain de temps par rapport aux techniques classiques de polissage par petits outils, place cette technique comme un candidat sérieux pour la production en masse des segments de l'E-ELT. La réalisation d'un prototype de segment avec cette méthode permettra de franchir une étape supplémentaire vers son industrialisation.

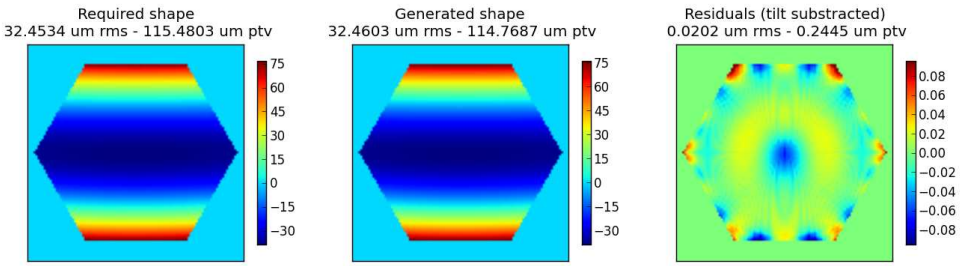

Figure A.2 : *Précision de la déformation du segment le plus hors-axe avec le harnais dédié (résultats de simulation - Unité:[µm]).*

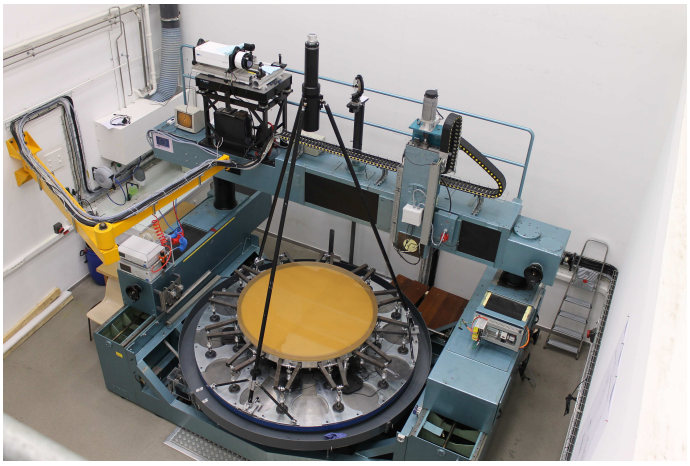

Figure A.3 : *Système complet pour le polissage sous contraintes: blank de Zérodur sur le harnais de déformation, sur la machine de polissage.*

Systèmes actifs optimisés: 1 actionneur - 1 mode

Les systèmes développés dans les parties précédentes, pour les projets MADRAS et E-ELT M1, possèdent 24 actionneurs. Pour MADRAS, ce nombre est nécessaire pour générer les modes spécifiés tout en assurant une certaine redondance. Pour les segments de l'E-ELT, il n'y a que trois modes à générer mais un système à 24 actionneurs est utilisé afin d'optimiser la déformation sur la périphérie du miroir.

Dans la plupart des instruments optiques, les besoins de correction sont limités à quelques modes. Un système actif ayant autant de modes propres que d'actionneurs, il est possible de concevoir des miroirs déformables simplifiés à l'extrême, avec un actionneur pour générer un mode optique. En partant d'un besoin de correction spécifique à un instrument, comme par exemple la compensation des aberrations dues à un chemin optique variable ou la compensation d'une déformation thermo-élastique, les modes à corriger peuvent être définis et le système optimal peut être conçu.

Dans cette partie, nous présentons deux concepts innovants de miroir actif avec un nombre minimum d'actionneurs: un actionneur par mode optique à corriger.
Les systèmes ont été développé à l'aide de la théorie de l'élasticité. La déformation de la surface optique est obtenue par l'application de moments mécaniques aux bords du miroir. Ces moments sont générés sur une plaque intermédiaire grâce à un actionneur appliquant une force. Ils sont ensuite transmis au miroir par un anneau flexible. Un tel système évite la génération d'effets d'empreinte de l'actionneur sur le miroir.
Ce design initial est ensuite modifié afin de générer les modes requis, pour cela des parties peuvent être ajoutés ou la géométrie adaptée.
VOALA (Variable Off-Axis paraboLA) est un concept de miroir actif à 3 actionneurs, permettant la génération de focus, astigmatisme et coma, qui sont les 3 principaux modes constituant une parabole hors axe. COMSA (Correcting Optimized Mirror with a Single Actuator) est un concept de miroir actif à actionneur unique, avec un contour adapté, il permet la génération d'une combinaison d'aberrations donnée.
Les performance de ces systèmes, dédiés à une application donnée, ont été optimisées et démontrées avec des analyses par éléments finis.

Grâce au nombre d'actionneur minimal, ce type de système est intéressant pour une application spatiale: il est facile à mettre en place et contrôler et il présente un poids et une consommation énergétique limités.
En offrant de nouvelles fonctions optiques, ces concepts ouvrent la voie à des architectures de télescope et d'instrument innovantes. Par exemple, un système de zoom basé sur deux miroirs actifs est à l'étude. Il est également envisagé d'inclure un miroir correcteur dans un interféromètre hors-axe, afin de compenser les aberrations non communes.
Les concepts développés permettront également une relaxation des contraintes et des coûts pour l'intégration des systèmes et leur stabilité.

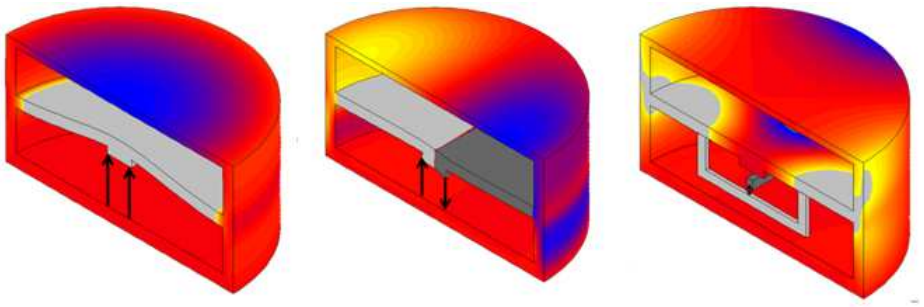

Figure A.4 : *Concept VOALA: Génération de focus, de coma et d'astigmatisme avec 3 actionneurs.*

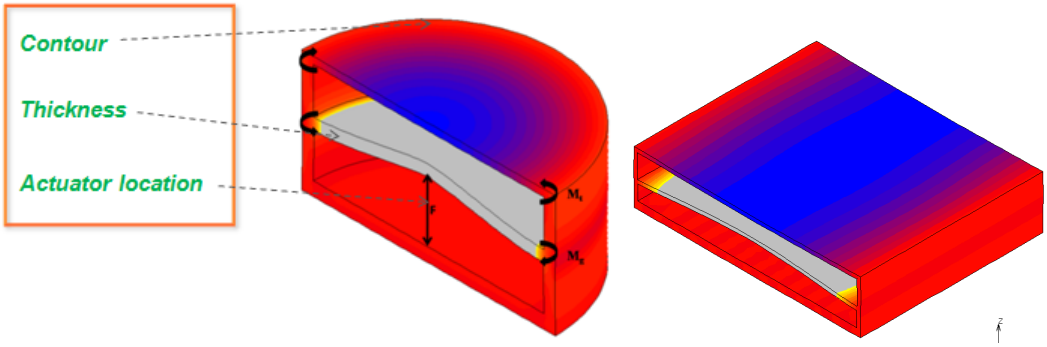

Figure A.5 : *Concept COMSA: Gauche: système circulaire générant du focus et paramètres à optimiser pour la génération des modes requis - Droite: exemple d'un système rectangulaire produisant une déformation cylindrique avec un unique actionneur.*

Conclusions

Afin d'atteindre une résolution angulaire et une puissance collectrice importante, le futur des télescopes réside dans les grands diamètres. Avec une telle évolution, l'obtention d'images de très bonne qualité nécessite un contrôle efficace du front d'onde, assurant la stabilité des systèmes.
La prochaine génération de télescopes spatiaux appartiendra à la classe 2-3 m pour l'observation de la Terre et à la classe 8 m pour l'observation de l'Univers. Ces dimensions impliquent l'utilisation de miroirs allégés, et éventuellement segmentés, afin de garder un poids et une taille raisonnable, compatible avec les coiffes de lanceurs. La future génération de télescopes terrestres appartiendra quant à elle à la classe 30-40 m. Pour des raisons de faisabilité, des miroirs segmentés et allégés seront également utilisés.

L'optique active est donc essentielle pour compenser la déformation de ces grands miroirs. Sur Terre, tous les télescopes de classe 8 m possèdent déjà des miroirs primaires actifs, compensant les effets de la gravité et les déformations thermo-élastique. Dans l'espace, les variations de l'environnement induiront également des déformations sur les structures allégées. Les deux contributions principales sont la différence de gravité entre l'intégration à $1g$ et les opérations à $0g$ ainsi que les variations thermiques dues aux cycles jour/nuit.
Dans ce cadre, le projet MADRAS, présenté dans la première partie de ce manuscrit, a conduit au développement et à la démonstration expérimentale d'un miroir correcteur actif capable de compenser les déformations attendues dans les futurs télescopes spatiaux.

L'optique active est également utilisée pour le développement de méthodes efficaces pour la fabrication de segments de télescopes. En combinant harnais de déformation et polissage par outils pleine taille, le polissage sous contraintes génère des surfaces optiques de grandes qualités, sans défauts de haute fréquence spatiale.
Dans ce cadre, le projet E-ELT M1, présenté dans la deuxième partie de ce manuscrit, a conduit au développement d'un harnais de déformation pour le polissage sous contraintes des segment du futur télescope géant européen.

Enfin, l'utilisation de systèmes correcteurs simples et dédiés permettrait de réduire le nombre d'éléments optiques, simplifiant ainsi les designs optiques. En offrant de nouvelles fonctions optiques, ceci permettrait l'émergence d'architectures d'instrument innovantes et relâcherait les contraintes quant à la stabilité des systèmes et leur intégration.
Dans ce cadre, les concepts VOALA et COMSA, présentés dans la troisième partie de ce manuscrit, proposent des systèmes d'optique active optimisés pour une application donnée, avec un nombre minimal d'actionneurs.

Les miroirs actifs présentés dans ce manuscrit permettent la génération d'aberrations optiques avec une grande précision, en considérant les erreurs de basse, moyenne et haute fréquences spatiales. Leur efficacité et leur nombre limité d'actionneurs rendent ces systèmes avantageux pour une utilisation dans les grands télescopes, notamment dans l'espace.

Perspectives

Le démonstrateur MADRAS a permis une avancée majeure en prouvant la possibilité et l'intérêt d'insérer un système actif simple dans un télescope spatial. Pour continuer ce développement, deux axes principaux doivent être étudiés: l'analyse de front d'onde et la technologie des actionneurs.

- Analyse de front d'onde
La meilleure stratégie à adopter pour le contrôle du miroir actif doit être déterminée. Les aberrations peuvent être mesurées dans le plan focal de l'instrument, grâce à des techniques de diversité de phase, dans le plan pupille, grâce à un analyseur de front d'onde de type Shack-Hartmann, ou encore directement sur le miroir, grâce à des capteurs mécaniques ou à de l'interférométrie. La référence doit aussi être définie, la correction peut être effectuée sur un front d'onde venant d'une étoile lointaine, d'une source de calibration interne ou de l'objet d'intérêt. Dans ce contexte, les techniques de diversité de phase et d'analyse de front d'onde de type Shack Hartmann sur une source défilante et étendue sont à l'étude et les deux techniques seront testées sur le banc de test MADRAS.

- Technologie d'actionneurs
Une étude importante sur les actionneurs doit être menée, notamment pour assurer la stabilité de la correction en boucle ouverte. Une étude comparative sera effectuée pour déterminer s'il est plus avantageux d'utiliser un système ultra stable ou une boucle de contrôle interne qui maintiendrait la position des actionneurs (avec des jauges de contraintes par exemple). Pour le moment, la meilleure solution semble être l'utilisation d'actionneurs mécanique, tel que des micro-moteurs,

capable de maintenir leur position même sans être alimentés.

Les performances des concepts VOALA et COMSA ont été caractérisées grâce à des analyses éléments finis. Comme pour le projet MADRAS, une validation expérimentale doit être effectuée. Dans ce but, un système de zoom hors axe contenant deux miroirs actifs basés sur ces concepts va être développé.
La fabrication de surfaces asphériques par polissage sous contraintes avec ce type de harnais de déformation pourrait également être démontrée expérimentalement et utilisée à moindre coût.
Enfin, de nombreuses applications peuvent être envisagées pour ces deux systèmes et la conception d'instrument innovant, basée sur ces miroirs actifs, constitue une étude intéressante. Parmi de nombreuses possibilités, trois développements peuvent être cités:

- l'insertion d'un système COMSA elliptique dans un interféromètre hors axe. Une telle application a déjà été étudiée mais doit toujours être réalisée.

- la conception d'un système actif pour la focalisation des étoiles laser, qui serait une avancée majeure pour l'optique adaptative assistée par étoile laser, pour les futurs télescope géants terrestres.

- l'élaboration d'un télescope segmenté reconfigurable, à pupille diluée avec des paraboles hors axes variables.

Pour les applications spatiales, la robustesse et la fiabilité des systèmes sont des aspects importants à considérer. Ainsi, la redondance des actionneurs est essentielle. Les systèmes développés ayant peu d'actionneurs, il est aisé d'intégrer plusieurs actionneurs en série afin d'éviter un point de panne unique. Nous avons vu que le miroir MADRAS présente une redondance intrinsèque, grâce au fait qu'il y a plus d'actionneurs que de modes à corriger. De la même manière, un miroir actif avec de nombreux actionneurs sous sa surface optique présentera une certaine redondance. Il permettra de plus l'utilisation de miroirs plus flexibles. Néanmoins, l'action directe des actionneurs sur le miroir va générer un effet d'empreinte et le poids des actionneurs et de leur électronique associée doit être pris en compte, tout comme la complexité de leur contrôle. Selon l'application, un choix doit être fait entre le poids du miroir, le nombre d'actionneur requis, la fiabilité du système et le coût.

L'intérêt de l'optique active a été démontré de nombreuses fois au cours des vingt dernières années. Cette technique a permis des ruptures technologiques dans le domaine de l'astronomie au sol, aidant ainsi à améliorer notre connaissance de l'univers. Il est maintenant logique de continuer cette approche en insérant des systèmes actifs dans la prochaine génération de télescopes spatiaux. A court terme, des miroirs correcteurs actifs seront utilisés pour compenser les déformations des grands miroirs primaires allégés, assurant l'obtention d'une qualité optique optimale. A long terme, le développement de systèmes d'optique active, offrant de nouvelles fonctions optiques, encouragera l'apparition d'architectures optiques innovantes et simplifiées qui amélioreront les possibilités d'observations.

Bibliography

M. Cayrel. M1 geometrical properties and construction parameters for the 39-M EELT. Technical report, ESO, 2011.

Z. Challita, E. Hugot, M. Ferrari, D. Le Mignant, S. Vives, and J.-G. Cuby. Extremely aspheric surfaces: toward a manufacturing process based on active optics. volume 8169 of *Society of Photo-Optical Instrumentation Engineers (SPIE) Conference Series*, September 2011.

CNES. *Cours de Technologie Spatiale - Technique et technologies des vehicules spatiaux*. 1998.

B. Delabre. Optical design for an adaptive anastigmatic five-mirror extremely large telescope. *Astronomy and Astrophysics*, 487:389–397, August 2008.

L. Feinberg, L. Cohen, B. Dean, W. Hayden, J. Howard, and R. Keski-Kuha. Space telescope design considerations. *Optical Engineering*, 51:011006, January 2012.

M. Ferrari. Development of a variable curvature mirror for the delay lines of the VLT interferometer. *Astronomy and Astrophysics*, 128:221–227, February 1998.

R. H. Freeman and J. E. Pearson. Deformable mirrors for all seasons and reasons. *Applied Optics*, 21:580–588, February 1982.

J. Gardner, J. Mather, M. Clampin, R. Doyon, and M. Greenhouse et al. The James Webb Space Telescope. *Space Science Review*, 123:485–606, April 2006.

J. W. Hardy. *Adaptive Optics for Astronomical Telescopes*. Oxford University Press, July 1998.

E. Hecht. *Optics 2nd edition*. Addison-Wesley Publishing Company, 1987.

S. Kendrew. *Lightweight Deformable Mirrors for Ground- and Space-Based Imaging Systems*. PhD thesis, University College London, 2006.

E.-D. Knohl. VLT primary support system. volume 2199 of *Society of Photo-Optical Instrumentation Engineers (SPIE) Conference Series*, pages 271–283, June 1994.

G. Lemaitre. New procedure for making Schmidt corrector plates. *Applied Optics*, 11:1630–1636, 1972.

G. R. Lemaître. Active Optics: Vase or Meniscus Multimode Mirrors and Degenerated Monomode Configurations. *Meccanica*, 40:233–249, 2005.

G. R. Lemaître. *Astronomical Optics and Elasticity Theory - Active Optics Methods*. Astronomy and Astrophysics Library. Springer, 2009.

B. K. McComas. *Configurable adaptive optics for the correction of space-based optical systems*. PhD thesis, University of Colorado at Boulder, 2002.

P. Murdin. *Active Optics*. Encyclopedia of Astronomy and Astrophysics, November 2000.

J. E. Nelson, G. Gabor, L. K. Hunt, J. Lubliner, and T. S. Mast. Stressed mirror polishing. 2: Fabrication of an off-axis section of a paraboloid. *Applied Optics*, 19:2341–2352, July 1980.

M. Postman, T. Brown, K. Sembach, M. Giavalisco, and W. Traub et al. Advanced Technology Large-Aperture Space Telescope: science drivers and technology developments. *Optical Engineering*, 51:011007, January 2012.

I.M. Smith and D.V. Griffiths. *Programming the Finite Element Method*. 4th edition. Wiley, 2004.

E. Thomas and A. Liotard. MADRAS - Spécifications de besoin de l'Optique Active. Technical report, Thales Alenia Space, 2010.

S. P. Timoshenko and S. Woinowsky-Krieger. *Theory of Plates and Shells*. Engineering Mechanics Series. McGRAW-Hill International Editions, 1959.

R. N. Wilson. *Reflecting Telescope Optics I. Basic Design Theory and its Historical Development.* Astronomy and Astrophysics Library. Springer, 1996.

R. N. Wilson. *Reflecting Telescope Optics II*. Astronomy and Astrophysics Library. Springer, 1999.

Appendix B

List of publications

Pending patents

M. Laslandes, M. Ferrari, E. Hugot, Correcting device with a deformable mirror for the compensation of at least one aberration with a known evolution, FR1153390 (CNES/TAS/CNRS/AMU), 2011.

M. Laslandes, E. Hugot, M. Ferrari, A. Liotard, Mirror with mechanical device to generate optical aberrations, FR1102805 (TAS/CNES/CNRS/AMU), 2011.

Publication in refereed journal

M. Laslandes, E. Hugot, M. Ferrari, Active optics: deformable mirrors with a minimum number of actuators, Journal of the European Optical Society, 2012.

SPIE proceedings

M. Laslandes, C. Hourtoule, E. Hugot, M. Ferrari, C. Lopez, C. Devilliers, A. Liotard, F. Chazallet, Space active optics: performance of a deformable mirror for in-situ wave-front correction in space telescope, SPIE 8442, 2012.

M. Laslandes, E. Hugot, M. Ferrari, Active Optics: deformation systems compensating for optical aberrations with a minimum number of actuators, SPIE 8450, 2012.

M. Laslandes, E. Hugot, M. Ferrari, G. Lemaitre, A. Liotard, Space active optics: toward optimized correcting mirrors for future large spaceborne observatories, SPIE 8167, 2011.

M. Laslandes, N. Rousselet, M. Ferrari, E. Hugot, J. Floriot, S. Vives, G. Lemaitre, J.F. Carré, M. Cayrel, Stress polishing of E-ELT segment at LAM - Full scale demonstrator status, SPIE 8169, 2011.

M. Laslandes, M. Ferrari, E. Hugot, G. Lemaitre, In-flight aberrations corrections for large space telescopes using active optics, SPIE 7739, 2010.

E. Hugot, M. Ferrari, S. Vives, **M. Laslandes**, K. El Hadi, S. Moindrot, G. Lemaitre, K. Dohlen, On the super polishing under stress of aspherical surfaces for exoplanet detection and solar instruments, SPIE 7739, 2010.

Other conferences proceedings

M. Laslandes, C. Hourtoule, E. Hugot, M. Ferrari, C. Devilliers, A. Liotard, C. Lopez, F. Chazallet, Last results of MADRAS, a space active optics demonstrator, International Conference of Space Optics, 2012.

M. Laslandes, M. Ferrari, E. Hugot, G. Lemaitre, Space Active Optics: in flight aberrations correction for the next generation of large space telescopes, International Conference of Space Optics, 2010.

M. Laslandes, M. Ferrari, E. Hugot, G. Lemaitre, Space Active Optics: in situ compensation of lightweight primary mirrors' deformations, Société Française de l'Astronomie et de l'Astrophysique (SF2A), 2010.

Appendix C

Active optics: deformable mirrors with a minimum number of actuators

---

Active optics: deformable mirrors with a minimum number of actuators

M. Laslandes Laboratoire d'Astrophysique de Marseille, 38 rue F. Joliot Curie, Marseille, France
marie.laslandes@oamp.fr

E. Hugot Laboratoire d'Astrophysique de Marseille, 38 rue F. Joliot Curie, Marseille, France

M. Ferrari Laboratoire d'Astrophysique de Marseille, 38 rue F. Joliot Curie, Marseille, France

We present two concepts of deformable mirror to compensate for first order optical aberrations. Deformation systems are designed using both elasticity theory and Finite Element Analysis in order to minimize the number of actuators. Starting from instrument specifications, we explain the methodology to design dedicated deformable mirrors. The work presented here leads to correcting devices optimized for specific functions. The Variable Off-Axis paraboLA concept is a 3-actuators, 3-modes system able to generate independently Focus, Astigmatism and Coma. The Correcting Optimized Mirror with a Single Actuator is a 1-actuator system able to generate a given combination of optical aberrations.
[DOI: http://dx.doi.org/10.2971/jeos.2012.12036]

Keywords: Active optics, deformable mirror, telescope, optical aberration, wave-front error correction, off-axis parabola

1 ACTIVE OPTICS TO CONTROL THE WAVE-FRONT

1.1 Active optics in astronomy

Using deformable mirrors, active optics allows a wave-front control at nanometric precisions, ensuring optimal performance for the optical instrument [1]. For about twenty years, Earth-based telescopes have benefited from active optics systems, in three main domains.

The first application of active optics is the maintaining of large mirrors optimal shape with actuators located under their optical surfaces. On Earth, the 8m-class telescopes have active primary mirrors, compensating for gravity effects and thermo-elastic deformations. Developed and proved by Wilson on the ESO New Technology Telescope [2], these systems are now widely used on 8-10 m-class telescopes, such as Gemini North and South, Keck, Gran Telescopio Canarias (GTC) or Very Large Telescope (VLT). For instance, the VLT 8.2 m primary mirror is maintained by 150 push/pull actuators [3].

The second application consists in the use of dynamic optical components: active mirrors are used in variable optical designs, to compensate for aberrations induced by moving elements. Variable Curvature Mirrors (VCM), developed by Ferrari [4], provide this type of correction for the VLT interferometric mode. The beams from the different telescopes are recombined through moving delay lines. An efficient pupil stabilization is achieved with the application of a pressure under the VCMs' optical surfaces.

The third application is the generation of high optical quality aspherical mirror, using stress polishing. Proposed in the 1930's by Schmidt [5] for the polishing of the entrance correcting lens of his wide field telescope, this method has been improved by Lemaitre in 1974 [6]. It allows the achievement of an aspherical mirror without high spatial frequency errors, by polishing a deformed optical substrate, under constraints, with a full size tool. An interesting application of stress mirror polishing is the manufacturing of off-axis parabola for large segmented mirrors, it has notably been used by Nelson for the 36 segments of the Keck observatory primary mirrors [7].

As we can see through these three types of use, the key element of active optics is a deformable mirror, designed and optimized to fit specific requirements.

1.2 Evolution of deformable mirror and correction needs

Active optics is complementary to adaptive optics. On the one hand, the goal of adaptive optics is to correct high temporal and spatial frequency errors [8]. On the other hand, the goal of active optics is to compensate for low order optical aberrations in the simplest and most efficient way. The Wave-Front Errors (WFE) are classically decomposed on an orthonormal polynomials base, such as the Zernike polynomials, describing the optical aberrations [9]. In many cases, the correction need is limited to a few modes. For Infra-Red and visible applications, the required precision of correction is on the order of tens nanometer ($\lambda/20$).

Received June 13, 2012; revised ms. received July 12, 2012; published September 06, 2012 ISSN 1990-2573

The problematic of maintaining mirrors' shapes begins to appear in space telescopes, large lightweight primary mirrors will be sensitive to the environment variations and the induced thermo-elastic deformations will have to be compensated [10, 11]. For a space use, the system simplicity and reliability are mandatory [12].

Stress polishing would also benefit from a simplification of warping systems. Nowadays, the main application of this technique lies in the manufacturing of large mirrors' segments. For instance, it is studied in the framework of the future European Extremely Large Telescope, for the mass production of the thousand segments forming the primary mirror [13]. In such a case, it is important to have a simple deformation system, optimized for the required optical shape, improving the process efficiency.

Finally, active systems optimization finds a direct application for variable optical components. As well as the thermo-elastic deformation can be predicted with Finite Element Analysis, the aberrations induced by an instrument reconfiguration can be easily anticipated in the early instrument design phases, using ray-tracing software. Knowing the wave-front errors that would have to be compensated, a dedicated correcting system can be conceived.

In this paper, we present active systems optimized to the extreme: an optical mode is corrected with a single actuation point. The interest of such a minimization lies in the set-up and monitoring easiness, but also in the limited weight and power consumption of the systems.

The design of deformation system is based on the elasticity theory, describing the mechanical behavior of plates under given boundary conditions [14]. A mirror can be deformed by many ways, such as the application of forces, displacements, bending moments or pressure [15]. There are also many actuator technologies: mechanic, magnetic, electric or piezoelectric.

Some works present deformable mirrors with a limited number of actuators but none have pushed the limits to a single actuator. For instance, Dainty has developed a 9 channels bimorph deformable mirrors, to generate focus, astigmatism, coma and spherical aberrations [16], and Freeman presents a 3-actuators deformable mirror able to generate focus and astigmatism [17]. In these systems, the forces are directly applied on the optical surface, inducing a print-through effect. The resulting high spatial frequency errors deteriorate the correction performance.

In the work presented here, the number of actuator is minimized by deporting the forces far from the optical surface. In this manner, the number of actuators is uncoupled from the mirror diameter and the generation of high spatial frequency errors is avoided. Moreover, it dissociates the actuator precision from the shape generation precision and it makes the deformable mirror independent of the actuator technology. By coupling elasticity equations and Finite Element Analysis, we detail hereafter innovative and simple concepts to warp mirrors.

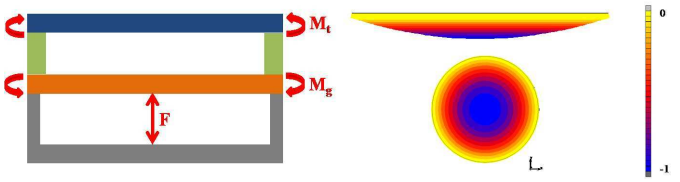

FIG. 1 Left: Transverse section of a circular system generating Focus (blank in blue, intermediate plate in orange, ring in green and clamping system in grey). The application of a force F on the intermediate plate induces bending moments at the plate edges ($M_g = Fa$), which are transmitted to the mirror edges ($M_t = M_g$). Right: Views of the deformation induced on the optical surface (from FEA).

2 ADAPTING THE INFLUENCE FUNCTIONS TO THE CORRECTION REQUIREMENTS

The concepts developed for the minimization of the number of actuators are based on the elasticity theory, and particularly on the deformation of a thin shell through the application of bending moments at its edges, as described by Timoshenko [14]. The input for the optimization is the correction requirement. The goal is then to match the system's influence functions with the optical modes to be corrected, in order to have one actuator per mode.

The first concept, Variable Off-Axis paraboLA (VOALA), allows the generation of focus, astigmatism and coma with three actuators, each actuator driving a mode [18]. The second concept, Correcting Optimized Mirror with a Single Actuator (COMSA), allows the generation of a given combination of aberrations with only one actuator [19].

2.1 Principle: mirror curvature modification

Both concepts are based on the modification of an optical surface curvature through the application of uniform bending moments at its edges. These moments are generated on an intermediate plate with a central force and transmitted to the mirror via a flexible outer ring. As it can be seen on Figure 1, such a system is constituted of five main parts: three plates (mirror, intermediate plate and rigid reference plate) and two rings linking the plates together. The central actuator, applying a force or a displacement on the system, is located between the intermediate and reference plates.

On a circular blank of semi-diameter a, the moments generated at the intermediate plate edges by the central force F are constant: $M_g = Fa$. These moments are transmitted at the edges of the mirror: $M_t = M_g$. The induced mirror deformation z_{mirror} is deduced from the elasticity equation describing this load-case (application of bending moments M_t at the edges of an axisymmetric clamped plate) [14]:

$$D\frac{\partial^2 z_{mirror}}{\partial r^2} = -M_t, \tag{1}$$

with D the plate rigidity, ν the Poisson ratio and the following boundary conditions:

$$z_{mirror}(r=a) = 0 \quad \text{and} \quad \frac{\partial z_{mirror}}{\partial r}(r=0) = 0. \tag{2}$$

The resolution of this differential equation conducts to a focus

	α_{ij} (RMS) - first order approximation	Z_{ij}
Focus	$\alpha_{20} = \frac{a^2}{2\sqrt{3}k}\frac{2-C\epsilon^2}{4(1-C\epsilon^2)^{3/2}}$	$Z_{20} = \sqrt{3}(2\rho^2-1)$
Astm3	$\alpha_{22} = \frac{a^2}{\sqrt{6}k}\frac{C\epsilon^2}{4(1-C\epsilon^2)^{3/2}}$	$Z_{22} = \sqrt{6}\rho^2 cos(2\theta)$
Coma3	$\alpha_{31} = \frac{a^3}{3\sqrt{8}k^2}\frac{C\epsilon[1-(C+1)\epsilon^2]^{1/2}(4-C\epsilon^2)}{8(1-C\epsilon^2)^3}$	$Z_{31} = \sqrt{8}(3\rho^2-2)\rho cos(\theta)$
Tref5	$\alpha_{33} = \frac{a^3}{\sqrt{8}k^2}\frac{C^2\epsilon^3[1-(C+1)\epsilon^2]^{1/2}}{8(1-C\epsilon^2)^3}$	$Z_{33} = \sqrt{8}\rho^3 cos(3\theta)$
Sphe3	$\alpha_{40} = \frac{a^4}{6\sqrt{5}k^3}\frac{8(C+1)-24K\epsilon^2+3C^2\epsilon^4(1-3C)-C^3\epsilon^6(2-C)}{64(1-C\epsilon^2)^{9/2}}$	$Z_{40} = \sqrt{5}(6\rho^4-6\rho^2+1)$
Astm5	$\alpha_{42} = \frac{a^4}{4\sqrt{10}k^3}\frac{-C\epsilon^2(1+5C-C\epsilon^2(6+5C)}{16(1-C\epsilon^2)^{7/2}}$	$Z_{42} = \sqrt{10}(4\rho^2-3)\rho^2 cos(2\theta)$

TABLE 1 Equations of Zernike coefficients and polynomials as a function of OAP characteristics (with the reduced parameter $\epsilon = R/k$).

mode:

$$z_{mirror}(r) = -\frac{M_t}{2D}(r^2 - a^2). \quad (3)$$

We will see thereafter how to adapt this principle to generate other aberrations.

2.2 Design and analysis methods

Minimizing the number of actuators is only possible with a strong preliminary work to specify the correction requirements. Starting with an instrument design and operating environment, the Wave-Front Error (WFE) can be predicted and decomposed on optical modes. An optical mode is defined as a given combination of optical aberrations (such as focus, astigmatism or coma). The problematic is then to design an active mirror compensating for the expected WFE with a single actuator for each required optical mode. This is achieved by adapting the geometry of the system described in Figure 1.

The elasticity equations give the right bending moments to apply at the edges of the mirror in order to generate the required optical surface deformation. It defines the main system characteristics. Then, Finite Element Analysis (FEA) is performed for optimization [20], considering both optical quality and mechanical system strength. The optimization output parameters are the system dimensions, its materials and the actuators characteristics while the optimization criteria are the optical surface shape z_{mirror}, compared to the required deformation $z_{required}$, but also the maximum level of stress in the material σ_{max}, and the required force F. A classical least square approach [21] is used to converge to the deformation system design minimizing the quantity α defined in Eq. (4):

$$\begin{aligned}&\alpha(geometry, material, actuator)\\ &=\lambda_{res}\| z_{mirror} - z_{required} \|^2 + \lambda_\sigma \sigma_{max} + \lambda_F F, \end{aligned} \quad (4)$$

where $z_{mirror} - z_{required}$ is the residual deformation and λ is a weight given to each parameter. The deformable mirror performance is characterized with its precision p, defined as:

$$p = \| z_{mirror} - z_{required} \|^2 / \| z_{required} \|^2. \quad (5)$$

3 OFF-AXIS PARABOLA GENERATION WITH A 3-ACTUATORS SYSTEM

3.1 Application domain

An Off-Axis Parabola is characterized by its pupil semi-diameter a, radius of curvature k, conic constant C and off-axis distance R. As described by Lubliner & Nelson [22], the optical surface shape z_{mirror}, can be deduced from these parameters. It is composed of a sphere plus terms corresponding to the first optical aberrations:

$$z_{mirror}(\rho, \theta, a, k, R, C) = \sum \alpha_{ij}(a, k, R, C) Z_{ij}(\rho, \theta) \quad (6)$$

where α_{ij} are the optical modes amplitudes and Z_{ij} the Zernike polynomials, described in Table 1.

Starting with the equations giving the amplitude of each Zernike polynomial as a function of the OAP characteristics, we can define a domain where the first three aberrations are predominant compared to the others. We consider that Trefoil5, Spherical3 and Astigmatism5 are negligible when their amplitudes are lower than a given threshold a_{th} which depends on the considered application. It gives conditions on quadruplets (a,k,C,R):

$$\begin{cases} \alpha_{33} < a_{th} => a < \left[a_{th}\sqrt{8}k^2 \frac{8(1-C\epsilon^2)^3}{C^2\epsilon^3[1-(C+1)\epsilon^2]^{1/2}} \right]^{1/3} \\ \alpha_{40} < a_{th} \\ => a < \left[a_{th} 6\sqrt{5}k^3 \frac{64(1-C\epsilon^2)^{9/2}}{8(C+1)-24C\epsilon^2+3C^2\epsilon^4(1-3C)-C^3\epsilon^6(2-C)} \right]^{1/4} \\ \alpha_{42} < a_{th} => a < \left[a_{th} 4\sqrt{10}k^3 \frac{16(1-C\epsilon^2)^{7/2}}{-C\epsilon^2(1+5C-C\epsilon^2(6+5C)} \right]^{1/4}. \end{cases} \quad (7)$$

The Variable Off-Axis paraboLA concept is a 3-actuators deformation device designed to generate any combination of Focus, Astigmatism3 and Coma3, in the limit of actuators stroke and system's mechanical strength. Thus, for a given maximal amplitude of residual aberrations, the set of OAPs achievable with the VOALA system can be defined.

3.2 Focus and coma generation

As explained in Section 2.1, a circular plate can be deformed in a focus mode by applying constant uniform bending moment at its edges. These moments are generated on an intermediate plate with a central force. On the same principle, we search for the moment distribution to apply at the mirror edges to generate a coma mode. The link between bending moments and plate deformation is given by the elasticity theory [14]:

$$M_t(r,\theta) = -D[\frac{\partial^2 z(r,\theta)}{\partial r^2} + \nu(\frac{1}{r}\frac{\partial z(r,\theta)}{\partial r} + \frac{1}{r^2}\frac{\partial^2 z(r,\theta)}{\partial \theta^2})], \quad (8)$$

with D the plate rigidity and $z(r,\theta)$ the required plate deformation in cylindrical coordinates:

$$z(r,\theta) = \left[\left(\frac{r}{a}\right)^2 - 1 \right] \frac{r}{a} cos(\theta), \quad (9)$$

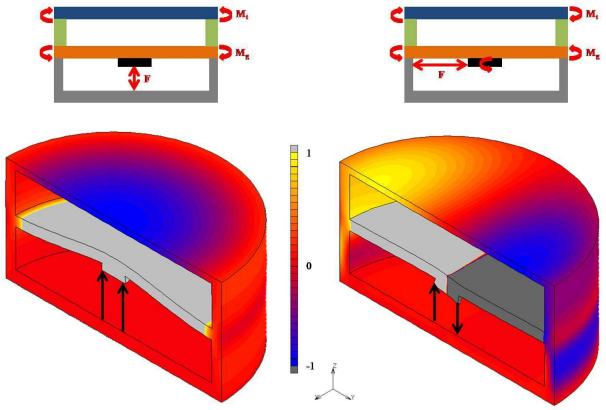

FIG. 2 Top: Principle of generation of Focus (left) and Coma (right) with the VOALA concept. Bottom: FEA model of the 2-actuators system presenting the deformations obtained with the load cases corresponding to Focus and Coma generations.

Combining Eq. (8) and (9), we obtained the expression of bending moments at the mirror edges:

$$M(r=a,\theta) = \frac{-2D}{a^2}(3+\nu)cos(\theta). \tag{10}$$

We deduce that the application of an azimuthal moment distribution at the mirror edges induces a coma mode on the optical surface.

As described by Timoshenko, such a moment distribution is achieved through the application of a central mechanical moment on the intermediate plate. To generate the central moment, a central pad is added on the intermediate plate and a transverse force is applied on this pad. Figure 2 presents the required load cases on the system to generate focus and coma. Combining the actions of two actuators located on a pad diameter, both modes can be generated. If the two forces are equal, it corresponds to a central force application and leads to a focus. If the two forces are opposite, it corresponds to a central moment application and leads to a coma. Other forces configurations correspond to combinations of focus and coma.

3.3 Astigmatism generation

The principle of astigmatism generation with one actuator, developed by Hugot [23], can be added to the previous system. An astigmatism figure can be generated by applying two pairs of opposite forces on two orthogonal diameters of the intermediate plate. On the finite element model, we study the evolution of the deformation in function of the forces diameter. The optimum diameter is the one minimizing the residual deformation. The four forces can be generated from a single point, located between two rigid orthogonal beams. Each beam is linked to two points of the diameter. Applying a central force pushing aside the two beams, the required forces are transmitted on the four points.

Figure 3 presents the FEA model for this astigmatism generation. We can note that the two-beams system can conveniently be installed on either side of the intermediate plate, depending on the available space.

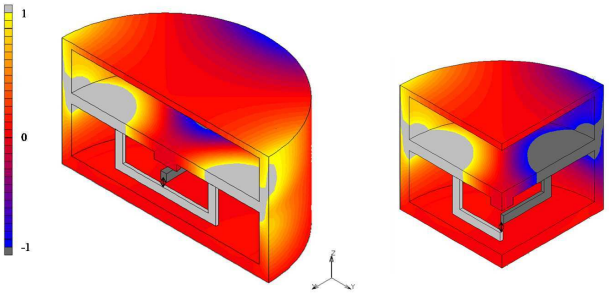

FIG. 3 FEA model presenting the principle of Astigmatism generation with VOALA.

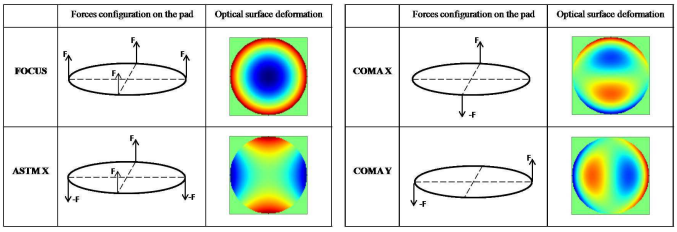

FIG. 4 Variant of the VOALA design: generation of 4 Zernike polynomials with 4 actuators on the pad. A fifth actuator allowing a system rotation can be added in order to generate the second astigmatism mode.

3.4 Modes combination and alternative design

The 3-actuators system described above is able to compensate for combinations of focus, astigmatism and coma. One actuator directly drives the astigmatism generation while focus and coma are generated with a combination of the two other actuators. But with this system, coma and astigmatism are oriented. Astigmatisms in both x and y directions could be generated with an additional beams system, turned of $\pi/4$ in comparison to the first one. It is also conceivable to integrate the deformable mirror on a rotating platform, driven by one actuator, the system rotation will then allow the generation of both astigmatisms.

An interesting alternative appears with the generation of the two comas: with 4 actuators, located on the pad, on two orthogonal diameters, focus, coma x, coma y and astigmatism x (or y) can be created. Figure 4 presents the load cases for the generation of each mode. As explained just above, a fifth actuator rotating the system would provide the last astigmatism. This improvement leads to a 5 actuators - 5 modes deformable mirror.

4 SINGLE ACTUATOR DEFORMABLE MIRROR

In some instruments, the wave-front to be corrected and its evolution can be predicted using ray-tracing models. If the correction need is a combination of optical aberrations, evolving linearly with time, the Wave-Front Error (WFE) can be defined as a composite optical mode:

$$WFE(t) = A(t)\sum \alpha_{ij} Z_{ij}, \tag{11}$$

with Z_{ij} given Zernike polynomials, α_{ij} their initial amplitudes and $A(t)$ a coefficient giving their evolution with time.

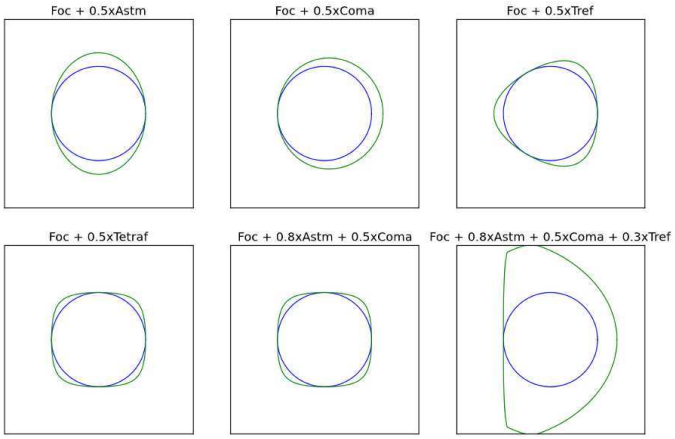

FIG. 5 Contours for different optical modes combinations (circular pupil contour in blue).

For instance, correcting mirrors can be used to compensate for Optical Path Difference (OPD) in off-axis interferometers, where differential aberrations in the instrument arms will be focus, astigmatism and eventually coma and tilt, evolving linearly with the interferometer arms length. It is then possible to adapt the single actuator concept presented in Section 2.1 to generate the required deformation (see Figure 1). The design method consists in modifying the system geometry to match the actuator influence function with the correction need. The three parameters to be optimized are the system contour, the intermediate plate thickness distribution and the actuator location.

4.1 Contour adaptation

An angular modulation of the radius of curvature can be achieved by modifying the system contour according to the combination of modes to be generated.

The contour ρ_c is defined as a function of the required deformation on the circular pupil: $z(\rho,\theta) = \sum \alpha_{ij} Z_{ij}(\rho,\theta)$. The system's boundary condition defines the contour: the mirror has clamped edges. So, the required deformation is extended until it crosses the $z = 0$ plane and the system contour corresponds to the intersection between this plane and the deformation surface. This contour is expressed as a function of the angular coordinate θ, and the modes amplitudes α_{ij}, as described in Eq. (12):

$$z(\rho_c,\theta) = \sum \alpha_{ij} Z_{ij}(\rho_c,\theta) = 0 => \rho_c = f(\theta,\alpha_{ij}). \quad (12)$$

Figure 5 presents examples of contour computed to generate given aberrations combinations.

4.2 Thickness distribution

The moment distribution at intermediate plate edges M_g, is generated with a central force on this plate. So, the system contour defines the bending moment modulation:

$$M_g(\theta) = F\rho_c(\theta) = F\frac{r_c(\theta)}{a}, \quad (13)$$

where F is the applied force, $r_c(\theta)$ is the distance from the center to the edge for a given orientation and a is the optical pupil radius.

On the other hand, as seen in Section 3.2, the bending moment modulation M_t to apply at mirror edges to produce the required deformation, $z(r,\theta)$ is given by the elasticity theory [14]:

$$M_t(\theta) = -\frac{Et^3}{12(1-\nu^2)}\Big[\frac{\partial^2 z(r_c,\theta)}{\partial r_c(\theta)^2} + \nu\Big(\frac{1}{r_c(\theta)}\frac{\partial z(r_c,\theta)}{\partial r_c(\theta)} + \frac{1}{r_c(\theta)^2}\frac{\partial^2 z(r_c,\theta)}{\partial \theta^2}\Big)\Big], \quad (14)$$

where t is the plate thickness, E its Young modulus and ν its Poisson ratio.

The generated moments M_g are transmitted to the mirror edges (M_t) and induce the optical surface deformation. Solving $M_g(\theta) = M_t(\theta)$ gives the angular thickness distribution of the intermediate plate, $t_c(\theta)$, generating the required bending moments with the system contour:

$$t_c(\theta) = \left[\frac{12(1-\nu^2)F}{E}\frac{r_c(\theta)}{a}\Big(\frac{\partial^2 z(r_c,\theta)}{\partial r_c(\theta)^2} + \nu\Big(\frac{1}{r_c(\theta)}\frac{\partial z(r_c,\theta)}{\partial r_c(\theta)} + \frac{1}{r_c(\theta)^2}\frac{\partial^2 z(r_c,\theta)}{\partial \theta^2}\Big)\Big)^{-1}\right]^{1/3}. \quad (15)$$

4.3 Actuator location

The last system parameter is the force location. We have seen in Eq. (13) that the transmitted bending moments depend on the distance between the force location and the edges. Considering a decentering of (x_d, y_d), the new distance $r'_c(\theta)$ induces a new bending moment modulation and Eq. (13) becomes:

$$M_g(\theta) = F\frac{r'_c(\theta)}{a} = \frac{F}{a}\sqrt{r_c(\theta)^2 + x_d^2 + y_d^2 - 2r_c(\theta)(x_d cos(\theta) + y_d sin(\theta))}. \quad (16)$$

The induced modulation in $cos(\theta)$ and $sin(\theta)$ corresponds to a generation of tilt and coma, their amplitudes depending on the shifting distance. So, these two modes can be generated either by defining a specific contour or by decentering the actuator. In order not to damage the other modes quality, the thickness distribution can be recalculated equalizing Eq. (14) and (16).

5 SYSTEMS PERFORMANCE ANALYSIS WITH A STUDY CASE

In order to use the deformable mirrors in optical systems for visible or infra-red observations, the systems' residual wavefront error is specified around $\lambda/20$. Thus, our goal is to design deformation systems accurate to a few tens of nanometers.

As a study case, we consider the generation of a 100 mm diameter Off-Axis Parabola, with a focal ratio of 1, and a 45° off-axis angle. Using the formulas describing an OAP [22], such

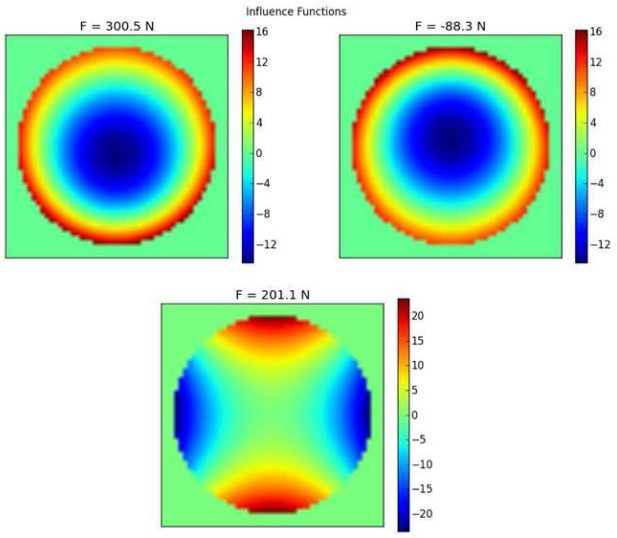

FIG. 6 VOALA system influence functions (1st actuator on the central pad - 2nd actuator on the central pad - 3rd actuator between the two beams) and their projection coefficients to generate the required OAP (deformation maps unit = nm) (FEA results).

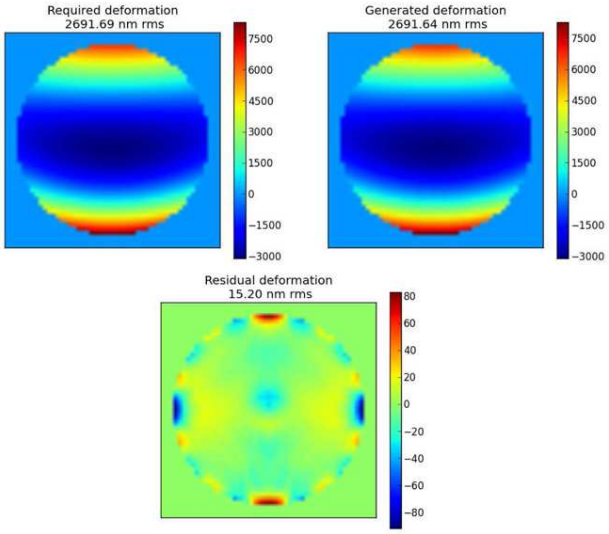

FIG. 7 VOALA system performance for the OAP generation: Required deformation - Deformation generated on the optical surface with the 3 actuators - Residual deformation (Unit = nm) (FEA results).

an optical shape can be decomposed as a sphere of radius 200 mm plus terms of focus ($\alpha_{20} = 1.73$ µm rms), astigmatism3 ($\alpha_{22} = 2.03$ µm rms) and coma3 ($\alpha_{31} = 0.35$ µm rms).

Both systems are designed as described in the previous sections and we present hereafter their performance, computed with Finite Element Analysis. For this example, the systems are simulated as monolithic pieces. The material chosen is aluminum, for its flexibility (Young's modulus $E = 75$ GPa, Poisson ratio $\nu = 0.33$). Both finite element models have 115230 hexaedral elements and 139350 nodes, with a sampling of 7600 nodes on the optical surface, allowing a good characterization of the optical quality. The back face of the reference plate is fixed and the forces are applied on the intermediate plate to simulate the actuators. For a prototyping it is planned to assemble 3 parts together: the central part will consist in the intermediate plate with the 2 rings, the mirror will be glued on the top ring and the reference plate will be glued on the bottom ring (see Figure 1). From the Finite Element Analysis, the systems' performance are characterized by computing the optical precision, defined as the difference between required and generated shapes.

5.1 VOALA performance

The required mirror shape is decomposed on the three system's influence functions, recovered on the Finite Element model: it gives the values of the forces to be applied by each actuator (see Figure 6). As we can see in Figure 7, the mirror shape is generated with a high precision: the residual deformation is 15.2 nm rms and is mainly composed of astigmatism harmonics.

Such a system is interesting to generate different OAPs, ie different combinations of focus, astigmatism and coma. To determine an optimal range of use, we characterize the generation of each mode separately (see Table 2). With a 0.2 % precision the focus generation is highly efficient and it does not require a lot of force, so it is not a critical mode. Astigmatism is generated with 0.7 % precision, the required force is almost twice higher than for the focus but it is split among 4 points on the system so this mode will not induce too much mechanical stress either. As the required amplitude of coma was lower of one order of magnitude compared to the other modes, its weight in the system optimization was less important. It leads to a generation of coma slightly less efficient: 1.1 % of residual deformation with higher forces required on the actuators.

5.2 COMSA performance

Starting with the given combination of optical aberrations, we apply the methodology explained in Section 4 to design the COMSA system. The computed contour and thickness distribution are presented in Figure 8. This Figure also shows the combinations of aberrations achievable with such a system and the corresponding OAPs: the optical shape evolves linearly with the value of the applied force:

$$z_{mirror}(\rho,\theta,F) = A(F)(\alpha_{20}Z_{20}(\rho,\theta) + \alpha_{22}Z_{22}(\rho,\theta) + \alpha_{31}Z_{31}(\rho,\theta)), \quad (17)$$

with $A(F)$ a coefficient linking the amplitude of the deformation to the force F.

The system design is finally optimized with Finite Element Analysis, as described in Section 2.2. The Finite Element model performance is promising: with only one actuator, the required mirror shape is generated with high precision: the residual deformation is 14.4 nm rms for an optical surface shape of 2.7 µm rms (see Figure 9), and it can generate the set of OAPs shown in Figure 8 with this precision of 0.5%.

6 CONCLUSION

The two concepts presented in this paper allow the generation of an optical mode with one actuator. Moreover, the number

	Act1 (pad) (N)	Act2 (pad) (N)	Act3 (beams) (N)	Residues (nm rms)
FOCUS	61.3	61.3	0	1.92
COMA	555.4	-555.4	0	10.94
ASTM	0	0	99.9	7.01

TABLE 2 System performance for the generation of 1 µm rms of each mode with the VOALA system (FEA results).

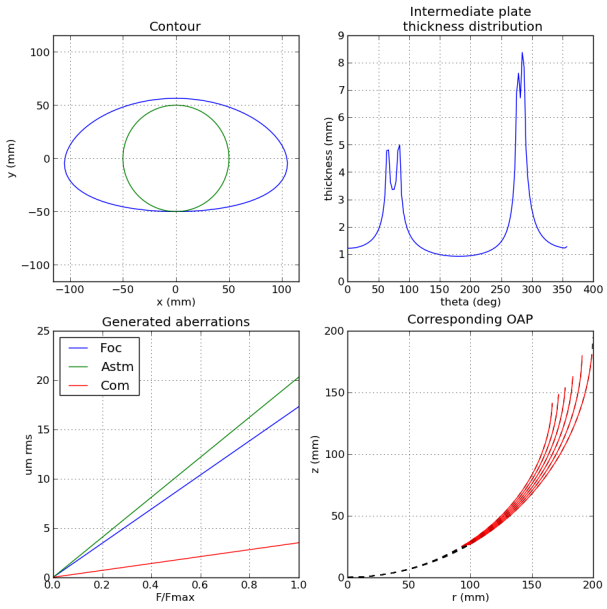

FIG. 8 Analytical solution for OAP generation with COMSA: System contour and thickness distribution defined by the required OAP - Aberrations achievable with such a system - Corresponding OAP.

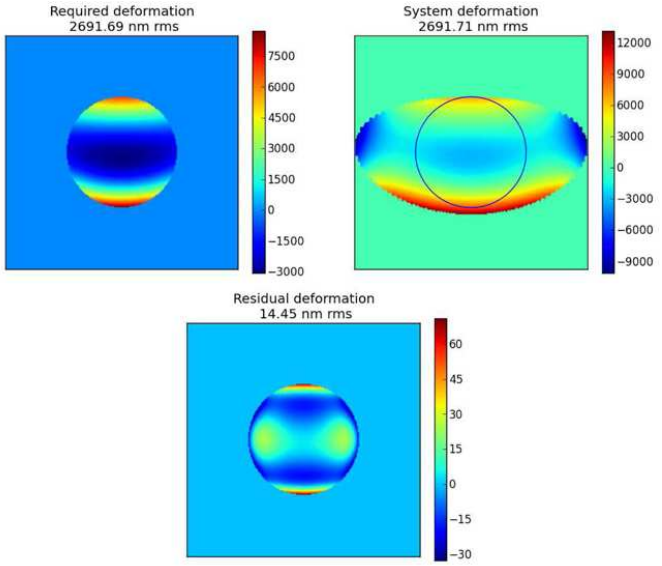

FIG. 9 COMSA system performance: Required deformation (deduced from the OAP characteristics) - Optical surface deformation (generated by the actuator force) - Residual deformation on the pupil (Unit = nm) (FEA results).

of actuators does not depend on the mirror size and its action does not induce high spatial frequency errors. The optical surface is deformed through the application of bending moments at the mirror edges. The system geometry is relatively simple: the bending moments are generated by the application of forces on an intermediate plate and they are transmitted to the mirror with a ring linking the plates together. This warping structure is clamped on a reference plate through another ring. The VOALA system is able to generate independently focus, astigmatism and coma with one actuator per mode. The COMSA system has a single actuator, generating a given combination of optical aberrations. Such optimized systems are designed to fill-in an optical function defined by a specific instrument design and they will allow an efficient wave front error compensation. The expected performance of these active optics systems have been computed with Finite Element Analysis, showing excellent performance for visible/IR applications. The next step is the manufacturing of prototypes to experimentally validate the simulation results. We have already done this work on different deformable systems [24, 25], allowing the validation of our Finite Element Analysis method and the correlation of simulated and experimental results.

With a minimum number of degrees of freedom, this type of system is convenient to use in many applications. The next generation of Earth- and Space-based large lightweight segmented telescopes will benefit of simple active mirrors, allowing an in-situ active shape error compensation with a minimal volume, weight and power consumption. For instance, Patterson [26] proposes a diluted, reconfigurable pupil telescope with a primary mirror constituted of several movable off-axis parabolas, whose asphericity depends on the required configuration. Still in the field of large telescopes, these simple deformation devices, generating OAP, can be coupled to stress polishing technique for the manufacturing of primary mirrors' segments. Another interesting application for the VOALA and COMSA concepts lies in zoom systems, composed of two active mirrors. Wick has developed a zoom with two 59-channels active mirrors [27]. In such a system, the mirrors need to generate focus for on axis beams and a combination of focus, astigmatism and coma for off-axis beams. These functions would be perfectly fulfilled by our systems with no more than 3 actuators per mirror. The compensation of field effects, non common path aberrations or optics deformation are also major applications: a simple correcting deformable mirror in the optical train will allow significant constraints relaxation on systems assembly and integration as well as on operational stability.

7 ACKNOWLEDGEMENTS

This work is performed with the support of a Ph.D grant from CNES (Centre National d'Etudes Spatiales) and Thales Alenia Space.

References

[1] P. Murdin (ed.), *Active Optics* (Institute of Physics Publishing, Bristol, 2000).

[2] R. N. Wilson, F. Franza, and L. Noethe, "Active optics. I. A system for optimizing the optical quality and reducing the costs of large telescopes.," J. Mod. Opt. **34**, 485–509 (1987).

[3] E.-D. Knohl, "VLT primary support system," Proc. SPIE **2199**, 271–283 (1994).

[4] M. Ferrari, "Development of a variable curvature mirror for the delay lines of the VLT interferometer," Astronomy and Astrophysics **128**, 221–227 (1998).

[5] B. Schmidt, "A coma-free telescope," Mitt. Hamburg Sternv. **7**, 15 (1932).

[6] G. Lemaitre, "New procedure for making Schmidt corrector plates," Appl. Optics **11**, 1630–1636 (1972).

[7] J. E. Nelson, G. Gabor, L. K. Hunt, J. Lubliner, and T. S. Mast, "Stressed mirror polishing. 2: Fabrication of an off-axis section of a paraboloid," Appl. Optics **19**, 2341–2352 (1980).

[8] J. W. Hardy, *Adaptive Optics for Astronomical Telescopes* (Oxford University Press, Oxford, 1998).

[9] R. J. Noll, "Zernike polynomials and atmospheric turbulence," J. Opt. Soc. Am. **66**, 207–211 (1976).

[10] L. E. Cohan, and D. W. Miller, "Integrated modeling for design of lightweight, active mirrors," Opt. Eng. **50**, 063003–063003-13 (2011).

[11] D. C. Redding, S. A. Basinger, A. E. Lowman, A. Kissil, P. Y. Bely, R. Burg, R. G. Lyon, et.al, "Wavefront sensing and control for a Next-Generation Space Telescope," Proc. SPIE **3356**, 758–772 (1998).

[12] M. Laslandes, M. Ferrari, E. Hugot, and G. Lemaitre, "In-flight aberrations corrections for large space telescopes using active optics," Proc. SPIE **7739**, 77393A–77393A-12 (2010).

[13] M. Laslandes, N. Rousselet, M. Ferrari, E. Hugot, J. Floriot, S. Vivès, G. Lemaitre, et.al, "Stress polishing of E-ELT segment at LAM: full-scale demonstrator status," Proc. SPIE **8169**, 816903–816903-10 (2011).

[14] S. P. Timoshenko, and S. Woinowsky-Krieger, *Theory of Plates and Shells* (McGRAW-Hill International Editions, New York, 1959).

[15] G. R. Lemaître, *Astronomical Optics and Elasticity Theory - Active Optics Methods* (Springer, Berlin, Heidelberg, 2009).

[16] J. C. Dainty, A. V. Koryabin, and A. V. Kudryashov, "Low-Order Adaptive Deformable Mirror," Appl. Optics **37**, 4663–4668 (1998).

[17] R. H. Freeman, and J. E. Pearson, "Deformable mirrors for all seasons and reasons," Appl. Optics **21**, 580–588 (1982).

[18] M. Laslandes, E. Hugot, M. Ferrari, and A. Liotard, "Mirror with mechanical device to generate optical aberrations" French Patent FR1102805 (2011).

[19] M. Laslandes, E. Hugot, and M. Ferrari, "Correcting device with a deformable mirror for the compensation of at least one aberration with a known evolution" French Patent FR1153390 (2011).

[20] I. Smith, and D. Griffiths, *Programming the Finite Element Method* (Fourth Edition, Wiley, Hoboken, 2004).

[21] J. Bonnans, J. Gilbert, C. Lemarechal, and C. Sagastizabal, *Numerical optimization: theoretical and practical aspects* (Springer, Berlin, Heidelberg, 2009).

[22] J. Lubliner, and J. E. Nelson, "Stressed mirror polishing. 1: A technique for producing nonaxisymmetric mirrors," Appl. Optics **19**, 2332–2340 (1980).

[23] E. Hugot, G. R. Lemaître, and M. Ferrari, "Active optics: single actuator principle and angular thickness distribution for astigmatism compensation by elasticity," Appl. Optics **47**, 1401–1409 (2008).

[24] E. Hugot, M. Ferrari, K. E. Hadi, P. Vola, J. L. Gimenez, G. R. Lemaitre, P. Rabou, et.al, "Active Optics: stress polishing of toric mirrors for the VLT SPHERE adaptive optics system," Appl. Optics **48**, 2932–2941 (2009).

[25] M. Laslandes, C. Hourtoule, E. Hugot, M. Ferrari, C. Lopez, C. Devilliers, A. Liotard, and F. Chazallet, "Space active optics: performance of a deformable mirror for in-situ wave-front correction in space telescopes," Proc. SPIE **8442** (2012).

[26] K. Patterson, S. Pellegrino, and J. Breckinridge, "Shape correction of thin mirrors in a recongurable modular space telescope," Proc. SPIE **7731**, 773121–773121-12 (2010).

[27] D. Wick, B. Bagwell, T. Martinez, D. Payne, S. Restaino, and R. Romeo, "Lightweight, Active Optics for Space and Near Space," in *Proceedings to The Advanced Maui Optical and Space Surveillance Technologies Conference,* 13 (The Maui Economic Development Board, Maui, 2006).

Appendix D

Space active optics: performance of a deformable mirror for in-situ wave-front correction in space telescopes

---

Space active optics: performance of a deformable mirror for in-situ wave-front correction in space telescopes

Marie Laslandes[a], Claire Hourtoule[a], Emmanuel Hugot[a], Marc Ferrari[a], Céline Lopez[b], Christophe Devilliers[c], Arnaud Liotard[c], Frederic Chazallet[d]

[a]CNRS and Aix Marseille Université - Laboratoire d'Astrophysique de Marseille
38 rue F. Joliot Curie, 13388 Marseille cedex 13, France;
[b]Thales SESO - 305 rue L. Armand, 13593 Aix en Provence, France;
[c]Thales Alenia Space - 100 bd du Midi, 06156 Cannes la Bocca, France;
[d]Shaktiware - 27 bd C. Moretti, 13014 Marseille, France.

ABSTRACT

MADRAS (Mirror Active, Deformable and Regulated for Applications in Space) project aims at demonstrating the interest of Active Optics for space applications. We present the prototype of a 24 actuators, 100 mm diameter deformable mirror to be included in a space telescope's pupil relay to compensate for large lightweight primary mirror deformation. The mirror design has been optimized with Finite Element Analysis and its experimental performance characterized in representative conditions. The developed deformable mirror provides an efficient wave-front correction with a limited number of actuators and a design fitting space requirements.

Keywords: Active optics, space telescope, large mirror deformation, wave-front error correction, deformable mirror

1. ACTIVE OPTICS IN THE SPACE CONTEXT

1.1 Use of active optics in astronomy

The purpose of active optics is to control mirrors' shape and deformation, and thereby the wave-front in optical instruments.[1] This control, at nanometrical precisions, makes possible the realization of high quality astronomical observations and facilitates the data reduction. Active optics is based on deformable mirrors, dedicated and optimized for specific needs. Allowing the use of very high optical quality components with complex shapes, variable or not, it presents many advantages and has various applications.[2] Three main fields of active optics can be defined: the maintaining of large mirrors optimal shapes,[3] the in-situ correction of optical aberrations with active deformable mirrors[4] and the generation of aspherical mirrors with stress polishing.[5] For about twenty years, active optics has allowed some technological breakthrough in astronomical instrumentation and is widely present on the large Earth-based telescopes. In this paper, we present the adaptation of active optics systems for future space observatories, dedicated to Earth or Universe study.

1.2 Evolution of space telescope and needs

Since their beginning, telescopes are evolving towards two main goals: increasing the collecting power and improving the angular resolution. These two characteristics directly depend on the optical aperture: access to finest observations would be possible with larger primary mirrors. However, the launch of space observatories imposes drastic constraints on satellites' weight and compactness. Thus, it becomes mandatory to use lightweight primary mirrors.[6,7] Up to 3 meters, these mirrors can be contained in a rocket cap in one piece. For larger diameters, it will not be possible to use monolithic mirrors with the actual rockets, segmented telescope concepts have to be adopted. Such as the James Webb Space Telescope, segmented systems could be launched folded and deployed in flight.[8] It is also envisaged to launch the instrument in separate pieces which would be assembled in flight.[9] Lightweight mirrors are sensitive to the environment variations, so the structure stability will become an important issue in telescopes' design. Thermal variation and absence of gravity will induce large mirrors' thermo-elastic

Further author information: marie.laslandes@oamp.fr

deformations, generating optical aberrations in the instrument.[10] An active telescope would be then required in order to keep optimal performance. Active optics systems used in Earth-based telescopes are not directly applicable for space instrumentation. Considerations about weight, size, power consumption, mechanical strength and reliability have to be addressed. Two different approaches are under study in order to compensate for these large lightweight mirrors deformations, privileging either the mirror weight or the system simplicity. The first solution consists in maintaining the primary mirror optimal shape with actuators under the optical surface, it requires an important number of actuators.[11,12] The second solution consists in performing the correction in a pupil relay, later in the optical train, it requires then a small active mirror with a limited number of actuators. While the first method is interesting for highly lightweight and flexible mirrors, the second one, simpler to carry out, is ideal for mirrors staying relatively rigid. A correcting mirror, designed for this second approach is presented in this paper.

1.3 MADRAS project

MADRAS (Miroir Actif Déformable et Régulé pour Applications Spatiales) is a collaborative project between Thales Alenia Space, Laboratoire d'Astrophysique de Marseille, Thales SESO and Shaktiware. It aims at developing a technological demonstrator of a correcting mirror for space telescopes.
As a study case, 3 meters class space telescopes are considered. Their expected primary mirror deformation are predicted thanks to telescopes' modeling and deformation data from flying telescopes. It gives the specifications for the MADRAS mirror: the system has to correct the 9 Zernike modes defined in Table 1, at amplitudes between 0 and 200 nm rms. The residual wave-front error after correction must be less than 5 nm rms for each modes separately and less than 10 nm rms for an actual wave-front error composed of a combination of these modes. Tip, tilt and focus are not addressed here, they will be corrected by a 5 degrees of freedom mechanism on the secondary mirror, adjusting the alignment. The correcting system addressing the effects of zero gravity and thermal dilatation, the required actuation frequency is low, the demonstrator works at 1 Hz.
The correcting system is designed taking into account space constraints. In order to have a light and compact system, the correction is done in a plane conjugated to the primary mirror, thus the aberrations generated by the large mirror deformation are compensated in a pupil relay of much more smaller dimensions. Considering 3-m class telescopes designs, the correcting mirror is 100 mm diameter, and the weight is limited to 5 kg. The system reliability and robustness are also studied: it is designed to survive space and launch environments.
The system performance are characterized in laboratory environment in order to improve its Technology Readiness Level to 4.

Table 1. Modes to correct with MADRAS and their maximum amplitudes (target precision of correction < 5 nm rms).

Mode	Maximum amplitude (nm rms)
Coma3	200
Astigmatism3	150
Spherical3	50
Trefoil5	30
Astigmatism5	30
Tetrafoil7	30
Trefoil7	30
Pentafoil9	30
Tetrafoil9	30

2. PRESENTATION OF THE CORRECTING MIRROR

2.1 Mirror geometry

The chosen mirror geometry has been developed by Lemaitre.[13] It is a piece of Zerodur, made up of a circular pupil with an external thicker ring and 12 arms. The optical surface is deformed through 24 actuators applying discrete forces on either sides of each arm. In addition a central clamping is holding the system (Figure 1).

This design is based on the similarity between the Zernike polynomials used in the optical aberrations theory[14] and the Clebsch polynomials used in the elasticity theory.[15] It allows the generation of Zernike defined by $n = m$ and $n = m + 2$, n and m being the radial and azimuthal polynomials' orders. With 12 arms, m is included between 0 and 6. Furthermore, the central clamping allows the generation of the spherical aberration ($m = 0$ and $n = 4$).
In this design, forces to deform the mirror are applied far from the optical surface. This way, it avoids the generation of high spatial frequencies errors due to over-constraints at the forces location, there is no actuator print-through. Moreover, it decouples the number of actuators from the mirror diameter: the number of required actuators is only driven by the maximal spatial frequency to be corrected. Finally, this design is not associated to one actuator technology: every actuator applying discrete forces can be used with this kind of mirror.

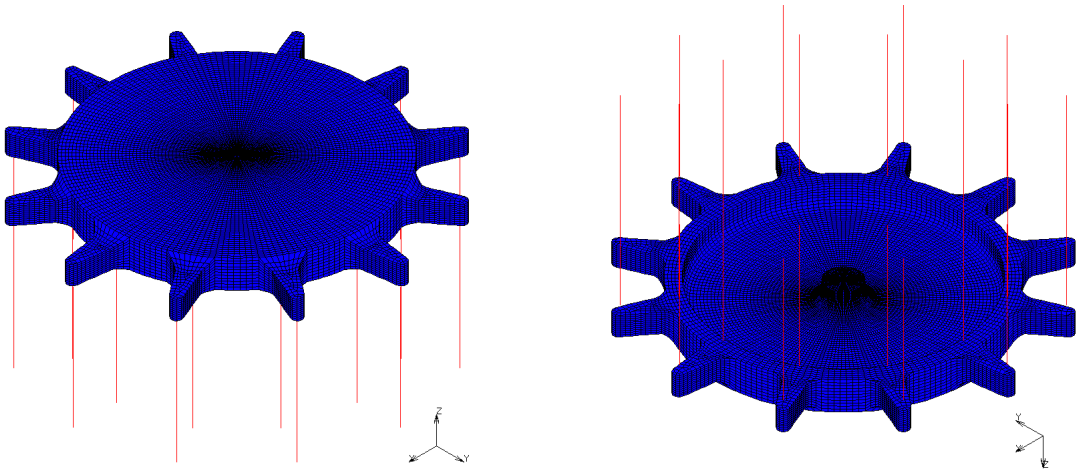

Figure 1. Finite Element Model of the MADRAS mirror (actuator are represented by springs, in red) - 63708 hexaedrical elements, 77979 nodes.

2.2 Optimization with Finite Element Analysis

The mirror is in Zerodur, this material has been chosen for its low Coefficient of Thermal Expansion, ideal for a space use.[16] The system dimensions have been optimized in order to meet the correction specifications but also to ensure the system mechanical strength. The optimization is done with Finite Element Analysis and is based on the system Influence Functions (IF).
An Influence Function is defined as the wave-front resulting from the unit command on one actuator.[17] With 24 actuators, the studied system has 24 IF, constituting a characteristic base B which is used to decompose the wave-front error to correct ϕ_{in}:

$$\phi_{in} = B\alpha, \tag{1}$$

with α a set of 24 coefficients corresponding to the actuators' commands.
These coefficients are determined by computing the generalized inverse of B:

$$\alpha = (B^t B)^{-1} B^t \phi_{in}. \tag{2}$$

Thus, the wave-front actually compensated by the system is:

$$\phi_{cor} = B(B^t B)^{-1} B^t \phi_{in}, \tag{3}$$

and the residual wave-front after correction:

$$\phi_{out} = \phi_{in} - \phi_{cor}. \tag{4}$$

For a given geometry, a Finite Element model is created and the Influence Functions are recovered by applying a unit displacement at each actuator location, while the other are fixed. Then, as described in Figure 2, the

generation of the 9 specified Zernike modes is characterized by determining:
- the actuators' commands α with the projection of the mode on the IF base (Eq. 2),
- the residues of correction ϕ_{out} with the reconstruction of the corrected wave-front (Eq. 4),
- the resulting stress σ with the injection of the actuators commands on the finite element model.
The goal of the optimization is to minimize these 3 criterions for each specified mode. A classical least square algorithm is used to converge to the optimal geometry. The optimization output parameters are the pupil thickness, the outer ring dimensions (thickness and diameter) and the arms dimensions (thickness and length). A coefficient β_i is allocated to each mode according to its maximum amplitude to be corrected (Table 1): Coma, Astigmatism and Spherical modes have more weight in the optimization. At the end, the quantity minimized by the least square algorithm is γ:

$$\gamma(geometry) = \sum_i \beta_i[||\phi_{out}||^2 + \sigma_{max} + \alpha_{max}], \tag{5}$$

with i varying from 1 to 9, representing the specified Zernike modes.

Once the optimal system geometry is defined, the mechanical and optical behavior is fully characterized with FEA. The precision of correction (ϕ_{out}) is known for each modes, such as the required actuators' stroke (α) and the level of stress in the mirror (σ). The worst case study allows the system validation : it consists in the correction of all the specified mode at their maximum amplitude, in the same time and orientation. In such a case, the characteristics computed for each modes are added. The expected precision of correction is then 10.2 nm rms, for a specification at 10 nm rms. The maximum level of stress in the Zerodur is expected at 5 MPa, for an elastic limit at 10 MPa. Both values are acceptable. This study also gives the maximum actuators' required stroke, 6.8 μm, which would drive the actuators choice.

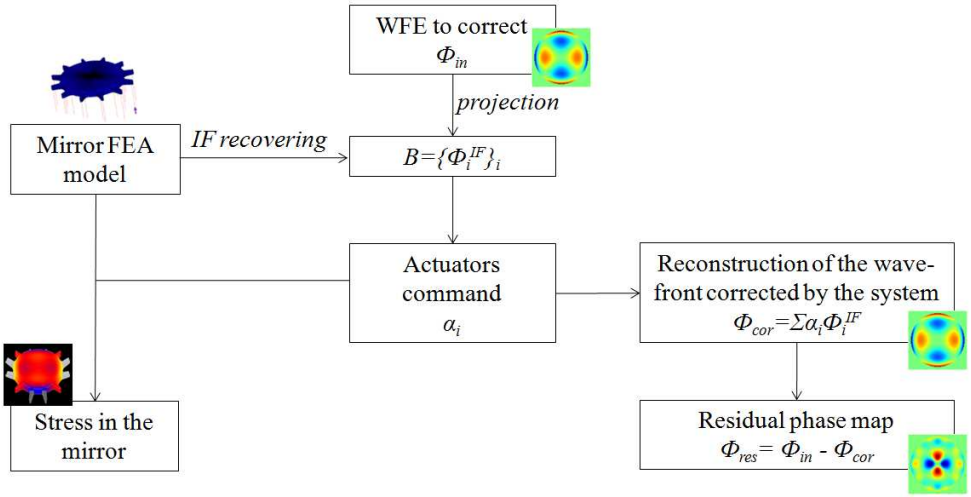

Figure 2. Method for design optimization, based on the finite element model's influence functions: the three minimized criterions are the stress in the mirror, the actuators commands and the residual wave-front error.

2.3 Integrated system

The correcting system is composed of three main parts: the mirror in Zerodur, the supporting structure in Invar and the 24 actuators. The overall system weighs 4 kg and is 80 mm height, for a diameter of 130 mm. As seen in the previous section, the mirror geometry has been optimized with Finite Element Analysis. The pupil diameter is 90 mm, for a thickness of 3.5 mm. The mirror is held on its center by a cone, linked to a rigid reference plate. The 24 actuators are clamped between the mirror's arms and the reference plate. They are piezoelectric PZT chosen to have the stroke specified by FEA results: they can apply ± 10 μm displacement, with a maximum voltage of 80 V. They are connected with a proximity electronics which is wired to an electronic housing. To

finish, the system is clamped on a tip/tilt plate with three bipods. This fixation device has been designed in order not to stress the system.
Except for the electronics, the entire system is designed for a space use. The entire system is modeled with FEA, in order to verify that the structure does not change the correcting performance or the mirror mechanical behavior. A dynamic analysis is also performed to simulate the launch vibrations.

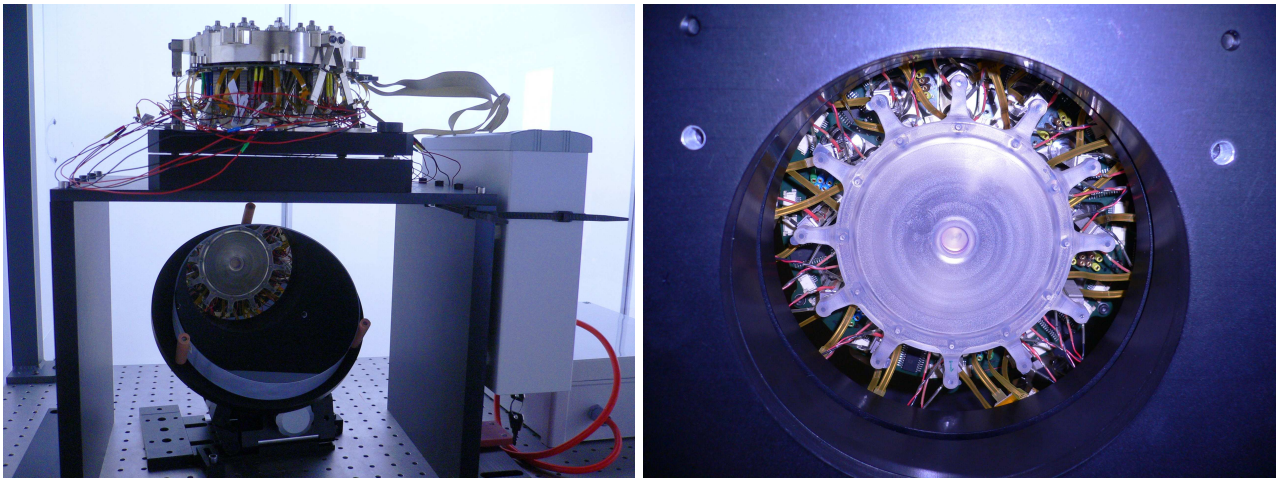

Figure 3. Integrated system on its test platform and optical surface viewed from below.

3. INTERFEROMETRICAL TESTS

Once the system is designed and integrated, a first round of test is conducted with a Fizeau interferometer, directly measuring the optical surface deformation. The mirror is tested horizontally, facing down, because it is the best configuration regarding gravity effects.

3.1 Influence functions and eigen modes

The 24 system's Influence Function are measured by applying a push/pull to each actuator while the others are at rest. The recovered IF (Figure 4) are compared to the ones expected from FEA. As we can see in Figure 6, their shapes are really similar. The only notable difference comes from their amplitudes: the ratio between internal and external IF is two times smaller on the measurements than on the simulation. This probably comes from the fact that the internal actuators are more constrained so their effect is minimized. This will not limit the mirror functioning because the stroke required for the internal actuators is small compared to the actuators available stroke.
The system eigen modes are determined by performing a Singular Value Decomposition on the IF base. As we can see in Figure 5, the eigen modes are well similar to Zernike polynomials.

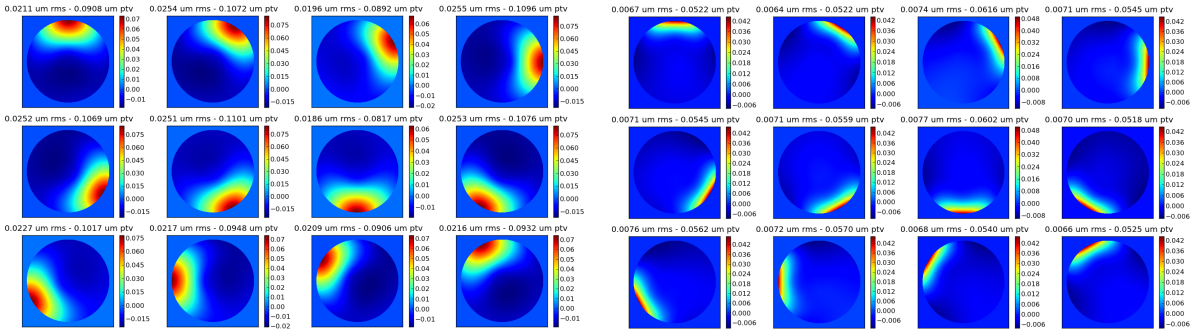

Figure 4. Mirror's Influence Functions, measured with a Fizeau interferometer [μm].

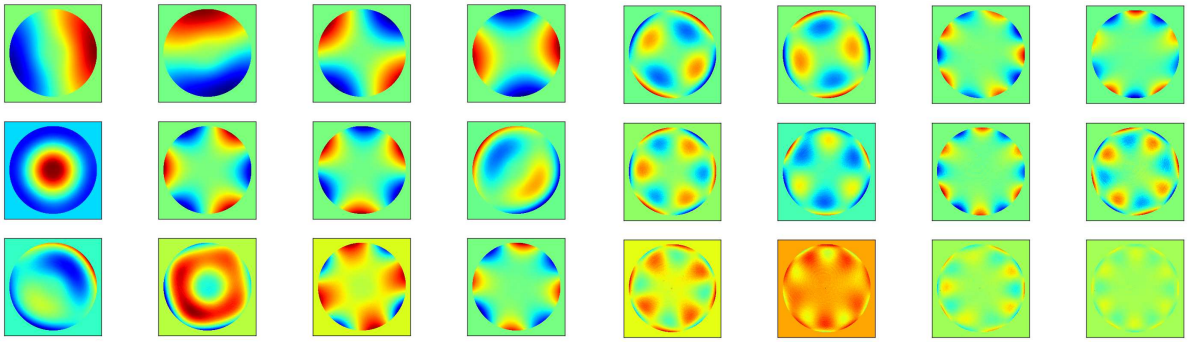

Figure 5. System's Eigen Modes, sorted from the less to the more energetical, deduced from a Singular Value Decomposition of the measured IF base.

3.2 Expected correction performance

As explained in Section 2.2, each specified mode, at its maximum amplitude, is projected on the measured IF base to determine the mirror correction capability. As the IF are similar to the FEA results, the system performance is well recovered (Figure 6). All the modes are corrected with a precision better than 5 nm rms, except from the spherical and pentafoil which are slightly above. The residuals of spherical generation come from the central clamping and the residuals of pentafoil are due to the symmetry mismatch between the system and the mode.
The precision of correction of a representative Wave-Front Error (WFE) is deduced from these results. The WFE is defined as a random combination of the 9 Zernike modes, weighted by their maximum specified amplitude. In the worst case, the total residuals will be 11.1 nm rms, to be compared to the 10.2 nm rms expected from simulation. Then the mean precision of correction is determined by studying the correction of 1000 random WFE: 6.3 nm rms, with a standard deviation of 1.5 nm rms.

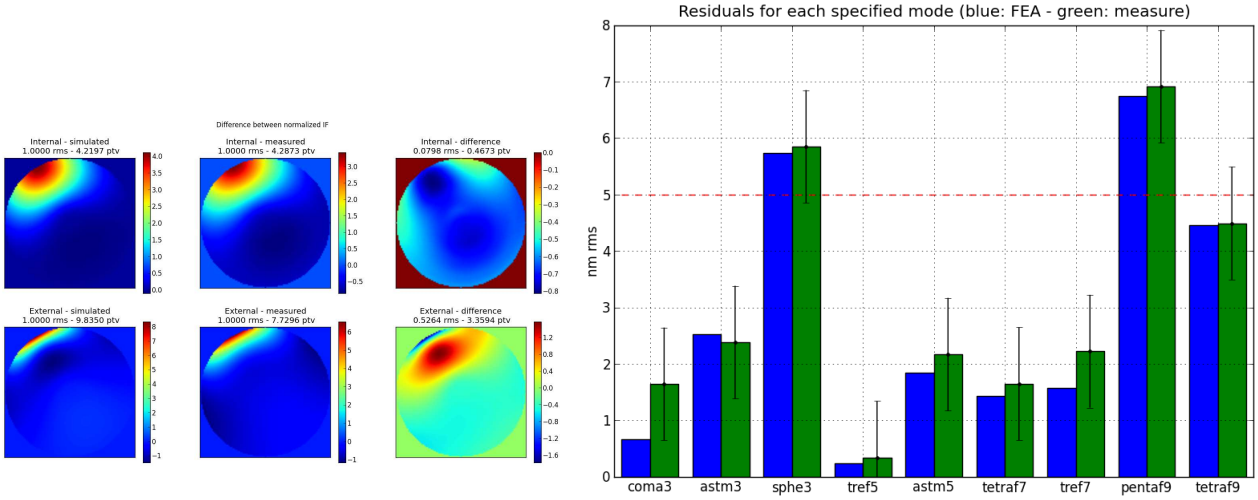

Figure 6. Comparison between simulation and measurement: Left: Difference between simulated and measured Influence Functions (on normalized maps) - Right: Residual WFE computed for each specified modes, with simulated and measured IF (errorbars correspond to the interferometer precision: ± 1 nm).

3.3 Dead actuator study

With the knowledge of the Influence Functions, the impact of a dead actuator can be characterized. A dead actuator is defined as a free point: the piezoelectric is not supplied any more but as it has a certain stiffness, the actuation point will follow the deformation, which is less perturbing than a clamped point.
A dead actuator occurrence can be modeled in two different ways, depending if there is a system recalibration or not. Without recalibration, the mode to be corrected is still projected on the 24 IF but the command of

the dead actuator is forced to 0 for the wave-front reconstruction. With a recalibration, the mode projection is done on the 23 remaining IF so the actuator absence will be compensated by its neighbors. This case being advantageous, we study it in more details.
The impact of a dead actuator will depend on the actuator location and on the mode to be corrected. The performance of correction is calculated for each mode and for each actuator, Figure 7 presents the mean resulting residuals and the worst and best cases, compared to the performance of the fully functional system. The loss of one actuator deteriorates the performance in a reasonable way: the correction stays within the specifications. Then the evolution of the mean correction performance with the number of dead actuators is studied: for a given number of dead actuators, 50 random sets of defective actuators are drawn and the correction of 100 random WFEs is performed for each deteriorated IF bases (Figure 7). Logically, the more there are dead actuators, the more the correction is damaged, but we can see that with 2 dead actuators the system is still well functioning: the mean precision is 10.7 nm rms, with a standard deviation of 2.1 nm rms. As a conclusion, we can say that such a system has an intrinsic redundancy: there are 24 actuators for 17 modes to correct. This fact, ensuring the system robustness and reliability, is really interesting and important for a space use.

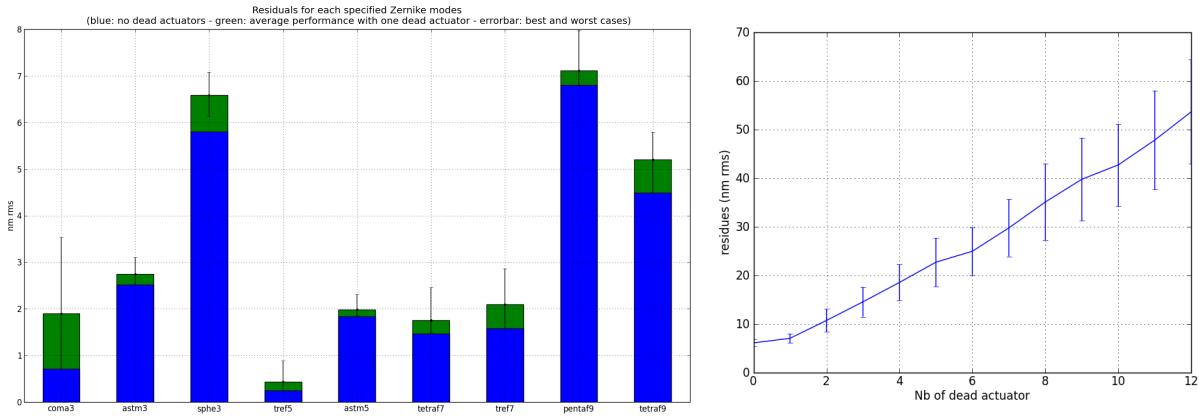

Figure 7. System performance with dead actuators (FEA results): Left: comparison of the precision of correction of a system fully functional and a system with one dead actuator - Right: evolution of the mean expected residual wave-front with the number of dead actuator (each point is a statistic on 50 random sets of dead actuators and 100 random WFE for each set).

4. ACTIVE LOOP PERFORMANCE

4.1 Test bed design

With the interferometrical tests, simulated and measured performance have been correlated. The mirror is actually tested in a representative configuration in order to validate its functioning in closed loop. The test bed is composed of a telescope simulator and the active correction loop. Shack-Hartmann wave-front sensing and imaging Point Spread Function will allow a complete validation of the mirror in term of wave-front precision. While functioning, the mirror deformation is monitored with the Fizeau interferometer and there are force sensors on the actuators, in order to validate the system mechanical behavior.
The telescope simulator is an adaptive optics loop with a 88-actuators Deformable Mirror (DM) and a Shack-Hartmann wave-front sensor (WFS). This first DM defines the entrance pupil plane, it simulates the telescope primary mirror and its deformations. This loop will inject calibrated Wave-Front Errors on MADRAS mirror, which is conjugated to the first DM. The active correction loop is composed of the MADRAS mirror, a second Shack-Hartmann WFS and a Real Time Computer which analyzes the measured wave-front and commands the mirror in order to converge to a flat wave-front. Two cameras, located in image plans before and after the correction, allow characterizing the correction effects on the PSF.

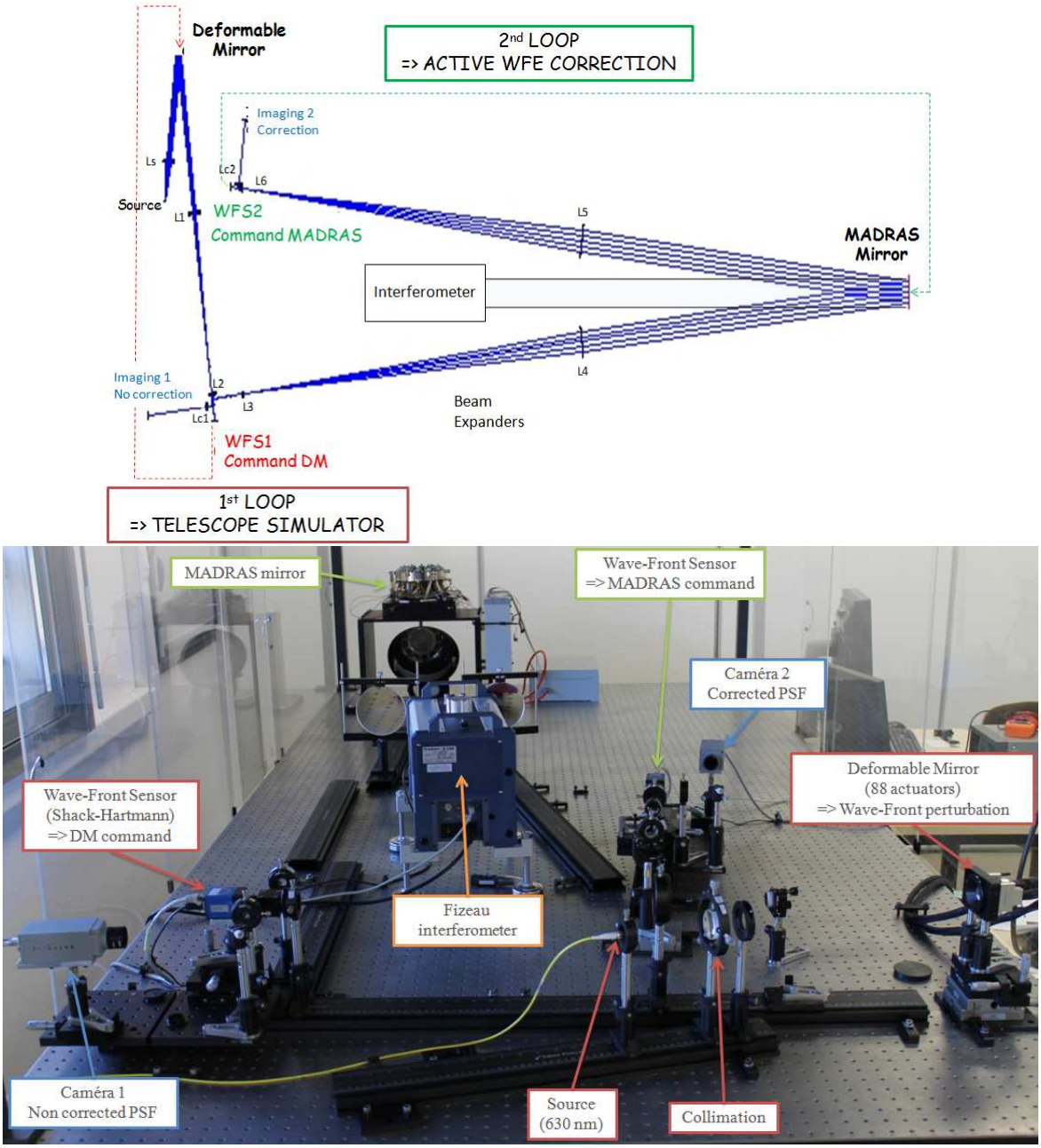

Figure 8. MADRAS test-bed: optical design and picture.

4.2 Calibration

The precision of the wave-front injected on our test-bed with the first loop simulating the telescope has been characterized with wave-front measurements: flat wave-front and specified Zernike modes are generated with a residual error of 5 nm rms.

The active system calibration consists in performing an interaction matrix: the influence function are measured with the wave-front sensor in order to compute a command matrix. To simulate the external handling of tip, tilt and focus, three virtual influence functions, corresponding to these three modes are added to the interaction matrix.

The loop noise is characterized by correcting the turbulent phase: a wave-front error is measured at $\pm$ 3.4 nm

rms. This precision is reduced to ± 0.5 nm rms by averaging 50 measurements.
Due to the actuators integration, MADRAS optical surface contains shape errors, inducing a WFE of 200 nm rms, mainly composed of focus, astigmatism and coma. Moreover, there are some aberrations in the optical path, due to misalignment, inducing a WFE of 18 nm rms. For an efficient PSF measurement, the first step is to correct these WFEs seen by the Wave-Front Sensor. This flattening is obtained with an error of 12.2 nm rms (see Figure 9, left). This residual wave-front will then be the target for the next corrections.

4.3 Mode correction

Once the reference taken and the test-bed characterized, we send the specified Zernike mode with the generation loop and we study the correction with the MADRAS system. The measured performance, presented on the right of Figure 9, are really satisfactory: the expected precision of correction are recovered for most of the modes.
Coma and Spherical modes are less well corrected, due to filtering in the command matrix. The mathematical expression of coma is linked to tilt, and our method to filter this mode probably impact the coma correction. The same problem appears with the focus filtering, impacting the spherical correction. We are currently investigating other methods to define our command matrix in order to improve the performance.
In conclusion, all of the specified Zernike modes are corrected with a precision better than 8 nm rms. As expected from simulations, the correction of Astigmatism3&5, Trefoil5&7 and Tetrafoil7&9 is efficient, with a precision below 5 nm rms, and Pentafoil9 correction precision is around 7 nm rms. Coma and Spherical are currently corrected with a precision of respectively 6 and 8 nm rms, it will be improved by working on the command matrix.

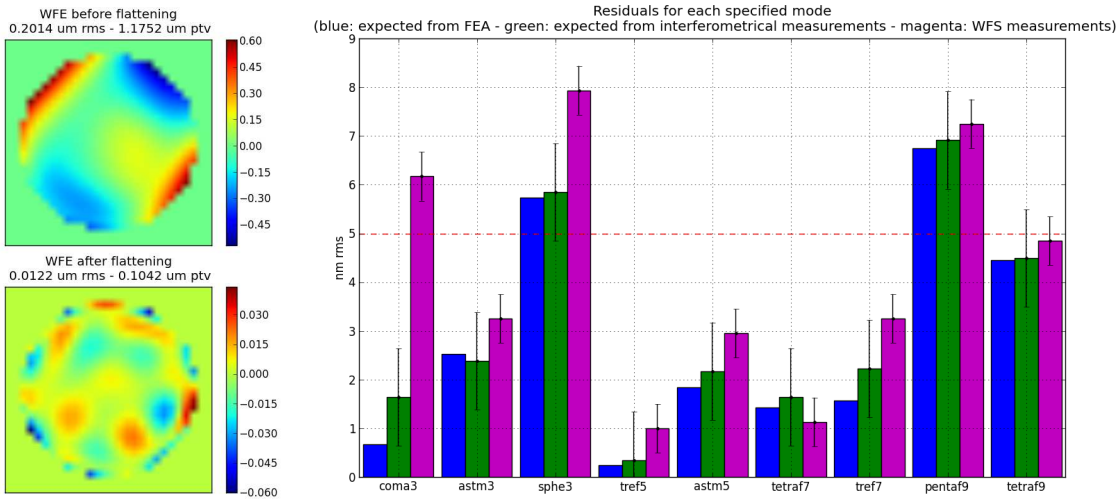

Figure 9. Closed loop MADRAS performance: Left: WFE before and after flattening (tip, tilt and focus subtracted) - Right: mode correction, compared to expected performance (errorbars correspond to the interferometer and WFS precisions).

4.4 Representative wave-front error correction

After having demonstrated the system capacity to correct each specified modes separately, we generate a more representative WFE. The correction of a random combination of the specified modes will validate the system's linearity and its correction performance regarding the deformation expected in space telescope.
Figure 10 presents a correction case with the injected wave-front error, the residual wave-front after correction and the corresponding PSFs. The gain for the PSF measurement is obvious and, with a residual wave-front of 8.7 ± 0.5 nm rms, we are within the 10 nm rms precision specification.
The mirror behavior is linear: if the injected WFE is a combination of Zernike modes, $\phi_{in} = \sum_i A_i Z_i$, the residual wave-front ϕ_{res} can be deduced from each specified modes measured precision of correction ($\phi_{res,i}$, presented in

Figure 9):

$$\phi_{res} = \sqrt{\sum_i \left(\frac{A_{spec,i}\phi_{res,i}}{A_i} \right)^2}, \tag{6}$$

with $A_{spec,i}$ the maximum amplitude specified for each mode.
Thus, a statistical study on 1000 random WFEs is performed, giving the mean residual wave-front after correction. MADRAS system is able to compensate for the deformations expected in space telescopes with a mean precision of 8.2 nm rms, with a standard deviation of 1.8 nm rms.

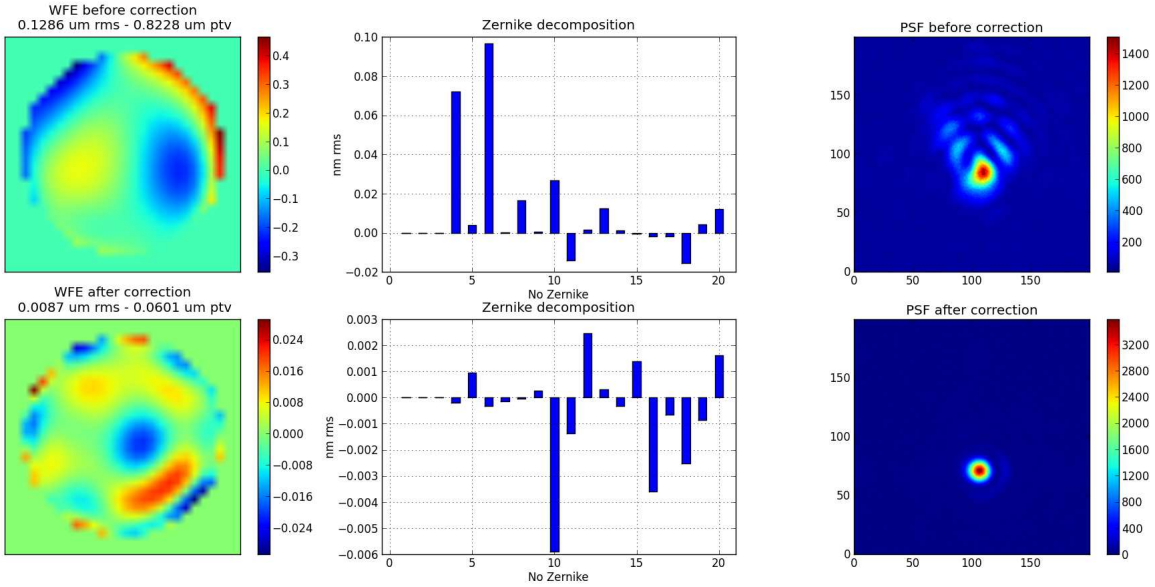

Figure 10. Correction of a random WFE (the given wave-front is an average of 100 measurements, tip, tilt and focus substracted).

5. CONCLUSION AND PERSPECTIVES

MADRAS project has been initiated to demonstrate the possibility and the interest of inserting a correcting active mirror in the next generation of space telescopes. The chosen design allows an efficient correction of 17 Zernike polynomials with only 24 actuators. The mirror is in Zerodur and its supporting system in Invar. It is light (4 kg) and small (80 mm high and 130 mm diameter). Such a design has been optimized with Finite Element Analysis in order to ensure the correction performance but also the mechanical strength and the system survival in launch and space environments. The correcting system has been realized and tested, demonstrating its ability to compensate for large lightweight primary mirrors deformations in space.
We have shown a really good match between simulation and measurement, validating the design method. The first experimental results demonstrate promising correction performance: most of the modes are individually corrected with a precision of 5 nm rms and statistical analysis of the correction of random representative WFEs gives the mean precision of correction around 8 nm rms. A study on the dead actuator has shown that the system performance are not too much impacted by the loss of 2 actuators. This redundancy is interesting for the system reliability and robustness.
With piezoelectric actuators, it is important to work in closed loop but if needed, the actuator technology could be changed in order to work in open loop and to converge to the required mirror shape in only one iteration.
With this project, the presented deformable mirror technology has reached a Technology Readiness Level 4. The next step is then the TRL5 with a validation in space environment.

ACKNOWLEDGMENTS

This study is performed with the support of a Ph.D grant from CNES (Centre National d'Etudes Spatiales) and Thales Alenia Space, within a project of the Research and Industry Optical Cluster 'PopSud/Optitec'.

REFERENCES

1. Murdin, P., ed., [*Active Optics*], Encyclopedia of Astronomy and Astrophysics (Nov. 2000).
2. Freeman, R. H. and Pearson, J. E., "Deformable mirrors for all seasons and reasons," *Applied Optics* **21**, 580–588 (Feb. 1982).
3. Wilson, R. N., Franza, F., and Noethe, L., "Active optics. I. A system for optimizing the optical quality and reducing the costs of large telescopes.," *J. Mod. Opt., Vol. 34, No. 4, p. 485 - 509* **34**, 485–509 (1987).
4. Ferrari, M., "Development of a variable curvature mirror for the delay lines of the VLT interferometer," *Astronomy and Astrophysics* **128**, 221–227 (Feb. 1998).
5. Lubliner, J. and Nelson, J. E., "Stressed mirror polishing. 1: A technique for producing nonaxisymmetric mirrors," *Applied Optics* **19**, 2332–+ (July 1980).
6. Feinberg, L., Cohen, L., Dean, B., Hayden, W., Howard, J., and Keski-Kuha, R., "Space telescope design considerations," *Optical Engineering* **51**, 011006 (Jan. 2012).
7. Postman, M., Brown, T., Sembach, K., Giavalisco, M., Traub, W., Stapelfeldt, K., Calzetti, D., Oegerle, W., Michael Rich, R., Phillip Stahl, H., Tumlinson, J., Mountain, M., Soummer, R., and Hyde, T., "Advanced Technology Large-Aperture Space Telescope: science drivers and technology developments," *Optical Engineering* **51**, 011007 (Jan. 2012).
8. Lightsey, P. A., Atkinson, C., Clampin, M., and Feinberg, L. D., "James Webb Space Telescope: large deployable cryogenic telescope in space," *Optical Engineering* **51**, 011003 (Jan. 2012).
9. Patterson, K., Yamamoto, N., and Pellegrino, S., "Thin deformable mirrors for a reconfigurable space telescope," *53rd AIAA Structures, Structural Dynamics, and Materials Conference* (2012).
10. McComas, B. K., *Configurable adaptive optics for the correction of space-based optical systems*, PhD thesis, University of Colorado at Boulder (2002).
11. Redding, D., Coulter, D., and Wellman, J., "Active Optics for Low-Cost Astronomical Space Telescopes," in [*American Astronomical Society Meeting Abstracts*], *American Astronomical Society Meeting Abstracts* **219**, 136.05 (Jan. 2012).
12. Cohan, L. E. and Miller, D. W., "Integrated modeling for design of lightweight, active mirrors," *Optical Engineering* **50**, 063003–+ (June 2011).
13. Lemaître, G. R., "Active Optics: Vase or Meniscus Multimode Mirrors and Degenerated Monomode Configurations," *Meccanica* **40**, 233–249 (2005).
14. Noll, R. J., "Zernike polynomials and atmospheric turbulence," *Journal of the Optical Society of America (1917-1983)* **66**, 207–211 (Mar. 1976).
15. Timoshenko, S. P. and Woinowsky-Krieger, S., [*Theory of Plates and Shells*], Engineering Mechanics Series, McGRAW-Hill International Editions (1959).
16. Döhring, T., Jedamzik, R., Thomas, A., and Hartmann, P., "Forty years of ZERODUR mirror substrates for astronomy: review and outlook," in [*Society of Photo-Optical Instrumentation Engineers (SPIE) Conference Series*], *Society of Photo-Optical Instrumentation Engineers (SPIE) Conference Series* **7018** (July 2008).
17. Paterson, C., Munro, I., and Dainty, J. C., "A low cost adaptive optics system using a membrane mirror," *Optics Express* **6**, 175–+ (Apr. 2000).

List of Figures

List of Tables

Merci! Thanks!

Après avoir passé 3 ans à travailler sur cette thèse, quelques mois à rédiger ce manuscrit, quelques semaines à préparer la soutenance, quelques heures à soutenir, quelques (beaucoup?) verres pour fêter ça et quelques jours pour récupérer, voici venu le temps des remerciements!

Firstly, a few more words in english to thank Sergio and Lars for taking the time (and maybe the energy!) to review my thesis. Thanks also to Hugues, Thierry, Vincent and Christian for participating in the evaluation of my thesis. I have really appreciated the comments and the encouragements. I'd also like to take this opportunity to thank the CNES and TAS for funding my PhD and for their trust.

Bien évidemment, j'aimerais dire 1000 mercis à l'homme aux 1000 casquettes, Marc, grâce à qui j'ai pu faire cette thèse dans de superbes conditions. Un directeur de thèse de l'espace disponible et efficace au laboratoire et au comptoir, ça ne court pas les rues! Juste pour le faire râler, je dirais bien maintenant 999 mercis à Manu, mais il mérite bien ses 1000 mercis aussi (+1 pour les couchers de soleil!). Le temps passé à cliquer sur des hexaèdres bleus, à faire des équations, ou à aligner des optiques fut tout aussi apprécié que les séances de racontage de vie!
Enfin bref, j'ai beaucoup aimé travailler avec vous 2 et je suis très heureuse de l'amitié qui en découle (snif, séquence émotion!). Les 3M on fait une bonne équipe, et j'espère bien qu'on aura encore de nombreuses occasions de le prouver.

Un grand grand merci également à Claire pour les super moments passés dans l'antre de MADRAS, dans le noir par 40 degrés! Le miroir aurait eu du mal à se déformer sans toi et moi j'aurais eu du mal à ne pas péter les plombs sans ton relativisme et ta bonne humeur!
Rien n'aurait été aussi bien non plus sans Mamadou mon funky co-bureau et Zalpha ma co-bureaute qui le vaut bien! L'ambiance toujours joyeuse de ce bureau (et en dehors!) était un vrai plaisir, heureusement que j'étais là pour râler!!
Un grand merci également à mon personnage d'héroic fantasy préféré, Thierry de la Comté pour les cafés du matin, les gros coups de pouce de l'après-midi et les bières du soir!
Un spécial kifikralala pour Princess Manal avec qui j'ai pu partager les bonheurs et les galères de la thèse.
Je souhaite aussi bien du courage à Marion et Clément qui reprennent vaillamment le flambeau de l'optique active spatiale, en espèrant ne pas vous avoir laissé trop de blagues, je vous remercie pour les moments bien sympas passés avec vous qui ont agrémentés ma fin de thèse!
Enfin, je voudrais remercier tout le reste du LOOM: Gérard, Johan, Kacem, Fred, Alain, Pierre et consort, c'était bien agréable de travailler dans cette sympathique équipe!

Puisque l'on parle d'opticiens, j'aimerais aussi remercier Amandine du pays des lapins bleus, Seb le plan pupille, David ou l'homme qui sait parler à la police américaine, Kjetil et Fabrice pour leur

gentillesse, leur sympathie (question ouverte: est ce qu'on peut être sympa sans être gentil?) et pour leur soutien.

Ces 3 années passées au LAM furent pleines de belles rencontres et de bons souvenirs, sans quoi la thèse aurait été beaucoup plus difficile, et beaucoup moins drôle! Merci donc à Anne-Laure et son talent pour la psychologie et la diplomatie, Julien et sa détermination à me caser avec tout ce qui bouge, Johan et ses chemises, Alex et ses bouteilles de vin, Mathilde et ses mojitos, Elo et ses potins, Laure et ses cours de sports, Arthur et son humour parfois douteux, Steph et ses coups de chance, Aurélie et Romain (le couple de l'année 2012), Jean et ses bons plans culturels (il en faut bien un peu!), Benj et son blanc d'oeuf dans le pisco, Christian et ses manucures, Vincent et son bip-bip, et à tout plein d'autres qui ont participé à faire briller le soleil marseillais!

Et parce qu'il n'y a pas que le labo dans la vie, un énorme merci à Claire et Marie, toujours là pour se marrer et se changer les idées, vous êtes les meilleures!
Merci à tous les autres fidèles du Petit Nice, du O'Malley ou d'ailleurs avec qui j'ai passé des super moments (dont je me rappelle pas forcément d'ailleurs!): Benoit, Emeline, Gwen, Juliana, Isa, Marie (encore une!), Ben le réparateur de four, Steph, Laure et plein d'autres.

Et je n'oublie bien sûr pas les vieux de la vieille, ceux qui m'ont entendu dire "je ferais jamais de prépa" ou "je ferais jamais de thèse", ceux sans qui rien n'aurait été pareil:
Marianne et Damien, on en a fait du chemin depuis les bancs de Marlioz, peut être que toute cette histoire a commencé grâce à mes fameux 2 centième de points de plus au bac!!
Les survivantes du CPP: Tillie la psychologue avocate ingénieur instit' et Audrey la supraconductiviste, heureusement que vous étiez là, toujours présentes et souvent dans les mêmes galères que moi, c'est toujours sympa d'avoir des amis solidaires!!
Daniel les bons plans, avec qui j'ai fait mes premiers pas dans le spatial et qui a grandement participé à mon futur, je te revaudrais ça!
Mes MAPLV from PG: Aurélie avec qui j'installerais bientôt des bâtiments à énergie positives sur la lune, Laetitia mon parasite préféré chez qui j'ai bien squatté pendant mes séjours parisiens, Blandinette la plus chouette et Véro qui nous fait toujours bien rire!

Et le mot de la fin revient à ma famille avec une mention spéciale pour mes parents qui m'ont toujours encouragé à faire ce que je voulais. Merci à eux pour m'avoir si bien soutenu (et aussi pour ne pas s'être endormi pendant ma soutenance)! Merci à Noémie pour m'avoir hébergé pendant mes 2 premières semaines à Marseille et pour avoir squatté chez moi pendant les 2 dernières années!! Merci à Léo pour m'avoir motivé en gagnant en 3 semaines plus que moi en 3 ans! Et merci à ma mini Emmy qui a grandi en même temps que ma thèse, j'espère qu'elle sera plus rigolote!

Je finirais par un remerciement général, merci donc à tous ceux qui aiment tellement les photons et qui ont trouvé la motivation de lire en totalité ou en partie ce manuscrit!

Abstract

The need for both high quality images and light structures is one of the main driver in the conception of space telescopes. An efficient wave-front control will then become mandatory in the future large observatories, ensuring the optical performance while relaxing the specifications on the global system stability. Consisting in controlling the mirror deformation, active optics techniques can be used to compensate for primary mirror deformation, to allow the use of reconfigurable instruments or to manufacture aspherical mirror with stress polishing. In this manuscript, the conception of active mirrors dedicated to space instrumentation is presented.

Firstly, a system compensating for large lightweight mirror deformation in space, is designed and its performance are experimentally demonstrated. With 24 actuators, the MADRAS mirror (Mirror Actively Deformed and Regulated for Applications in Space) will perform an efficient wave-front correction in the telescope's pupil relay.
Secondly, a warping harness for the stress polishing of the 39 m European Extremely Large Telescope segments is presented. The performance of the process is predicted and optimized with Finite Element Analysis and the segments mass production is considered.
Thirdly, two original concepts of deformable mirrors with a minimum number of actuators have been developed. The Variable Off-Axis parabola (VOALA) is a 3-actuators system and the Correcting Optimized Mirror with a Single Actuator (COMSA) is a 1-actuator system.

The active systems presented in this manuscript offer many advantages for the future large space-borne observatories: limited number of degrees of freedom, compactness, low weight, robustness and reliability. They will allow some technological breakthroughs and lead to innovative telescope architectures.

Résumé

Le besoin tant en haute qualité d'imagerie qu'en structures légères est l'un des principaux moteurs pour la conception des télescopes spatiaux. Un contrôle efficace du front d'onde va donc devenir indispensable dans les futurs grands observatoires spatiaux, assurant une bonne performance optique tout en relâchant les contraintes sur la stabilité globale du système. L'optique active consiste à contrôler la déformation des miroirs, cette technique peut être utilisée afin de compenser la déformation des grands miroirs primaires, afin de permettre l'utilisation d'instrument reconfigurable ou afin de fabriquer des miroirs asphériques avec le polissage sous contraintes. Dans ce manuscrit, la conception de miroirs actifs dédiés à l'instrumentation spatiale est présentée.

Premièrement, un système compensant la déformation d'un grand miroir allégé dans l'espace est conçu et ses performances sont démontrées expérimentalement. Avec 24 actionneurs, le miroir MADRAS (Miroir Actif Déformable et Régulé pour Applications Spatiales) effectuera une correction efficace du front d'onde dans un relais de pupille du télescope.
Deuxièmement, un harnais de déformation pour le polissage sous contraintes des segments du télescope géant européen de 39 m (E-ELT) est présenté. La performance du procédé est prédite et optimisée avec des analyses éléments finis et la production en masse des segments est considérée.
Troisièmement, deux concepts originaux de miroirs déformables avec un nombre minimal d'actionneurs ont été développés. VOALA (Variable Off-Axis parabola) est un système à trois actionneurs et COMSA (Correcting Optimized Mirror with a Single Actuator) est un système à un actionneur.

Les systèmes actifs présentés dans ce manuscrit offrent de nombreux avantages pour une utilisation dans les futurs grands observatoires spatiaux: nombre de degrés de liberté limités, compacité, légèreté, robustesse et fiabilité. Ils permettront d'importantes ruptures technologiques et l'apparition d'architectures de télescope innovantes.